ANALYSIS AND TESTING OF A TAPERED END CONNECTION FOR LASER WELDED STEEL SANDWICH PANELS

for

Dr. Roshdy Barsoum, Program Officer,

Office of Naval Research

One Liberty Center
875 North Randolph Street, Suite 1425
Arlington, VA 22203-1995

By

Serdar Yorulmaz,	Graduate Research Assistant, Mechanical Engineering, University of Maine
Dr. Larry Thompson,	Principal Research Engineer, Applied Thermal Sciences
Dr. Vincent Caccese,	Professor of Mechanical Engineering, University of Maine (PI)
Dr. Senthil S. Vel	Assoc. Professor of Mechanical Engineering, University of Maine (Co-I)

Grant No: N00014-05-1-0735

ATS subcontract No: UM-591

Report No. C-2004-015-RPT-04

August 15, 2009

ABSTRACT

This report summarize the analysis and cyclic testing of a laser welded steel sandwich panel end connection. Also included are monotonic tests of stake welded lap shear coupons with welds oriented both longitudinally and transverse. Steel sandwich panels consist of two face sheets connected by a relatively low-density core result in high strength and stiffness, which lead promising design advantages. Steel sandwich panels offer substantial resistance to static and dynamic loads due to their high stiffness and substantial energy absorbing capacity. Panels of this kind are interest of potential use in ships and are especially efficient in resisting extreme events such as impact or shock loading.

This research is conducted to investigate the mechanical behavior of a tapered steel sandwich panel end connection using finite element analysis techniques and experimental test methods. A verification study, performed comparing finite element analysis and an analytical model to an experimental study documented in the literature, demonstrates good agreement between the approaches. Finite element analyses are employed to study the response of a laser welded steel sandwich panel tapered end connection designed specifically for use in an aircraft carrier hangar door. Performance of this connection is verified with experimental test procedures to demonstrate that the connection has adequate strength and the failure location is outside the connection region. Photogrammetry techniques are used to visualize and quantify the deflection response. Static tests to failure of the stake weld in a lap-shear configuration provide quantification of the weld resistance per unit length.

ACKNOWLEDGEMENTS

The authors gratefully acknowledge funding for this project through the Office of Naval Research under grant number N00014-05-1-0735. Dr. Roshdy G.S. Barsoum of ONR is the cognizant program officer. The authors would also like to thank the assistance of the project team at the University of Maine including undergraduate students Jacob Folz, Brendan Owen, Anthony Fessenden and graduate students Keith Berube and Radek Glaser. Also the support of the University of Maine's Advanced Manufacturing Center, under the direction of John Belding, is gratefully acknowledged.

TABLE OF CONTENTS

Page

Page

Page

1. INTRODUCTION

Sandwich structures composed of stiff outer layers connected by a relatively low-density core result in high specific strength and stiffness, which may lead toward substantial design advantages. Properly designed steel sandwich panels offer substantial resistance to static and dynamic loads due to their high relative stiffness and inherent energy absorbing capacity. To that end, steel sandwich construction has great potential for use in ships, building, and bridge structures, especially for hazard reduction in situations of high wind, storm surge, earthquake and accidental or terrorist blast. Laser welded steel sandwich panels perform especially well in situations of hazard reduction due to their high energy absorbing potential. Steel sandwich construction also has other advantages. Lok and Cheng (2000) listed several including simplification of traditional connection processes (since stiffeners or joist members can be eliminated), accurate construction, less surface distortion, rapid fabrication practices, better retention of pressure and water leakage, greater flexibility for designers to create curved structures, and ease of material transportation. They also noted that difficulty in fabrication and reliability of the face-sheet/core connection has been a continual problem. Laser welding of the face sheet to the core using a stake weld overcomes this problem. Assessment of the strength and fatigue resistance of the weld and connection details is essential to the implementation of laser welded steel sandwich panels.

1.1 Objectives and Current Study

The focus of this research is to assist in the further development of laser welded steel sandwich panels for ship construction. Response of an end connection for laser welded steel sandwich panels to be used in a hangar door was studied using a finite element analysis, numerical model and experimental test. Experimental studies of the sandwich panel using LVDT's, strain gages and photogrammetry are performed to quantify the panel response. The steel sandwich panel is constructed of stainless steel and consists of discontinuous corrugated prismatic stiffeners attached to the top and bottom of the panel with laser stake welds along the length. Experimental analysis is performed on sandwich panels beam test sections in the Hybrid Structure Laboratory (HSL), University of Maine, Orono.

The finite element analysis technique is used to compare to theoretical models and experimental testing of mechanical behavior of the steel sandwich panels under quasi-static loading. Steel sandwich panels with a tapered end connection were tested quasi-statically under 4 point load using LVDT's, strain gages and photogrammetry targets.

Studies performed under this effort include:

1. A verification study performed based on Tan's et al. (1989) work and finite element analysis technique for simply supported boundary conditions are standardized for both continuously and discontinuously corrugated steel sandwich panels.
2. A theoretical analysis program was implemented using MATLAB™, which can be easily modified in order to analyze prismatic sandwich panels with different corrugation configurations.
3. Finite element analysis techniques are developed for sandwich panels bolted from two ends using tapered connection plates.
4. Experimental and photogrammetric techniques are used to determine the adequacy of the end connection and to investigate the accuracy of the finite element analysis techniques used in this research.
5. Static monitonic tests of the laser stake weld strength is quantified using lap-shear subcomponents.

1.2 Literature Review

Laser welding is a relatively new technique for structures, which has potential to achieve excellent static and dynamic load resistance as well as good fatigue life. Dimensional accuracies far superior to those describe in ASTM A6 (2005) have been realized in laser welded beam fabrication as a natural outcome of the process. Laser welding occurs at much greater speeds than conventional welding. In plate fabricated beam production speeds of 5-10 times that of conventional welding has been attained with the goal to develop automated systems capable of welding up to 600 in/min. (Blomquist et al., 2004). Good control over weld quality and profile is demonstrated along with greatly reduced residual stresses when compared to conventional

welding (Caccese and Berube, 2003, Caccese et al. 2006). Laser welding is a high energy density process that can be used on a wide variety of metals and alloys. Some of the advantages that can be achieved through laser welding are ease of process automation, high welding speed, high productivity, increased process reliability, low distortion of the finished part, low residual stresses and no requirement for filler metal. With current laser welding techniques it is possible, for example to achieve full penetration welds in one pass on materials up to 1-inch thick, depending on laser power and weld speed, with no filler and preparation as simple as precision cutting of the edges (Duhamel, 1996). The automotive industry has used laser welding in production since the 1980's. Recently, the ship building industry has looked toward laser welding to provide fabricated components in ship production due to improvements and cost benefits that can be achieved compared to hot rolled stripped-T or split-I stiffeners. Efforts to develop laser welded sandwich panels (LASCOR) were initiated by the U.S. Navy in 1988 and resulted in the use of stake welds to attach the face-sheets to the core. LASCOR panels were produced using a 14-kW CO_2 industrial laser. The prototype panels were installed on the USS Mt. Whitney in 1994 and have performed well in the marine environment. The use of the CO_2 laser and stainless steel corrugated core design of LASCOR results in a product that is economically unfeasible for many structures, where price competitive square-foot product cost is essential. The significantly more efficient fiber laser facility at ATS in Sanford ME, and the increased flexibility in core design may yield a product that has the improved economics compared to earlier laser welding systems. Laser welded sandwich construction has the potential to be a widely used structural form in ship, building and bridge construction. This type of system offers high strength-to-weight and stiffness-to-weight ratios compared to other types of construction methods. In sandwich construction, two face-sheets are separated by a core giving high flexural rigidity in both directions compared to an unstiffened plate of the same weight. With the laser, a stake weld can precisely attach the face-sheets to the core providing a robust construction method.

Core designs for sandwich panels can take on many forms and shapes depending upon the end use. Some of the basic core designs ideal for laser stake welding (Kujala et al., 2004) is presented in Figure 1.1. Prismatic cores, such as shown in Fig. 1.1, are preferred in sandwich construction because they are simple to manufacture and because their high longitudinal stiffness

makes them ideal in cases where orthotropic plate action is preferred. The core is an essential element, resists predominately shear force much like the web in an I-beam, and can be used to mitigate severe dynamic effects.

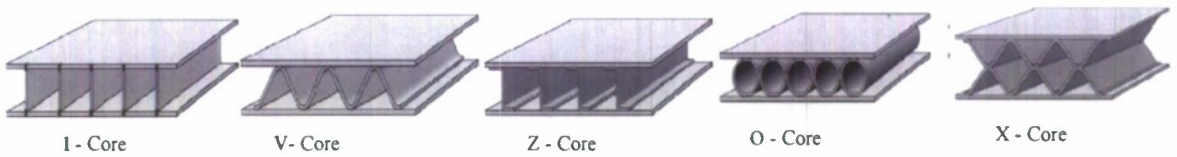

Figure 1.1 Some Examples of Prismatic Core Designs Ideal for Laser Stake Welding

Some core geometries, such as the X-core, inherently have more capacity for energy absorption than others.

The connection between the core and face-sheets is a key element in the long-term performance and has historically been accomplished by spot welding, rivets, self-tapping screws or adhesive (Fung et al., 1996). Laser welding adds a new dimension to steel sandwich construction. Using a stake weld, the core material is metallically bonded directly through the face-sheet, resulting in a continuous and reliable attachment that can be created at much higher rates than typical in conventional welding. The effect of the relatively low core transverse shear rigidity on overall response of sandwich panels as presented by Plantema (1966), Allen (1969), Zenkert (1995), and others has been intensely studied. Vel et al. (2005) discussed the couplings that occur between axial, bending and shear resistances for tapered connections and unsymmetrical sandwich panels.

The configuration used in steel sandwich panels typically results in a highly orthotropic structure where it is absolutely necessary to consider effects of shear deformations even at large length to depth ratios. The same is true in truss type sandwich panels as indicated by Chang et al. (2005) and Cheng et al. (2006). Tan et al. (1989) performed experiments and analysis on a V-core type sandwich panel system and found good correlation between experimental results and analytical models. The effect of a discrete face-sheet/core connection in a C-core type sandwich panel was studied by Fung et al. (1996) for use in building structures. The C shaped core material they analyzed was connected to the face-sheets using screws. They modeled this connection as a line of contact and developed a mathematical formulation for the panel response including the weak axis shear stiffness, which considers the local response of the core and the face-sheet/core

connection. A stake weld can be treated mathematically in much the same manner, although, the non-linear response to ultimate capacity of a stake welded connection will be substantially different than a screw connection. Lok and Cheng (2000) developed a mathematical formulation for truss-core type sandwich panels. They developed expression to predict the orthotropic stiffness and quantified the effect of the core angle on the response. Their work was analytical and they expressed a need to have reliable fabrication methods.

Shock and impact resistance of sandwich construction has been studied intensely for use as ship hulls. Sandwich structures offer significant advantages in terms of higher flexural rigidity and flexural strength, for a given weight, in comparison to single skin structures (Zenkert, 1995). Under a blast load, the core typically absorbs more than a half of the total kinetic energy of the blast (Hutchinson and Xue, 2005). Xue and Hutchinson (2004) and Fleck and Deshpande (2004) have shown that prismatic geometries are nearly optimal for shock resistant sandwich construction. Fleck and Deshpande (2004) also indicated that sandwich construction is more effective in resisting dynamic shock loading than conventional construction. This is especially true for fluid loading where fluid-structure interaction has more of an influence and is an additional benefit in structures where an abnormal event such as blast, hurricane, wave surge or earthquake, might place higher energy demands on the structure than foreseen in design under normal loads.

1.3 Hybrid Laser Arc Welding

Hybrid laser arc welding (HLAW) holds many advantages over current conventional welding technologies in steel fabrication and construction. Hybrid laser arc welding is automated as shown in Figure 1.2. Abbott et al. (2008) described that fabricators have the ability to control the power input intensity, geometry, and accuracy of welds. HLAW can be done at increased speeds, is more tolerant of lack of fitup and reduces demand on clamping system. Automated control allows minimum part distortion and welding near heat sensitive components due to small heat affected zones (HAZ). Non-contact operation permits welding in hard to reach areas and repeatable weld placement. By adjusting various parameters such as the laser energy and focal point position, HLAW permits geometric ratio control of the welds and consistent weld depth and width control. Although there are limitations on maximum width, that can be achieved with

a laser stake weld. Automated systems as shown in Figure 1.2 are also cost competitive due to minimum set-up time, low fixturing costs, and high feed rates.

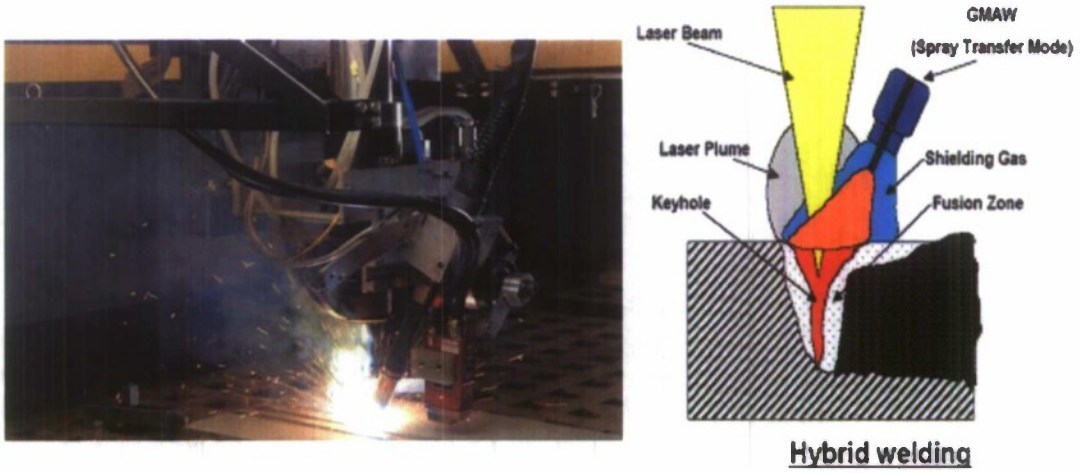

Figure 1.2 Hybrid Laser Arc Welding (HLAW) (Abbot et al. 2008)

Speed is a major advantage HLAW possesses over conventional welding technologies. It is five to ten faster than conventional methods saving crucial money and time. Meanwhile, HLAW produces oxide free welds to improve weld quality and to enhance safety conditions. Also, HLAW can be applied to carbon steels, HSLA steels, stainless steel, aluminum, and titanium, and have little influence on the material properties or physical state of the material. Contained weld joints have no flash or particulate outside the joint to cause problems, and the assembly sees no heat or vibration because the parts do not move relative to one another in the laser welding process. More importantly, HLAW reduces the residual stresses (Abbott et al. 2008) induced upon the material, which can improve the overall stability and nonlinear dynamic response.

All things considered, HLAW is ideal for connecting face-sheets to the cores. Laser welding of the core to the face-sheets, in a steel sandwich panel system, results in a robust reliable connection. Additionally, HLAW improves methods for manufacturing high strength welded girders, plate-to-stiffener welds for orthotropic bridge decks, and the development of lightweight sandwich panel decks. Also, the use of thinner steel plates may be achievable, thus reducing

material and installation costs, and facilitating the use of higher cost stainless steels. Figure1.3 shows hybrid laser arc welding on a section of a sandwich panel.

Figure 1.3 Hybrid Laser Welding on Sandwich Panel (Abbot et al. 2008)

One major barrier to the advancement of laser welding is the limited availability of published technical welding guidance for designers, welding engineers, and fabricators. According to Abbot et al. (2008), the American Welding Society has developed a draft specification available for qualification of laser welding, but it is not yet available to fabricators. The ASME addresses laser processes in Section IX of the Boiler and Pressure Vessel Code, but this is highly restrictive in nature, and not necessarily applicable to other types of fabrication. Additional development is needed in this area of welding codes, procedures, and specifications, especially as applied to steel bridge components, if laser welded steel sandwich panels are to become viable in this arena.

1.4 Hybrid Laser Welding of Steel Components

Applications such as HLAW structural shape fabrication from plate material including T's, wide flange and channels will allow for more flexibility in choosing sizes, potentially less weight, the use of specialty plate material and less distortion in the end product (Blomquist and Forrest, 1999). Specialty shapes made from plate also result in less material inefficiencies. In ship fabrication for example, deflanginig an I-beam into a T-shape results in the scrapping of 25% of the purchased material (Blomquist et al, 2004). In fabricated shapes, the deep penetration of the laser reduces the requirement for filler material and the reduced distortion lessens or eliminates the need for straightening and rework. Cost-effective, and weight efficient designs are the

result. As with any new process, qualification studies are required to demonstrate that the strength and fatigue life is not compromised by the process. Also, HLAW makes the efficient fabrication of metallic sandwich panels possible using a stake weld which can be done through the outer plating material to connect the core. Roland et al. (2004) discusses the numerous advantages of steel sandwich panels in shipbuilding including high strength, high stiffness, high accuracy, modular design and ease of assembly. They reported that in some cases structural weight can be reduced up to 40 % using sandwich panels in lieu of other structural systems. Myer Werft operates a plant that includes a fixed gantry with a 12 kW CO2 laser and sliding table that moves the workpiece and a welding head that is equipped with a pressure roller used to minimize gap between the face sheet and core elements.

The development of automated gantry type and robot laser welding machines is facilitated by fiber lasers (Rooks, 2000). Cost effective system for accurate edge prep will enhance laser welding Roland et al. (2002) further machine development and integration.

In the U.S., a closed loop process control system was developed to actively monitor the laser welding process by Applied Thermal Sciences (ATS) of Sandford, Maine, in conjunction with ESAB (Defalco, 2007). This system uses a 10 kW fiber laser mounted on a movable gantry. The system can be configured with laser only, laser with cold wire feed or HLAW. It includes active weld joint tracking, weld monitoring and control of critical welding parameters, automated weld surface inspection, automatic flaw detection and process documentation and reporting. This system is being used in fabrication of laser fabricated shapes from plate material and steel sandwich panels. It was developed to work with material that is laser and/or plasma cut and then welded with no subsequent operations other than cleaning. This is ideal for situations where machining of edges is cost prohibitive. This system is operated as a 2D gantry or 3D robotic, (Orozco et al., 2004). When defects occur, they are marked and the system automatically modifies the welding process parameters (Blomquist et al., 2004). Near zero tolerance is required to minimize the undercut of a laser welded connection. As the tolerance is increased, undercut occurs if an inadequate amount of filler metal is added. This results in poor weld geometry that can substantially reduce the fatigue life. The control system tracks the weld

geometry and other parameters and supplies the appropriate amount of filler resulting in good geometric profile.

1.5 Laser Welded Steel Sandwich Connection Panel for Ships

In the mid-1980's the US Navy developed a new structural system known as "LASCOR" or LASer welded CORrugated core structure. These structures consisted of two metal skins laser fused to a corrugated metal core. This cellular sandwich structure was capable of achieving twice the strength-to-weight ratio of conventional beam-stiffened steel structures that are typically used in ship construction. The earliest implementation of this concept on a ship was accomplished in 1994, when more than 2,100 square feet of LASCOR panels were fabricated an installed on the USS Mt. Whitney (LCC-20). Figure 1.4 shows the Mt. Whitney indicating the sandwich panel design. This installation saved more than 20,000 lbs., or 40% compared to typical beam-stiffened plate designs. Although this was a highly successful project, the cost per square foot remained high, and few actual implementations followed. At the time no US companies were capable of cost-effectively producing these structures in the sizes or volumes desired by the Navy. Subsequently, an automated fiber laser welding system was developed in the United States by Applied Thermal Sciences. It is anticipated that the laser welding control and automation will result in a cost efficient process.

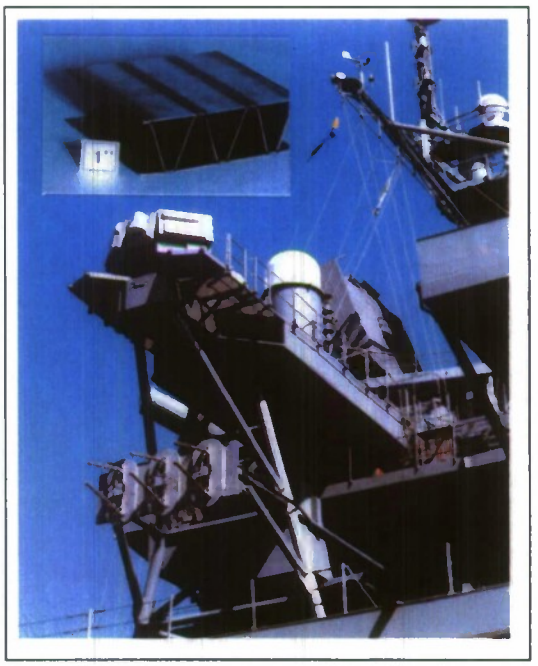

Figure 1.4 USS Mt. Whitney (LCC-20)

A recent study of us of laser welded steel panels on Navy ships includes the development of hangar door connection panels. A tapered connection test model is shown in Figure 1.5 consists of 3 discontinuous prismatic stiffeners top and bottom sheet metal finished with a tapered closure designed to operate under 8000 lbs of service load. Face sheets of this subcomponent were fabricated with 2003 stainless steel and the core from 2205 CRES. The connection used in this panel is a key element and is also the objective of this research to investigate the strength of the connection using finite element analysis techniques and verifying the predicted design

requirement and finite element results with a testing procedure using strain gages, linear variable displacement transducers (LVDTs) and photogrammetry techniques.

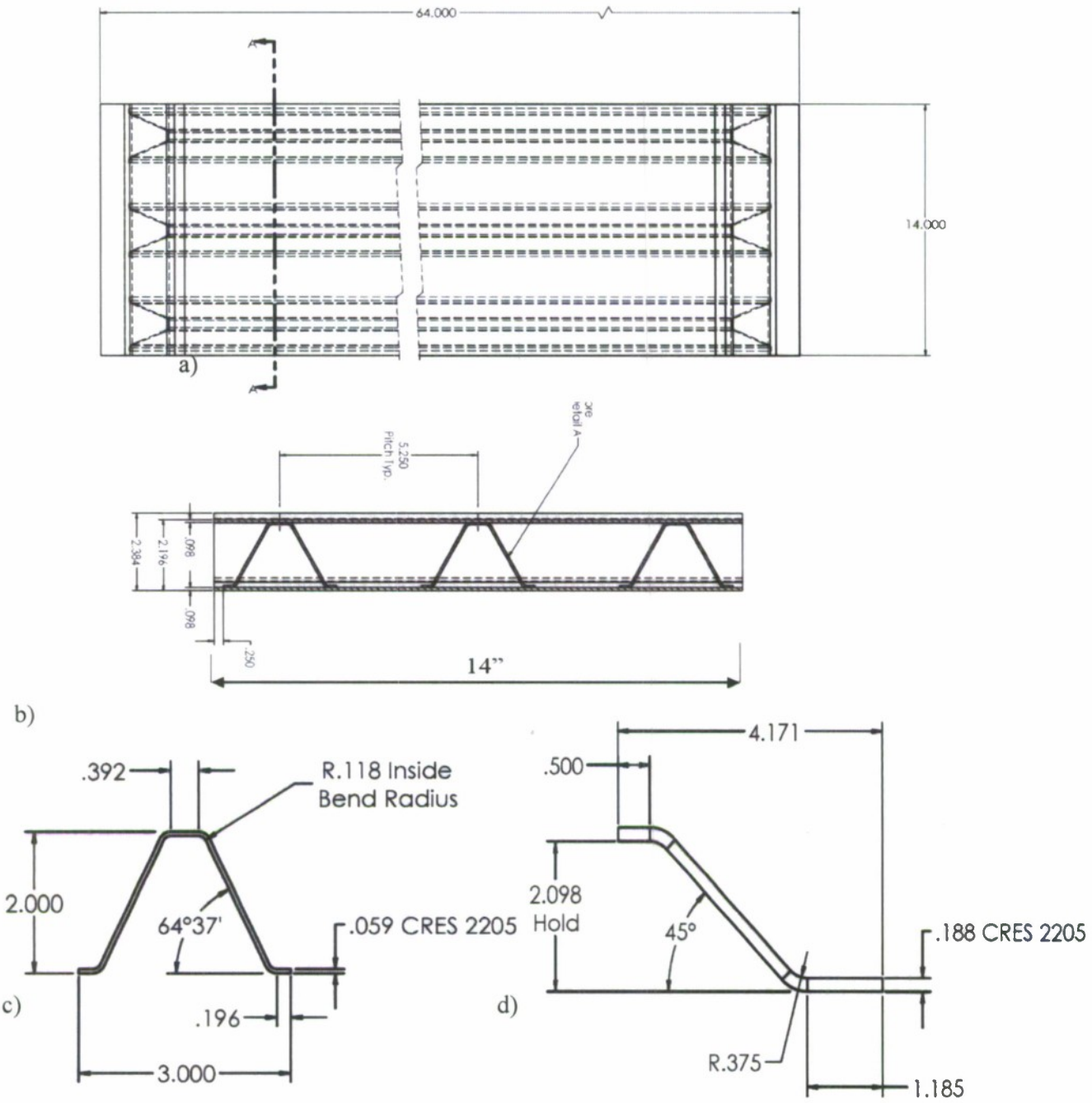

Figure 1.5 – Tapered Connection Test Model a)Plan View; b) Section through cores; c) Prismatic Stiffener Detail; d) Tapered Close Out Detail

2. ANALYSIS OF TRUSS CORE SANDWICH PANELS

This section describes the analysis of structural sandwich panels that was carried out using the commercially available finite element packages ABAQUS and ANSYS. Theoretical calculations are also performed using orthotropic plate analysis that includes shear deformation using the MATLAB software. Sandwich panel models are created using CAD modules of the finite element software. In complicated cases SOLIDWORKS, which is a dedicated computer aided design (CAD) program, is utilized. Modeling methods are verified using work performed by Tan et al. (1989). Two case studies are presented including the analysis of a prismatic panel subjected to patch loading and a panel including a tapered end bearing connection.

2.1 Verification of Finite Element Model

The verification model used in this study is based upon testing and analysis performed by Tan et al. (1989). Figure 2.1 shows the panel geometry used in their study. The sandwich panel was detailed with a continuous corrugated steel core attached with spot welding to the top and bottom sheets in their verification study. Their model was a 6 m long and 2.12 m wide truss core panel at a total depth of 107.5 mm. It consists of 4 corrugations in the long direction. A boundary plate of 12 mm thick and entirely made of 2.5 mm structural steel was welded to close the specimen.

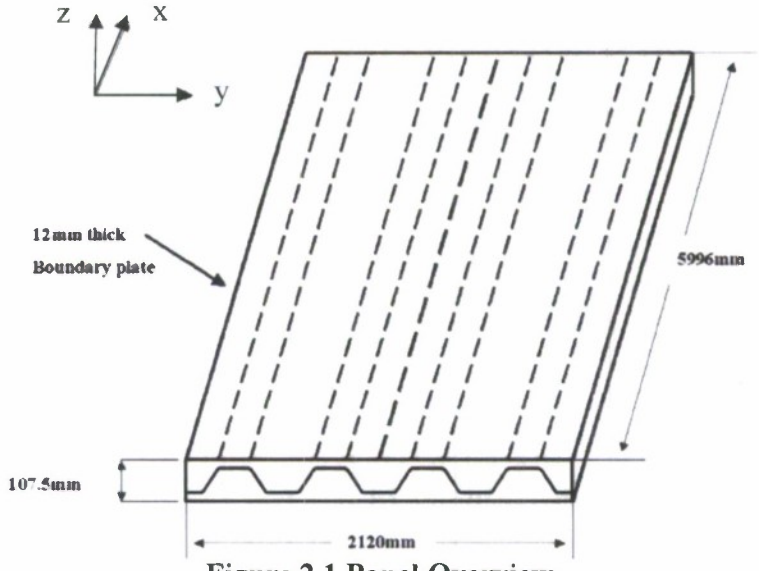

Figure 2.1 Panel Overview

In this current effort Tan's case is verified with an independent finite element analysis using the ABAQUS computer program. Once verified, the same process will be used to analyze the test panel case studies presented in the remainder of this section. Cross section of a single core cell modeling Tan's case is presented in the Figure 2.2, which shows the welding locations, side boundary plate, top and bottom sheets. Dimensions are shown in Figure 2.2 as they are used to create the quarter part of the sandwich panel in ABAQUS.

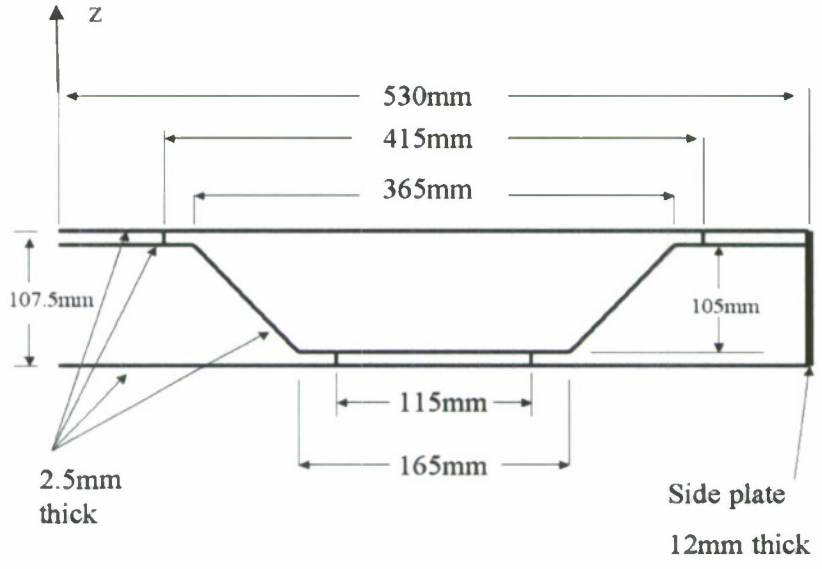

Figure 2.2- Core Section with Boundary Plate on right

The sandwich panel studied is made of a linear elastic steel material, with a Young modulus of $209{,}000N/mm^2$ and Poisson's ratio of 0.3 (Tan et al. 1989). In this three dimensional static analysis a general-purpose conventional stress and displacement element, ABAQUS S8R6 is used which is shown in Figure 2.3

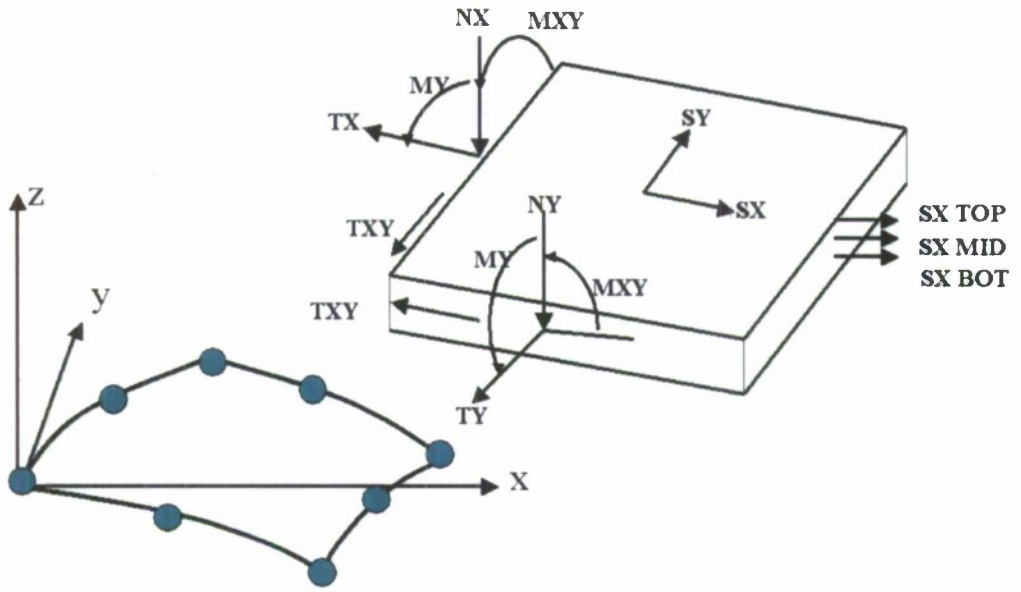

Figure 2.3 S8R6 Quadrilateral Shell Element

S8R6 is a quadrilateral shell element, which offers a total of 8 nodes along the edge of the element boundary 6 degrees of freedom at each node allowing three rotations and three displacements. In the analysis a reduced integration option is selected. This method provides more accurate results along with economical analysis cost, when compared with three-dimensional analysis of thin plates. This element type uses quadratic interpolation, also capable of simulating transverse shear deformation, which is especially appropriate for meshing the corrugated web core due to its periodically fluctuating geometry, which essentially requires fine meshing at locations where the web core changes direction. The corrugation plays a critical role in sandwich panel response providing shear resistance and some flexural resistance predominately in the strong direction of the panel.

2.1.1 Model of the Laser Welded Connection

In this study, the spot welding of the panel is assumed to be continuous along the length of the corrugation at the weld locations. Modeling of the weld uses a connecting plate with the same element type (S8R6) as the corrugation, top and bottom face sheets. This was done due to the difficulties and complexity in high fidelity modeling of spot welding. The model's cross-section with the continuous stake weld is shown in Figure 2.4. The plate thickness of the representative

weld element was taken as 2.5mm; equivalent to the minimum thickness of the structural panel. This value was based upon a study of the effect of weld thickness presented in Section 2.1.4. A continuous welding, which joins the corrugation to the bottom and the top plate through the length of the panel is also modeled with using shell elements. These elements are also of the same type as the ones that the sandwich panel is meshed.

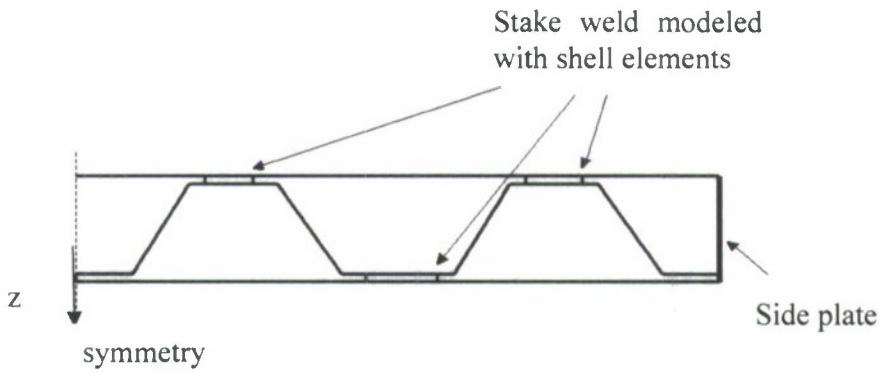

Figure 2.4 Stake Weld and Web-Core Configuration

In the final analysis, approximately 13,000 plate elements shown in Figure 2.5 are used to mesh the quarter of the sandwich panel. This model also assures achievement of appropriate element aspect ratio and convergence. Proper aspect ratio of plate element is essential in order to obtain reliability of the results in finite element analysis. This is accomplished by performing a mesh convergence study presented in the next section.

Figure 2.5 Meshed Panel

2.1.2 Convergence Study

In finite element analysis, a finer mesh generally results in a more accurate solution. However, as the mesh gets finer, the computation time and the memory requirements increase. In this sense it is important to satisfactorily balance the accuracy and computing resources. As part of the verification effort, a mesh convergence study was performed by first analyzing the structure using a coarse mesh. Subsequently, the mesh is recreated with a denser element distribution and the analysis results compared to the previous mesh. This procedure is followed by another finer mesh density and the model analyzed once again until the results converged. This approach enables one to obtain a converged solution with a mesh that is sufficiently dense and not overly demanding of computing resources. The convergence of the results checked by displaying the displacement contours which shows the graphical representation of the stepped changes in results from one element to next element. This contour also can be used to determine the effect of the mesh on accuracy by plotting the maximum displacement of the bottom facing versus the number of elements as shown in Figure 2.6. This figure shows that a mesh with over 10,000 elements results in adequate convergence. This approach applied to the Tan's sandwich panel as explained and accurate results obtained. In Tan's case particular attention given to the meshing of the corrugation, which is the critical structural component in the sandwich panel. After meshing the sandwich panel and running the analysis for different mesh densities, an element size of 25 mm was found to be sufficient to have converged results. Ultimately, the sandwich panel is meshed with 17000 elements.

a)

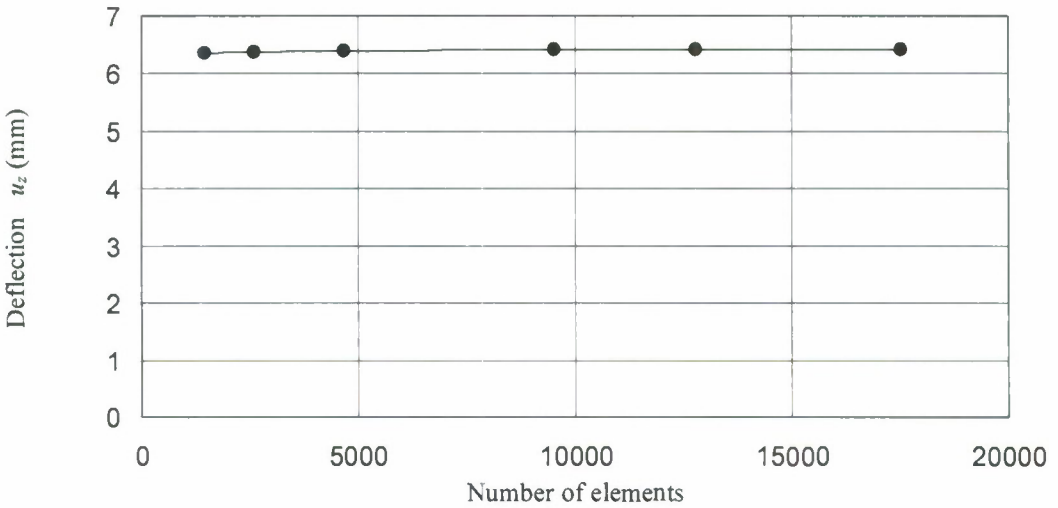

b)

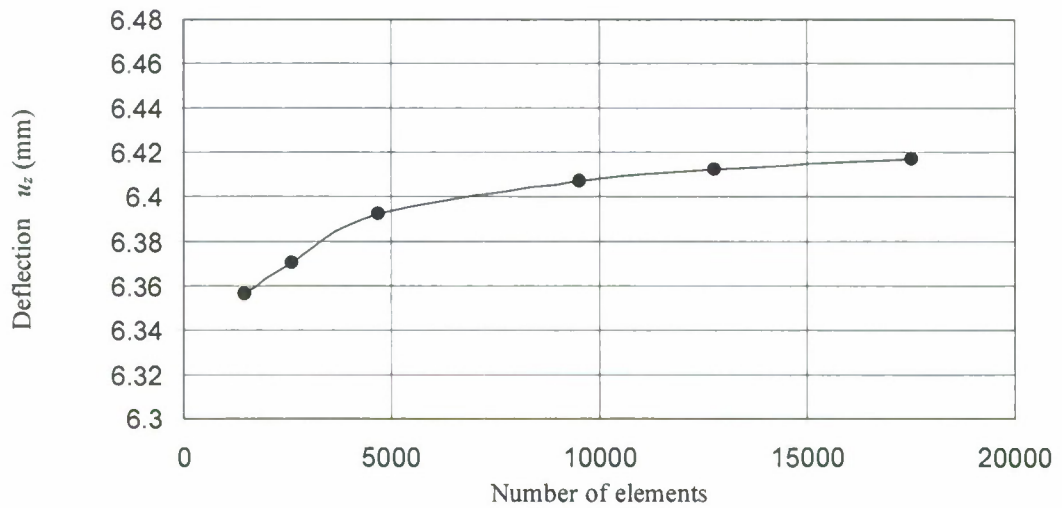

Figure 2.6 Convergence Study a) Convergence Rate of Tan's Current Study
b) Magnified View of Convergence Study

2.1.3 Modeling: Load and Boundary Conditions

The distributed load is applied as a pressure of 5.5 kN/m^2 acting normal to the surface of the plate elements on the top of the panel as shown in Figure 2.7. Symmetry on a quarter model was used for application of boundary conditions. Cross-section of web-core and continuous stake weld configuration of quarter model symmetry is also shown in Figure 7. In the finite element (FE) model the boundary plate on the front and the backside of the model is omitted to reduce the number of elements used. This condition was modeled by forcing the U2 displacements to zero along this boundary.

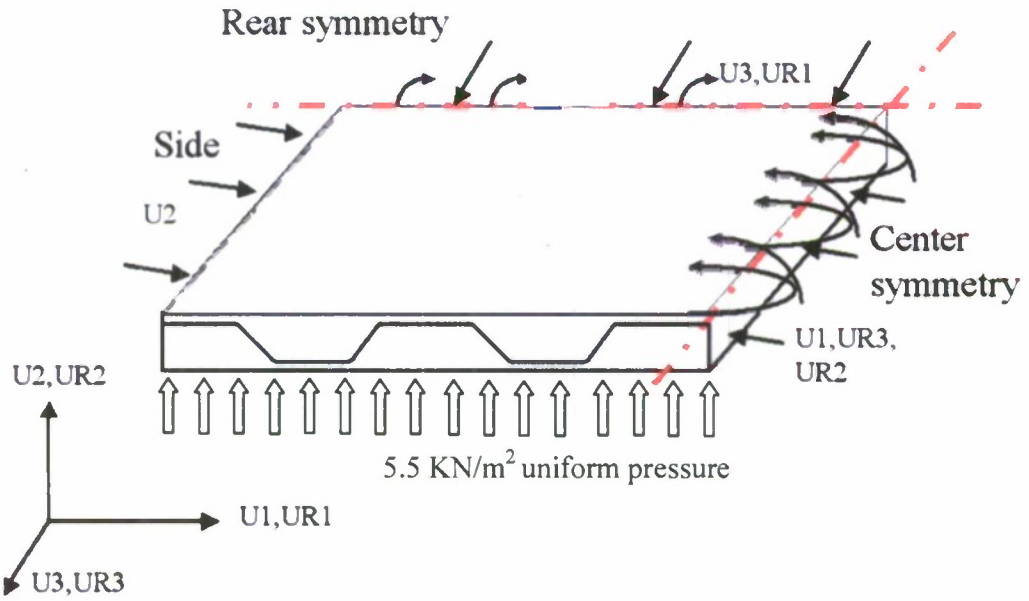

Figure 2.7 Applied Boundary Conditions to the Quarter Model

The boundary conditions and applied distributed load are shown in Figure 2.8 along with the panel modeled in ABAQUS. In the quarter model simply supported boundary conditions (BC) applied to the entire front face by fixing U2, which sufficiently simulates the existence of such boundary plate. However, this approach does not restrict the rotation of the front face due to the moment created at the center of the panel by the uniform load. That being emphasized, the

boundary condition applied in the U2 direction is on the entire face including the top plate, bottom plate and core elements.

Figure 2.8 Finite Element Model BCs and Load

On the left hand side of the panel where the boundary plate exists, the boundary condition is applied again to the entire face of the plate in the U2 direction. On the rear symmetric face, while taking the advantage of symmetry, the boundary condition applied to restrain the rotation, UR2, to eliminate the drilling effect. Also fixity is applied in the U3 direction to restrain the motion in the longitudinal direction and the fixed rotation UR1 will result in zero slope along this face. On the right hand side, the center symmetry axis along the length of the panel used, all edges are restrained against drilling rotation UR2, horizontal motion along the U1 and rotation UR3 about the U3 axis.

2.1.4 Weld Link Thickness Effect

A study was performed to investigate the effects of the weld link thickness on the overall results. It is important to understand the effect of this parameter on the response of the panel by varying effective weld link thickness assigned to the link section in the finite element model. It is

important to have weld link stiffness high enough to have continuity but not too high to influence results. The results of the weld thickness study are presented in the Figure 2.9, which plots the normalized centerline deflection versus the non-dimensional weld link element thickness t_w/t_p, where t_p is the minimum plate thickness of 2.5 mm.

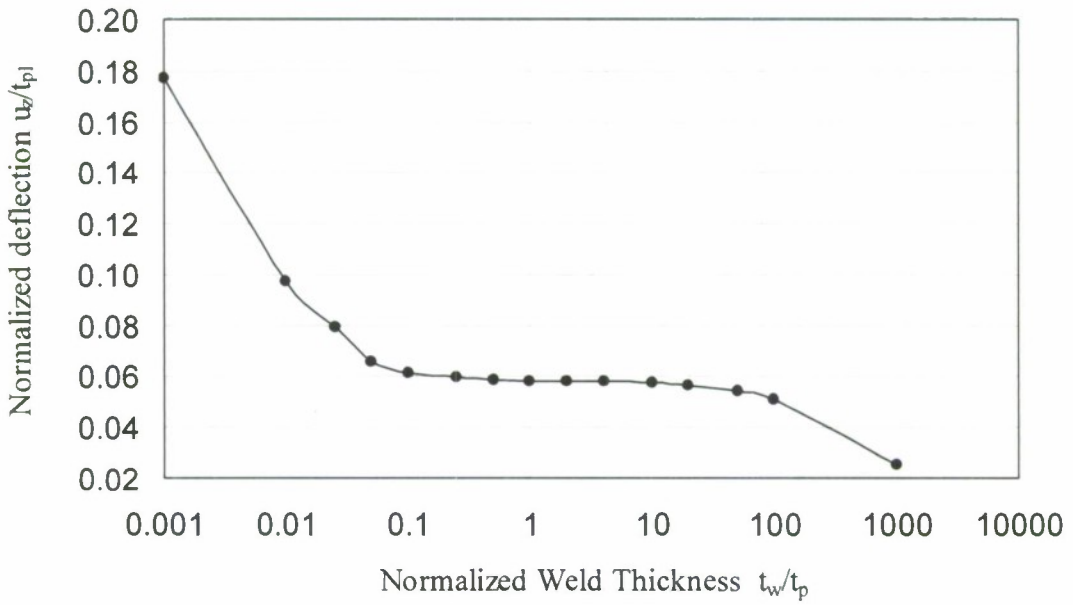

Figure 2.9 Weld Link Thickness Effect

Global and local deflections read from the output files and data plot using MS-Excel to visualize the effects of the weld link thickness. This study performed for only one case with weld link at the center only. In the graph it is seen that increasing or decreasing weld link thickness by an order of magnitude does not have significant contribution to the stiffness of the sandwich panel.

It is discovered that the weld thickness does not have significant contribution to the overall stiffness of the sandwich panel when it is selected in a range between 0.1 t_p to 50 t_p. Accordingly, a weld link thickness equal to the plate thickness was chosen for this study.

2.1.5 Tan's Finite Element Analysis Displacement Results

Resulting displacements for Tan's case are obtained at the center of the panel, which corresponds to the front right hand side corner of the quarter model as shown in Figure 2.10. This shows that the maximum local deflection occurs in the top plate at the centerline.

A summary of deflections along with Tan et al. (1989) experimental results and Lok and Cheng (2000) results by FEM are summarized in Table 2.1. Disagreement between the current finite element analysis and Tan's experimental result is 8.3%. This verification process was necessary to take further steps in the analysis of sandwich panels with different corrugation and weld configuration.

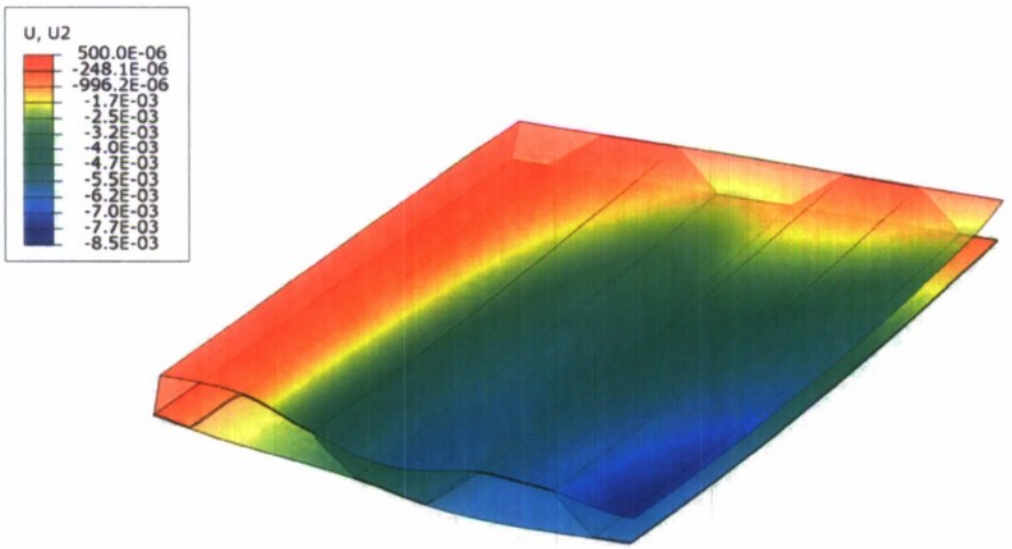

Figure 2.10 Displacement Contour Results

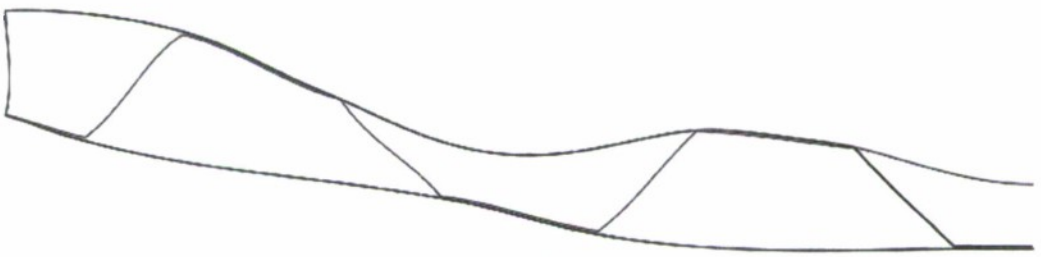

Figure 2.11 Displacement Profile Across Centerline

Table 2.1 Magnitude of Deflection

Weld Configuration	Bottom CL	Top CL	Average
Current FEM of Tan's case	6.42 mm	8.48 mm	7.45 mm
Lok and Cheng (2000) FEM study	6.78 mm	unknown	unknown
Tan et al. (1989) FEM study	5.82 mm	unknown	unknown
Tan et al. (1989) experimental study	7.39 mm	unknown	unknown

2.1.6 Tan's Finite Element Stress Results

Shown in Figure 2.12 are contours of the Von Mises stress results through the thickness of the plate elements. The peak Von Mises stress is shown to be 349.2 MPa. Top and Bottom views of the Von Mises stress are shown in Figure 2.13. The location of the peak Von Mises stress is localized and occurs at the support as show in Figure 2.14.

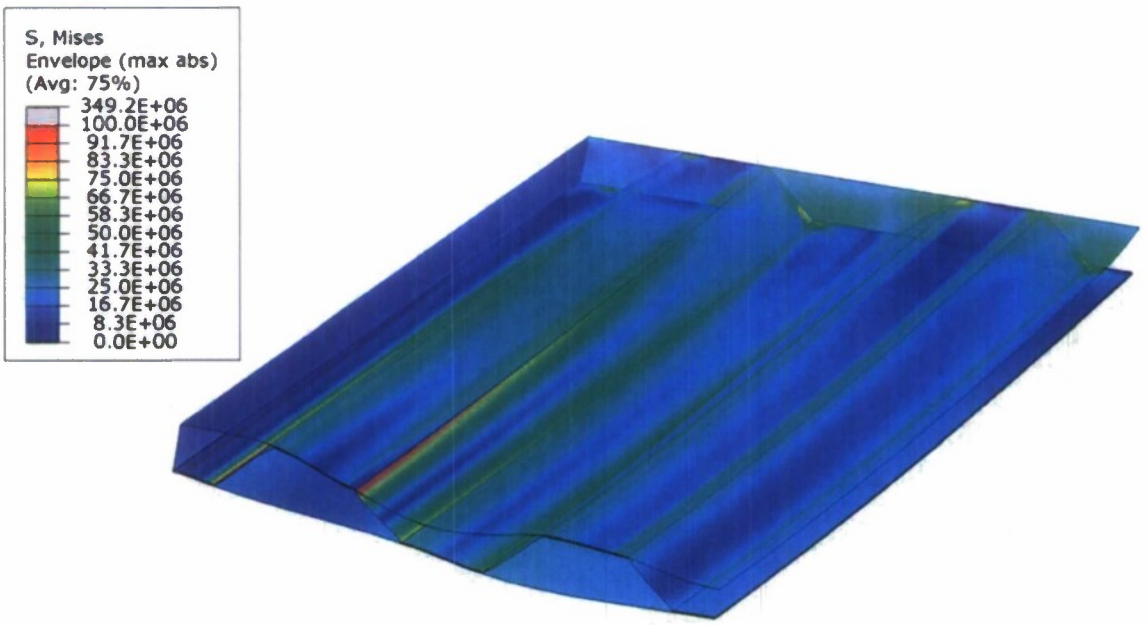

Figure 2.12 Von Mises Stress Contour

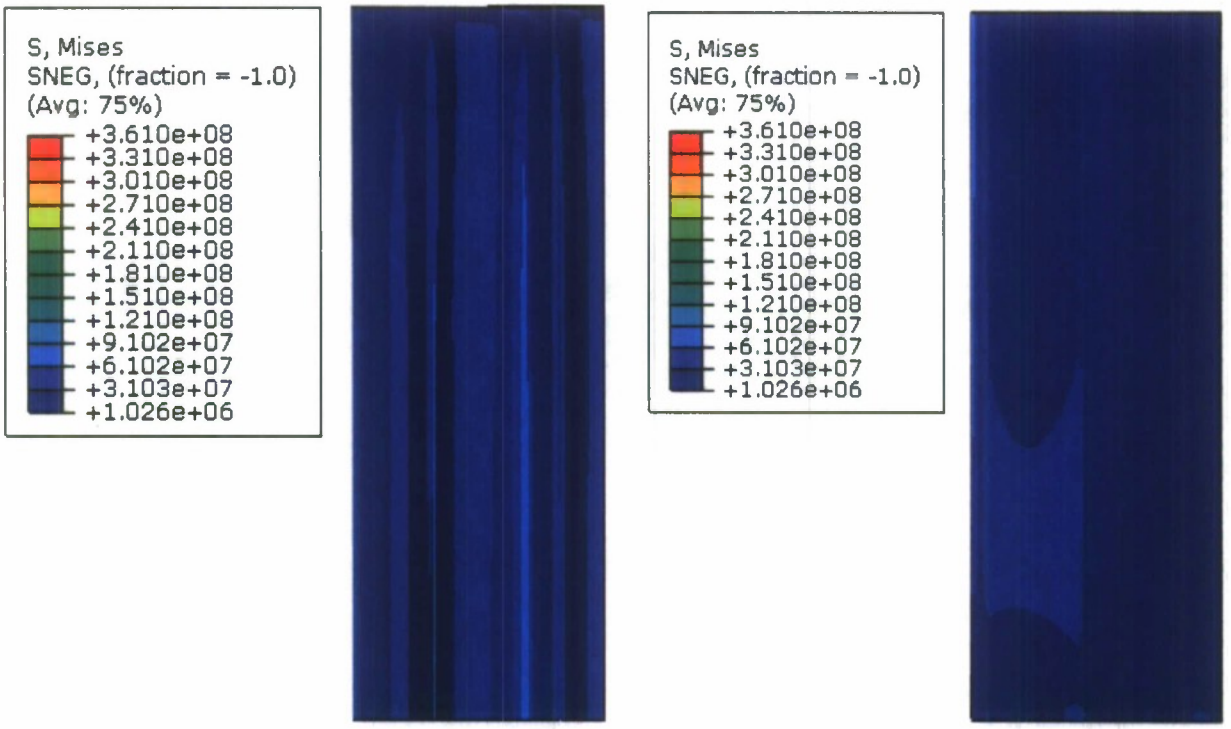

a) top view b) bottom view

Figure 2.13 – Von Mises Stress Contour

Figure 2.14 – Von Mises Stress Contour-Location of Peak Stress

Figure 2.15 illustrates the in maximum principal stress distributions in x-direction for top and bottom plates. The location of the peak maximum principal stress, which occurs on the boundary is shown in Figure 2.16.

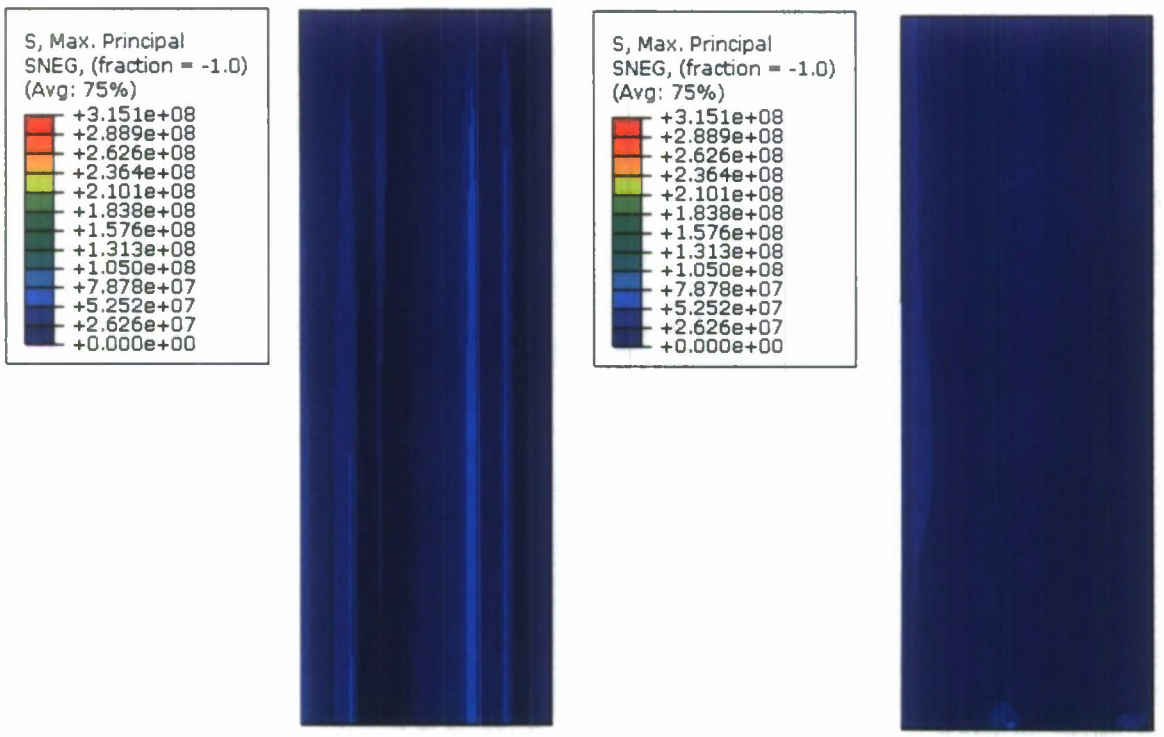

a) top view b) bottom view

Figure 2.15 – Maximum Principal Stress Contour

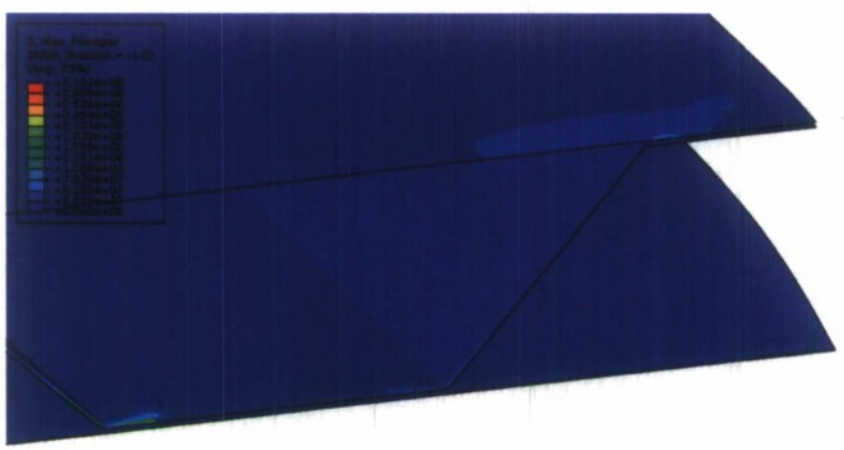

Figure 2.16 – Maximum Principal Stress Location of Stress Concentration

Figure 2.17 illustrates the in minimum principal stress distributions in x-direction for top and bottom plates. The location of the peak minimum principal stress, which occurs on the boundary is shown in Figure 2.18.

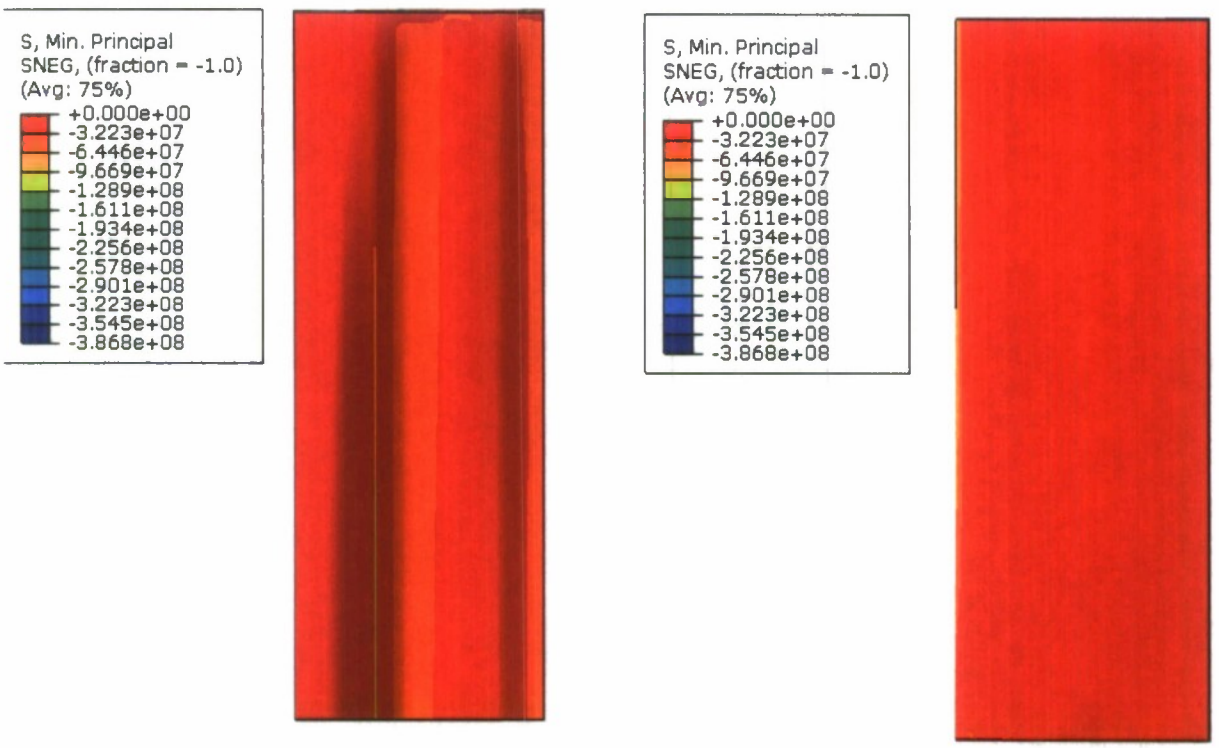

a) top view b) bottom view

Figure 2.17 – Minimum Principal Stress

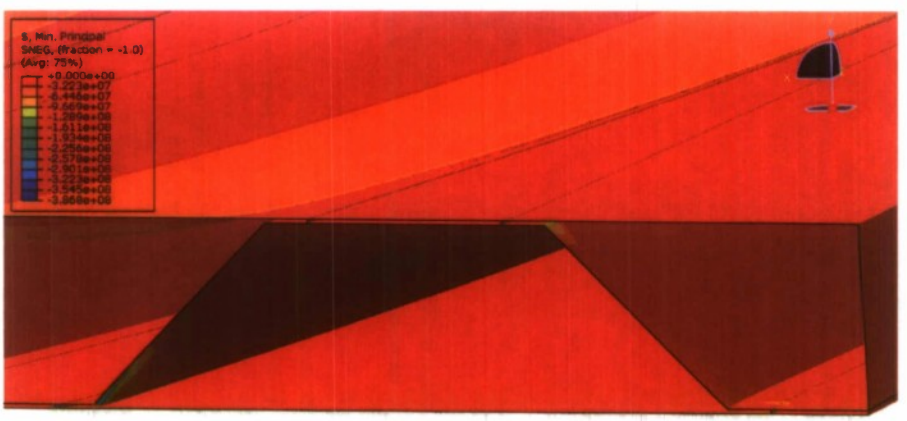

Figure 2.18 – Minimum Principal Stress Location of Stress Concentration

2.1.7 Effect of Weld Placement

In addition to the Tan's sandwich panel configuration, the effect of weld placement for a model with the geometry the same as Tan's was also studied. Three other configurations were used as shown in Figure 2.19 also having continuous welds like Tan's model. These configurations are designated as; 1) Center - where the weld is placed at the centerline of each corrugation flat; 2) Corner - where two continuous welds are placed at the corners of the web-core and at the corner along with the center point; and 3) Center plus Corner - a combination of the previous 2 cases. In this analysis, the sandwich panel's dimensions were not modified and the weld thickness was taken as 2.5mm same as the plate thickness of the sandwich panel. The boundary conditions are applied exactly the same as applied on Tan's model and the magnitude of the load was also identical.

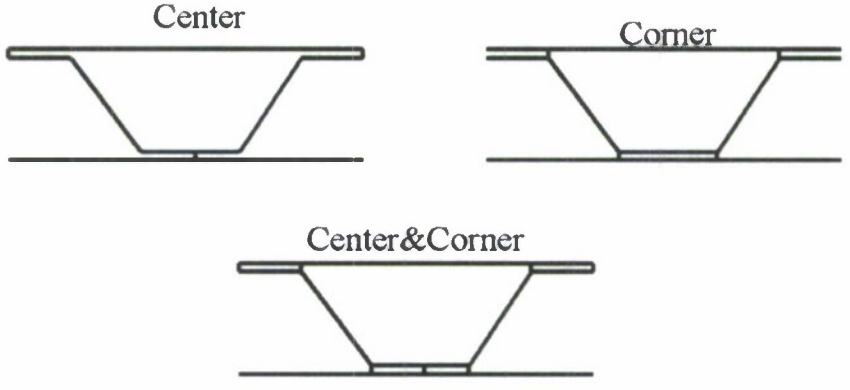

Figure 2.19 Welding Configurations

Deflection values are taken at the same location as explained in the Section 2.1.5. The maximum deflection, top and bottom deflection with the average deflection are given in the Table 2.2 along with the Tan's results. It is important to see that these most common welding configurations can have a significant effect on the overall response. This is predominately due to the influence that the weld location has on the shear rigidity.

This study comes to the conclusion that using one weld link at the center results in a 62% higher displacement at the centerline compared to the case with welds at the center and corners. Using two weld links at the corners instead of 1-weld increases the stiffness by 32% and using three

weld links instead of two weld links improves the stiffness by 9%. On the other hand using one weld link instead of two or three weld links will save manufacturing time by two or three times and still may offer a more economical design.

Table 2.2 - Weld Configuration Results

Weld Configuration	BottomCL(mm)	Top CL(mm)
Tan's current case	6.42	8.48
Center weld	6.92	11.01
Corner weld	6.10	7.48
Corner&center weld	5.37	6.80

2.2 Orthotropic Model Using MATLAB

This section discusses the use of an orthotropic model of the sandwich panel system computed on a theoretical basis. The application of general small deflection theory for flat sandwich panels or curved sandwich panels to any sandwich structure requires knowledge of elastic constants pertaining to that sandwich structure. These elastic constants consists of two transverse shear stiffness D_{Qx} and D_{Qy}, two bending stiffness D_{xx} and D_{yy}, one twisting stiffness D_{xy}, two elastic modulus and Poisson's rations in x and y directions describe the deformations associated with the applied load. In order to calculate these elastic constants for the corrugated sandwich panel of Tan's a series of MATLAB routines are created and used for calculation.

2.2.1 Closed Form Solution of Governing Equation

Mathematical series sum solutions used in the optimization routine are based upon the Mindlin-Reissner plate theory. This theory is for static analysis and includes the influence of shear deformations. The equation of equilibrium for plate bending can be written in terms of the shear forces, Q_x and Q_y, bending moments, M_x, M_y and M_{xy}, and applied load, q, as follows:

$$\frac{\partial M_x}{\partial x}+\frac{\partial M_{xy}}{\partial y}-Q_x=0 \quad , \quad \frac{\partial M_{xy}}{\partial x}+\frac{\partial M_y}{\partial y}-Q_y=0 \quad , \quad \frac{\partial Q_x}{\partial x}+\frac{\partial Q_y}{\partial y}+q=0 \qquad (2.1)$$

The shear forces and moments are related to the transverse displacement, w, and the mid-plane slopes, θ_x and θ_y, as follows.

$$M_x = D_{xx}\left(\frac{\partial \theta_x}{\partial x} + \nu_y \frac{\partial \theta_y}{\partial y}\right) \quad , \quad M_y = D_{yy}\left(\nu_x \frac{\partial \theta_x}{\partial x} + \frac{\partial \theta_y}{\partial y}\right) \quad ,$$

$$M_{xy} = \frac{D_{xy}}{2}\left(\frac{\partial \theta_x}{\partial y} + \frac{\partial \theta_y}{\partial x}\right) \quad , \tag{2.2}$$

$$Q_x = D_{Qx}\left(\theta_x + \frac{\partial w}{\partial x}\right) \quad , \quad Q_y = D_{Qy}\left(\theta_y + \frac{\partial w}{\partial y}\right)$$

The governing equations are then solved with respect to the orthotropic flexural and shear stiffness', D_{xx}, D_{yy}, D_{xy}, and D_{Qx}, D_{Qy}. The solution for the displacement and slopes in a simply supported plate can be cast into a double harmonic series form in terms of a set of unknown coefficients, w_{mn}, A_{mn} and B_{mn}.

$$w = \sum_{m=1}^{\infty}\sum_{n=1}^{\infty} w_{mn} \sin\left(\frac{m\pi x}{a}\right)\sin\left(\frac{n\pi y}{b}\right),$$

$$\theta_x = \sum_{m=1}^{\infty}\sum_{n=1}^{\infty} A_{mn} \cos\left(\frac{m\pi x}{a}\right)\sin\left(\frac{n\pi y}{b}\right), \tag{2.3}$$

$$\theta_y = \sum_{m=1}^{\infty}\sum_{n=1}^{\infty} B_{mn} \sin\left(\frac{m\pi x}{a}\right)\cos\left(\frac{n\pi y}{b}\right)$$

To simply the solution these expressions can be written in matrix form for each term m and n. Plugging into the equilibrium equations results in a system of equations as follows:

$$\begin{bmatrix} L_{11} & L_{12} & L_{13} \\ L_{21} & L_{22} & L_{23} \\ L_{31} & L_{32} & L_{33} \end{bmatrix}_{mn} \begin{Bmatrix} A \\ B \\ w \end{Bmatrix}_{mn} = \begin{Bmatrix} 0 \\ 0 \\ q \end{Bmatrix}_{mn} \tag{2.4}$$

which can be solved by matrix operations as follows:

$$L_{mn}U_{mn} = P_{mn} \quad , \quad U_{mn} = L_{mn}^{-1}P_{mn} \tag{2.5}$$

setting

$$\alpha_m = \frac{m\pi}{a} \quad , \quad \beta_n = \frac{n\pi}{b} \tag{2.6}$$

The components of the L matrix are computed as:

$$L_{11} = D_{xx}\alpha_m{}^2 + \frac{D_{xy}}{2}\beta_n{}^2 + D_{Qx} \ ,$$

$$L_{22} = \frac{D_{xy}}{2}\alpha_m{}^2 + D_{yy}\beta_n{}^2 + D_{Qy} \ ,$$

$$L_{33} = D_{Qx}\alpha_m{}^2 + D_{Qy}\beta_m{}^2 \ ,$$

$$L_{12} = \left[\nu_y D_{xx} + \frac{D_{xy}}{2}\right]\alpha_m\beta_n \quad , \tag{2.7}$$

$$L_{13} = D_{Qx}\alpha_m \ ,$$

$$L_{23} = D_{Qy}\beta_n \ ,$$

$$L_{21} = L_{12} \quad , \quad L_{31} = L_{13} \quad , \quad L_{32} = L_{23}$$

The load coefficient q_{mn} depends upon the load distribution and can be determined using a Fourier series. For the case of uniform load q_{mn} is written as:

$$q_{mn} = \frac{4p_o}{\pi^2 mn}\left[(1-\cos(m\pi)\cdot(1-\cos(n\pi)\right] \tag{2.8}$$

Once the load and stiffness coefficients are known the system of equations can be solved for the resulting displacement, w and slopes, θ_x and θ_y.

2.2.2 Computation of Elastic Stiffness

Computation of elastic stiffness properties is performed using a combination of closed form solutions and simple frame finite element analyses used to determine properties. Expressions for

closed form computation of elastic stiffness properties are implemented for all but the transverse shear stiffness, D_{Qy}, where frame finite element analysis is used.

Analysis is based upon the methodology set forth by Libove and Hubuka (1951) where several simplifying assumptions are made as follows:

1) Thickness of the core remains essentially constant
2) Cross section of the sandwich panel is undistorted
3) Local buckling of the top is not considered
4) 4- Loading remains perpendicular to the midplane of the loading area.

2.2.3 Computation of D_{xx}, D_{yy}, D_{xy}, and D_{Qx}

Expressions for the orthotropic plate rigidities, D_{xx}, D_{yy}, D_{xy}, and D_{Qx}, are given in Equation (2.9). D_{xx} is computed by a conventional strength of materials approach. It includes the combined effect of the moment of inertia of the facesheets, I_f, and core, I_c, both computed about the centroid of the unit cell section. The predominant contribution to D_{yy} is the facing moment of inertia. It is modified to account for the combined Poisson's effect of both the facesheets and the core. Only the facesheets are used in the computation of D_{xy}.

$$D_{xx} = \frac{E(I_c + I_f)}{2p(1-\nu^2)} \quad , \quad D_{yy} = \frac{E \cdot I_f}{2p\left(1 - \frac{\nu^2 I_c}{I_c + I_f}\right)} \quad , \tag{2.9}$$

$$D_{xy} = \frac{E \cdot I_f}{2p(1+\nu)} \quad , \quad D_{Qx} = \frac{Et_c^2}{p(1+\nu)A_c}\left(h - \frac{t_1}{2} - \frac{t_2}{2}\right)^2$$

2.2.4 Numerical Computation of D_{Qy}

The transverse shear stiffness, D_{Qy}, has been derived for numerous specific cases of core geometry including the continuous truss core (Libove and Hubuka, 1951) including a simplified derivation for the truss core (Lok and Cheng, 2000), Z-core (Fung et al., 1994), C-core (Fung et al., 1996). A numerical analysis approach was set described by Cheng et al (2006), which used a

shell analysis finite element method to determine all of the elastic constants. Since this method proved to be general virtually any geometry truss core can be analyzed.

Implementation of the frame analysis into the analysis routine is a relatively simple process. Figure 2.20 shows the model that can used for either a continuous or non-continuous truss core. Rigid links are provided between the core and the face sheet between nodes 2 and 10, 3 and 11 etc. In the continuous core case the dimension, w_1, is taken to be zero and the nodes 1 and 9 are removed from the analysis. The cut nodes along the cut edges of the unit cell (1 or 2 and 19, 9 or 8 and 23) are constrained to move the same distance in the vertical direction. In reality the unit cell is under plane strain conditions, therefore, the resulting displacements must be multiplied by the factor $(1-\nu^2)$.

If a single laser stake weld is used only links at 3-11, 7-14 and 17-21 are retained. The model is fixed against rigid body motion at node 5. A total unit vertical shear force is applied at the right and left hand cuts ($Q_1 + Q_2 = 1$). The horizontal forces are such to keep the unit cell in equilibrium ($H_1+H_2 = 2p(Q1+Q2)/h$). By symmetry $H_1 = H_2$.

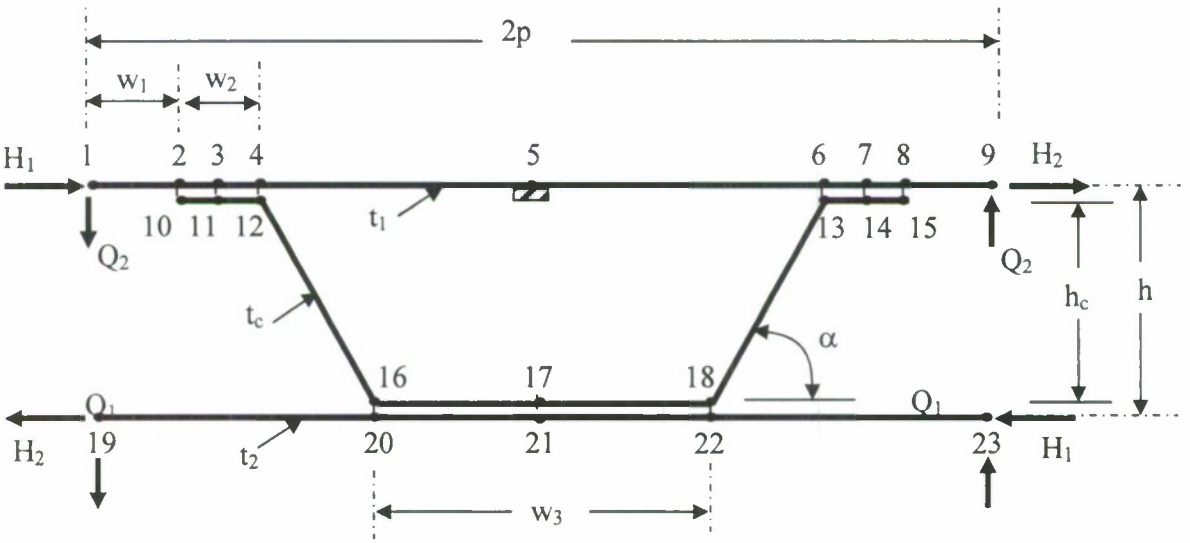

Figure 2.20 Frame FEM for Computation of D_{Qy}

2.2.5 MATLAB Results

The method was coded into the MATLAB computer program, which is an interactive computer program for solving technical computing problems especially powerful with matrix and vector formulations. In the numerical computations, two cases are considered one including and the other ignoring the Poisson's effect on the computation of D_{QY}. The results are given in Tables 2.3 and 2.4, respectively.

Table 2.3 Poisson's Effect Included.

Weld Placement	Center Defection (mm)	Max(mm)	Mx(N.mm	My(N.mm	Mxy(N.m
Center	6.7333	10.48	$6.01x10^3$	-576.0655	0
Corner	6.2742	7.1214	$5.62x10^3$	-295.7196	0
Center and Corner	5.9224	6.7713	$5.32x10^3$	-81.5144	0
Tan Current Case	6.467	7.5692	$5.78x10^3$	-413.3901	0
Weld Placement	**Dx(N.mm)**	**Dy(N.mm)**	**Dxy(N.m**	**Dqx(N.m**	**Dqy(N.m**
Center	$4.11x10^6$	$3.23x10^6$	$2.32x10^5$	$2.85x10^7$	$1.66x10^5$
Corner	$4.11 x10^6$	$3.23x10^6$	$2.32x10^5$	$2.85x10^7$	$2.04x10^5$
Center and Corner	$4.11 x10^6$	$3.23x10^6$	$2.32x10^5$	$2.85x10^7$	$2.38x10^5$
Tan Current Case	$4.11 x10^6$	$3.23x10^6$	$2.32x10^5$	$2.85x10^7$	$1.87x10^5$

Table 2.4 Poisson's Effect Excluded.

Weld Placement	Center	Max(mm)	Mx(N.mm	My(N.mm	Mxy(N.m
Center	7.036	10.7853	$6.23x10^3$	-759.4097	0
Corner	6.5684	7.4144	$5.84x10^3$	-457.2506	0
Center and Corner	6.202	7.0497	$5.53x10^3$	-221.0796	0
Tan Current Case	6.7645	7.8654	$6.00x10^3$	-583.846	0
Weld Placement	**Dx (N.mm)**	**Dy (N.mm)**	**Dxy(N.m**	**Dqx(N.m**	**Dqy(N.m**
Center	$4.11 x10^6$	$3.23x10^6$	$2.32x10^5$	$2.85x10^7$	$1.51x10^5$
Corner	$4.11 x10^6$	$3.23x10^6$	$2.32x10^5$	$2.85x10^7$	$1.86x10^5$
Center and Corner	$4.11 x10^6$	$3.23x10^6$	$2.32x10^5$	$2.85x10^7$	$2.18x10^5$
Tan Current Case	$4.11 x10^6$	$3.23x10^6$	$2.32x10^5$	$2.85x10^7$	$1.71x10^5$

The current finite element analysis result for the centerline deflection in Tan's case is in good agreement with the MATLAB results. Comparison is made on the bottom centerline where local effects on the deformation due to the pressure load do not exist. The discrepancy between the current FEA result and the MATLAB result is reported as 0.7%. The discrepancy between the Tan's experimental study and the MATLAB result is -12%. When the Poisson's effect are

excluded in the MATLAB solution the centerline deflection and Tan's experimental result come closer and the disagreement is -8.5%.

2.3 Finite Element Analysis of Sandwich Panel Connection Model

This case study focuses on the analysis of tapered sandwich panel connections. This design consists of a 64 inches long 14 inches wide sandwich panel shown in Figure 2.42 designed to use as a connection plate for hangar doors on a ship. It is made of linear elastic high strength steel material with a Young modulus of 29,000 ksi and a Poisson's ratio of 0.3. The maximum yield strength of the material is 75 ksi. This sandwich panel design is studied in two load cases. In one case the panel is subjected to a four point bending analysis and in the other panel is subjected to a three point bending analysis. In both cases finite element analysis techniques are used.

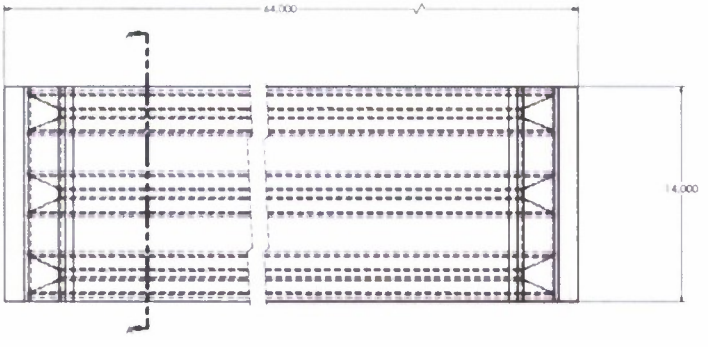

Figure 2.42 Panel Overview

The sandwich panel consists of three non-continuous corrugations, which are continuously stake welded to the top and the bottom plate and pitches 5.250 inches. The cross section and side view of the panel are given in Figures 2.43 and 2.44, respectively.

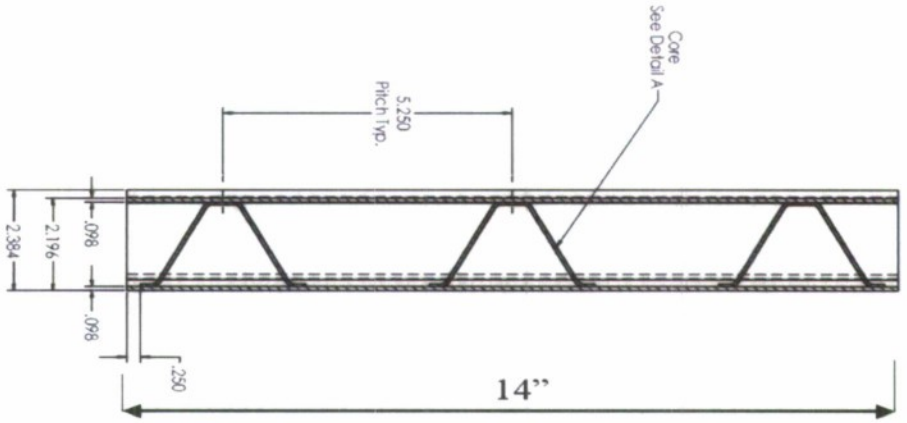

Figure 2.43 Cross Section of Sandwich Panel

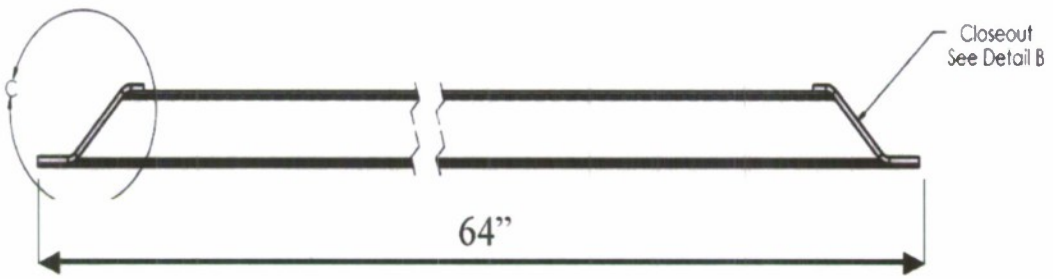

Figure 2.44 Side View

The sandwich panel connection test specimen is made of high strength structural steel plates. It spans 64" from the connection plates, which have 2x4 - 1-inch diameter bolthole patterns with a 14" width. Top and bottom plates each have same thickness of 0.098 inches. The core cell dimensions are shown in Figure 2.45. The core cells are continuous along the length of the panel and made of same material as of the top and bottom plates with a thickness of 0.059 inches and a pitch of 5.25 inches. The sandwich panel utilizes three cores one being at the center of the panel. The close out at the connection end, shown in Figure 2.46, is tapered with an angle of 45 degrees on both ends and each end is covered with a 0.188 inch thick steel plate. The bearing connection plates are 1-inch thick and 14 inches x 10 inches in plan. They are welded on top of the panel from each side housing the bolt hole pattern for mounting.

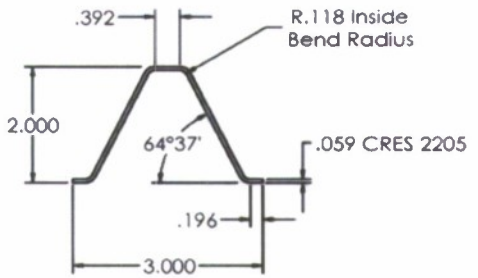

Figure 2.45 Core Cell Shape and Dimensions

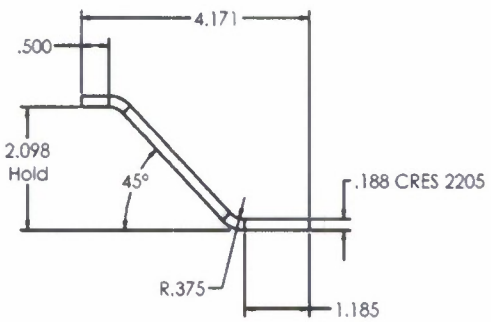

Figure 2.46 Close Out Geometry and Dimensions.

2.3.1 Finite Element Model of the Tapered Connection Test Article

Commercially available interactive finite element analysis software program ANSYS is used to analyze the sandwich panel due to the compatibility reasons with Applied Thermal Sciences, which is the fabricator of the sandwich panel. Difficulties in creating the complex geometry of sandwich panel using finite element software are avoided by using a CAD program. Figure 2.47 shows the resulting geometry of the shell model. The shell model of the sandwich panel analyzed is created using SOLIDWORKS, which is another software package for computer aided design.

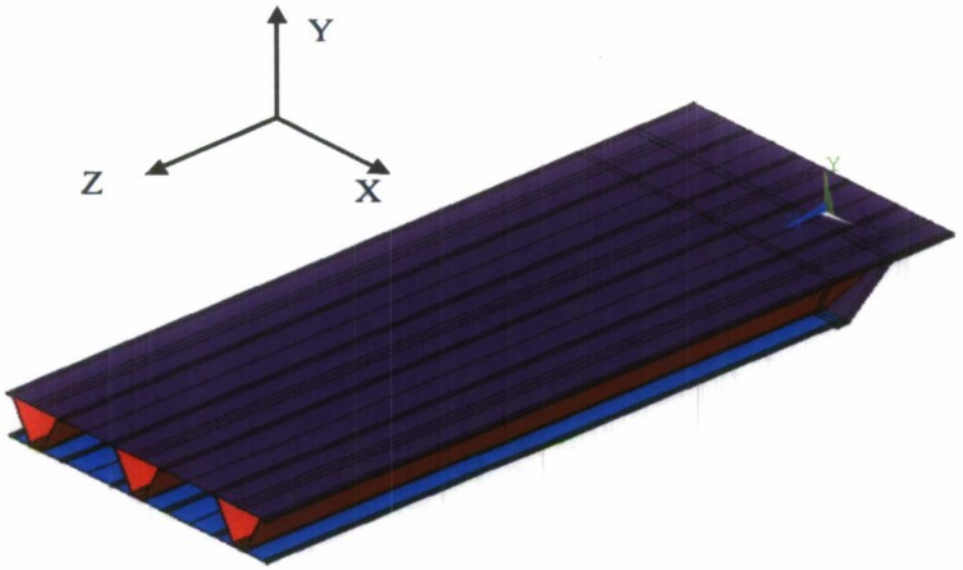

Figure 2.47 Shell Model Created by CAD.

In the static analysis of the model, the bolts, and the connection plate are not taken into consideration. The bolted sandwich panel from both ends through the connection plate is considered as a fixed-fixed beam. The 14 inch wide 64 inch long panel is modeled without the connection plate while using the symmetry in the longitudinal direction. In so doing, half of the panel is created; which reduces the number of elements used in the mesh increasing computational efficiency. The boundary conditions, shown in Figure 2.48, are applied to the right hand side such that panel is fixed i.e., displacement and rotation restricted by selecting all degrees of freedom in the program menu. On the cut surface where the symmetry is assumed in the transverse direction, the boundary conditions are applied such that panel motion restricted in z- direction and rotation is not allowed about the x-axis. Therefore, under the load, panel is allowed to deflect while simulating a fixed-fixed condition properly.

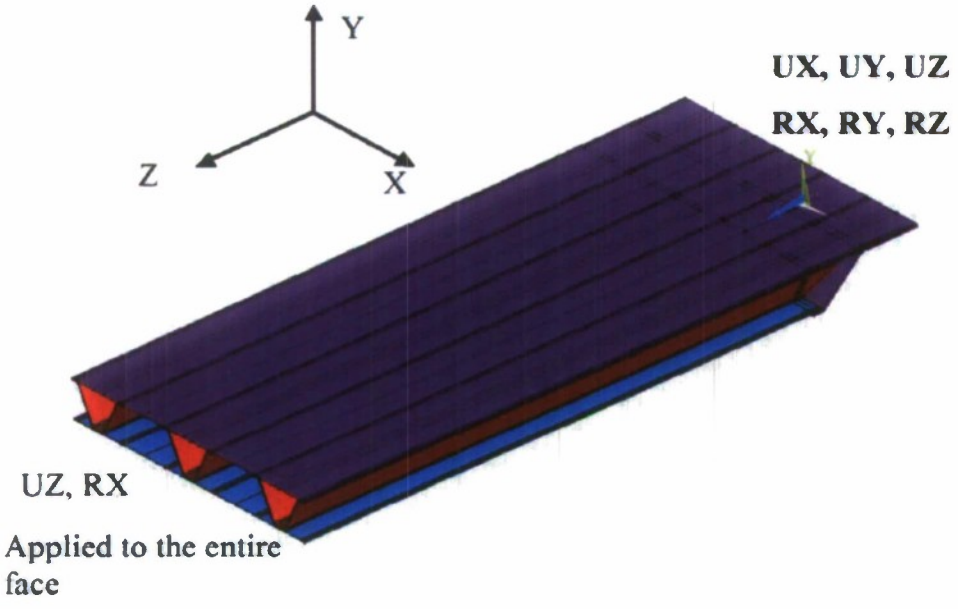

Figure 2.48 Applied Boundary Conditions

2.3.2 Case 1: Four Point Bending Analysis

In the four point bending case the sandwich panel is supported from each end and subjected to a force over a patch of material uniformly distributed across the panel. A sketch of the analysis set up is shown in the Figure 2.49.

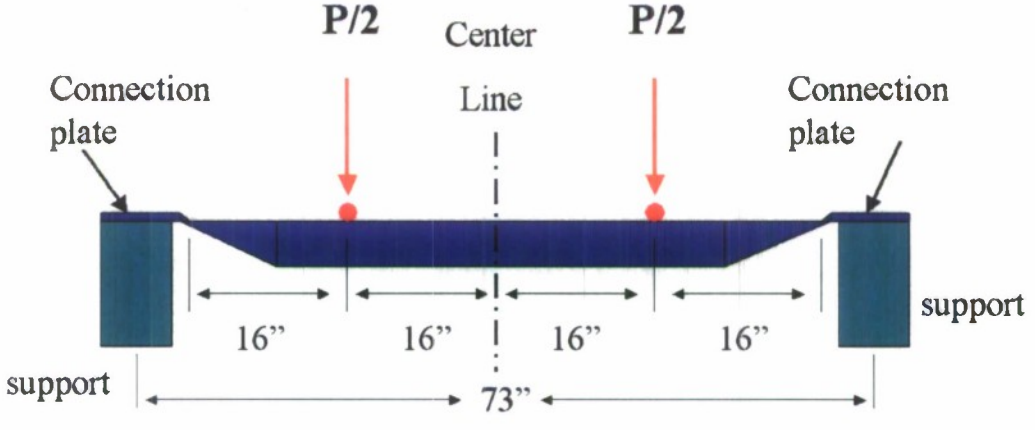

Figure 2.49 Sketch of the Four-Point Load Analysis Set Up

2.3.2.1 Details: Mesh, Loading and Boundary Conditions

Shell 181 finite element is used to mesh the sandwich panel. Four different thicknesses are assigned to the element and parts are meshed with the corresponding element. Shell 181 element is an appropriate element for analyzing thin to moderately thick shells. It is a 4-node element, which offers six degrees of freedom at each node both translation in each direction and rotation about each axis. For the tapered part of the core degenerate triangular option is selected as filler element in mesh generation. Shell 181 is especially appropriate for many modeling sandwich structures and has converges easily and it is very accurate even with coarse meshes. The thickness of the shell defined at its nodes and constant thickness for top and bottom, weld and cover and core are assigned individually. All these geometrical properties are assigned in the real constants option. In the analysis reduced integration option is selected and proper aspect ratio achieved by a fine mesh.

The integration scheme was verified by testing a model using reduced integration over the entire structure. This resulted in a maximum deflection of 0.004509 inches. This is compared to a model using reduced integration on the top and bottom face sheets and closure and full integration on the core, which resulted in a maximum deflection of 0.004513 inches. Accordingly, the choice of integration scheme results in no significant difference for this model.

Convergent is accomplished by using 32800 Shell 181 elements for the half model. 4"x14" patch load applied 16" from the end of the sandwich panel as shown in Figure 2.50. A nominal value of 1 psi is applied by selecting the elements on the top surface of the sandwich panel. This is equivalent of 56lbs total force.

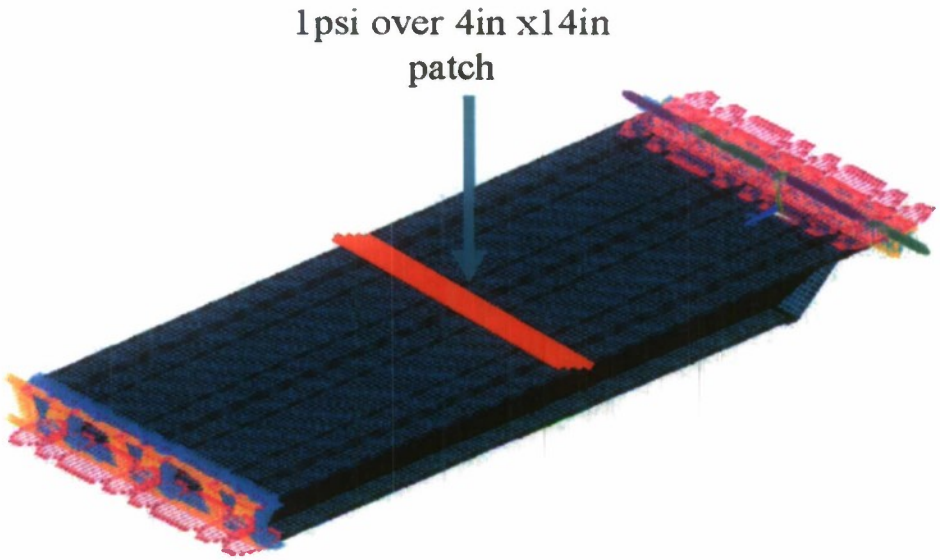

Figure 2.50 Load, Mesh and Boundary Conditions

2.3.2.2 Finite Element Displacement Results

Maximum global deflection of 0.004509" is shown in Figure 2.51 obtained through the analysis by applying 1 psi over 4-in by 14-in patch (56 lbs total) averaging the maximum deflection of the top and the bottom plates at the center nodes. The maximum deflection of the bottom plate occurs under the center cell which is 0.004515" is shown in Figure 2.52.

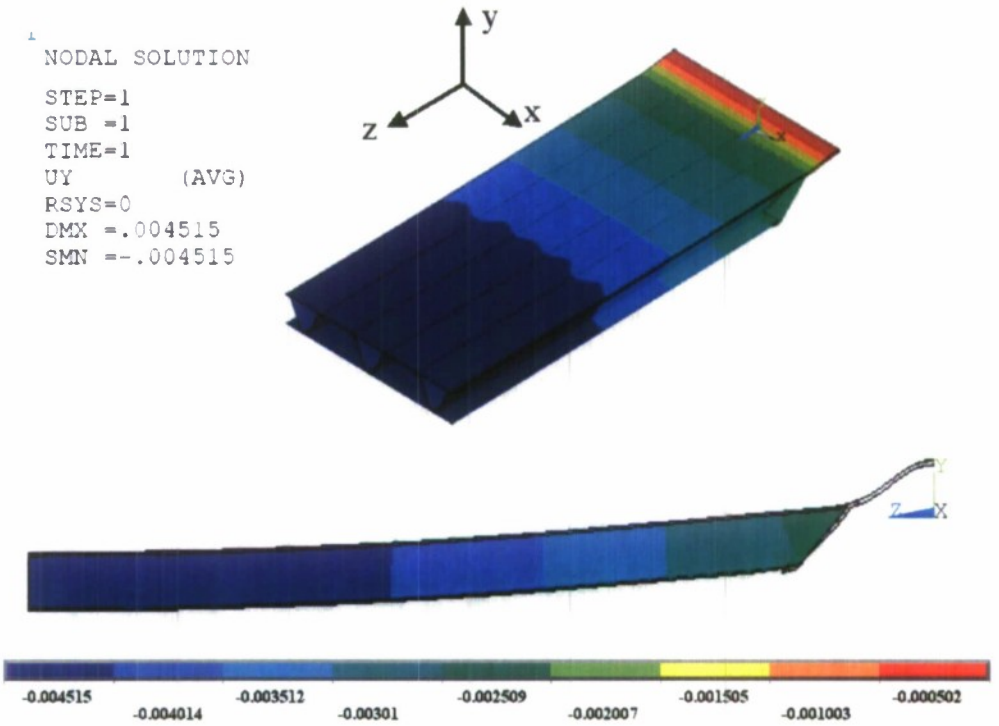

Figure 2.51- Global Deflection

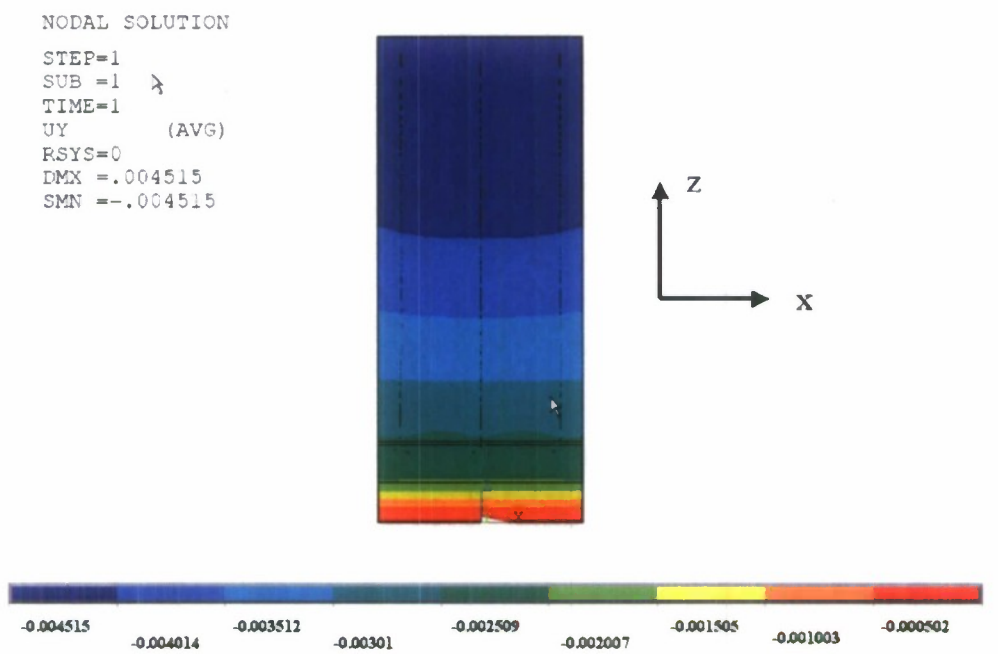

Figure 2.52 -Bottom Plate Deflection

The maximum deflection of the top plate is 0.0045079" and occurs at the center of the top plate is illustrated in Figure 2.53.

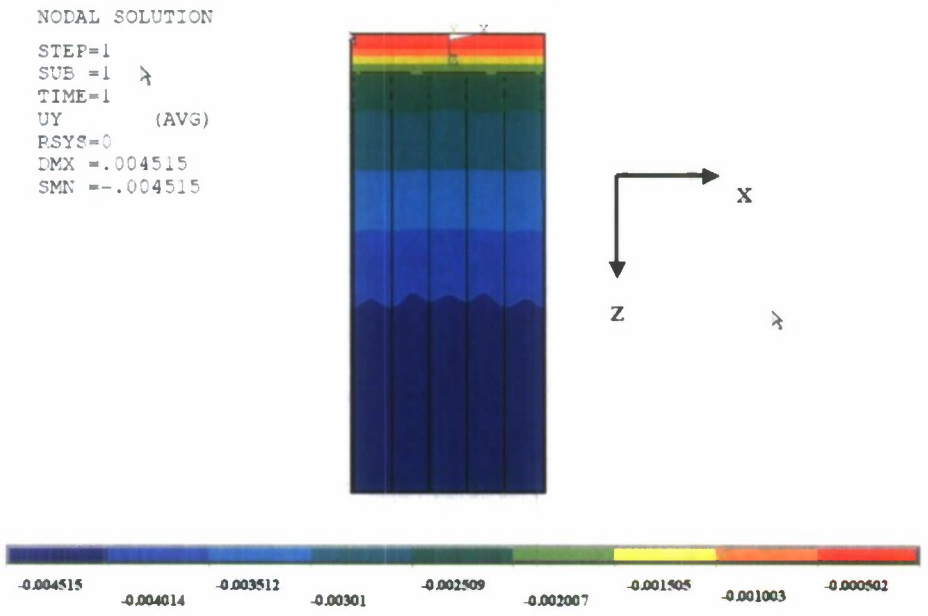

Figure 2.53 Top Plate Deflection

2.3.2.3 Finite Element Stress Results

The maximum in plane stress occurs on top of the extended surface of the top plate of the sandwich panel. The value of the stress in z-direction is +2238psi as shown in Figure 2.54. The maximum in-plane stress occurs at the connection part of the tapered closeout and the magnitude of the stress is –2054psi in z-direction as shown in Figure 2.55.

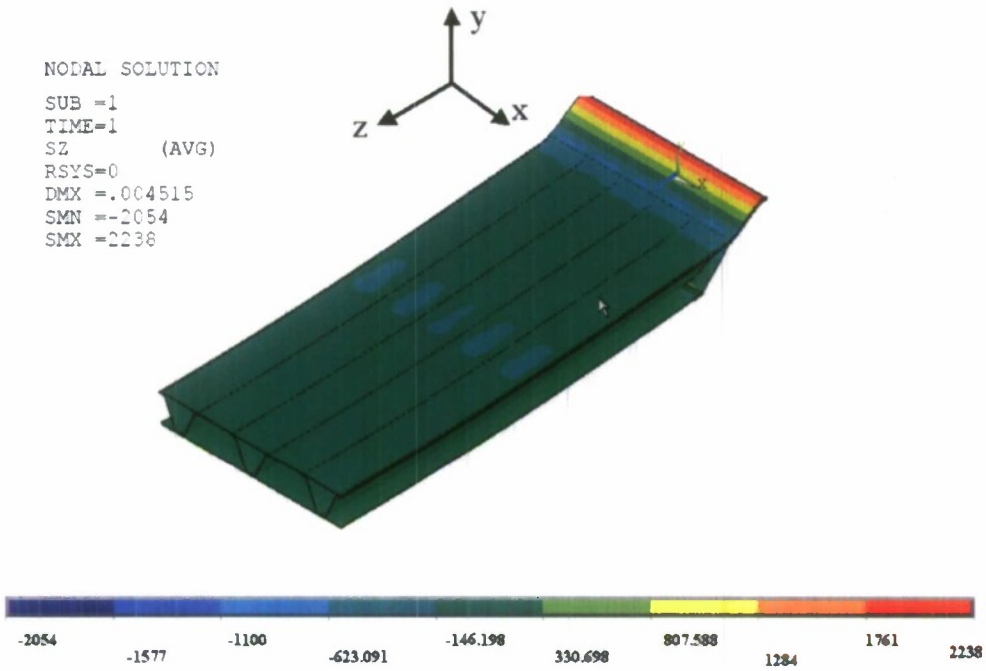

Figure 2.54 Top Plate Maximum In-Plane Stress in z-Direction

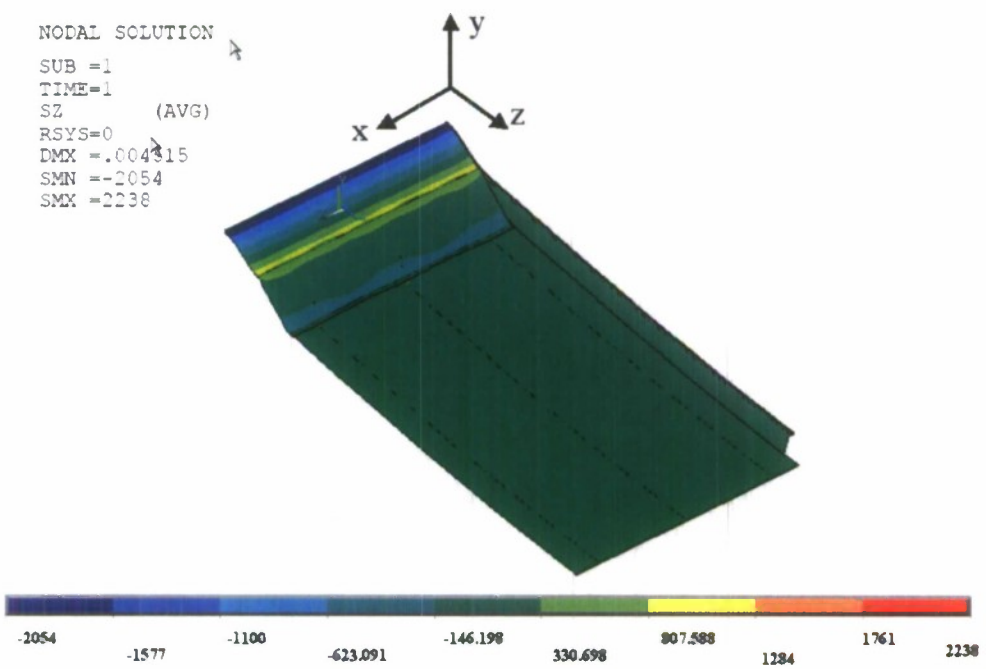

Figure 2.55 Close Out Maximum In-Plane Stress in z-Direction

Maximum in-plane stress distribution in x-direction is shown in Figure 2.56. Due the homogeneous like contour plot of stresses in this direction table of elements created under the ANSYS main menu. After creating the menu, results are listed using the "list results" command tree and then element results are displayed in a tabulated format in the ANSYS output window. Maximum in-plane stress occurs in the node #13806, which corresponds to element #12850 and the magnitude is +2773psi. The minimum value of stress is –3089psi and this corresponds to node #13808 in element #12852.

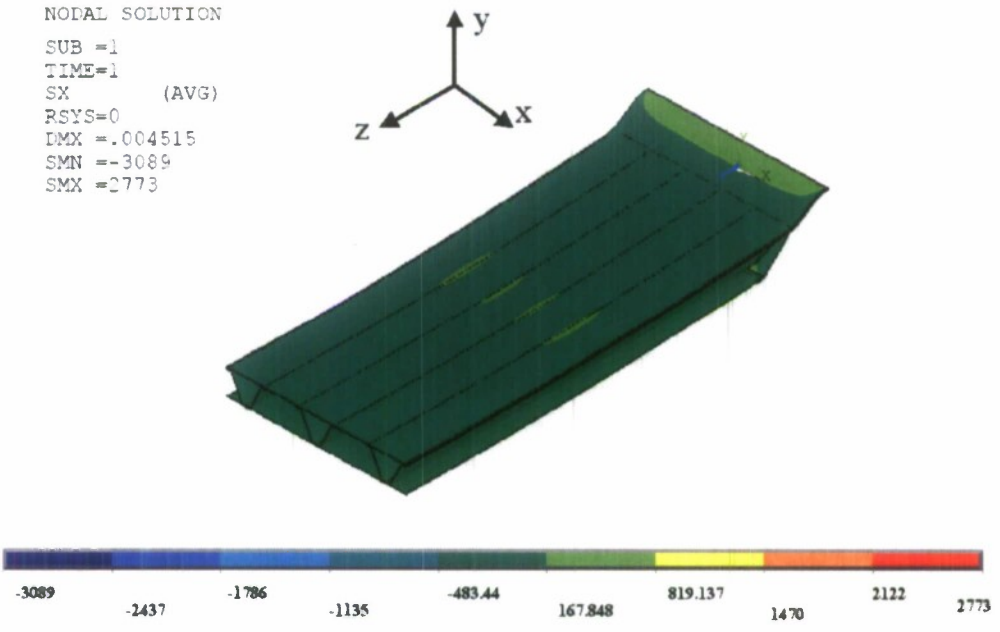

Figure 2.56 Global View of Maximum In-Plane Stress Distribution in x-Direction

2.3.3 Case 2: Three Point Bending Analysis

In the three point bending shown in Figure 2.57 the sandwich panel is subjected to a similar patch load as in the four point bending analysis. The load is applied at the center of the panel, which is 32 inches from the connection plate.

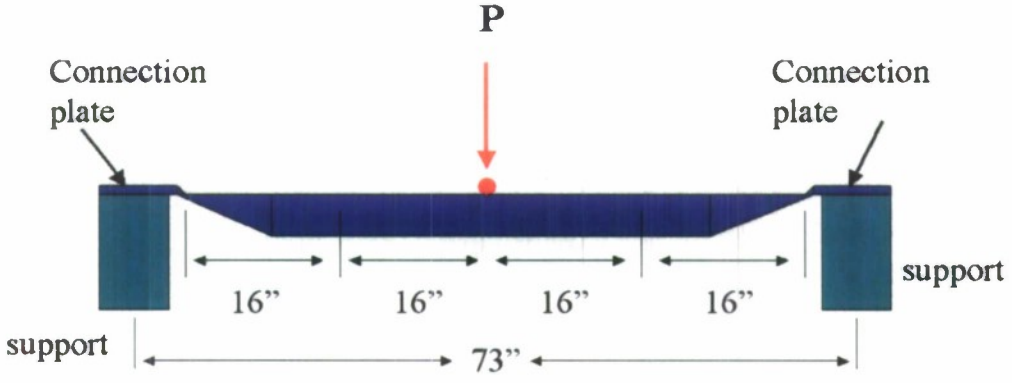

Figure 2.57 Sketch of the Three Point Bending Analysis Set Up

2.3.3.1 Details: Mesh, Loading and the Boundary Conditions

Section 2.4.2.1 summarizes the analysis approach and the element used in detail.
The only exception is that patch load is applied at the centerline in the transverse direction of the plate as shown in Figure 2.58.

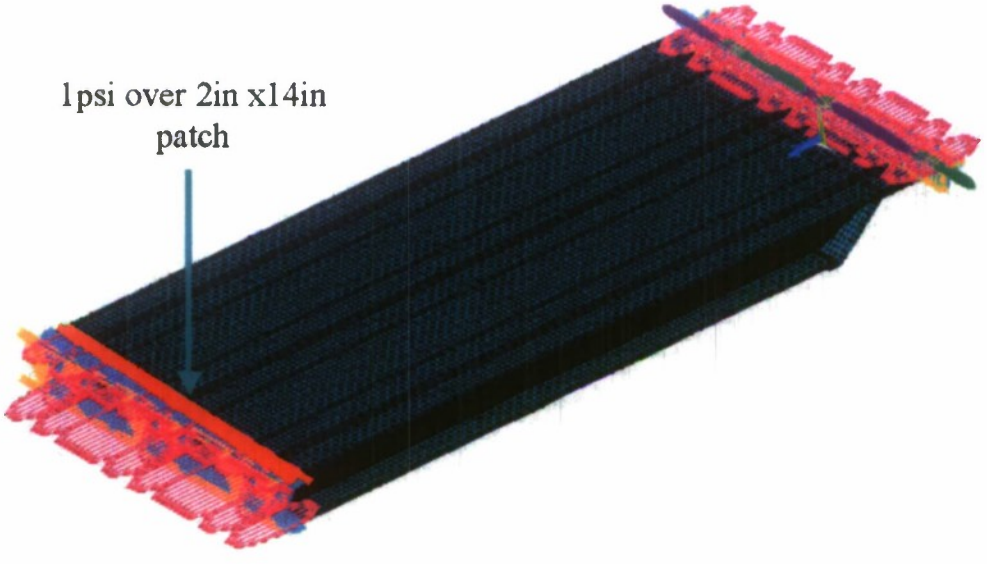

Figure 2.58 - Load, Mesh and Boundary Conditions

2.3.3.2 Finite Element Stress and Displacement Results

The location of the interest on the deflection and the stresses are explained in the four point analysis. In the three point bending analysis same approach is followed. The results are given in Table 2.5.

Table 2.5 Three Point Bending Analysis Summary

Applied Load	56psi
Maximum Deflection	0.003053"
Maximum in-plane stress (x)	1374psi
	(-)1517psi
Maximum in-plane stress (z)	1167psi
	(-)1134psi

3. EXPERIMENTAL TEST PROCEDURES

The objective of the experimental testing is to investigate the mechanical behavior of a 3-core steel sandwich panel with continuous laser stake weld utilizing LVDT's, strain gages and photogrammetry techniques under a 4-point bending test. Section 3.1 through Section 3.2 summarizes the test set up for 4-point bending analysis. The analysis of this panel was described in Section 2.3.

3.1 General Test Setup for Connection Test

Figure 3.1 graphically portrays the test configuration. The specimen is supported at its ends by a connection plate, which is bolted to a rigid support. The sandwich panel is loaded at its quarter points by a concentrated line load applied over a 4inch wide patch load across the width of the top plate as shown in Figures 3.2 and 3.3.

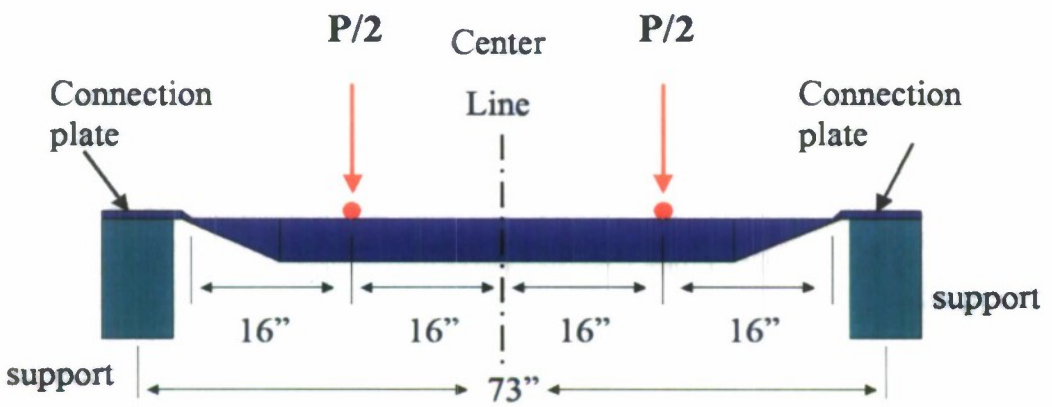

Figure 3.1 Shows the Test Set Up Used for Experimental Study

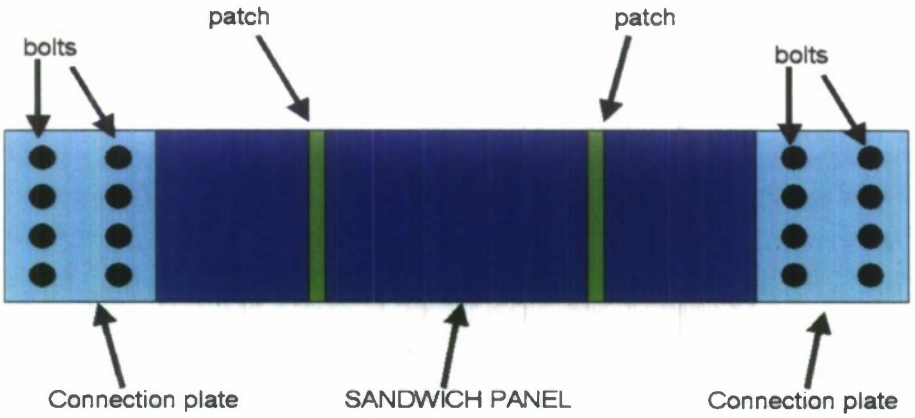

Figure 3.2 Top View of Sandwich Panel

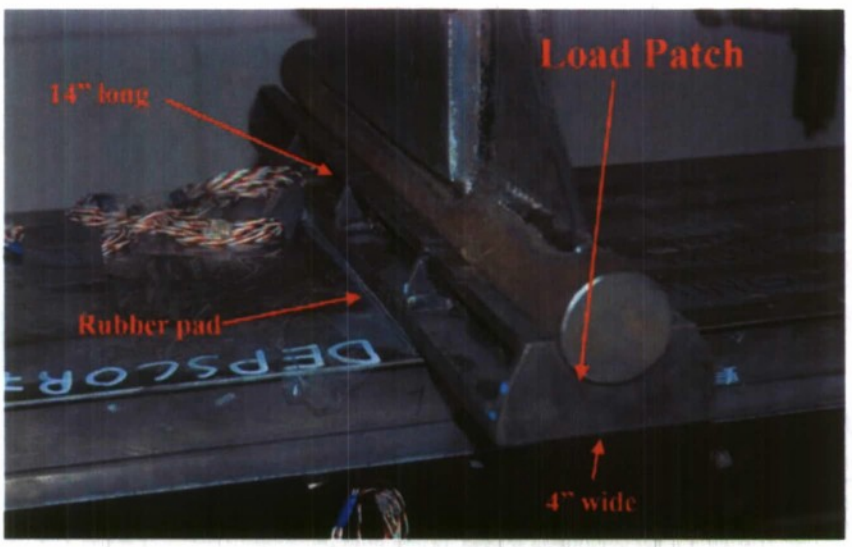

Figure 3.3 Shows Load Patch

The 300kip capacity reaction frame in The Hybrid Structures Laboratory (HSL) located at the University of Maine Orono Campus is utilized to perform the static testing of the sandwich panel as shown in Figure 3.4. A W24-104 top beam used to connect a 55kip capacity MTS hydraulic actuator that spans between two main columns reinforced with shoulder brackets at the connections. A 55K hydraulic actuator is connected to the W24x104 beam through a four hole pattern 1" thick connection plate at the center of the beam using 7/8" threaded stud along with 4 nuts at both bottom and top face of the plate.

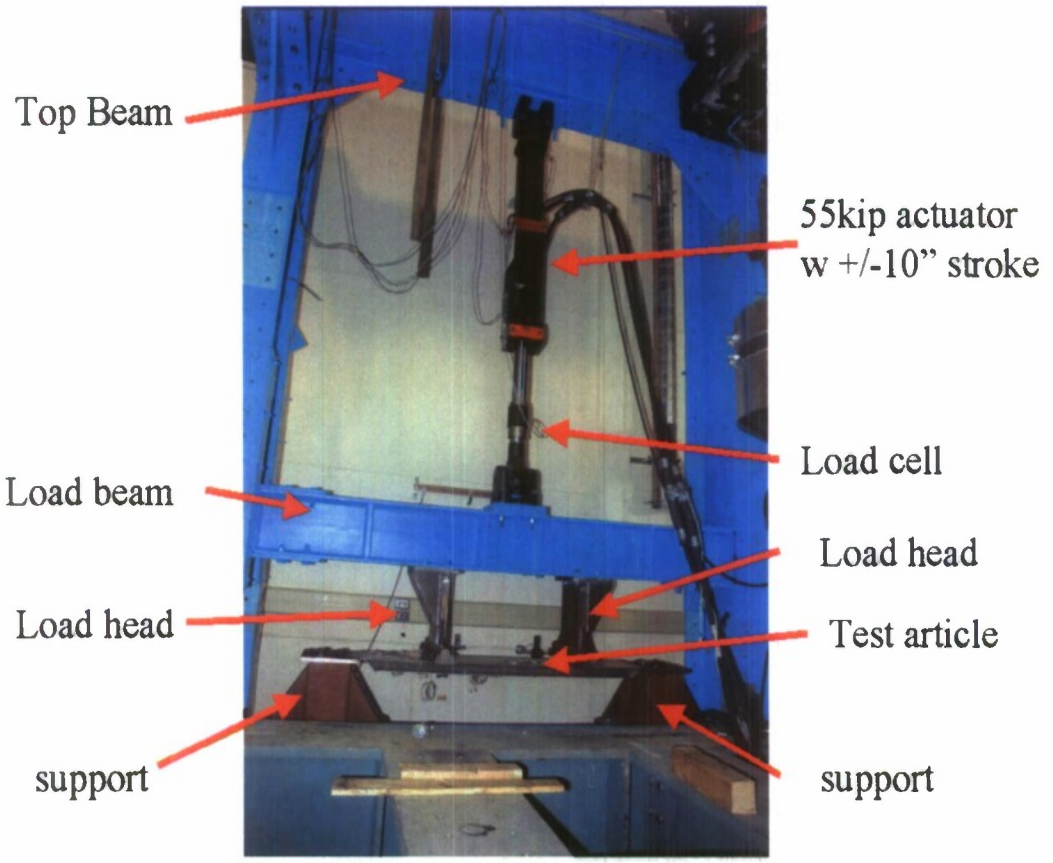

Figure 3.4 General View-Test Setup

A MTS-458 system is used to control and monitor the actuator load and displacement. The load cell calibration was verified prior to testing using an MTS-810 Material Test system located at HSL. After the calibration check the load cell is screwed into the place between the hydraulic actuator and the actuator swivel end.

The swivel end is connected to a the W12 load beam, which has stiffeners between the top and the bottom flange, using a 2" thick connection plate with a square hole pattern with 1" grade 8 bolts which has stiffeners between the top and the bottom flange. The load beam is able to slide between two main columns of the reaction frame. In order to prevent undesired motion of the W12 beam such as rotation about the actuator axis, guides on both ends are used. These guides help to prevent excessive lateral movement.

Load transmitted to the sandwich panel is applied using load heads designed at the University of Maine and manufactured by Alexander's Welding and Machine, Inc., of Greenfield, Maine. The two load heads for the 4 point bending test are connected to the load beam with a spacing of 16inch from the centerline of the sandwich panel as depicted in Figure 3.5. The load heads, made of A36 structural steel, 16inch high welded to a base plate and reinforced with stiffeners. The mounting plate, brackets and 2" diameter 18inch long solid cylinder, are welded together along the width of the panel. The base plate of the load head has 4 holes in a square pattern bolted to the load beam using grade 5 bolts. Washers are used where the nut is connected to the upper side of the W12 beam.

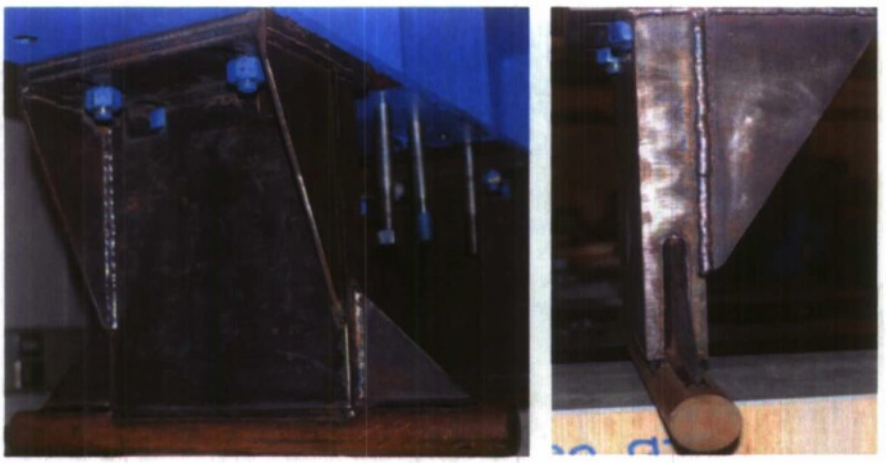

Figure 3.5 Load Head

Two end bearings were interfaced to the connection plate of the sandwich panel as shown in Figures 3.6 - 3.9. The sandwich panel is bolted to each end bearing using eight 1" diameter bolts with a 2"x3" bolt hole pattern. Supports are connected to bottom reaction frame beam of W24-104 by 1-inch bolts via a 5"x6" bolt hole pattern. Both supports measures 73" from the center of the bolt pattern located at the top surface of the supports.

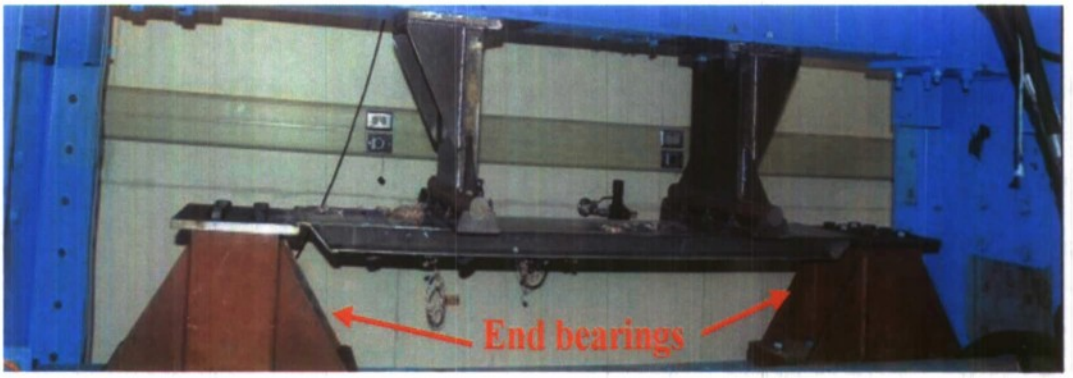

Figure 3.6 End Bearings

Figure 3.7 Detailed View of Support

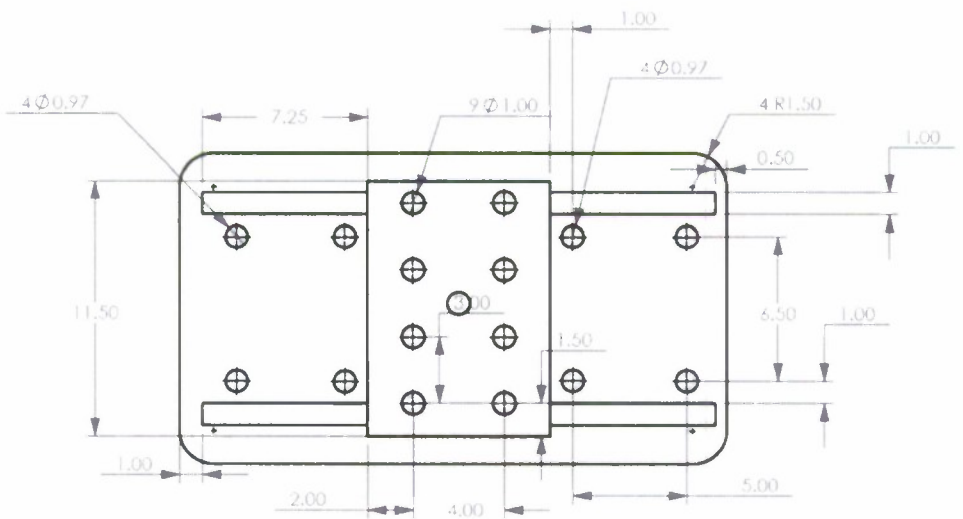

Figure 3.8 SOLIDWORKS™ Rendering of End Bearing Bolthole Pattern

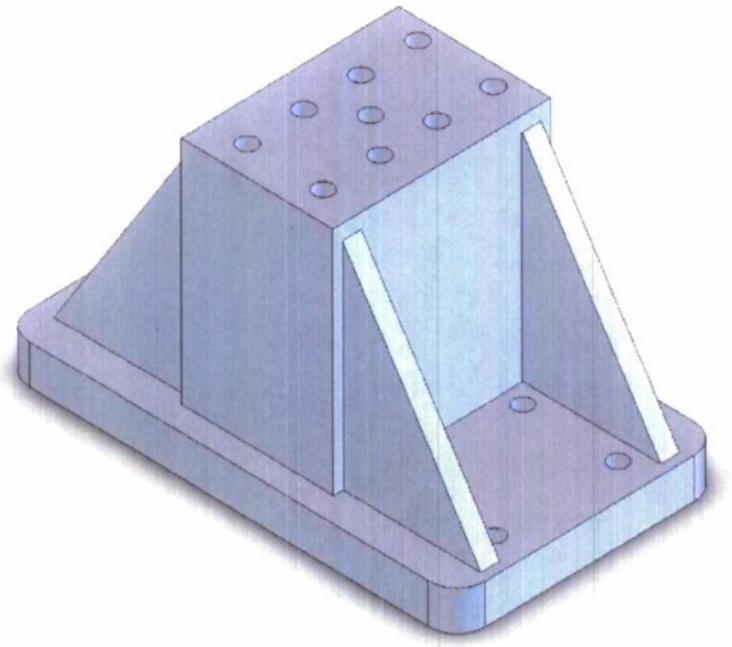

Figure 3.9 3D Rendering of End Bearing

3.2 Instrumentation

Electronic instrumentation consists of displacement and strain sensors. In addition load displacements are recorded as output through the MTS™ system. Photogrammetry is used to estimate the displacement contours at preselected intervals during test.

3.2.1 Displacement Transducers

Displacements are measured using Linear Variable Displacement Transducers (LVDT). The LVDT plan is shown in Figure 3.10. It includes 11 LVDT's and placed at strategic location on the underside of panel. LVDT were held in place using adjustable fixtures as shown in Figure 3.11 made of a solid steel bar fabricated at the AMC.

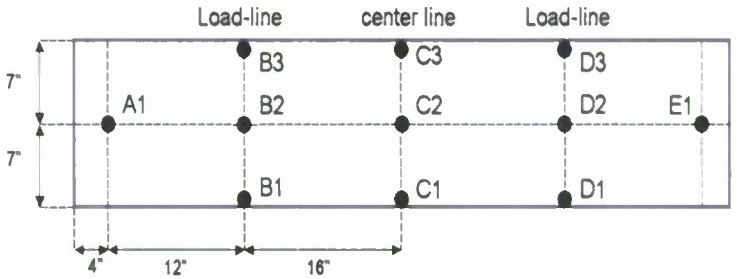

Figure 3.10 - LVDT Layout

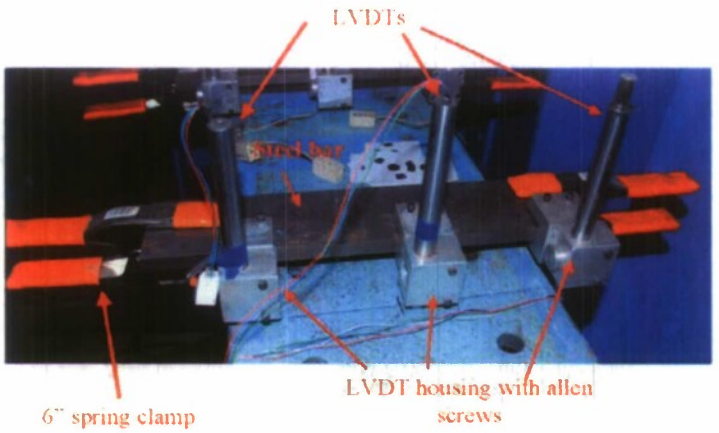

Figure 3.11 LVDT Fixture

The bottom steel bar of the LVDT fixture measures 2"x1" and the top portion measures 4"x1". These two bars connected to each other using 8mm allen screws and the holes tapered to provide a flat finish with the screw heads and the steel block.

Each fixture houses three LVDTs one being at the center of the fixture, which also corresponds to the center of the panel and the other two LVDTS are placed 7-inches apart equally spaced from the center LVDT to monitor the deflection near the longitudinal edges of the panel. The LVDT mounting fixtures are secured to the bottom W24x104 beam using 6-inch spring clamps on each side. The need to prevent the horizontal motion of the fixtures is ignored since there are no significant forces acting on these fixtures. Monitoring the end bearing support motion was also accomplished using one LVDT on each support placed using commercially available magnetic blocks located at the center of the supports between the shoulder brackets. This allowed placing LVDT directly beneath the connection plate.

Due to the difficulties in placing the brass rods of the LVDTs to the sandwich panel, Neodymium cylindrical magnets used to obtain a secure connection between the panel surface and the brass rods. Each LVDT has -/+ 1" range except the ones used under the supports which have a -/+0.5" range.

3.2.2 Strain Gage

Six metal foil 3-grid strain gage rosettes manufactured by Vishay Micro-Measurements™ are used to measure local strains in the sandwich panel. The strain gage plan is shown in Figure 3.12. The strain gages are general-purpose CEA-06-062UR-120 gages manufactured by Vishay Micro-Measurements™. Each grid has 120.0 +/- 0.4% ohm resistance. Gage factor is @24C proposed to be 2.080 +/- 0.5% and the transverse sensitivity is +1.4 +/- 0.2%. For the installation process M-Bond AE-10 Adhesive kit is used. AE-10 cures at 70F in 6 hours with a capability of approximately 6% elongation without creeping.

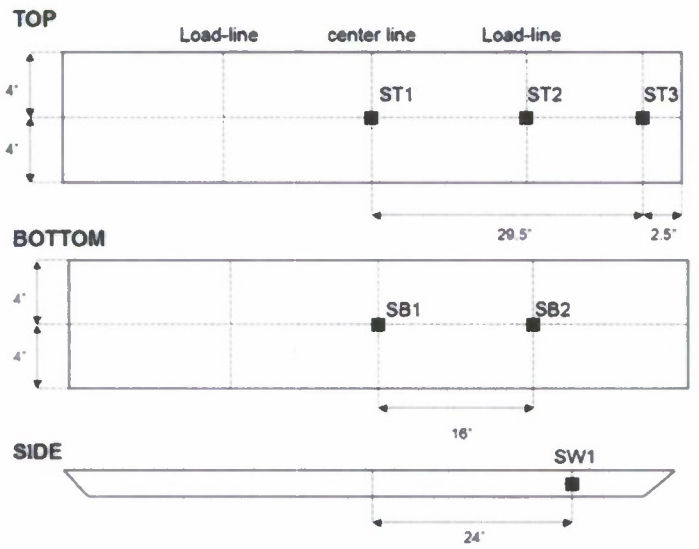

Figure 3.12 - Strain Gage Layout

To mix the adhesive, calibrated droppers used provided in the kit and original jar of the bonding material used for mixture. For the application process Instruction Bulletin B-137 written by Vishay Micro-Measurements™ is used following step 1 through step 11. These steps are

explained in details on page 2 through 4 in this bulletin. Strain gages are then soldered to the cable using conventional techniques based on the strain gage layout. It is assumed that the mechanical behavior is symmetric about the center of the panel in short direction due that strain gages are applied only to the one half of the panel. The instrumentation is interfaced to the data acquisition system using cables with phone jacks.

3.3 Photogrammetry

In this project photogrammetric techniques are used in addition to the LVDT's to measure the deflection of the sandwich panel. Photogrammetry is a technique, which determines the geometric properties of objects from photographs. Three dimensional coordinates of the points located on a particular object of interest can be determined by measurements made from at least two but preferably 4 or more photographs taken from different angles. Points of interest on the object are identified in each photograph. These points are referenced to one another in a systematic order through the cameras original location where the pictures taken. This process enables points to intersect and determines the three dimensional location of each point. The orientation of the camera defines its location in space and its view direction. After defining the points in three-dimensional space, coordinates of each point recorded and used for further processing. This technique is used in topographic mapping, architecture, engineering, forensic engineering and many other areas.

Photomodeler™ is the software used to process the image and is a commercially available software package is purchased from EOS Systems of Vancouver, Canada. The program offers two different methods to define points of interest; one where the user defines the points using a simple marker or the second where the program generates more sophisticated target points. The target point sizes can be customized depending on the user's objective, size of the object to be analyzed, number of targets points to be used etc. Some typical target points with 2mm, 6mm and 8mm inner diameters and sophisticated ring shapes are shown in Figure 3.13.

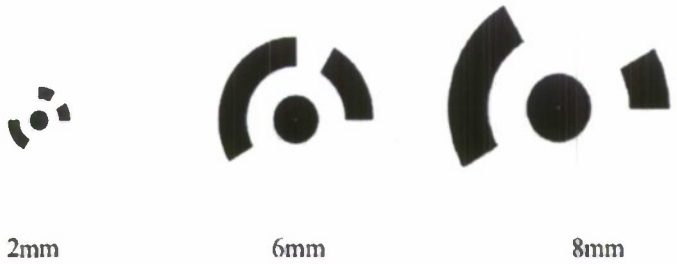

Figure 3.13- Unique Coded Target Points

Photomodeler program can automatically determine the X-Y-Z coordinates of the center dot on the target with the coded targets. Resolution of the target points can play an important role from the viewpoint of camera as well. Photomodeler enables the user to set the resolution to meet the objectives as well. In some cases especially in poor lighting conditions it is found to be essential to use high-resolution target points printed in high quality photographic papers. In some cases it is required to use relatively dull target points. It is essential to go through a trial and error processes in order to select the most appropriate target resolution and target size. In the photogrammetric test, 6 mm target size selected. Ideally it is beneficial to go through a target size selection process for capturing target points of interest at critical locations. These two processes can be redundant, however. Once the target selection process is completed and the program captures target points, processing the data takes only utilizing a few commands in the Photomodeler. This is the most efficient way in terms of processing the data gathered from the software. The only disadvantage can that sometimes the program does not recognize every single target point even though target points are in the photographs. It is found that this happens randomly for instance a target point may be recognized in one photograph but it may not be recognized in the other. The possible solution to this handicap is to take more than suggested number of photographs and run the target recognition module in the program. In addition to that, program generates a number of target points based on the parameters input to generate targets and user is restricted to use that particular number of targets at once. The user cannot use the same target point more than once on the object as it will cause an error in the software. Placing the target points to the desired exact location can also be a challenge. The center of the target point should be placed to the point of interest. Using conventional methods and considering involved human factor some error is associated with the data collected. On the other hand if

target are created by the user points then the user will have to manually capture these target points and reference each point to one another in a systematic order. This process is tedious and could take a full day of labor depending on the number of user-defined targets. The advantage of this approach even though it is labor intensive, user is capable of capturing every single target point. In some instances this may be the only alternative. In both methods a user-defined coordinate system must be introduced and a known length of any object, which exists in the photographs. This should be entered to the program; however, the coordinate system can be an object as simple as a carpenter's square. It is extremely important that length of the coordinate system object should not be part of the object being measured.

3.3.1 Camera Calibration and Technical Factors

In this photogrammetry test Photomodeler V6 is used with a Nikon D300 12.1MP digital camera. It is essential to use high quality camera since the resolution of the photographs taken have significant impact on the accuracy and target capturing. Nikon D300 12.1MP camera coupled with a Nikon 24mm fixed-focus manual-focus lens with a constant aperture of 2.0, which is very sharp and has low linear and perspective distortion. Camera and lens system are shown in the Figure 3.14.

Figure 3.14- Camera and Lens Used in Photogrammetry

Photography lenses are complex engineering designs. Lenses are made of layers of multiple elements working either individually or working in groups within the barrel of the lens. Each

lens has its own advantages such as delivering sharp and crisp results with almost no linear or barrel distortion, which renders the straight lines straight or disadvantages such as delivering soft and distorted results. Due to these factors lens selection is also important since it has an effect on the accuracy of the results and significant importance on the software's recognition system. Fixed focal lenses work better than variable focal lenses for photogrammetry. Even though Photomodeler claims to compensate for such disadvantages, the procedure for correcting lens distortion is unknown to the user. Due to lack of such information these mentioned factors considered for selecting this particular lens.

After selecting the lens and camera combination Photomodeler's calibration process using special calibration sheet provided with the software performed. In this process user is required to take 6 or more photographs of the grid paper, which was taped from the four edges to the wall in the HSL. Photographs were taken from different angle as well as holding camera in a rotating pattern such that in each photograph camera was rotated about the axis of the lens. This procedure provided with a multiple camera location with different angles of photographs to reference all the grid points with respect to the camera position as shown in Figure 3.15. This process helps to increase the accuracy of the calibration.

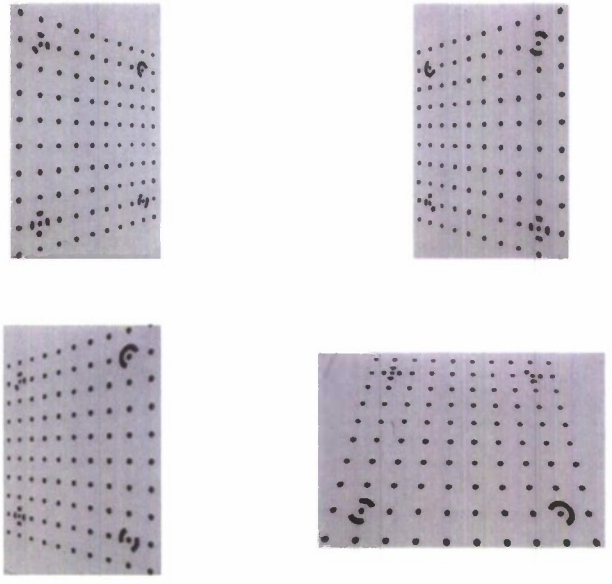

Figure 3.15 Photographs Used to Calibrate the Camera System

After taking photographs, Photomodeler started with a new project and Photomodeler Calibration project selected in the options. The camera was given a unique name, its type entered to the program and any requested information by the software entered to the program. Photographs added to the calibration wizard and then Photomodeler automatically completed the rest of the calibration process. This unique method lets user use more than one camera in the program. However, in each project using multiple photographs taken with different cameras is not possible.

3.3.2 A Guide to Photomodeler

This section is intended to create a step by step guide on how to obtain displacements using Photomodeler's user defined target module. In this procedure Canon EOS 20D and 24mm f/2.8 camera lens manufactured by Canon are used. The calibration process and the selection of this system is explained in details in Section 3.3.1. It is emphasized that this procedure is only going through the operating procedures of Photomodeler and the accuracy of the results are not discussed. As a test specimen 30"x30" fiber reinforced composite plate is used as shown in Figure 3.16.

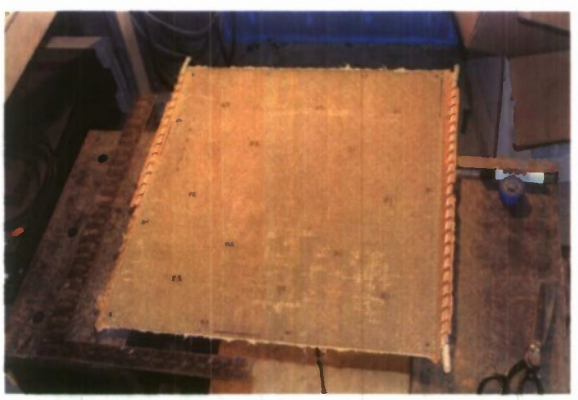

Figure 3.16 Composite Plate with User Defined Points

The user defined target points are marked on the panel using a permanent marker on several points. There can be as many points as user wants to mark. There are no limitations on the number of points can be used. First of all, photographs must be taken before the load is applied

and the study must be named as "undisplaced". This will let the user to capture the coordinates of the user defined points in the x-y-z coordinate system before the structure is subjected to loading.

Step1:

Photomodeler is initiated and the camera is selected which is used to take picture in the software's camera database as shown in Figure 3.17. Photomodeler can introduce more than one camera and any introduced camera can be selected. However, using more than one camera in analysis is not acceptable.

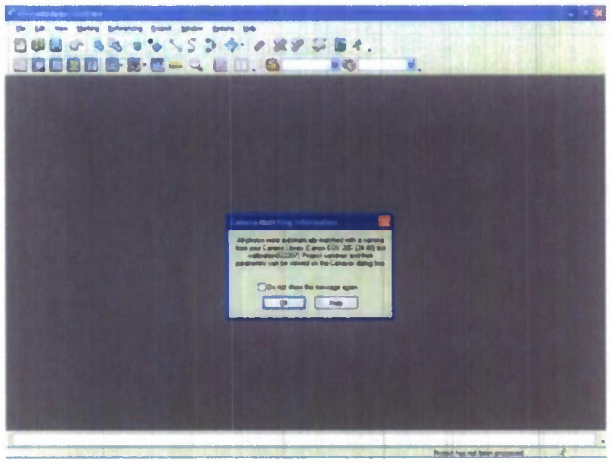

Figure 3.17 Camera Matching Information – Canon 20D with 24mm Prime Lens.

Step 2:

After selecting the camera, photographs must be selected to use in the analysis from the photograph library. Here user can create and organize photographs and store them in folders. As seen in the Figure 3.18 four photographs are selected.

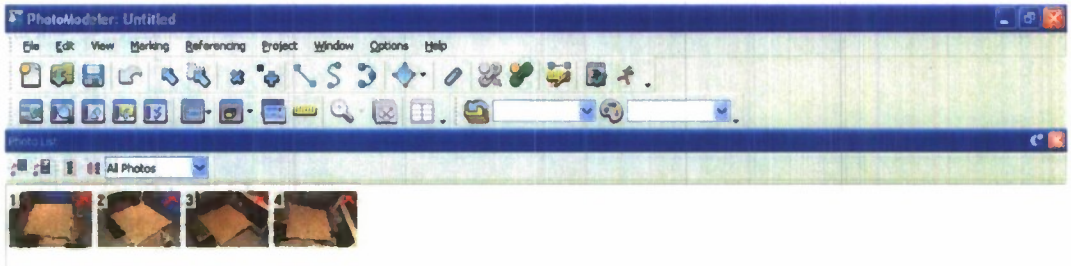

Figure 3.18 Photographs Used in the Analysis

Step 3:

In this step user needs to double click on each photograph to activate them as shown in Figure 3.19. This way user can use the selecting tool to introduce the user defined points to the software.

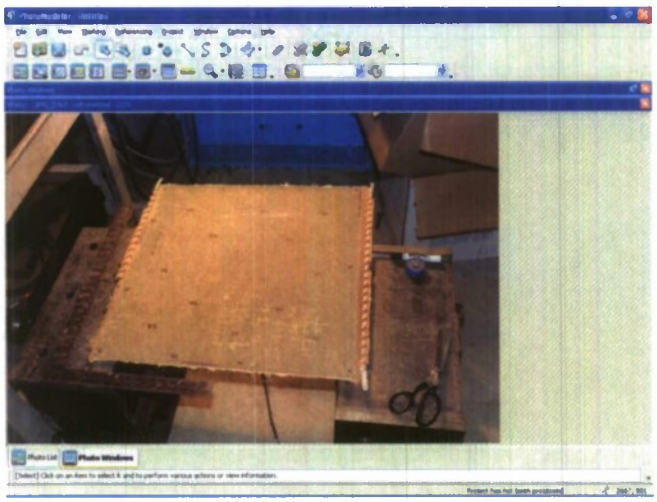

Figure 3.19 Active Photograph

Step 4:

In this step user must reference the user defined points in the photographs to one another by activating the reference mode in the tool bar as shown in Figure 3.20. However, this can be done also using the Referencing drop-down menu. Referencing drop-down menu is located on the 5th menu from the left hand side of the menu options.

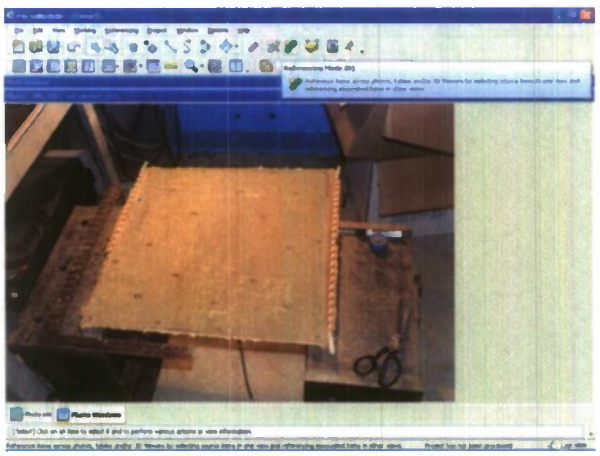

Figure 3.20 Reference Mode

This way, referencing control is activated as shown in Figure 3.21, which enables Photomodeler to recognize the locations of the user defined points in 3D space.

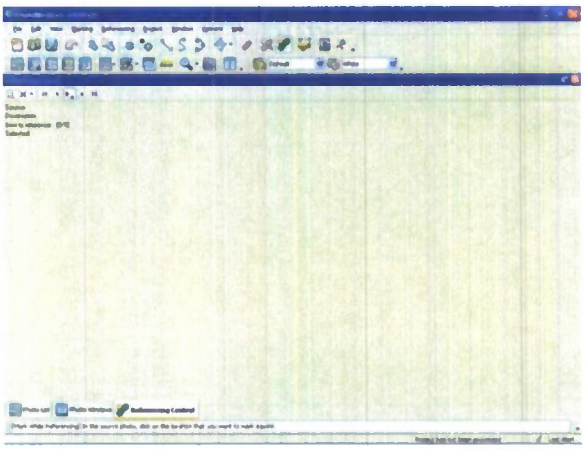

Figure 3.21 Active Referencing Control

Step 5:

In this step user is ready to mark the user defined points on the model by clicking on the mark points mode as shown in Figure 3.22. This tool enables user to mark the photographs. If accidentally clicked on any other location or point other than the user defined points, software lets user delete these unwanted marks.

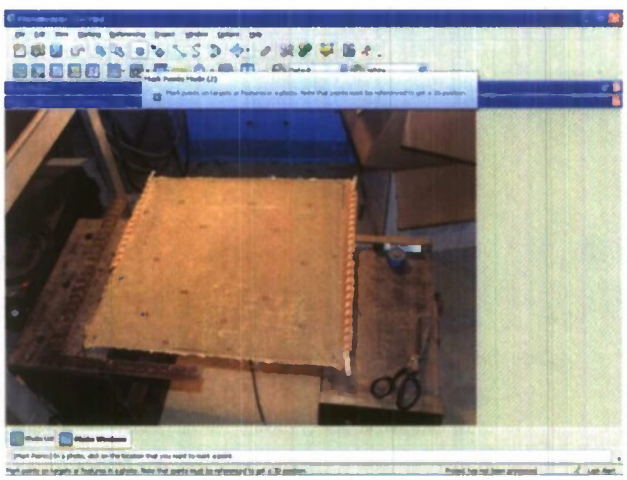

Figure 3.22 Mark Points Mode

Marking small points can be a challenge. Photomodeler offers a local magnification feature by pressing the Alt key. The area will be magnified where the mouse cursor is located and user can mark the point in that magnification window as shown in Figure 3.23.

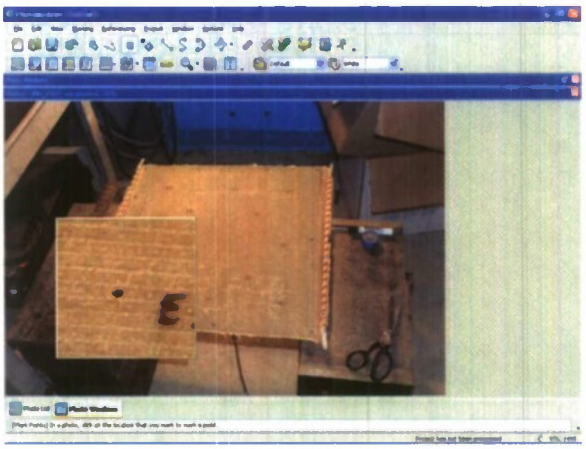

Figure 3.23 Location Magnification Window

By clicking the points using mark tool, selection is done and completed as show in Figure 3.24.

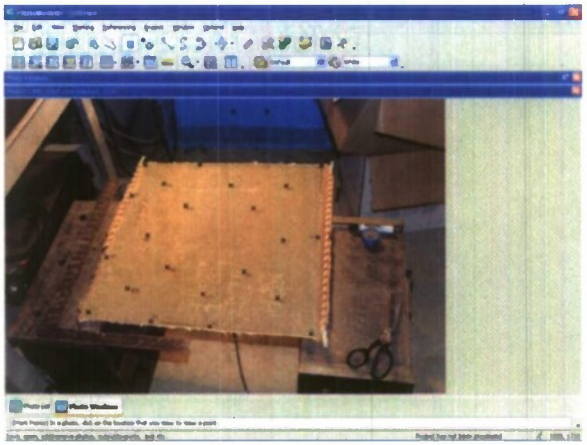

Figure 3.24 -Selected User Defined Points

Step 6:

After selecting all the points in the first photograph, user is ready to insert the second photograph as shown in Figure 3.25 and follow the procedure explained in Step 5.

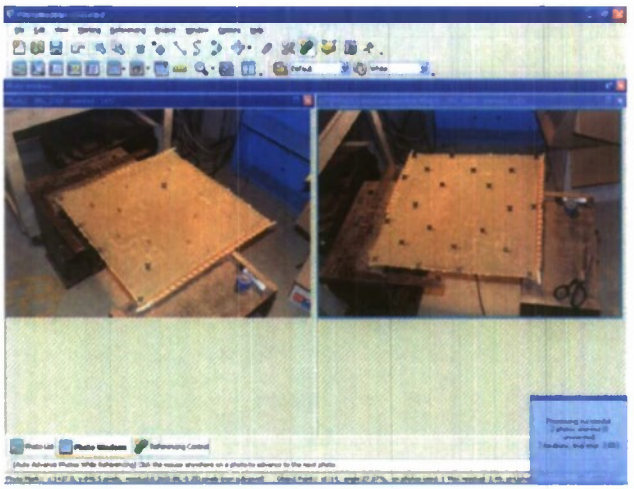

Figure 3.25 Added Photograph

While following the Step 5 on the second photograph, a message window appears on the right hand side lower corner of the screen regarding to the successfulness of the orientation after selecting three or four points. It may take more points to select to achieve this depending on the number of points selected in the first photograph. This information window lets user that the photographs are oriented with respect to each other in the 3D space and location of the user defined points are known by the program. After the orientation, user can click on the points on the first photograph, also known as main photograph, Photomodeler creates lines that pass through the points to make the searching of the points easier on the second photograph as shown in Figure 3.26. These lines are also known as orientation lines.

Figure 3.26 Orientation Line on the Left Photograph

However, it must be noted that these orientation lines does not necessarily pass through the user defined points as shown in Figure 3.27. Photomodeler gives relatively good estimation if there are two or three photographs present in the working space. The accuracy increases, as the number of photographs increases, although this statement may not be true for every case.

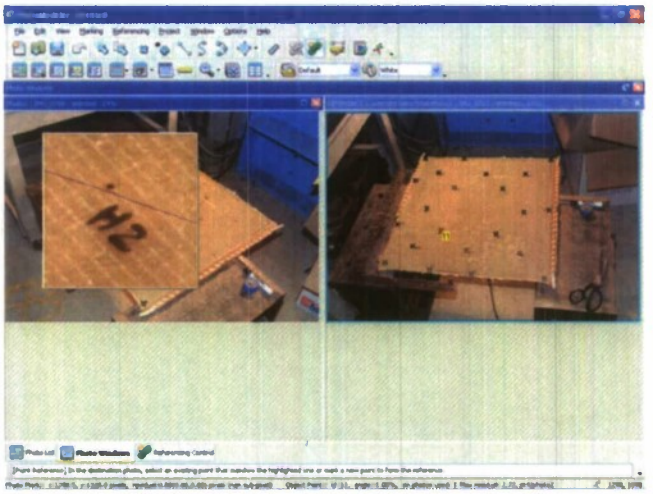

Figure 3.27 Inaccuracy of the Orientation Line

The third photograph is inserted, Step 5 is followed, and orientation of the third photograph is completed as shown in Figure 3.28.

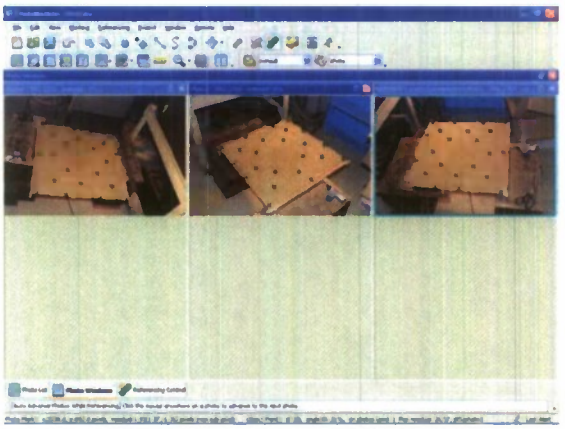

Figure 3.28 Oriented Three Photographs

Step 7:

After completing the orientation of the photographs of the object, user can visualize the location of the user defined points in 3D space by clicking on 3D view command button on the toolbar as shown in Figure 3.29.

Figure 3.29 3D View Command Button in Toolbar

Photomodeler generates user defined points and presents them on a blue-screen as shown in Figure 3.30.

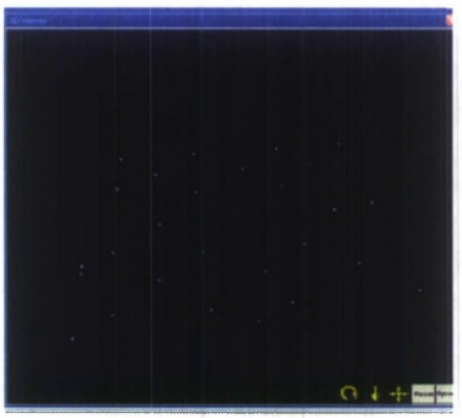

Figure 3.30 Defined Points in 3D

This step does not play an important role in the analysis part or it does not help user to process the data easier way. However, it gives user a good idea on how the data is processed in the software. Basically, defining the points and introducing the coordinate system is constructing the programs input file and then data is progresses based on the information collected through this screen. This step is not mandatory to follow. It may be skipped and will not effect the results of

the analysis under any circumstances based on the assumption that previous steps are followed accurately.

Step 8:

After following or skipping the Step 7, user should right click on any of the photographs in the screen. By doing so, another list of command window will open with several options in it as shown in Figure 3.31.

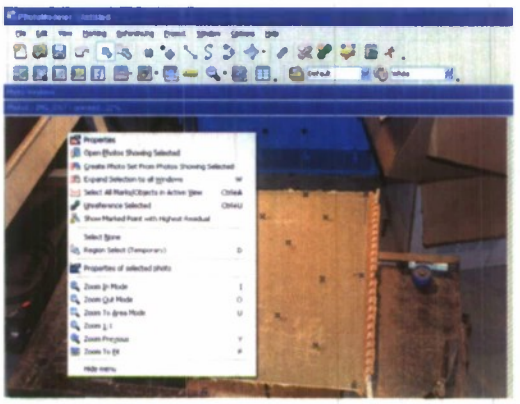

Figure 3.31 Options Menu

User should click on the properties button which will open another window on the screen as shown in Figure 3.32.

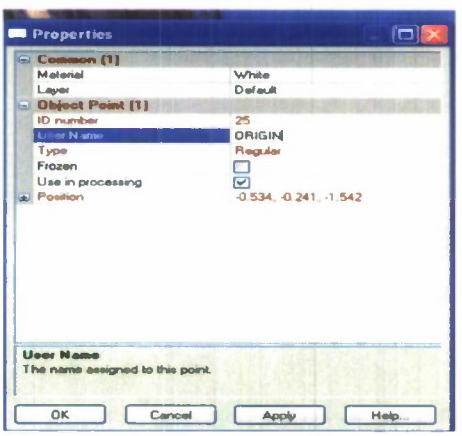

Figure 3.32 Properties Window

User should name each user defined point in a systematic manner carefully. This step is for convenience only but it is strongly recommended not to skip. If there are not more than a few points of interest in the analysis and the user believes that leaving the points without giving them names would not make the post data processing confusing; it is user's judgment. On the other hand, it is strongly recommended to label each point regardless of the number of points.

Step 9:

In this step user needs to define the x-y directions and the origin. To do so, click on the Project drop down menu as shown in Figure 3.33 and select scale & rotate option.

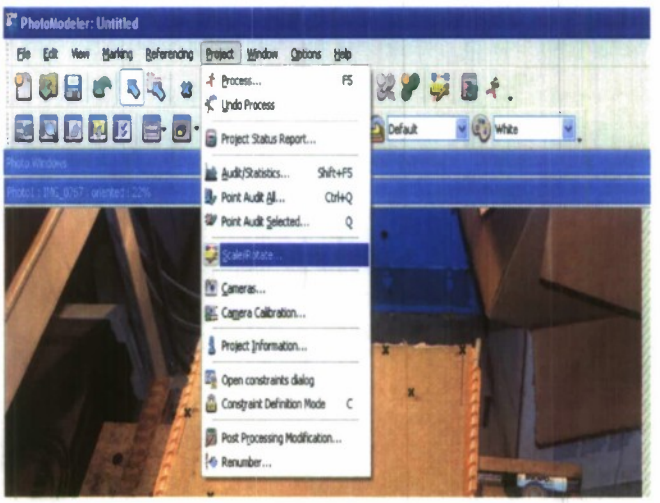

Figure 3.33 Scale and Rotate

A small window will open that contains four tabs as shown in Figure 3.34. User needs to click on the Translate tab to enter the x-y-z coordinates and then should hit the define button to assign the location of the coordinates. After then, user may introduce the unit system to the software. This information is optional. User may skip the units & scale tab if no unit output is desired. In the last tab, user should enter the position of the x-y coordinates. This should be done in a systematic manner. For the x axis, user is expected to click on the coordinate system in the photographs from left to right in a positive direction and similarly for the y axis from front to back as positive direction. This step can be done in any order, first x and then y or vice versa. Z-axis is automatically defined by the program due to that it can be left blank. It is found out that

Photomodeler defines the z axis in the upward direction as positive so any deflection analysis results are given with the negative sign.

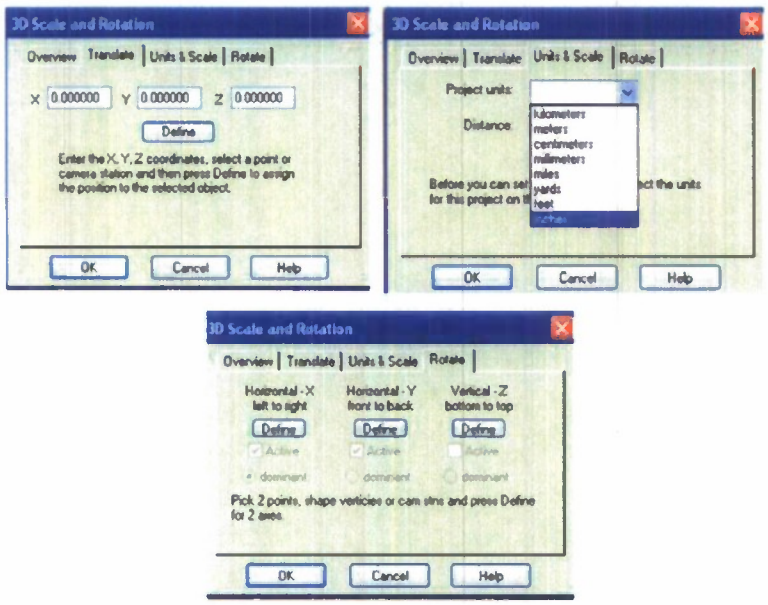

Figure 3.34 Scale & Rotation Tab

Step 10:

Step 1 through Step 9 orients the photographs and locates the points in the 3D space and software calculates the coordinates of each point and stores them. Step 10 allows user to create a table, which displays the results. To do so, user needs to click on the generate table command button on the toolbar as shown in Figure 3.35.

Figure 3.35 Generate a Table

This will open another window with Table options as shown in Figure 3.36.

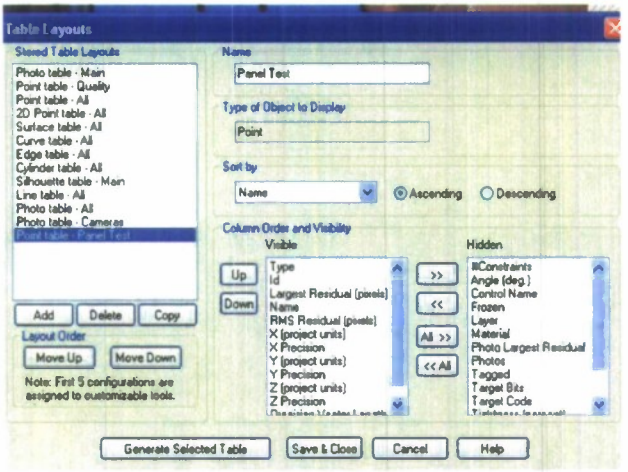

Figure 3.36 Table Layouts

In this window user can name the project under the Name and the type of the project will be displayed automatically. User can select the Column Order and Visibility and then sort the results either in ascending or descending order. The output table will look like an MS-Excel Sheet as shown in Figure 3.37.

Type	Id	Large Resid (pi...	Name	RMS Residual (pixels)	X ()	X Precision	Y ()	Y Precision	Z ()	Z Precision	Precision Vector Length
Regular	8	0.1247...		0.113640147940	0.189404184777	0.001154473999	-0.178727142657	0.001147015265	-1.631415233670	0.001608383255	0.002286088622
Regular	15	0.3148...		0.309490716914	-0.400066213216	0.003361622425	0.218858458205	0.001583969708	-1.981405996039	0.005349842745	0.006506623132
Regular	7	0.3338...		0.276631771212	0.291810280072	0.001259909058	-0.280783573626	0.001108144866	-1.546909141793	0.001861723076	0.002504257464
Regular	9	0.4852...		0.368534132896	0.077652518203	0.001089458001	-0.092759483651	0.001097724286	-1.700671069862	0.001453231859	0.002122214326
Regular	19	0.8509...		0.412177838081	0.005206936879	0.001157019962	0.231244624914	0.001095754312	-1.980133288946	0.001389188866	0.002114052604
Regular	14	0.8566...		0.680409240156	-0.164126849401	0.001142032326	0.157632439725	0.001064370724	-1.907180967316	0.001451778931	0.002131850121
Regular	22	0.8973...		0.704650449735	0.211330309254	0.001056689071	0.005905696333	0.001183453906	-1.793192066494	0.001425835529	0.002133110850
Regular	6	1.0563...		0.819124091855	-0.021220447702	0.001311583843	-0.251297598846	0.001014963875	-1.557820860670	0.001533899721	0.002259037892
Regular	23	1.2095...		0.957343108294	0.331953401037	0.001070188055	0.008414531531	0.001317476393	-1.800758086778	0.001468456999	0.002244418071
Regular	21	1.2337...		0.880916096811	0.101901710900	0.001074471438	0.130120530772	0.001063339478	-1.896989017993	0.001369561487	0.002039823125
Regular	13	1.2338...		0.984797414985	-0.292125815529	0.001192154104	0.051691989815	0.001057918891	-1.806904387477	0.001485484335	0.002178781195
Regular	24	1.2866...		1.051203354374	0.369385256952	0.001157283999	0.290207260745	0.001404958280	-2.048117111654	0.001243389627	0.002204366527
Regular	16	1.3087...		0.989850296616	-0.274232885487	0.001311157468	0.260670937358	0.001275583923	-1.991158609572	0.001483214997	0.002358031842
Regular	27	1.3140...		0.964192390451	-0.314899205862	0.001342471723	-0.072335717140	0.001090469506	-1.693815697470	0.001551402265	0.002444416073
Regular	18	1.4689...		1.056914514879	-0.133032817370	0.001334274820	0.339208918367	0.001342435753	-2.067337874426	0.001422695250	0.002367801665
Regular	10	1.4700...		1.287627985297	-0.084799322746	0.001180947320	-0.156756531826	0.001040152360	-1.638784021621	0.001468408318	0.002143640734
Regular	11	1.5349...		1.182514794636	-0.193577113404	0.001157093003	-0.065867133523	0.001019173884	-1.710215382642	0.001441885721	0.002111069410
Regular	20	1.9297...		1.525139809381	0.225663249014	0.001126083332	0.211068565073	0.001185742056	-1.972900046509	0.001318102992	0.002100343365
Regular	28	1.9418...		1.549711636092	-0.912403030303	0.001522132399	-0.048863810832	0.001108588035	-1.715386201991	0.001951368196	0.002438425223
Regular	17	2.1144...		1.667338215333	-0.376221086353	0.001571284634	0.361812840423	0.001560092470	-2.073870852236	0.001487995604	0.002667762140
Regular	12	2.2636...		1.753844876754	-0.429046191102	0.001367348097	-0.023003383585	0.001080853555	-1.733174080036	0.001523362788	0.002314847599
Regular	29	6.9312...		4.686966553582	0.152187677960	0.001225806837	0.310313902897	0.001243776456	-2.057192070656	0.001319681923	0.002188667892
Regular	26	8.6860...		4.424621618144	-0.113524292843	0.001406795440	-0.282040071946	0.000979383214	-1.538935799579	0.001526071389	0.002295029277
Regular	25	11.230...		5.983903838129	-0.534467522636	0.001817693686	-0.241270066198	0.000997724652	-1.542363433246	0.001577147839	0.002605160287
Regular	4	22.075...		15.711352052753	-0.441627252471	0.001589944860	-0.200645867018	0.001007833939	-1.574232351483	0.001528094848	0.002421987657

Figure 3.37 First Set of Results

Each column holds the coordinates of the user defined points and with the defined precision by the user. This table can be copied and pasted to an MS-Excel sheet for further data processing.

Step 11:

After obtaining the results by performing the procedure explained Step 1 through Step 11 without displacing the object in analysis load can be applied and Step 1 through Step 11 can be performed to obtain the second set of results. Assuming that this is a deformation analysis under a load the difference between the undisplaced results and the displaced results will give the deflection of the object under loading.

3.4 Data Acquisition

Overall, all data gathered from LVDTs and strain gages through a 32-channel analog data acquisition system. The heart of the system is a control program DAQFI written at University of Maine. It interfaces a DAQ Board 2000 system from IOTECH. This is a 16 bit +/-10V data acquisition card with 16 single ended analog input and 2 analog output channels per card. This system simultaneously sends analog control signal to MTS while recording the data. Figure 3.38 shows a schematic of the Data Aquisition System (DAS) setup used for these tests. Strain gages are conditioned using a Vishay 2100 Amplifier. LVDT's are supplied their required direct current (DC) input voltage through a power supply. The DC output of these units is then read directly by the DAS. Load and displacement output signals from the MTS controller are also sent to the DAS.

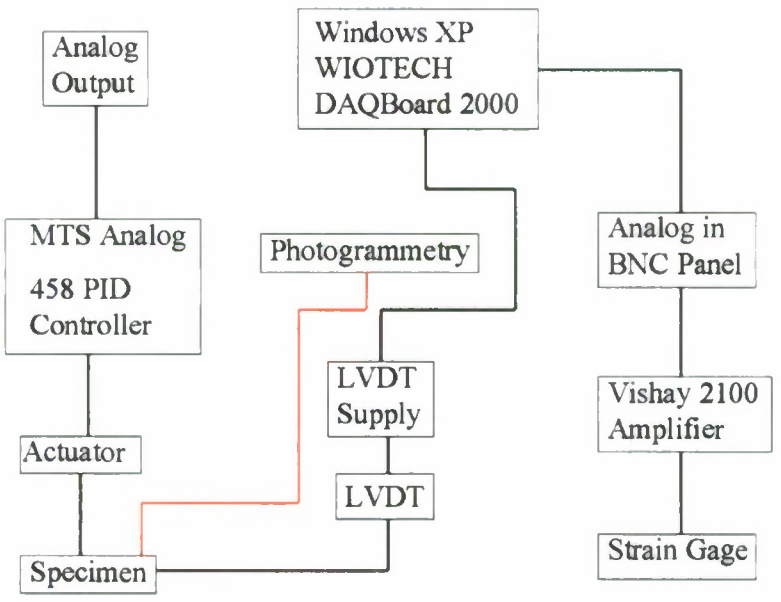

Figure 3.38 Schematic of Data Acquisition System

3.5 Cyclic Loading

Each sandwich panel is loaded cyclically to reach the maximum deflection of approximately 1.5 inches at the center in 10 steps. Load is cycled every 300 seconds and each step has 3 cycles. Figure 3.39 illustrates the cyclic loading pattern.

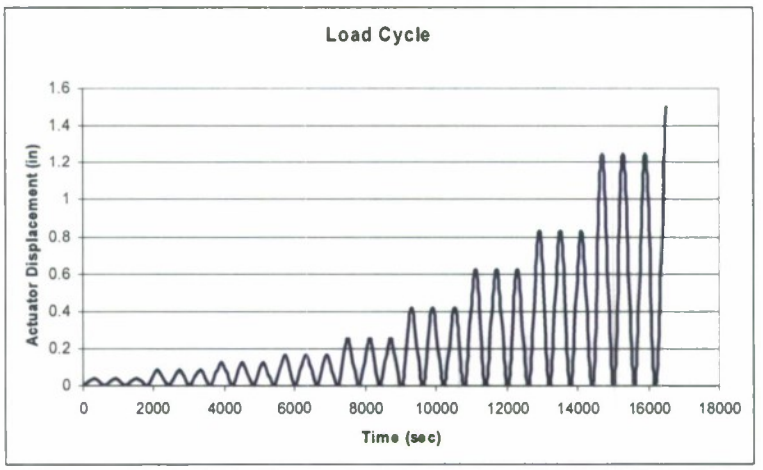

Figure 3.39 Cyclic Displacement History

In the four point bending test the load is applied at the quarter points of the sandwich panel as illustrated in Section 3.1. Using the finite element analysis results the load head displacement is scaled to reach the proposed deflection criteria at the center point and scale factor is found to be 0.833. The deflection at the center point for each step given with the scaled actuator deflection is given in Table 3.1

Table 3.1 Deflection History at Center Line and Load Points

Step	Estimated center line deflection	Actuator
1	0.05	0.042
2	0.1	0.083
3	0.15	0.125
4	0.2	0.167
5	0.3	0.25
6	0.5	0.417
7	0.75	0.625
8	1	0.833
9	1.5	1.25
10	2	1.66

4. TEST RESULTS

The information herein consists of the experimental results from the two tests. The first test consisted of loading of the thick closure panel to failure, and the second test consisted of loading the thin closure panel to failure. In the results, the thick panel is referred to as Panel #1, and the thin panel is referred to as Panel #2. The only difference between the two panels is the closure thickness. The closure thickness for Panel #1 was 0.188 inches whereas the closure thickness for Panel #2 was 0.142 inches. The test procedures, physical and material properties, and post-data analysis for both panels were the same to allow appropriate comparisons between the results of each test. For each test, the experimental data consisted of MTS load, MTS displacement, and measured displacement and strain in the panel. Based on this data, stiffness values were calculated. In terms of the results, the center locations were of interest for both panels. So, for each test, the results consist of an analysis of the relationship between the MTS data and the measured displacements and strains of the panel, the peak displacements and strains at the center, the peak stiffness at the center, and the displaced shape. This profile of results was created to allow appropriate comparisons with the theoretical results obtained from the FEA analyses.

4.1 Displacement Results

A number of hypotheses were established to generate a criterion for determining the validity of the experimental data because Panel #1 had a thicker closure than Panel #2. It was assumed that Panel #1 would have a smaller mid-span deflection, and thus experience smaller strains and possess greater stiffness than Panel #2. Ultimately, these assumptions held true based on the results. However, as shown in Figure 4.1 both panels experienced significant local buckling at the left loading location and minor local bucking at the right loading location.

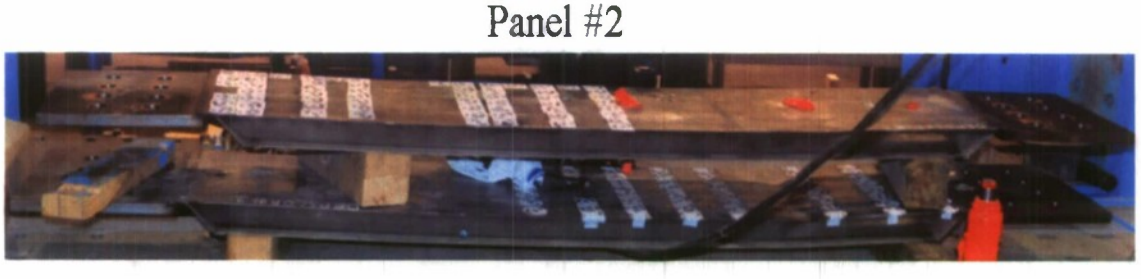

Figure 4.1 Tested Panels

This may have resulted in larger strains being measured near those locations. The centerline deflections experienced by two panels through out the experiments during the cyclic tests are given in the Figure 4.2 and Figure 4.3. For both tests, LVDT C-3 measured the greatest displacement, which is also the maximum center deflection (C-3 is located at the center of the panel). Figure 4.2 shows that for panel #1, the maximum center deflection was 1.842 in. at a load of 48259 lb. For Panel #2, the maximum displacement was 1.407 in at a load of 42773 lb as shown in Figure 4.3. Individual cycles are given in Figure 4.4

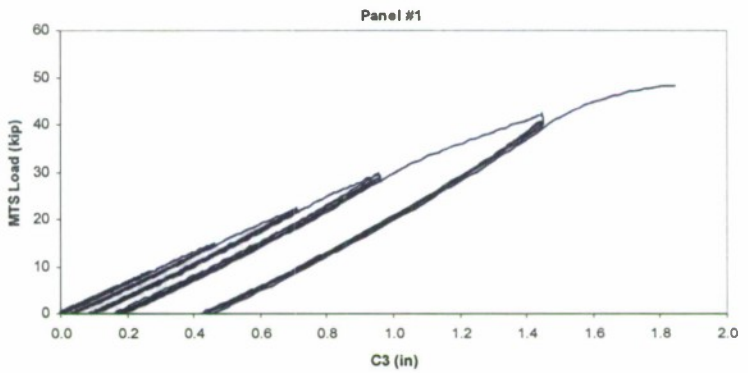

Figure 4.2 Deflection of the Panel #1 at Center Line

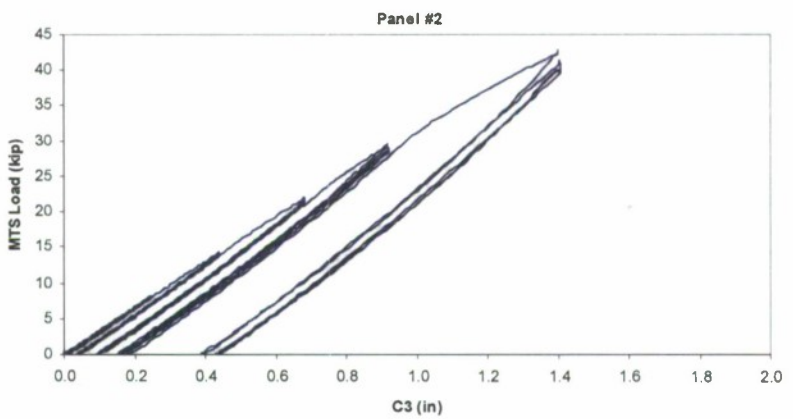

Figure 4.3 Deflection of the Panel #2 at Center Line

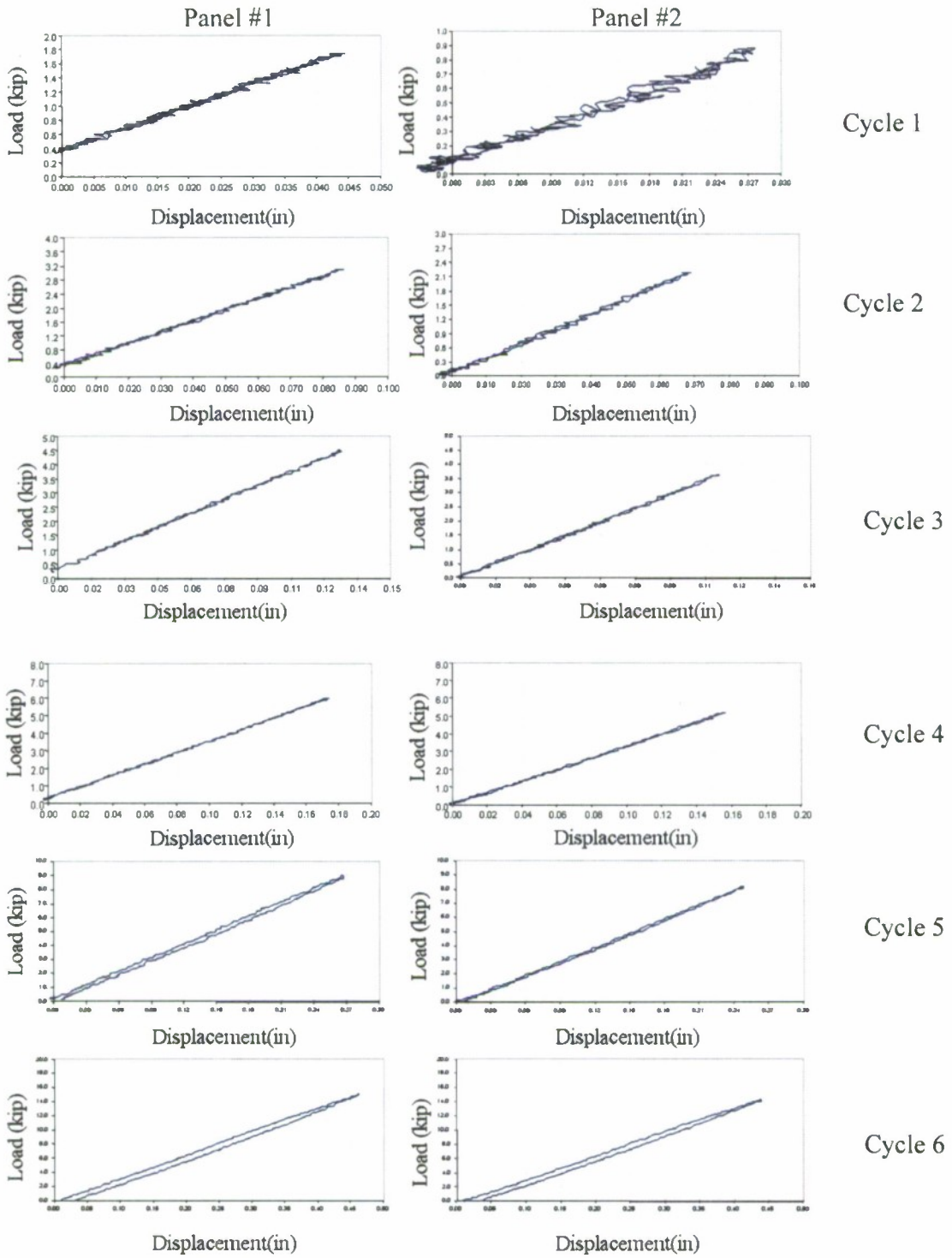

Figure 4.4 LVDT C-3 Outputs at the Center of the Panel

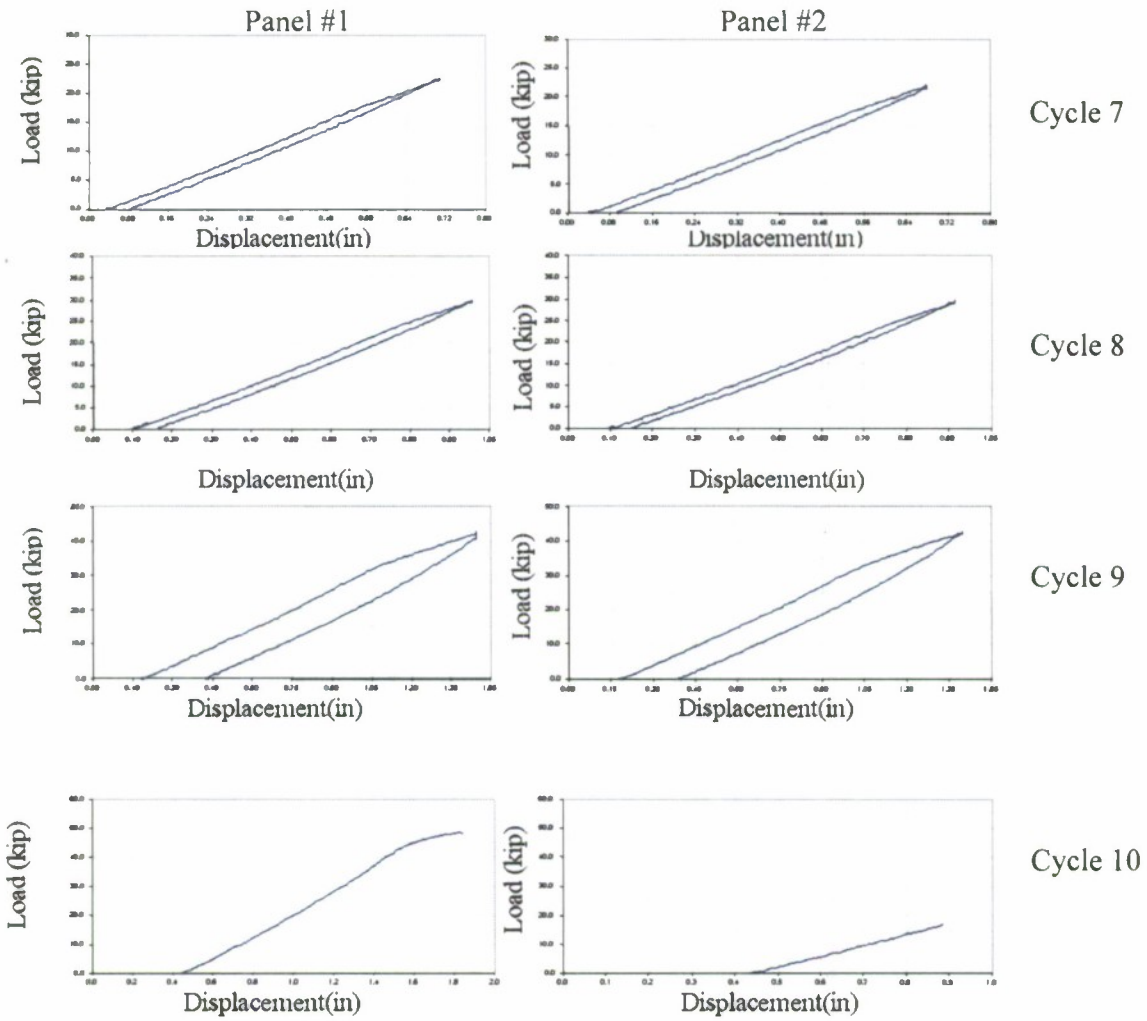

Figure 4.4 Continued LVDT C-3 Outputs at the Center of the Panel

For both tests, the displaced shape is a curve with the maximum displacement at the center and zero displacement at the supports. The progression of peak displacement with cycle number is shown in Figure 4.5 and 4.6. Figure 4.5 shows that Panel #1 failed in the tenth cycle with a maximum center deflection of 1.842 in. Panel #2 as shown in Figure 4.6 failed at the beginning of the tenth cycle but experienced maximum center deflection in the ninth cycle at 1.407 in.

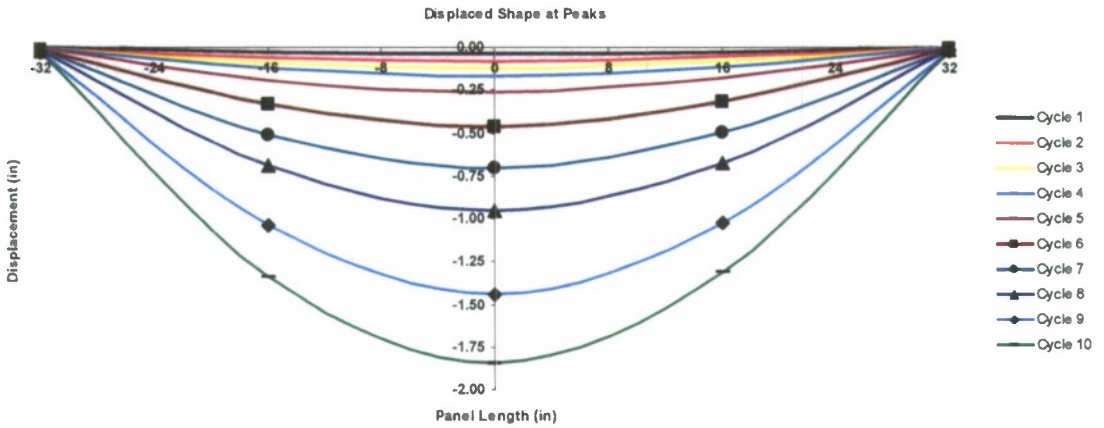

Figure 4.5 Progression of Displacement Shape Over the Test Duration for Panel #1

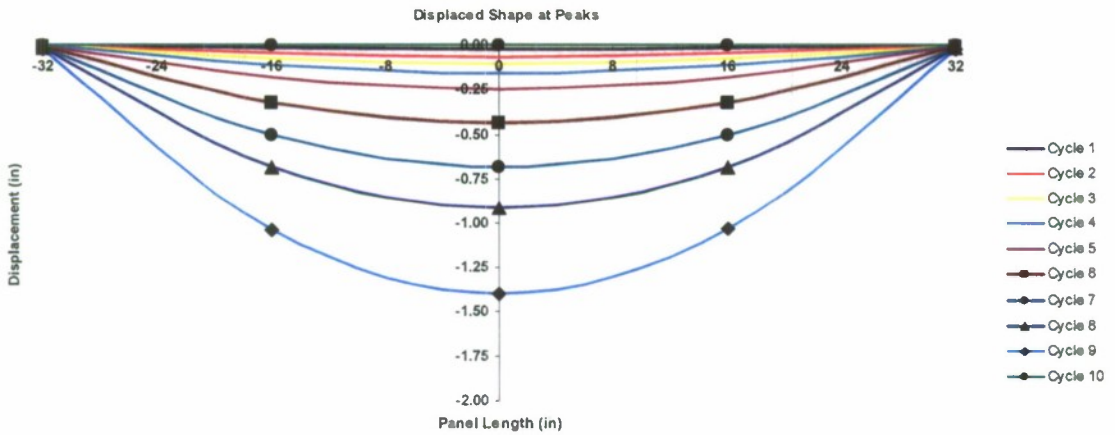

Figure 4.6 Progression of Displacement Shape Over the Test Duration for Panel #2

4.2 Stiffness Results

Based on the experimental data, the peak values of MTS displacements and MTS loads are tabulated in the Table 4.1 for each cycle. Using the peak values for each cycle, secant stiffness of the panel is calculated by dividing the MTS load by MTS displacement. The difference in the first couple cycles as compared to the cycle between 3 and 6 is as expected due to the fact that panel has had to settle down under first couple cycles.

The major difference, which takes place after the 6th cycle, is expected due to the membrane effect since the tapered enclosure is not only bending but also stretching under the plastic deformation of the sandwich panel.

Table 4.1 Peak Stiffness at Each Load Cycle

Cycle	Stiffness (kip/in)	LVDT-C3 Displacement (in)	Load (kip)	Actuator Displacement (in)
1	31.368	0.042022	1.718383	0.040131
2	31.763	0.085098743	3.098711	0.076447
3	32.403	0.1279037	4.447132	0.120697
4	32.677	0.171475232	5.953566	0.161896
5	32.865	0.267482817	8.808421	0.244598
6	33.124	0.462101489	15.032431	0.408783
7	33.941	0.708884627	22.455965	0.617371
8	34.699	0.958143413	29.743519	0.821686
9	34.946	1.446870208	42.331318	1.240082
10	37.542	1.842304587	48.259056	1.589813

The change in the stiffness for each cycle is given in the Figure 4.7 for comparison purposes. For each cycle the peak value of the displacement at the centerline is considered.

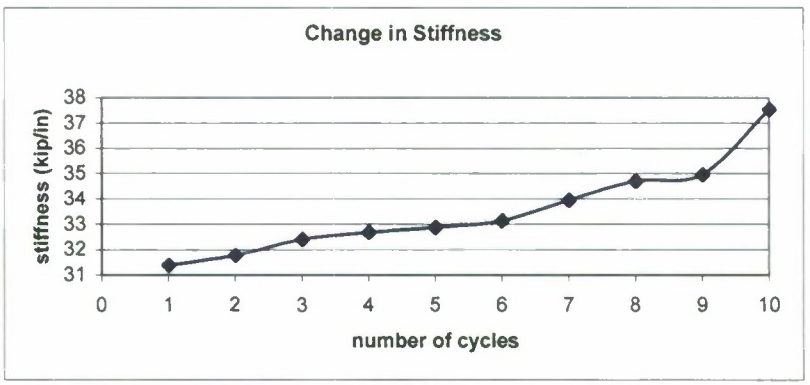

Figure 4.7 Change in the Stiffness for Each Cycle

Similarly, stiffness is given in Table 4.2 for the Panel #2 and change in stiffness through out the testing is given in Figure 4.8

Table 4.2 Peak Stiffness at Each Load Cycle

Cycle	Stiffness (kip/in)	LVDT-C3 Displacement (in)	Load (kip)	Actuator Displacement (in)
1	26.826	0.025986433	0.860711	0.035858154
2	30.433	0.068855226	2.185582	0.077667236
3	32.043	0.110462248	3.639598	0.117645264
4	32.686	0.155311584	5.171861	0.161743164
5	33.021	0.248380363	8.213596	0.247650146
6	33.537	0.437568516	14.350244	0.407104492
7	34.729	0.677978832	22.045742	0.617523193
8	35.907	0.91476351	29.443447	0.819549561
9	36.807	1.397692442	42.772690	1.240844727

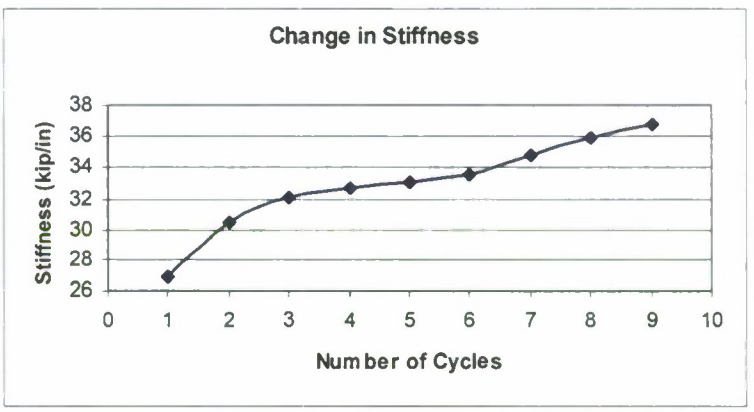

Figure 4.8 Change in the Stiffness for Each Cycle

4.3 Strain Results

Table 4.3 and Table 4.4 show that the strain in Panel #1 is greater than Panel #2 along the x-axis at the center-top location, center-bottom location, and the 45°-axis at the center-bottom location. The strain in Panel #2 is greater than Panel #1 along the 45°-axis at the center-top location and along the y-axis at the center-bottom location. Strain was not measured along the y-axis at the center-top location for either panel due to inoperative instrumentation. Theoretically, Panel #2 should experience higher strains than Panel #1 due to its smaller thickness and thus greater deflections; however, this was only the case along certain axis at certain locations.

Table 4.3 Peak Center Strains for Panel #1

	Center Top			Center Bottom		
Cycle	**S3-1(x)**	**S3-2(45)**	**S3-3(y)**	**S4-1(x)**	**S4-2(45)**	**S4-3(y)**
1	-139.1	-91.52	N/A	143.38	64.01	12.57
2	-221.47	-112.01	N/A	257.96	96.06	27.81
3	-314.99	-124.72	N/A	367.69	133.51	41.2
4	-431.4	-185.39	N/A	493.59	183.28	40.69
5	-647.45	-252.41	N/A	757.92	276.69	59.43
6	-1089.8	-418.33	N/A	1269.1	464.24	105.07
7	-1729.9	-691.28	N/A	1915.47	713.16	148.79
8	-2489.3	-1101.9	N/A	2610.64	996.67	165.74
9	-4840.3	-2816.8	N/A	4280.57	1724.79	218.78
10	-5420.3	-3503.6	N/A	4862.78	1955.99	264.83

Table 4.4 Peak Center Strains for Panel #2

	Panel #2: Peak Strains at Center					
	Center Top			Center Bottom		
Cycle	**S3-1(x)**	**S3-2(45)**	**S3-3(y)**	**S4-1(x)**	**S4-2(45)**	**S4-3(y)**
1	-71.23	-60.99	N/A	55.78	32.48	13.38
2	-215.32	-173.8	N/A	168.88	60.48	51.46
3	-336.78	-268.66	N/A	282.07	94.79	84.34
4	-461.59	-362.6	N/A	405.75	141.53	119.26
5	-697.31	-538.34	N/A	657.39	238.97	160.2
6	-1202.2	-918.58	N/A	1174.7	440.68	256.69
7	-1988.6	-1481.1	N/A	1832.6	706.99	385.8
8	-2789.5	-2152.3	N/A	2488.76	977.68	508.38
9	-4663.8	-4161	N/A	4087.33	1667.72	762.41

The Figure 4.9 through Figure 4.16 illustrate the peak strains at the center top and bottom locations of the Panel #1 and for Panel #2 for the over their test duration respectively.

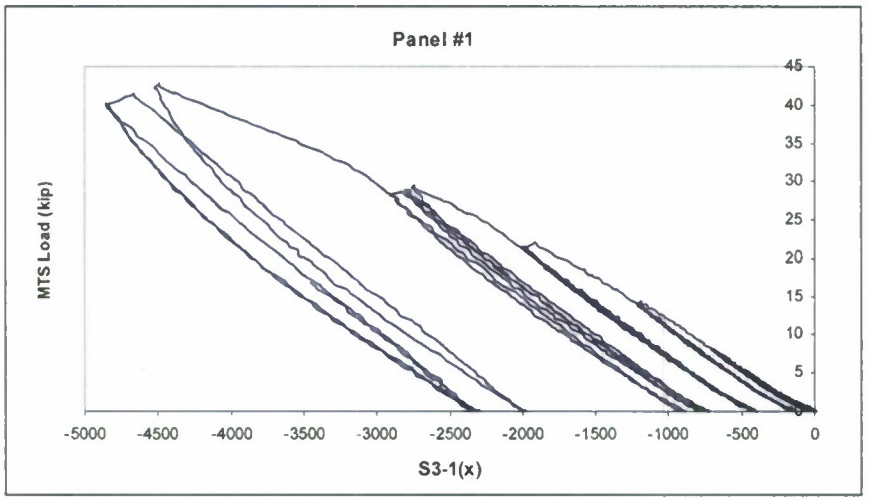

Figure 4.9 Measured Strain Along the x-Axis at the Center Top Location of Panel #1 for Every Cycle

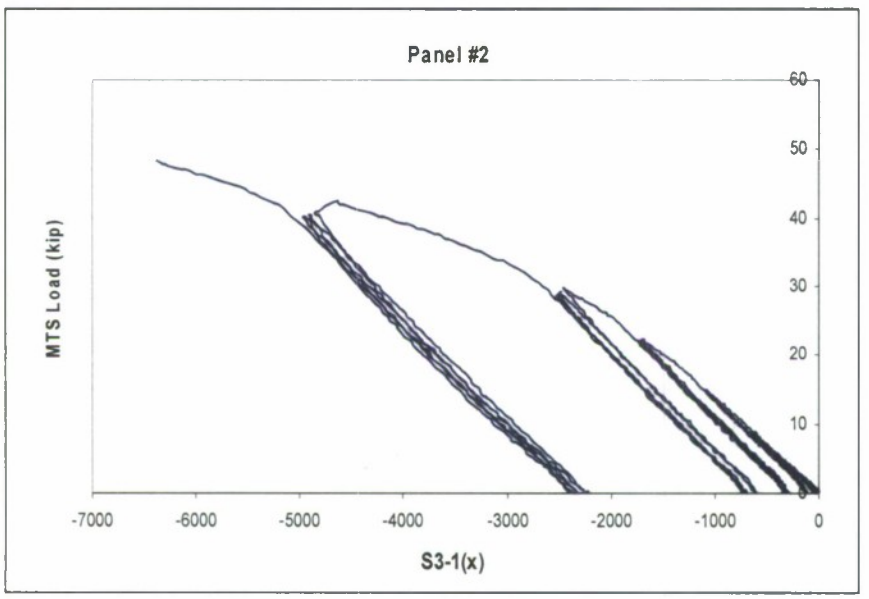

Figure 4.10 Measured Strain Along the x-Axis at the Center Top Location of Panel #2 for Every Cycle

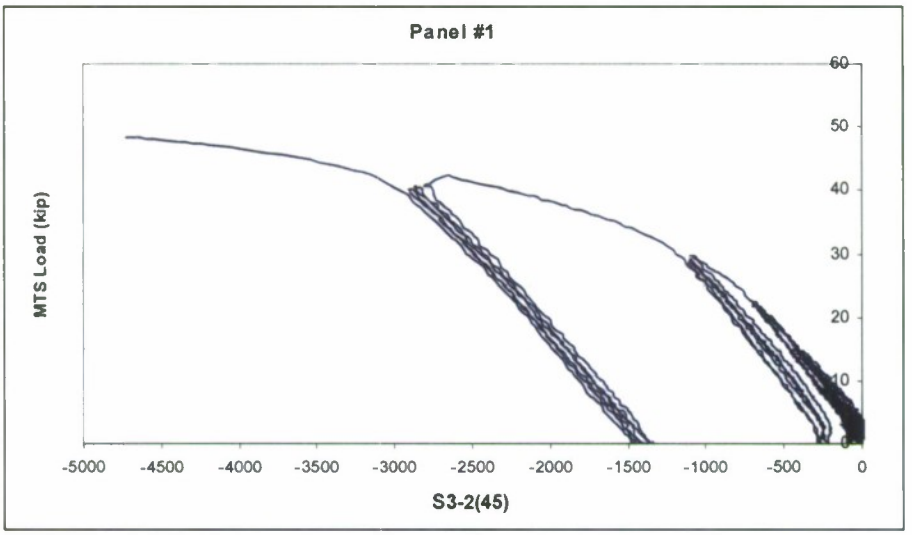

Figure 4.11 Measured Strain Along the 45°-Axis at the Center Top Location of Panel #1 for Every Cycle

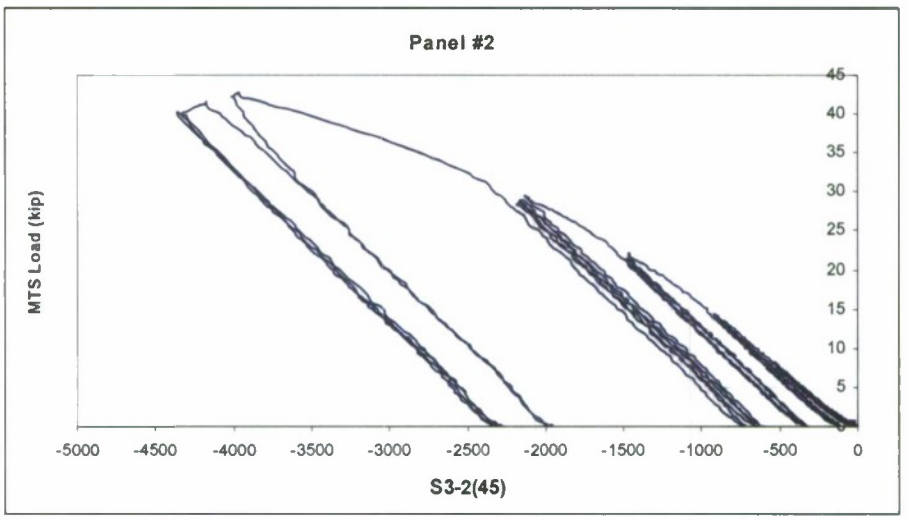

Figure 4.12 Measured Strain Along the 45°-Axis at the Center Top Location of Panel #2 for Every Cycle

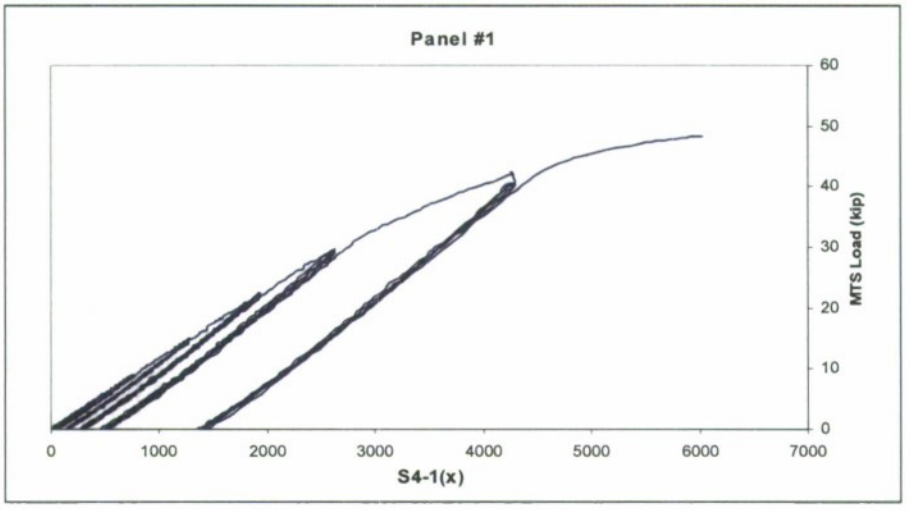

Figure 4.13 Measured Strain Along the x-Axis at the Center Bottom Location of Panel #1 for Every Cycle

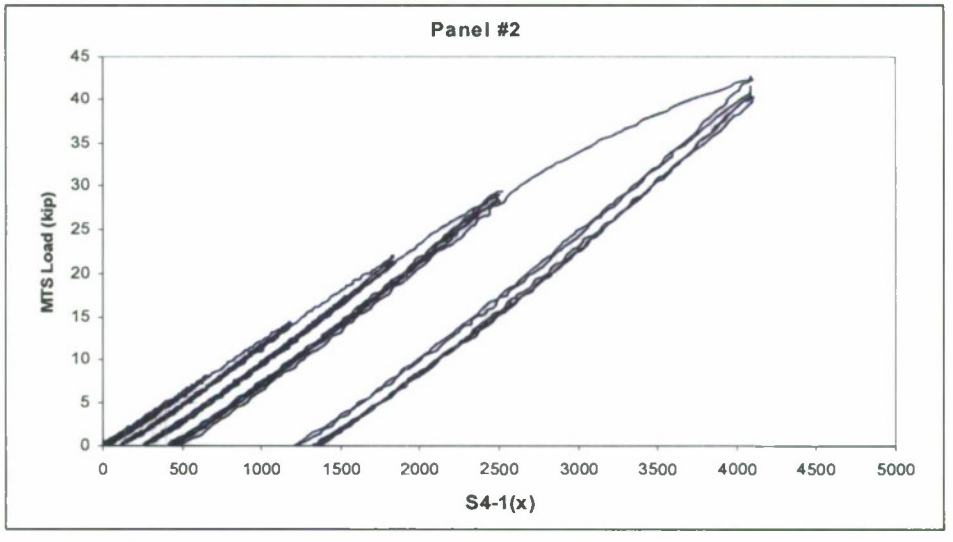

Figure 4.14 Measured Strain Along the x-Axis at the Center Bottom Location of Panel #2 for Every Cycle

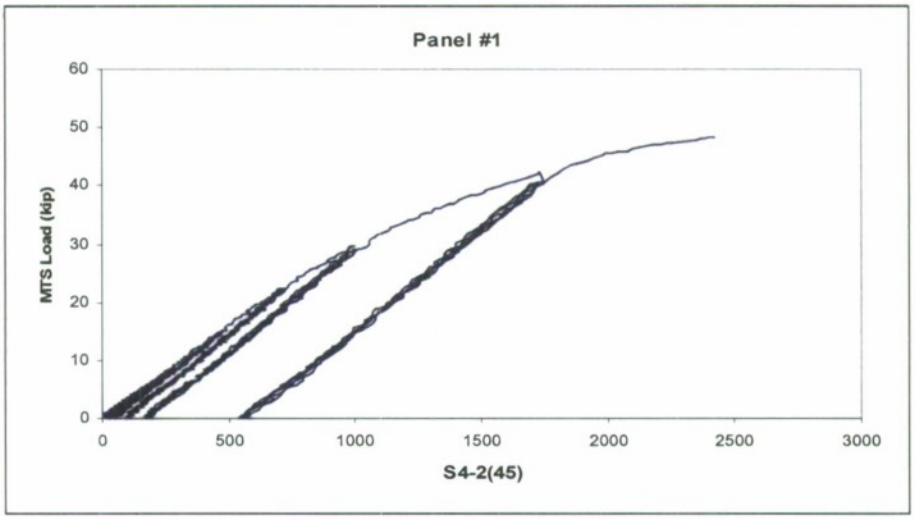

Figure 4.15 Measured Strain along the 45°-Axis at the Center Bottom Location of Panel #1 for Every Cycle

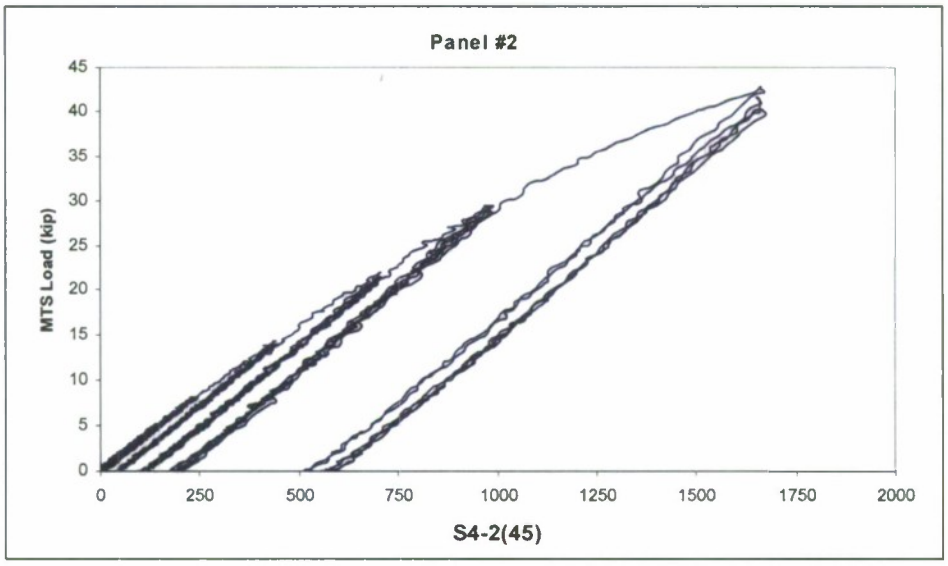

Figure 4.16 Measured Strain Along the 45°-Axis at the Center Bottom Location of Panel #2 for Every Cycle

4.4 Photogrammetry Results

All photogrammetric data collected based on the directions explained in Section 3.3. In order to obtain accurate results, six photographs were taken: three from the front of the panel and three from the back of the panel and the data collected from at least four best photographs for each set. The collected data processed based on the automated-target module procedures. Automated target module is only available if program generated reflective target points are used. The only difference between the automated target module process and user defined target point process is Photomodeler is able to recognize and locate the reflective targets automatically instead of user defines them on the object individually.

For the Panel #1 only the permanent deformation shape are given for 1.5 inches of center deflection and the results are compared to those obtained by LVDTs as shown in Figure 4.17.

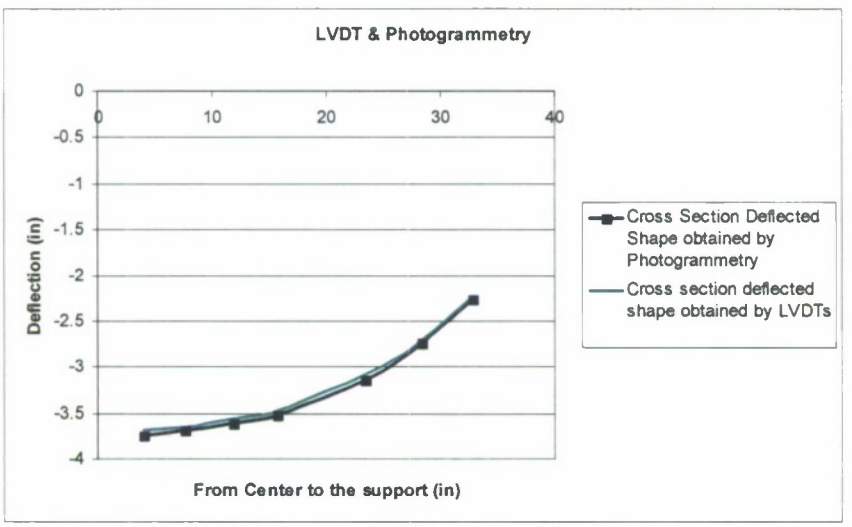

Figure 4.17 Deflection Comparison LVDTs vs Photogrammetry

As clearly seen on the graph Photogrammetry results compares to LVDT results. The discrepancy between the two is 2.6%. However, with the current test set up LVDTs measured the deflection only at the bottom plate whereas the photogrammetry targets were located on the top plate.

The permanent deformation along the length of the Panel #1 is given in the Figure 4.18. The Figure 4.18 illustrates the deflection of the top sheet at the points where the target points are located. The data is collected and each section deflection value averaged individually and one single deflection value assigned to each location. This way, the deformation of the cross section of the top plate was approximately visualized conveniently.

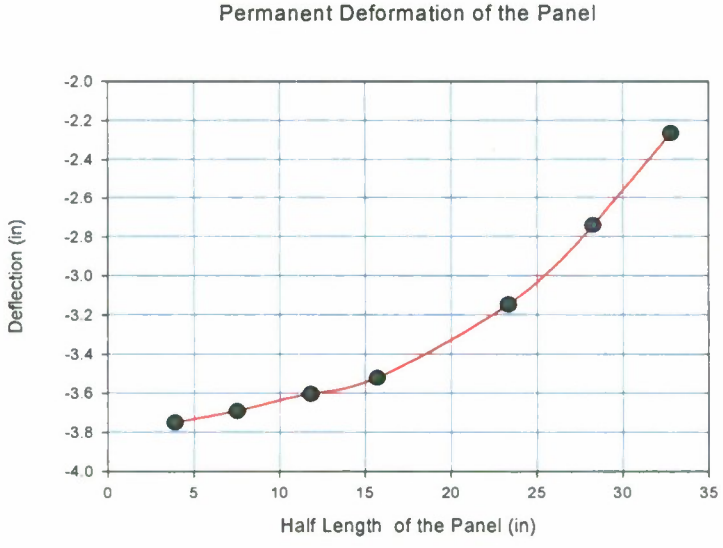

Figure 4.18 The Deformation Along the Length of the Panel #1

In the Figure 4.19 the surface plot is given based on the data collected from the ptogrammetry study. Each location has 6 to 8 target points and the values of these target points are gathered from Photomodeler.

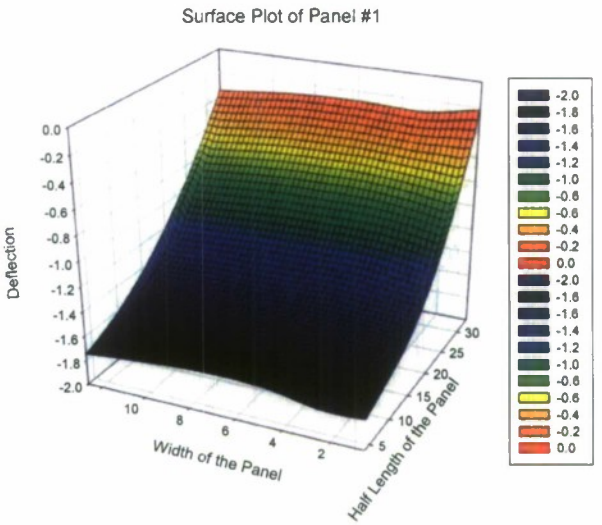

Figure 4.19 Surface Plot of Top Plate on Panel #1

Photogrammetry results are given in the Figure 4.20 for the 1.5" predicted centerline deflection, which corresponds to 1.24" actuator displacement. 1.24" of actuator displacement buckled the sandwich panel's corrugation under the left load head, which set a permanent deformation.

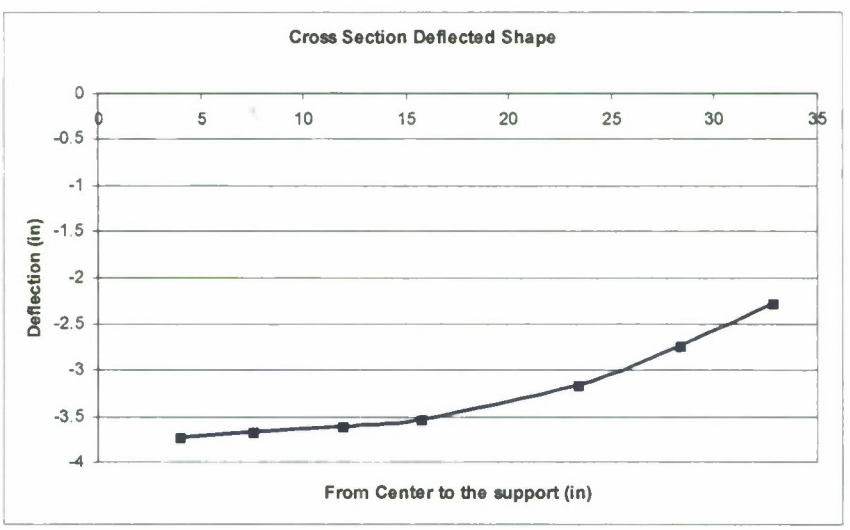

Figure 4.20 The Deformation Along the Length of the Panel #2

It is found out that the discrepancy between the photogrammetry result and the LVDT output is 3%. Using photogrammetry results deflected surface shape of the top plate is obtained as shown in Figure 4.21 for Panel #2.

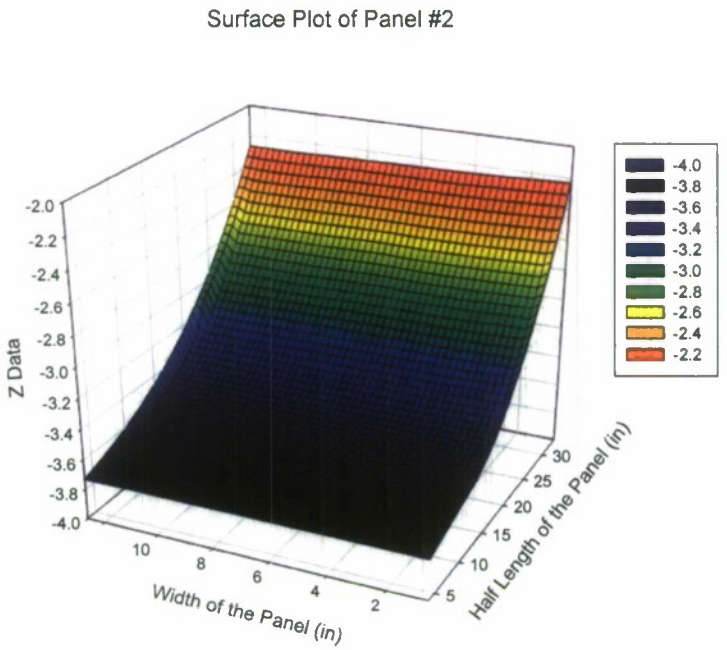

Figure 4.21 Surface Plot of Top Plate on Panel #2

4.5 Experimental and Finite Element Analysis Stress Results Compared

The peak strains along the x-axis, y-axis and 45-degree axis at the center-bottom location were calculated for the Panel #1 using the data collected from strain gages.

$$\varepsilon_{xx} := \begin{pmatrix} 143.38 \\ 257.96 \\ 367.69 \\ 493.59 \\ 757.92 \\ 1296.1 \\ 1915.47 \\ 2610.64 \\ 4280.57 \\ 4862.78 \end{pmatrix} \cdot 10^{-6} \qquad \varepsilon_{45} := \begin{pmatrix} 64.01 \\ 96.06 \\ 133.51 \\ 183.28 \\ 276.69 \\ 464.24 \\ 713.16 \\ 996.67 \\ 1724.79 \\ 1955.99 \end{pmatrix} \cdot 10^{-6} \qquad \varepsilon_{yy} := \begin{pmatrix} 12.57 \\ 27.81 \\ 41.2 \\ 40.69 \\ 59.43 \\ 105.07 \\ 148.79 \\ 165.74 \\ 218.78 \\ 264.83 \end{pmatrix} \cdot 10^{-6}$$

The peak strains were used to calculate the stresses using a plane stress assumption at the center-bottom location for each cycle for Panel #1. Notice that in the sandwich panel the transverse stress, σ_{yy} is significant.

$$\sigma_{xx} = \begin{pmatrix} 4.689\times 10^{3} \\ 8.487\times 10^{3} \\ 1.211\times 10^{4} \\ 1.612\times 10^{4} \\ 2.472\times 10^{4} \\ 4.231\times 10^{4} \\ 6.246\times 10^{4} \\ 8.478\times 10^{4} \\ 1.385\times 10^{5} \\ 1.575\times 10^{5} \end{pmatrix} \text{psi} \qquad \sigma_{yy} = \begin{pmatrix} 1.771\times 10^{3} \\ 3.352\times 10^{3} \\ 4.828\times 10^{3} \\ 6.016\times 10^{3} \\ 9.14\times 10^{3} \\ 1.574\times 10^{4} \\ 2.305\times 10^{4} \\ 3.024\times 10^{4} \\ 4.79\times 10^{4} \\ 5.493\times 10^{4} \end{pmatrix} \text{psi} \qquad \sigma_{xy} = \begin{pmatrix} 1.428\times 10^{3} \\ 2.143\times 10^{3} \\ 2.978\times 10^{3} \\ 4.089\times 10^{3} \\ 6.172\times 10^{3} \\ 1.036\times 10^{4} \\ 1.591\times 10^{4} \\ 2.223\times 10^{4} \\ 3.848\times 10^{4} \\ 4.363\times 10^{4} \end{pmatrix} \text{psi}$$

The plane stresses and shear stress were used to calculate the principle stresses for each cycle for Panel #1

$$\sigma_1 = \begin{pmatrix} 5.272\times 10^3 \\ 9.263\times 10^3 \\ 1.317\times 10^4 \\ 1.757\times 10^4 \\ 2.687\times 10^4 \\ 4.587\times 10^4 \\ 6.809\times 10^4 \\ 9.27\times 10^4 \\ 1.526\times 10^5 \\ 1.735\times 10^5 \end{pmatrix} \text{psi} \qquad \sigma_2 = \begin{pmatrix} 3.501\times 10^3 \\ 5.911\times 10^3 \\ 8.346\times 10^3 \\ 1.155\times 10^4 \\ 1.773\times 10^4 \\ 3.013\times 10^4 \\ 4.503\times 10^4 \\ 6.245\times 10^4 \\ 1.047\times 10^5 \\ 1.186\times 10^5 \end{pmatrix} \text{psi}$$

This procedure was repeated for the Panel #2.

$$\varepsilon_{xx} := \begin{pmatrix} 55.78 \\ 168.88 \\ 282.07 \\ 405.75 \\ 657.39 \\ 1174.7 \\ 1832.6 \\ 2488.76 \\ 4087.33 \end{pmatrix} \cdot 10^{-6} \qquad \varepsilon_{45} := \begin{pmatrix} 32.48 \\ 60.48 \\ 94.79 \\ 141.53 \\ 238.97 \\ 440.68 \\ 706.99 \\ 977.68 \\ 1667.72 \end{pmatrix} \cdot 10^{-6} \qquad \varepsilon_{yy} := \begin{pmatrix} 13.38 \\ 51.46 \\ 84.34 \\ 119.26 \\ 160.2 \\ 256.69 \\ 385.8 \\ 508.38 \\ 762.41 \end{pmatrix} \cdot 10^{-6}$$

$$\sigma_{xx} = \begin{pmatrix} 1.906\times 10^{3} \\ 5.874\times 10^{3} \\ 9.795\times 10^{3} \\ 1.407\times 10^{4} \\ 2.248\times 10^{4} \\ 3.989\times 10^{4} \\ 6.209\times 10^{4} \\ 8.417\times 10^{4} \\ 1.375\times 10^{5} \end{pmatrix} \text{psi} \qquad \sigma_{yy} = \begin{pmatrix} 959.677 \\ 3.255\times 10^{3} \\ 5.384\times 10^{3} \\ 7.68\times 10^{3} \\ 1.139\times 10^{4} \\ 1.941\times 10^{4} \\ 2.982\times 10^{4} \\ 3.999\times 10^{4} \\ 6.337\times 10^{4} \end{pmatrix} \text{psi} \qquad \sigma_{xy} = \begin{pmatrix} 724.554 \\ 1.349\times 10^{3} \\ 2.115\times 10^{3} \\ 3.157\times 10^{3} \\ 5.331\times 10^{3} \\ 9.831\times 10^{3} \\ 1.577\times 10^{4} \\ 2.181\times 10^{4} \\ 3.72\times 10^{4} \end{pmatrix} \text{psi}$$

The plane stresses and shear stress were used to calculate the principle stresses for each cycle for Panel #2.

$$\sigma_{1} = \begin{pmatrix} 2.298\times 10^{3} \\ 6.444\times 10^{3} \\ 1.065\times 10^{4} \\ 1.537\times 10^{4} \\ 2.463\times 10^{4} \\ 4.384\times 10^{4} \\ 6.852\times 10^{4} \\ 9.313\times 10^{4} \\ 1.53\times 10^{5} \end{pmatrix} \text{psi} \qquad \sigma_{2} = \begin{pmatrix} 1.338\times 10^{3} \\ 3.19\times 10^{3} \\ 5.261\times 10^{3} \\ 7.688\times 10^{3} \\ 1.324\times 10^{4} \\ 2.443\times 10^{4} \\ 3.87\times 10^{4} \\ 5.313\times 10^{4} \\ 8.962\times 10^{4} \end{pmatrix} \text{psi}$$

The change in the plane stress in x, y and xy direction are given in the Figure 4.22 through Figure 4.24 for Panel #1 and in the Figure 4.25 through Figure 4.27.

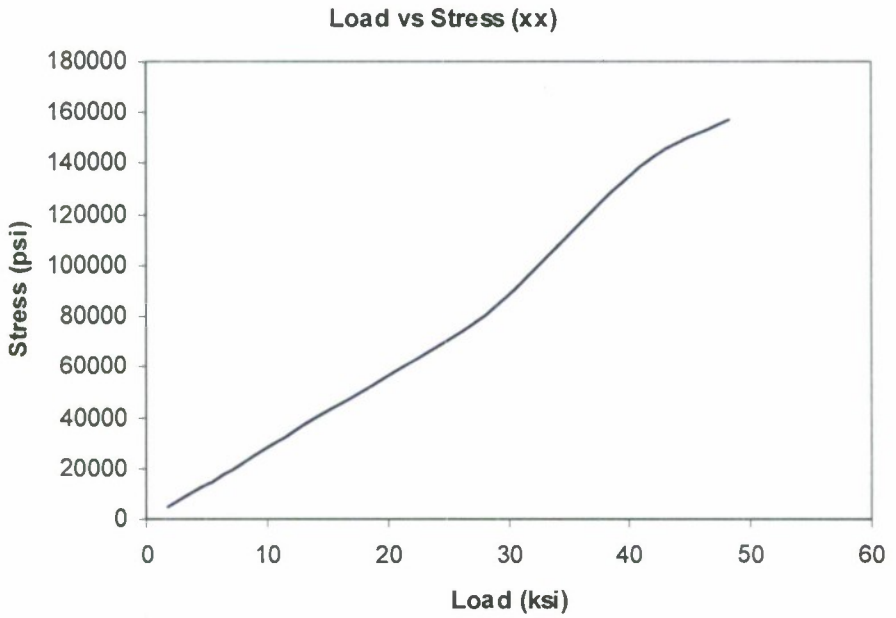

Figure 4.22 Plane Stress in x-Direction for Panel #1

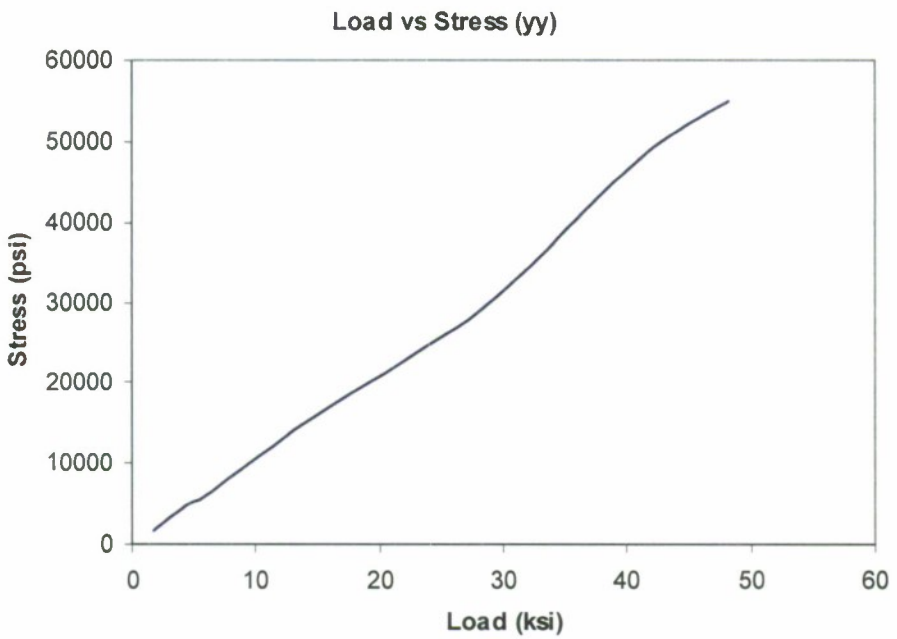

Figure 4.23 Plane Stress in y-Direction for Panel #1

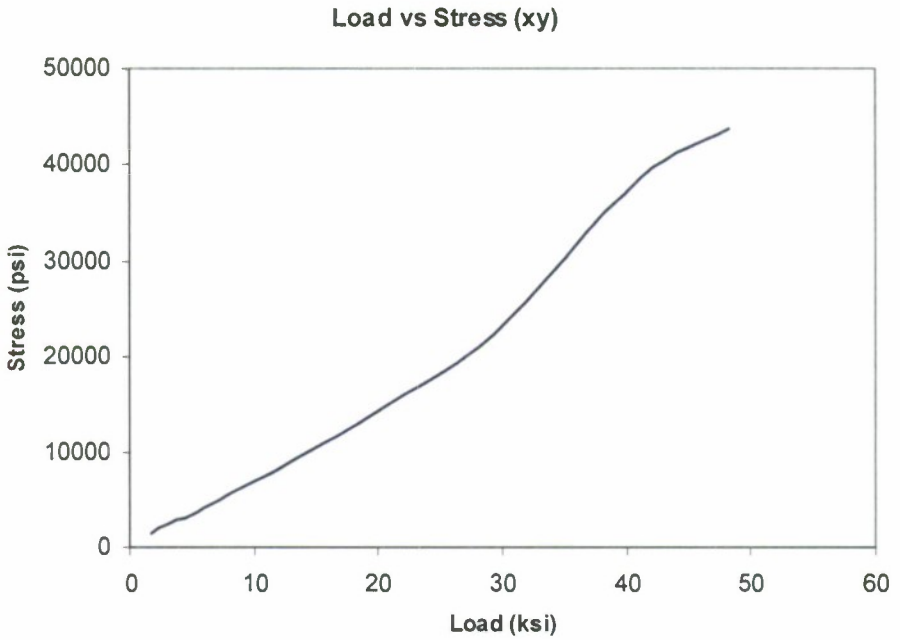

Figure 4.24 Plane Stress in xy-Direction for Panel #1

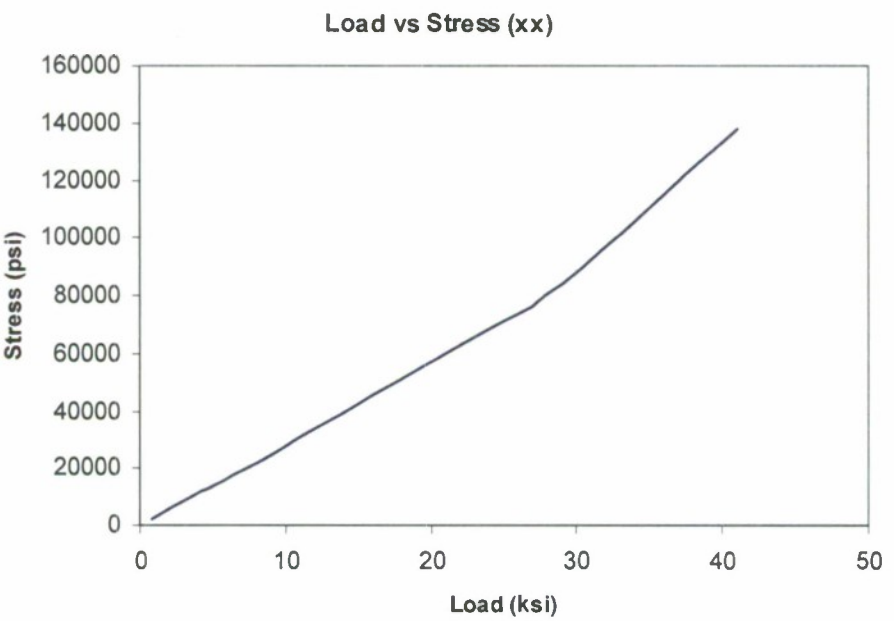

Figure 4.25 Plane Stress in x-Direction for Panel #2

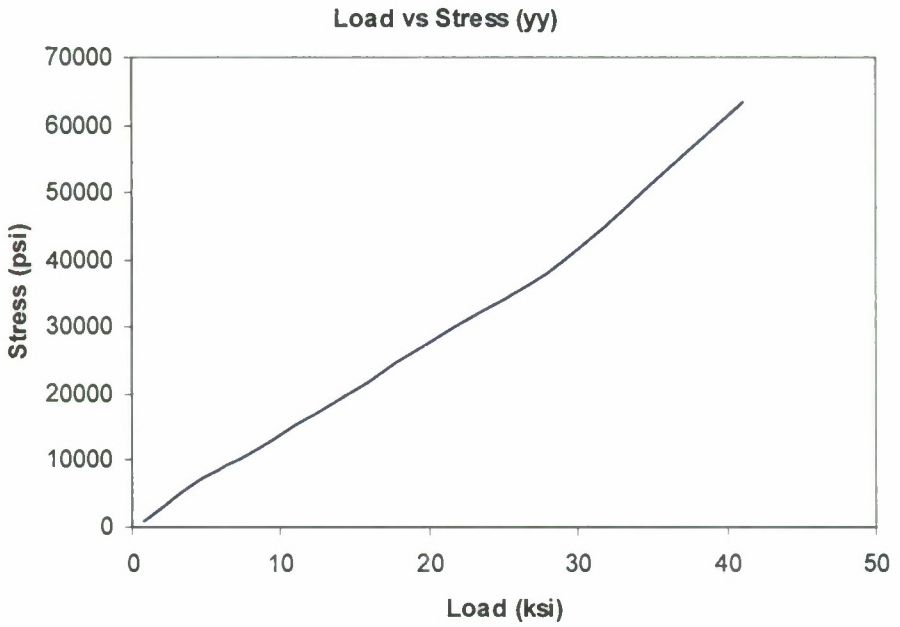

Figure 4.26 Plane Stress in y-Direction for Panel #2

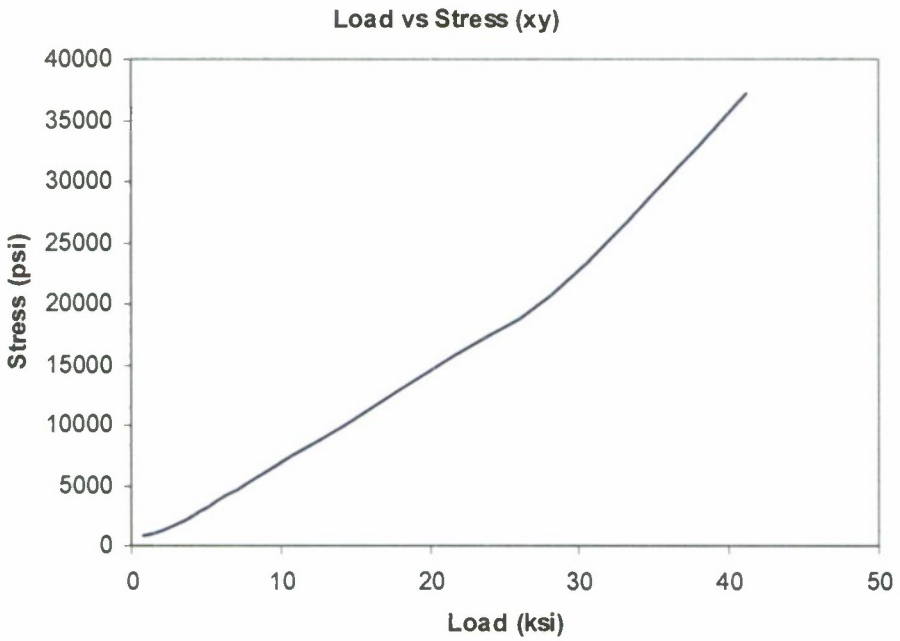

Figure 4.27 Plane Stress in xy-Direction for Panel #2

Finite element analysis was conducted and results are read from where the strain gage is located on the bottom sheet over a 0.25" x0.25" patch and averaged. Plane stress and principle stress

graphs show that the linear assumption is valid for the first 4 cycles. Plane stress and principle stress results are given in Table 4.5 for the first 4 cycles for Panel #1.

Table 4.5 Finite Element Analysis Stress Results

Cycle	Plane Stress (psi)			Principle Stress (psi)	
	σ_x	σ_y	σ_{xy}	σ_1	σ_2
1	5556	1907	1754	6159	4478
2	7380	2976	2325	8426	5456
3	11843	4436	2746	12985	8446
4	16659	6250	4128	18256	12023

The discrepancy between the theoretical and finite element analysis results is given in Table 4.6 for the first 4 cycles for panel #1

Table 4.6 Discrepancies Between FEA and Experimental Stress Results for Panel #1

Cycle	Plane Stress (psi)			Principle Stress (psi)	
	σ_x	σ_y	σ_{xy}	σ_1	σ_2
1	15%	7%	18%	14%	21%
2	15%	12%	7%	9%	8%
3	2%	8%	8%	1%	1%
4	3%	3%	9%	3%	3%

Similarly plane stress and principle stress results for the first 4 cycles are given in Table 4.7 for the Panel #2.

Table 4.7 Finite Element Analysis Stress Results for Panel #2

Cycle	Plane Stress (psi)			Principle Stress (psi)	
	σ_x	σ_y	σ_{xy}	σ_1	σ_2
1	2787	1393	742	3108	1715
2	7405	3702	1412	7882	4180
3	11883	5941	2324	12680	6743
4	16716	8358	3448	17950	9547

The discrepancy between the finite element analysis and theoretical results are given in Table 4.8

Table 4.8 Discrepancy Between FEA and Experimental Stress Results for Panel #2

Cycle	Plane Stress (psi)			Principle Stress (psi)	
	σ_x	σ_y	σ_{xy}	σ_1	σ_2
1	46%	32%	2%	26%	21%
2	20%	12%	4%	18%	23%
3	17%	9%	8%	16%	21%
4	17%	8%	8%	14%	19%

4.6 Static Strength of Laser Stake Welds in Single Lap-Shear

In addition to the cyclic panel testing, static tests were performed on laser stake welded subcomponents. These tests were conducted monotonically to failure. Fatigue tests are planned for the future. Test specimens were made using two plates stake welded together with either longitudinal or transverse welds. Figure 4.28 shows the test coupon layout. Figure 4.29 shows photographs of each specimen type. Specimens were fabricated from 0.118 in thick and 0.060 in thick AL2003 stainless steel. The 0.118 inch thick material has a yield strength of 87 ksi, ultimate tensile strength of 117 ksi and elongation at failure of 29%, whereas the 0.060 inch thick material has a yield strength of 88.5 ksi, ultimate tensile strength of 118 ksi and elongation at failure of 27%.

4.6.1 Specimen Geometry and Test Setup

Lap shear specimens were cut from the plates and a slot of nominally ¼" was machined through the plates as shown in Figure 4.28 to isolate the weld in the test section. Two plate thicknesses were studied, nominally 0.06 in and 0.118 inch. Laser weld power, LP, was also varied to assess its influence on strength and weld width and range from 4kW to 6.5kW. Welds were performed at a speed of 100 in/min. The hybrid process was used with GMAW voltage set at 24.5 VDC and current varying from 81-126 A. The GMAW wire was fed at 375 in/min. Heat input, HI, can be approximated as HI(kJ/in)=(LP(watts)+V*A)*60(s/min)/Weld speed(ipm).

Dimensions of the test specimens are summarized in Table 4.9 including the test section width B, the specimen width, W, and the plate thicknesses, t_1 and t_2. The weld width W_w was estimated post test by measuring the width across the weld root after the two plates were separated. The weld area, Aw, is then estimated as the product of the weld length and the weld width. Accordingly, the weld area is $B*W_w$ and $W*W_w$ for the longitudinal and transverse specimens, respectively.

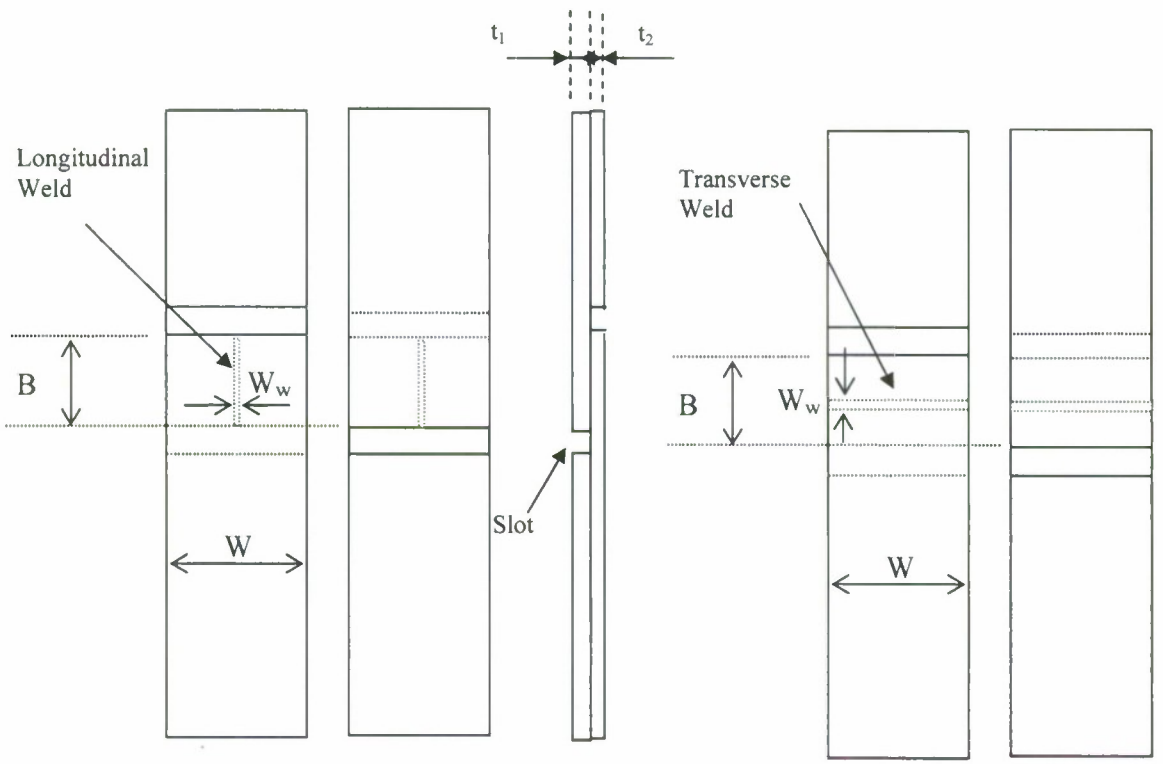

Figure 4.28 – Lap Shear Test Coupon Layout

Table 4.9 – Stake Weld Lap Shear Test Specimen Dimensions

	Mat. Ref #	B in.	W in.	W_w in.	A_w in.	t_1 in.	t_2 in.	LP kW
Logitudinal								
LS-060x060-1								
1	3303	0.997	2.368	0.0855	0.0852	0.0648	0.0638	4
2	3303	1.019	2.158	0.0775	0.0790	0.0643	0.0645	4
3	3303	1.007	2.201	0.0930	0.0937	0.0638	0.0640	4
LS-118x060-1								
6	3305	1.022	0.273	0.0735	0.0751	0.1210	0.0638	4
7	3305	0.999	2.611	0.0965	0.0964	0.1205	0.0635	4
8	3311	1.002	2.041	0.0903	0.0905	0.1208	0.0635	4
LS-118x060-2								
11	3314	1.028	2.307	0.0703	0.0722	0.1205	0.0638	6.5
12	3314	1.069	2.041	0.0730	0.0780	0.1205	0.0638	6.5
13	3314	1.025	1.895	0.0765	0.0784	0.1203	0.0635	6.5
Transverse								
TS-060x060-1								
9	3322A		2.185	0.0755	0.1650	0.0635	0.0640	4
14	3321A		2.181	0.0655	0.1429	0.0640	0.0638	4
15	3321A		2.172	0.0633	0.1374	0.0638	0.0640	4
TS-118x060-1								
42	3319A		2.096	0.1030	0.2159	0.1203	0.0648	4
43	3319A		1.834	0.0753	0.1380	0.1210	0.0638	4
44	3319A		2.143	0.1045	0.2239	0.1200	0.0633	4
TS-118x060-2								
26	3316A		2.097	0.0760	0.1593	0.1200	0.0640	6.5
27	3316A		2.187	0.0700	0.1531	0.1200	0.0643	6.5
28	3316A		2.175	0.0623	0.1354	0.1200	0.0640	6.5

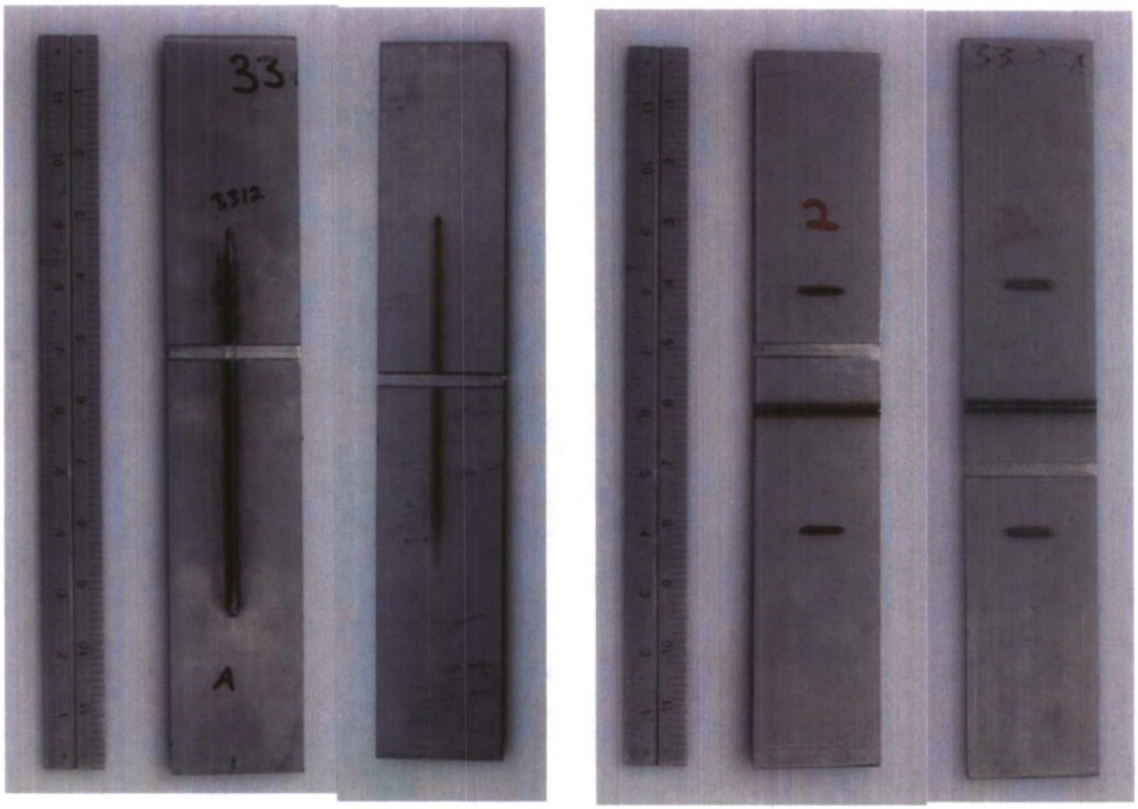

a) Longitudinal b) Transverse

Figure 4.29 – Photographs of Sample Specimens

Tests were conducted using an MTS 810 test machine equipped with a 22-kip load cell. The test setup is shown in Figure 4.30. Tests were performed in displacement control at a rate of 0.005 in/min. Load and displacement data were supplemented with two specially designed gap measurement instruments consisting of an ETI – LCP8P-10 linear motion potentiometer with a peak travel of 0.5 inches.

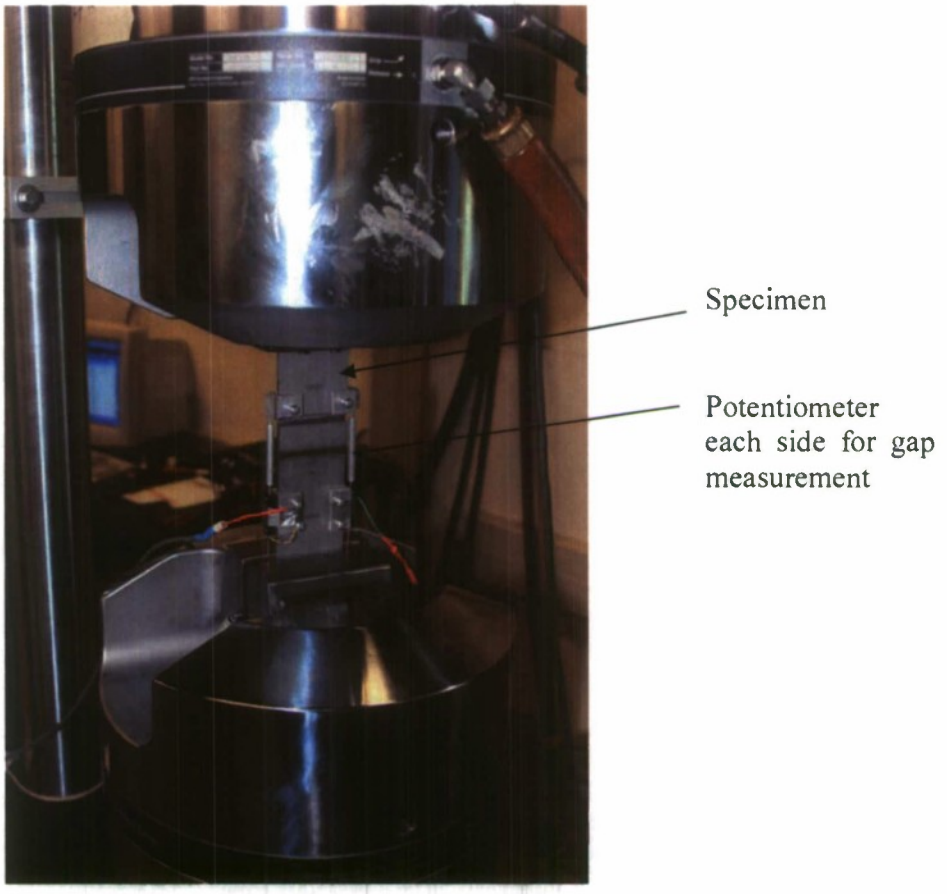

Figure 4.30 – Lap Shear Test Setup in MTS 810

4.6.2 Lap-Shear Test Results

Table 4.9 presents a results summary of the longitudinal and transverse lap-shear stake weld tests. A typical load versus displacement plot for the longitudinal and vertical cases are shown in Figure 4.31. Displacement is the average of the position recorded from the 2 gap measurement instruments. The average weld resistance per unit length of the transverse welds is 4.63 kip/in with a standard deviation of 0.30 kip/in and the longitudinal weld resistance is 4.56 kip/in with a standard deviation of 0.39 kip/in. Little difference is observed in the resistance between a weld made with 4kW or 6.5kW laser power. Typical failures are shown in Figure 4.32 with a closeup photograph of the failure in Figure 4.33. Figure 4.44 shows the permanent set photographed after the test was completed. This is due to bending inherent in a single lap shear test. A larger amount of bending is observed in the thicker plate.

Table 4.6 – Lap Shear Test Results Summary

	Peak Load kip	Weld Length in.	Weld Width in.	Weld Area in^2.	Weld Resistance kip/in	Weld Strength ksi
Logitudinal						
LS-060x060-1						
01	4.85	0.9968	0.0855	0.085	4.87	57.16
02	4.91	1.0190	0.0775	0.079	4.82	62.49
03	5.20	1.0215	0.0735	0.075	5.09	69.29
LS-118x060-1						
01	4.87	0.9993	0.0965	0.096	4.87	48.85
02	4.70	1.0023	0.0903	0.090	4.69	52.40
03	4.36	1.0275	0.0703	0.072	4.24	60.50
LS-118x060-2						
01	4.46	1.0690	0.0730	0.078	4.17	57.38
02	4.21	1.0250	0.0765	0.078	4.11	53.95
03	4.24	1.0125	0.0730	0.074	4.19	57.78
Transverse						
TS-060x060-1						
01	9.56	2.1853	0.0755	0.165	4.37	58.00
02	9.64	2.1810	0.0655	0.143	4.42	67.71
03	9.91	2.1723	0.0633	0.137	4.56	72.34
TS-118x060-1						
01	10.50	2.0960	0.1030	0.216	5.01	48.79
02	8.13	1.8343	0.0753	0.138	4.43	59.01
03	11.04	2.1425	0.1045	0.224	5.15	49.39
TS-118x060-2						
01	9.02	2.0965	0.0760	0.159	4.30	56.64
02	9.94	2.1865	0.0700	0.153	4.55	65.14
03	10.49	2.1753	0.0623	0.135	4.84	77.73

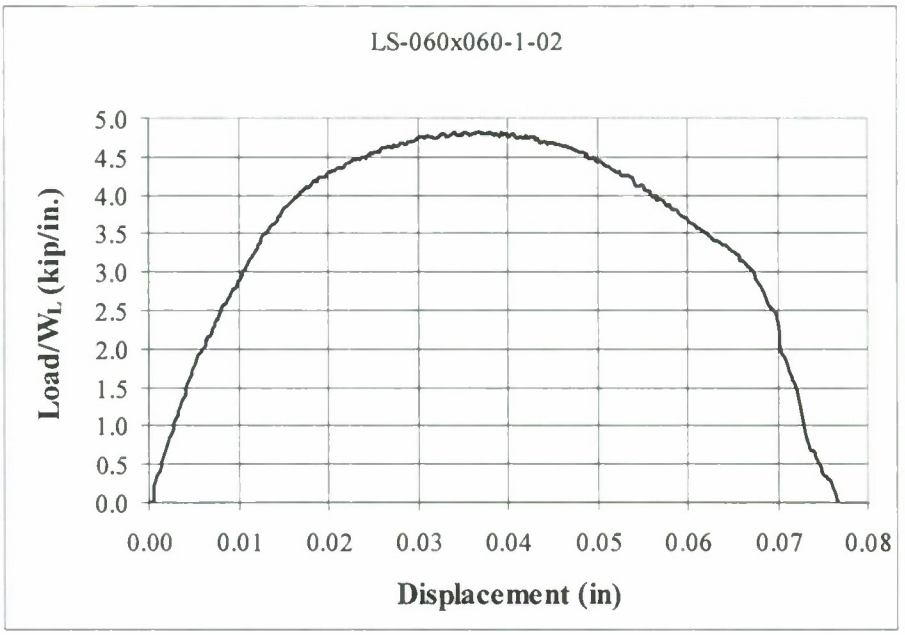

a) Longitudinal test

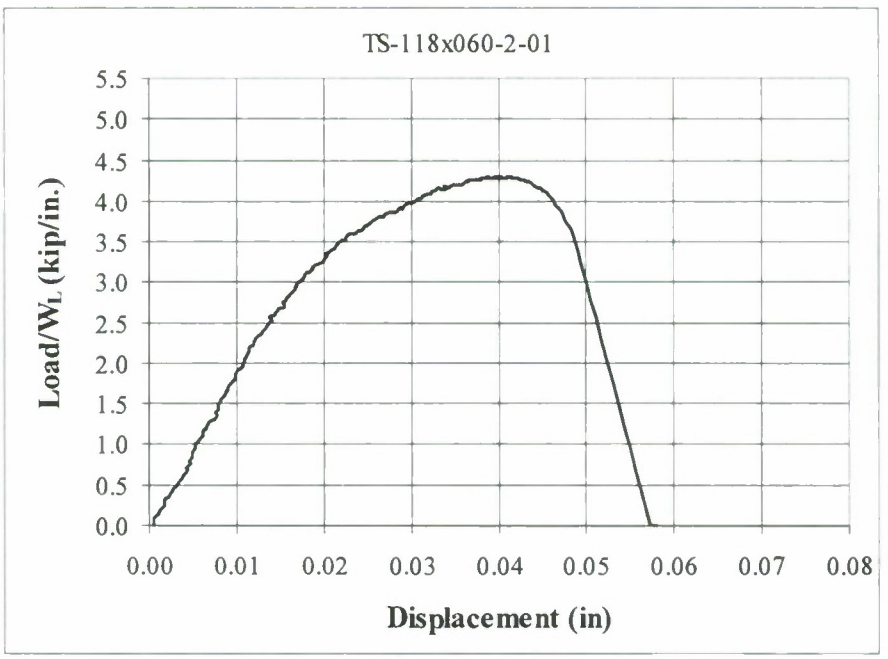

b) Transverse test

Figure 4.31 - Typical Weld Resistance vs. Displacement for Stake Weld Lap Shear Specimens

LS-060x060-1-03

TS-060x060-1-02

Figure 4.32 - Typical Failure of Stake Weld Lap Shear Specimens

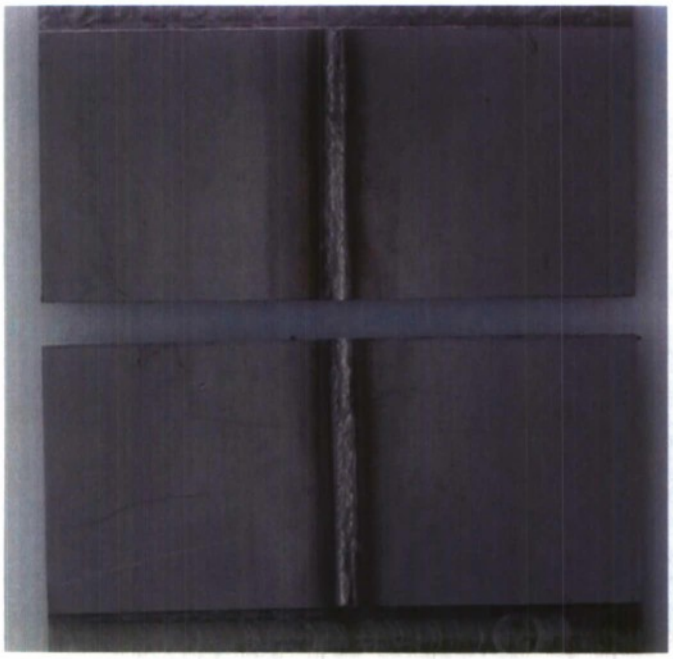

LS-060x060-1-03

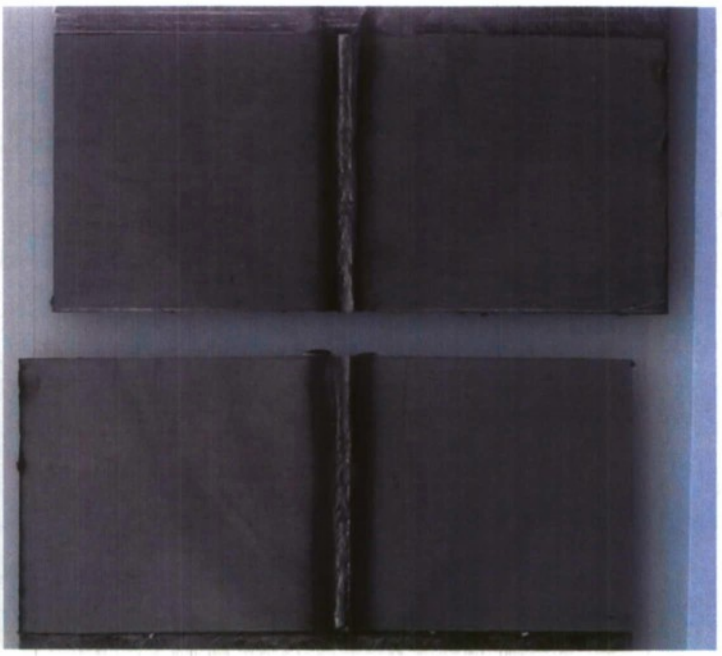

LS-118x060-1-01

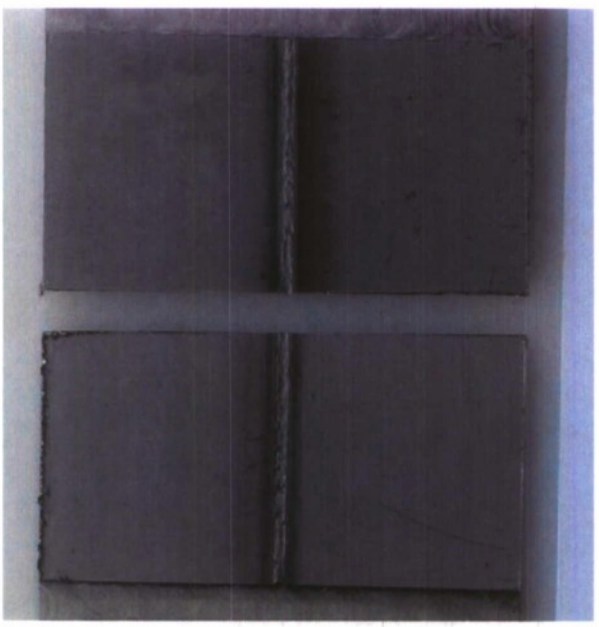

LS-118x060-2-01

Figure 4.33 – Close-up of the Longitudinal Failures.

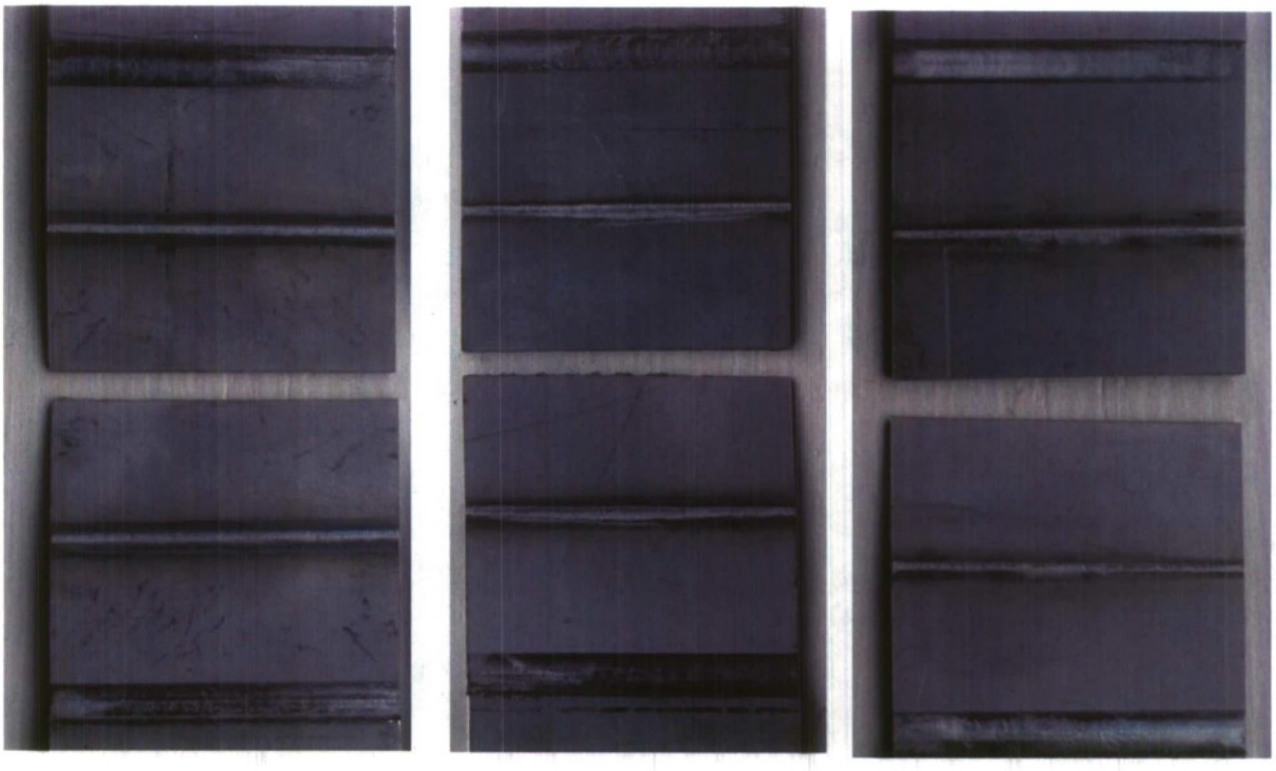

TS-060x060-1-01 TS-118x060-1-01 TS-118x060-2-01

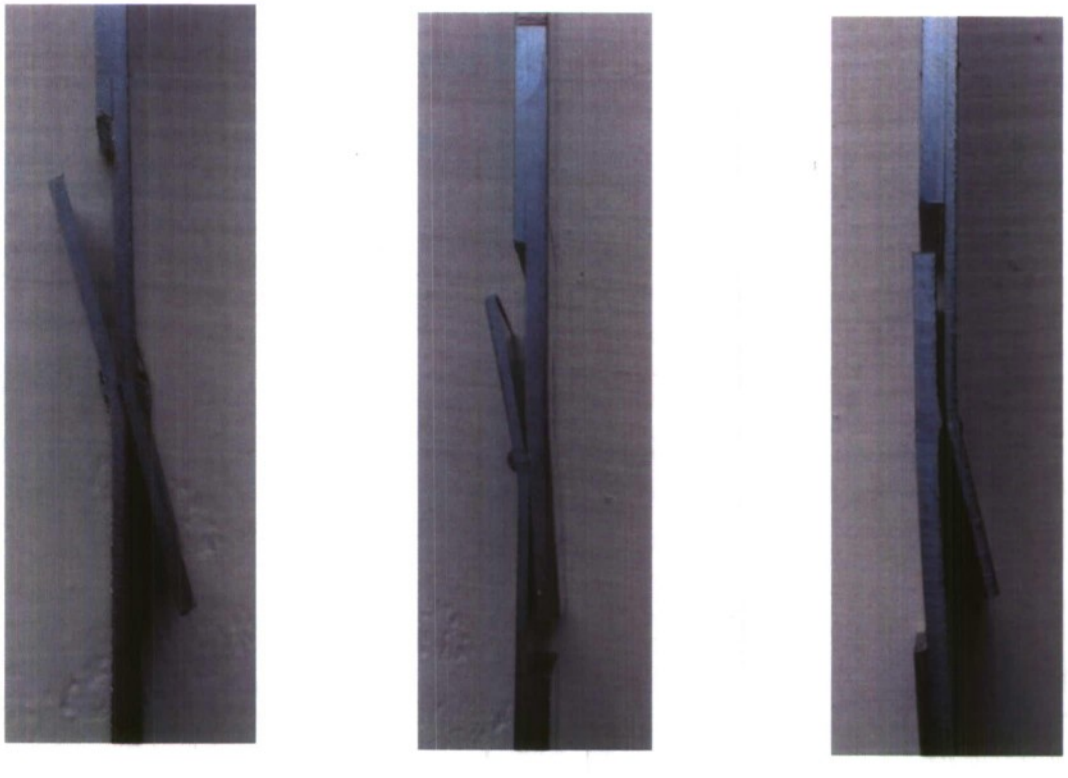

Figure 4.4 – Closeup of the Transverse Failures and Side View of the Permanent Set.

5. CONCLUSIONS

This study consists of the analysis and testing of a tapered end connection for laser welded steel sandwich panels. As a verification study, an analysis of a steel sandwich panel based on former study performed by Tan et al. (1989) was conducted. In this study, the connection region was modeled with continuous shell elements along the length of the panel due to the difficulties in modeling the intricate details of the weldment. In this verification effort, finite element analysis and theoretical analysis techniques are used. Theoretical modeling was performed with the aid of the MATLAB™ computer program. Finite element analysis techniques are applied using ABAQUS™ computer program using 8 node 6 degrees of freedom (DOF) elements, S8R6, for modeling the sandwich panel plates and the continuous stake weld. The influence of the effect of the weld link thickness on the sandwich panel's mechanical response was studied. It was determined that a weld link thickness equal to the minimum plate thickness works well. The influence of the weld placement was also studied. Models with welds at the center of each core landing showed a more flexible response than a model with welds at the corners, as expected. Therefore, there is a design trade-off between the cost of additional welding and the benefit of the additional stiffness. In addition to the verification study, laser welded steel sandwich panel with discontinuous prismatic stiffeners are analyzed using finite element method. The analysis was based upon the procedures used in the verification study.

The case of a laser welded steeel sandwich panel for use in a aircraft carrier hangar door was investigated using finite element analysis and was verified experimentally. A test set up was established in Hybrid Structures Laboratory (HSL) of the University of Maine and two laser welded steel sandwich panels with tapered end connections were tested under cyclic loading. These two sandwich panels are part of hangar connection panels with discontinuous laser stake-welded corrugations and a tapered close-out. The significant difference between the two panels is the thickness of the tapered close out. The objective is to investigate the performance of the welded connection plates under the service load of 8000 lbs. In order to simulate the service conditions of such panel in investigation, a 10 cycle quasi static 4 point bending test performed. Based on the information collected from the prior finite element analysis of connection panel, it was found that the yield strength of the material is reached when the centerline deflection is

greater than 0.15 inches. Cycle step size was selected based upon this result with the first set of cycles well within the linear response range. The mechanical response of the sandwich panel was observed via Linear Variable Displacement Transducers (LVDTs) and strain gages, which were installed on critical locations such as the top and bottom of the center panel, under the load heads and supports and on the outside of the web. The information collected using a 32 channel data acquisition system and then reduced using MS-Excel™ spreadsheet. In addition to the conventional experimental methods photogrammetry techniques were also used for recording displacements. A commercially available computer program Photomodeler™ was used to process the photographs. This program generated targets that are located on critical locations on the half of the panel and symmetric behavior is assumed for simplicity. Photogrammetry data gathered via special target points and used to visualize the final deformed shape. Unique targets were glued to the top plate of each sandwich panel. The deformed shape and the surface contour are obtained for both panels. Photogrammetric data compared well with LVDT readings.

Theoretical stress results are calculated based on a plane stress assumptions at the location of the strain gages. Data for the first four cycles are compared to the finite element analysis results. Both results are tabulated and reported in a table format with percent disagreements for each cycle in each direction. Stress results are shown to compare reasonably well with the experimental data. As far as connection strength is concerned, the panel withstood substantially more than the design load without distress in the tapered closeout connection.

Static testing of lap-shear specimens were performed in a both a longitudianal and transverse configuration with 2 different plate thicknesses. These tests resulted in an average weld resistance per unit length of 4.63 kip/in for the transverse stake-welds with a standard deviation of 0.30 kip/in and 4.56 kip/in for the longitudinal stake-welds with a standard deviation of 0.39 kip/in. Little difference is observed in the resistance between a weld made with 4kW or 6.5kW laser power.

REFERENCES

1. Abbott, S.P., Caccese, V., Thompson, L., Blomquist, P.A., Hansen, E.E, 2008, Automated Laser Welded High Performance Steel Sandwich Bridge Deck Development, 17 pages.

2. Allen H.G., 1969, Analysis and Design of Structural Sandwich Panels. Oxford, UK: Pergamon.

3. ASTM A6, Standard Specification for General Requirements for Rolled Structural Steel Bars, Plates, Shapes, and Sheet Piling.

4. Blomquist PA, and Forrest, DL 1999, Laser-cutting and welding of DDG-51 structural shapes, 1999 Ship Production Symposium, Arlington, VA, July.

5. Blomquist, PA, Orozco, N, & Patch, D 2004, 'Laser fabricated structural shapes for new construction, overhaul and repair', *Journal of Ship Production*, Vol. 20, No. 2, pp. 114-121.

6. Caccese, V., and Berube, K.A., 2003, "Stub Column and Residual Strain Tests for HSLA-65 Laser Fabricated Structural Shapes" University of Maine Department of Mechanical Engineering, Report No. C2000-001-RPT-001, September, 28 pp.

7. Caccese, V., Berube, K., Blomquist, P.A., Webber, S.R., & Orozco, N.J., 2006, "Effect of Weld Geometric Profile on Fatigue Life of Cruciform Welds Made by Laser/GMAW Processes", Marine Structures J. , Vol. 19, No 1, pp. 1-22.

8. Chang, W.S., Ventsel, E., Krauthammer, T., John, J., 2005,Bending Behavior of Corrugated-Core Sandwich Plates, *Composite Structures*, Vol. 70, pp. 81-89

9. Cheng, Q.H., Lee, H.P., Lu, C., 2006, A Numerical Analysis Approach for Evaluating Elastic Constants of Sandwich Structures with Various Cores, *Composite Structures* Vol.74, pp.226-236. 3.

10. Defalco, J 2007, Practical applications for hybrid laser welding, *Welding Journal*, October, pp. 47-51.

11. Duhamel R,F., 1996, Laser welding of thick plates, Structural and Heavy Plate Fabrication Conf., New Orleans, LA, Nov. 1996.

12. Fleck, N.A and Deshpande, V.S., 2004 The Resistance of Clamped Sandwich Beams to Shock Loading, *Journal of Applied Mechanics*, ASME Vol. 71, pp. 386-401.

13. Fung T.C, Tan K.H, Lok T.S., 1994, Elastic Constants for Z-core Sandwich Panels. *Journal of Structural Engineering, ASCE* Vol.120, pp.3046-3055.

14. Fung, T.C., Tan, K.H., Lok, T.S., 1996, Shear Stiffness D_{Qy} for C-Core Sandwich Panels, *Journal of Structural Engineerin.*, ASCE., Vol. 128, N5, pp.683-689.

15. Hutchinson, J.W., Xue, Z., 2005, Metal Sandwich Plates Optimized for Pressure Impulses, *International Journal of Mechanical Sciences,* Vol. 47, pp. 545-569.

16. Klanac, Alan., Kujala, P., 2004, Optimal Design of Steel Sandwich Panel Applications in Ships, 9th Symposium on Practical Design of Ships and Other Floating Structures, Shiffbautechnische Gesellschaft e.V, 8 pages.

17. Kujala, P., Romanoff, J., Tabri, K., Ehlers, S. 2004, All Steel Sandwich Panels-Design Challenges for Practical Applications on Ships, 9th Symposium on Practical Design of Ships and Other Floating Structures, Shiffbautechnische Gesellschaft e.V, 8 pages.

18. Libove, C., Hubka R.E., 1951, Elastic Constants for Corrugated Core Sandwich Plates. *Technical Note 2289. National Aeronautics and Space Administration (NASA).*

19. Lok, T.S., and Cheng, Q.H., 2000, "Elastic stiffness properties and behavior of truss-core sandwich panel", *ASCE Journal of Structural Engineering*, Vol.126, pp.552-559.

20. Orozco, NJ, Blomquist, PA, Rudy, RB, & Webber, SR, 2004, 'Real-time control of laser-hybrid welding using weld quality attributes', Proceedings of the 23rd International Congress on Applications of Lasers & Electro-Optics (ICALEO 2004), October, San Francisco.

21. Plantema, F., 1966, Sandwich Construction. John Wiley and Sons, Inc., New York, USA.

22. Rooks, B 2000, Lasers become the acceptable face of precision welding and cutting *Industrial Robot*, Vol. 27, No. 2, pp. 103-107.

23. Roland, F, Reinert, T, & Pethan, G 2002, 'Laser welding in shipbuilding- an overview of the activities at Meyer Werft', Welding in the World, Vol. 46, Copenhagen, DE, pp. 39-50.

24. Roland, F, Manzon, L, Kujala, P, Brede, M, & Weitzenbock, J,. 2004, Advanced joining techniques in European shipbuilding, *Journal of Ship Production*, Vol. 20, No. 3, August, pp. 200-210.

25. Tan K.H, Montague P, Norris C., 1989, Steel sandwich panels: Finite Element, Closed Solution, and Experimental Comparisons, on a 6 m · 2.1 m Panel. *Structural Engineering* Vol 67, pp.159-166.

26. Vel, S.S., Caccese, V., Zhao.,H, 2005, Elastic coupling effects in tapered sandwich panels with laminated anisotropic composite facings, *Journal of Composite Materials,* Vol. 39, No. 24, pp. 2161-2183.

27. Vinson, J.R. (1999), "The behavior of sandwich structures of isotropic and composite materials",Technomic Publications., Lancaster, PA.

28. Xue, Z., Hutchinson, J.W., 2004, A Comparative study of Impulse-Resistant Metal Sandwich Plates. *International Journal of Mechanical Sciences,* Vol. 30, pp.1283-1305.

29. Yang, M., Qiao, P., 2005, Higher-Order Impact Modeling of Sandwich Structures with Flexible Core. *International Journal of Solids and Structures,* Vol. 42, pp.5460-5490.

30. Zenkert, D., 1995, An Introduction to Sandwich Construction. EMAS Ltd., Solihull, UK.

APPENDICES

APPENDIX A

Instrumentation calibration factors

LDVT	Cal Factor
A-1	1.02E-01
B-1	2.07E-01
B-2	4.76E-02
B-3	2.07E-01
C-1	1.05E-01
C-2	1.03E-01
C-3	1.05E-01
D-1	1.05E-01
D-2	9.94E-02
D-3	1.04E-01
E-1	5.18E-02

Strain Gage	Cal Factor	Strain Gage	Cal Factor
S1-1	-2.01E+03	S4-1	-1.99E+03
S1-2	-2.01E+03	S4-2	-2.00E+03
S1-3	-1.99E+03	S4-3	-2.03E+03
S2-1	-2.00E+03	S5-1	-2.00E+03
S2-2	-2.01E+03	S5-2	-2.00E+03
S2-3	-2.00E+03	S5-3	-2.01E+03
S3-1	-2.01E+03	S6-1	2.00E+03
S3-2	-2.01E+03	S6-2	-2.01E+03
S3-3	-2.02E+03	S6-3	-1.99E+03

Modulus of Elasticity	2.90E+07	psi

APPENDIX B

Thick Panel Displacements at LVDT Locations

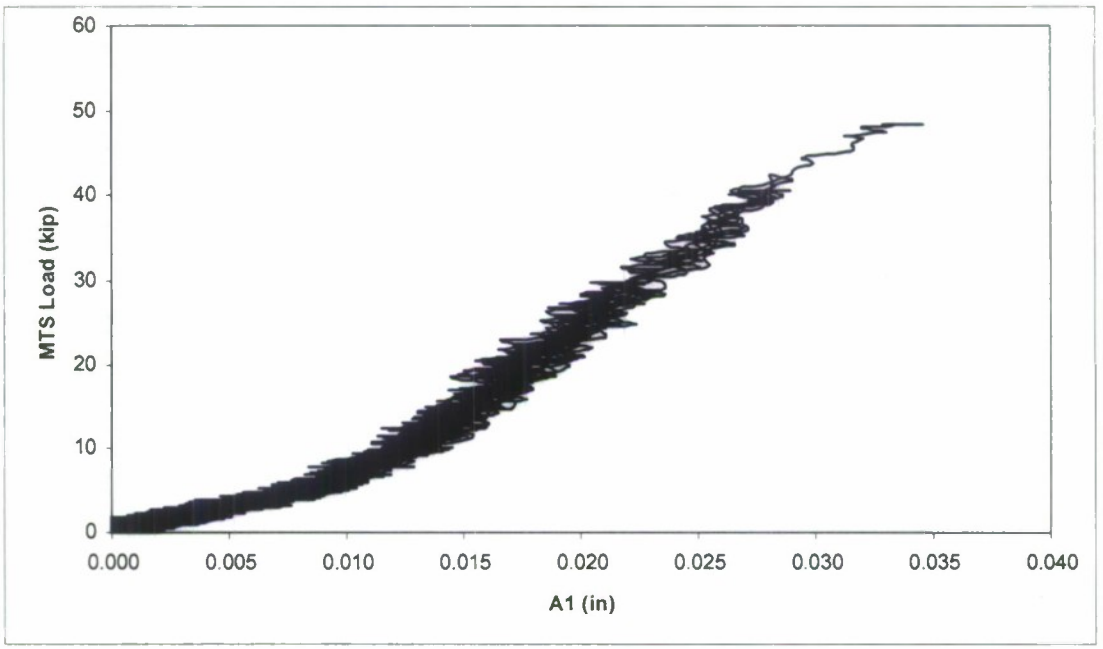

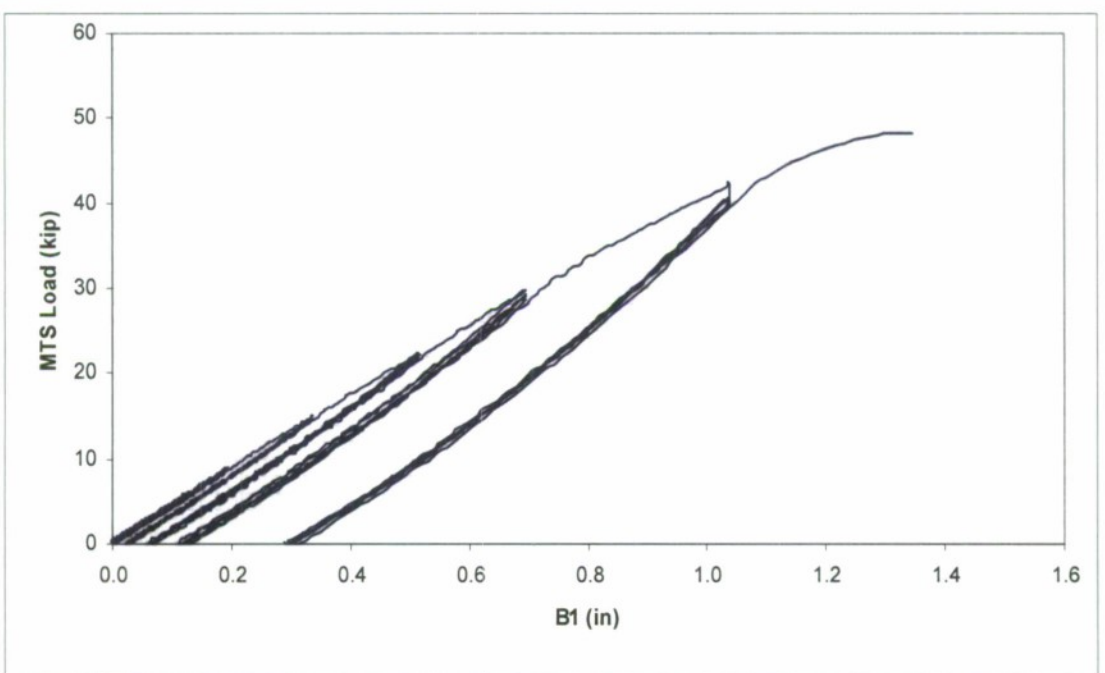

Appendix B Continued

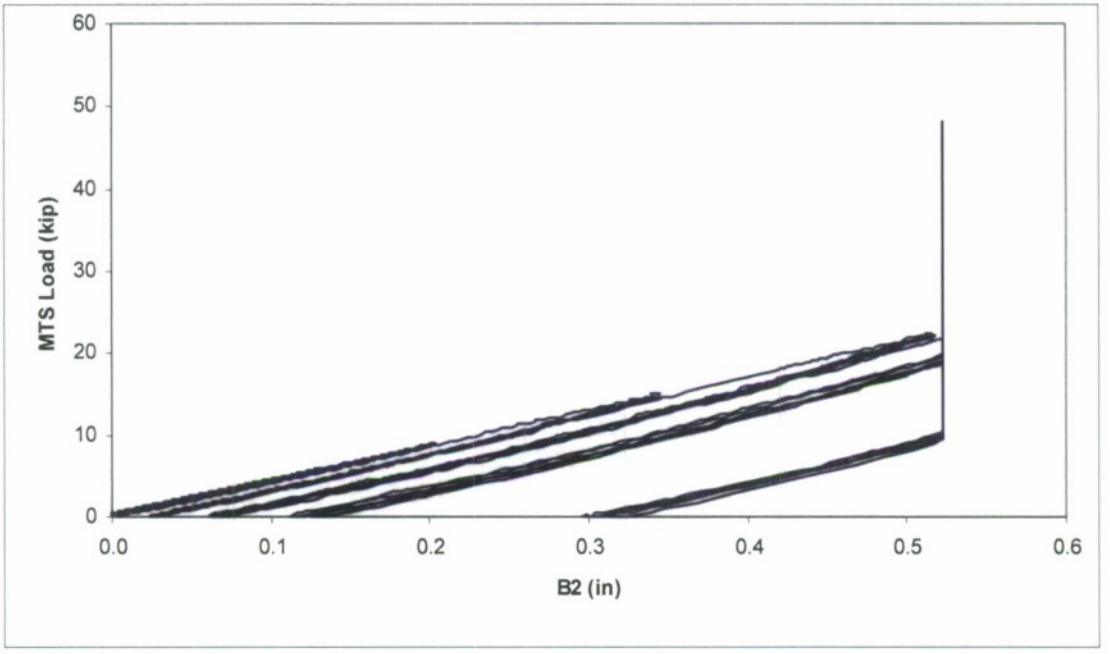

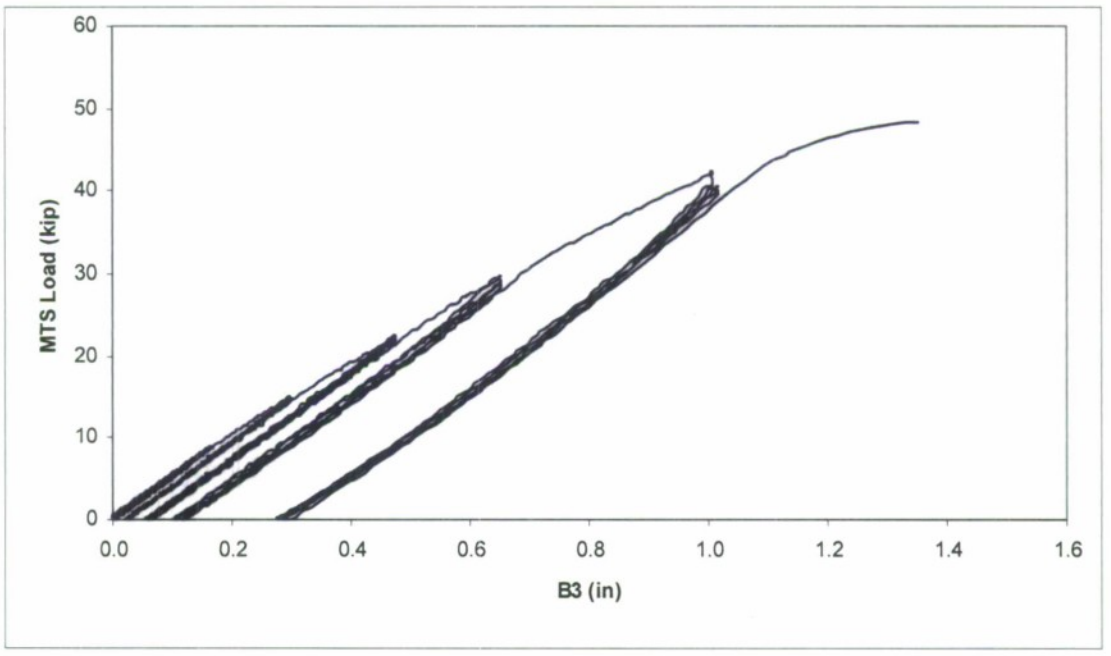

Appendix B Continued

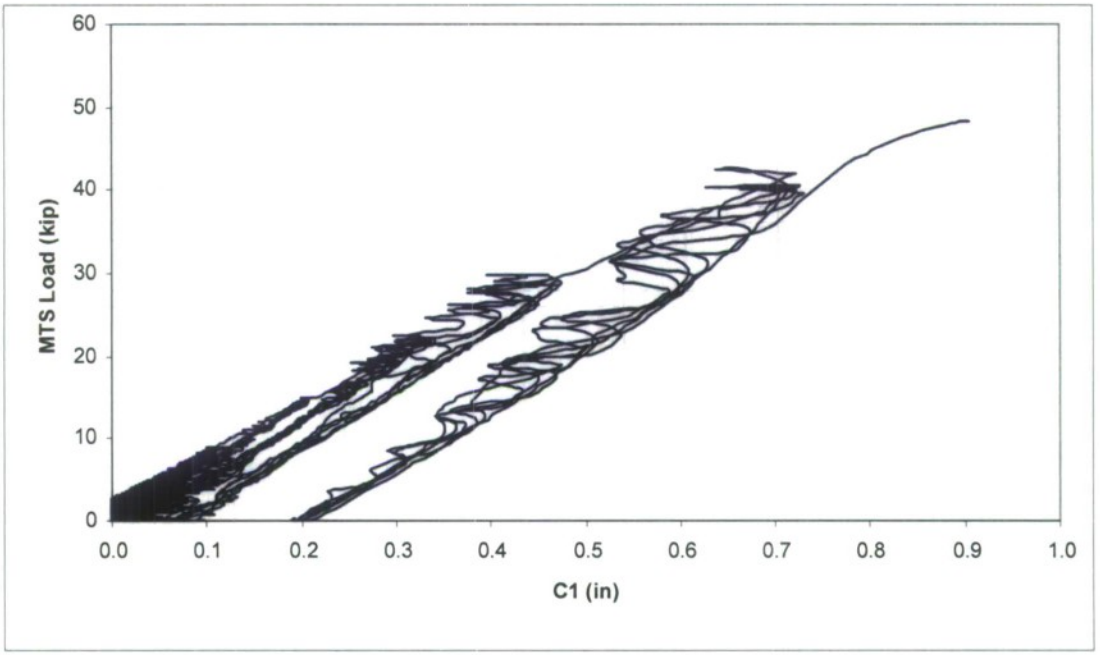

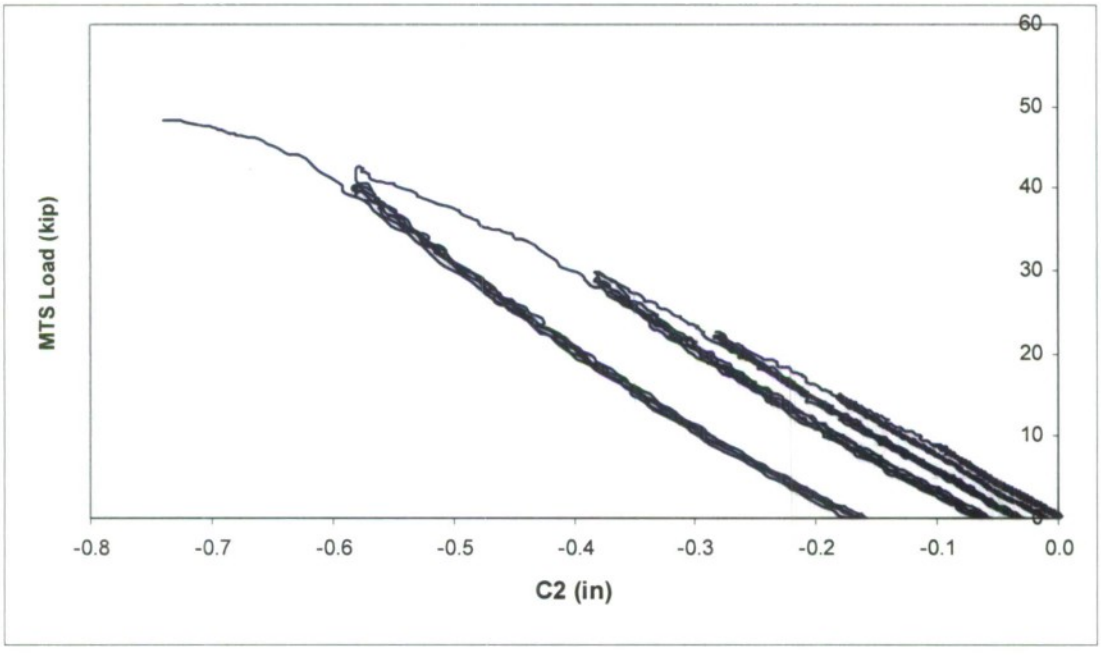

Appendix B Continued

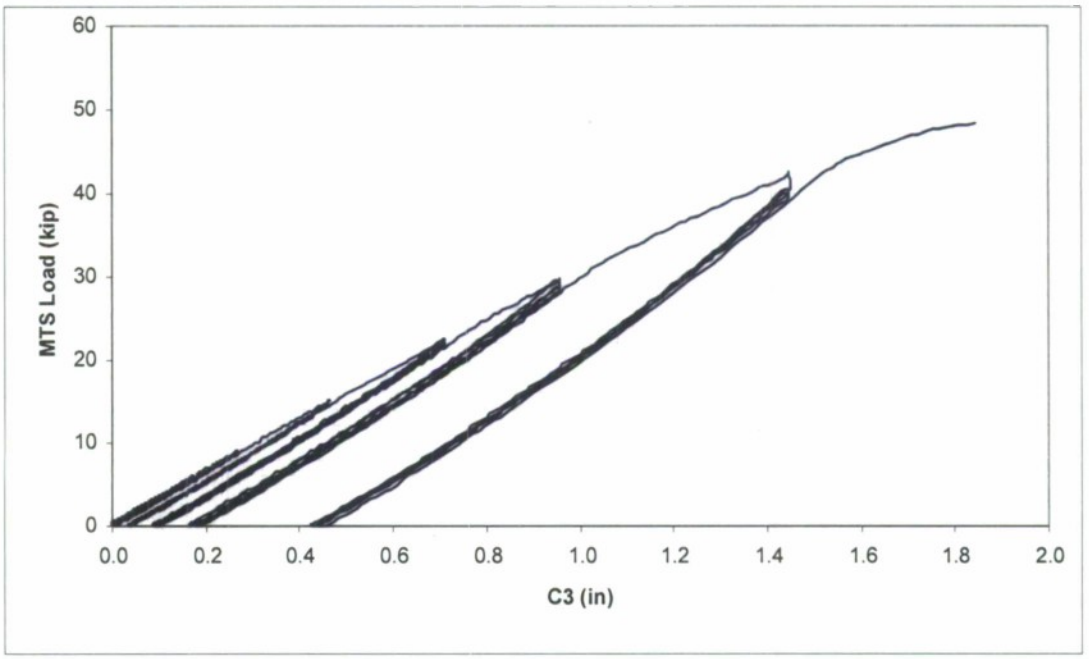

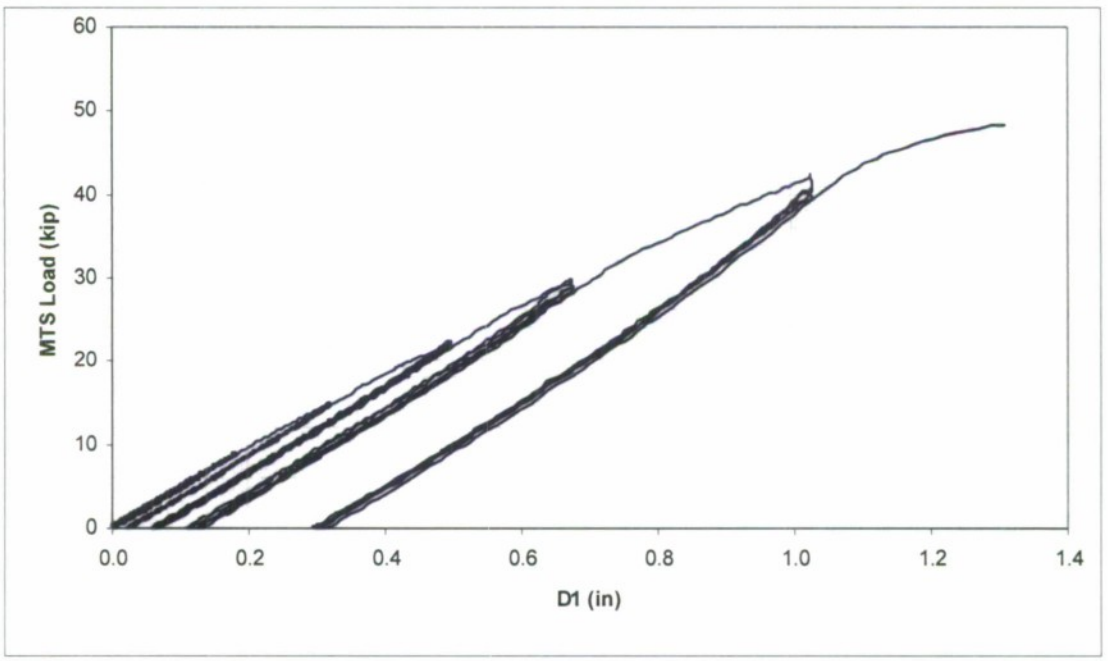

Appendix B Continued

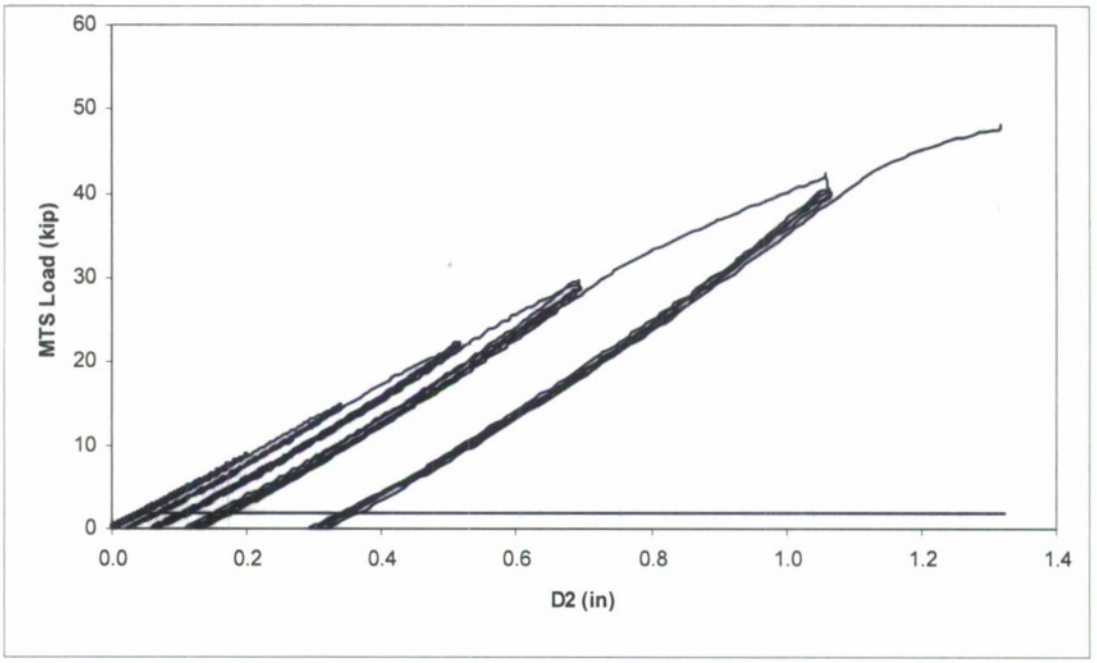

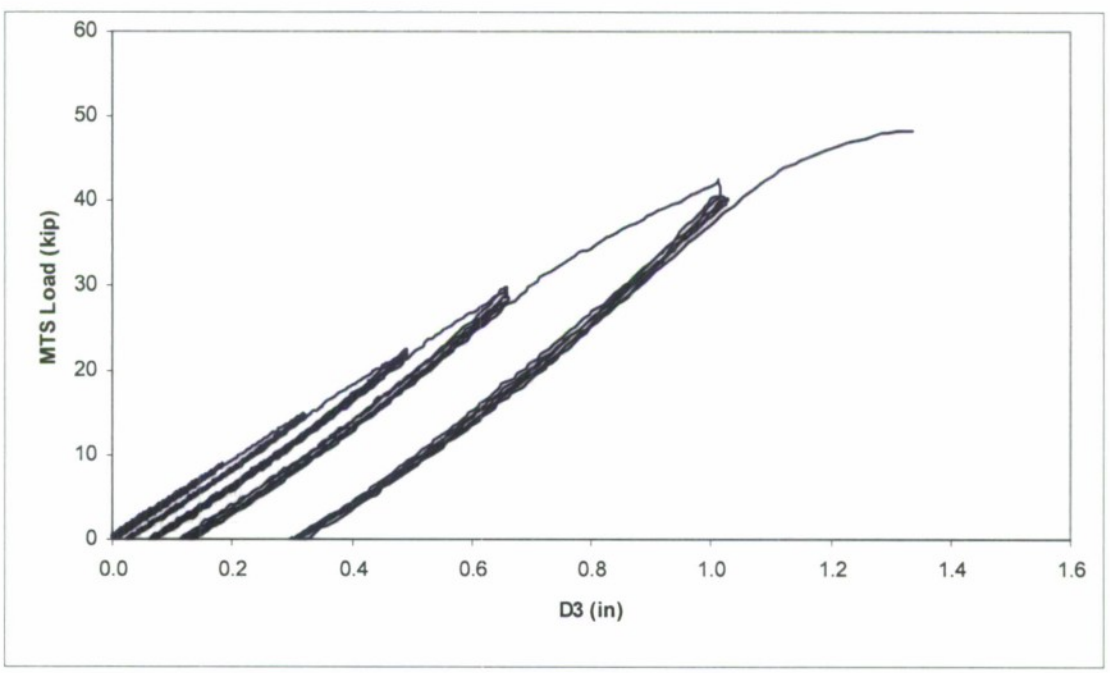

Appendix B Continued

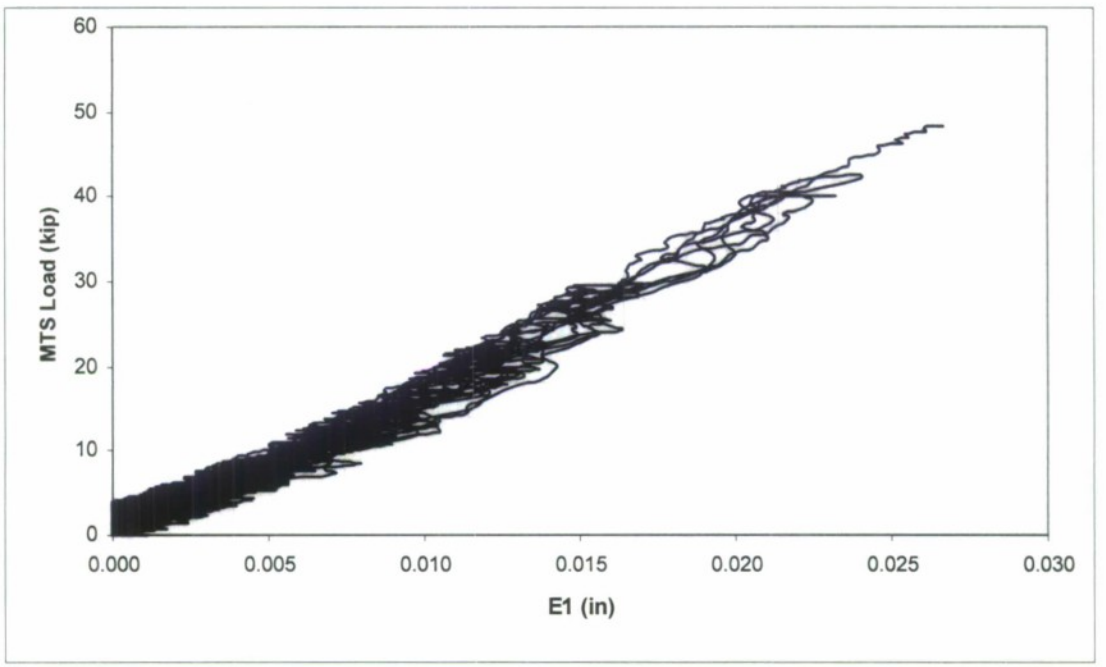

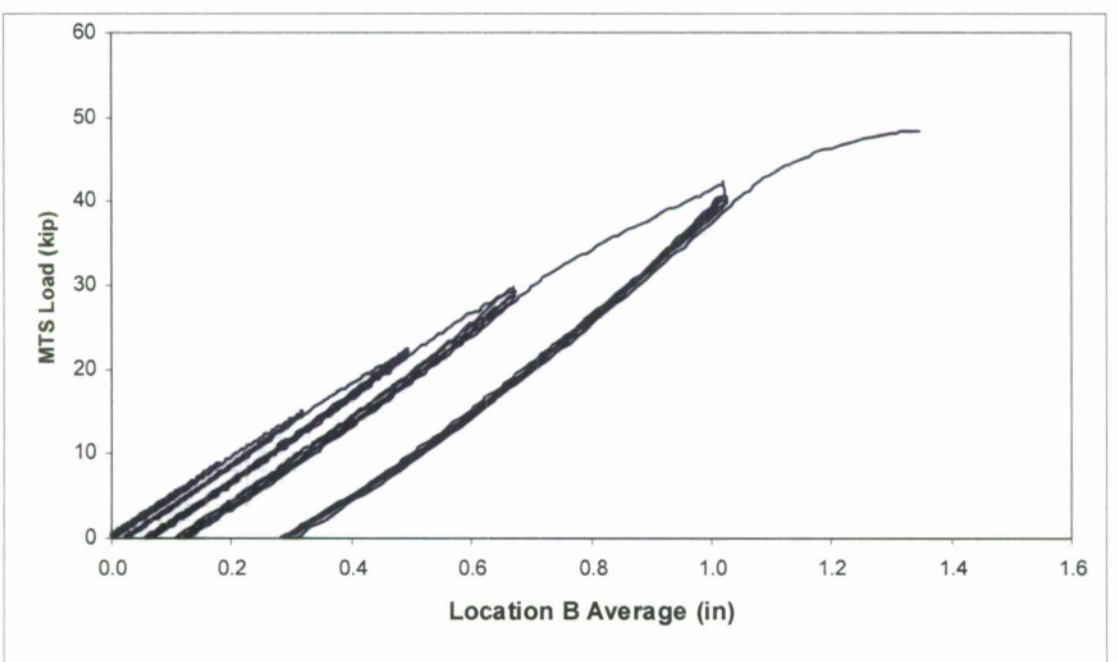

Appendix B Continued

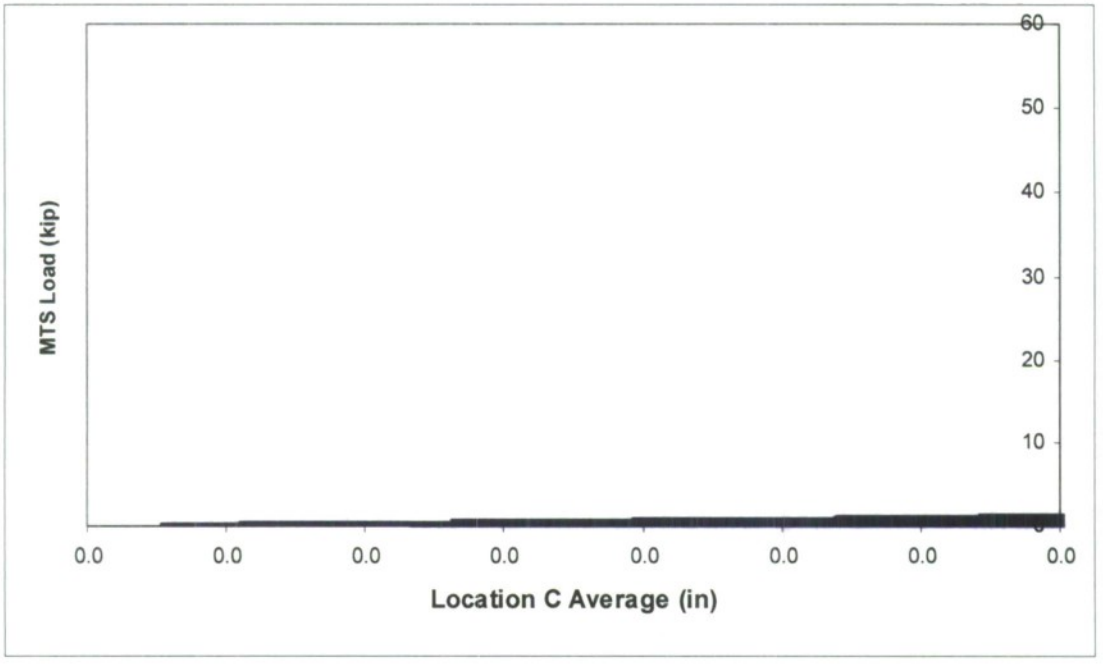

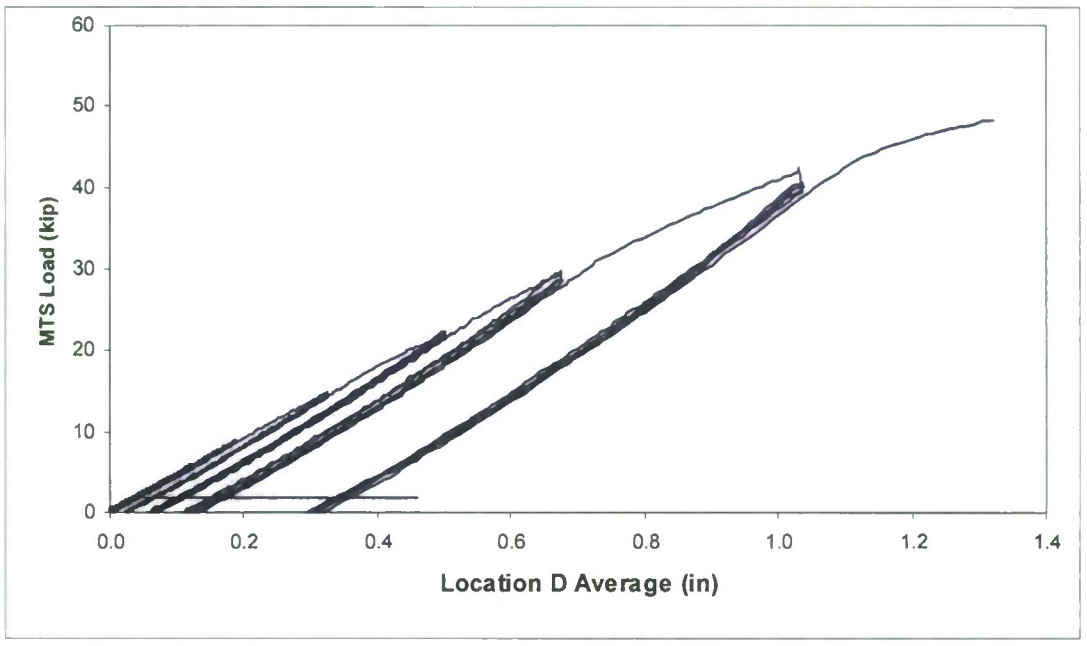

APPENDIX C

Thick Panel Displacements and Stiffness at the Center

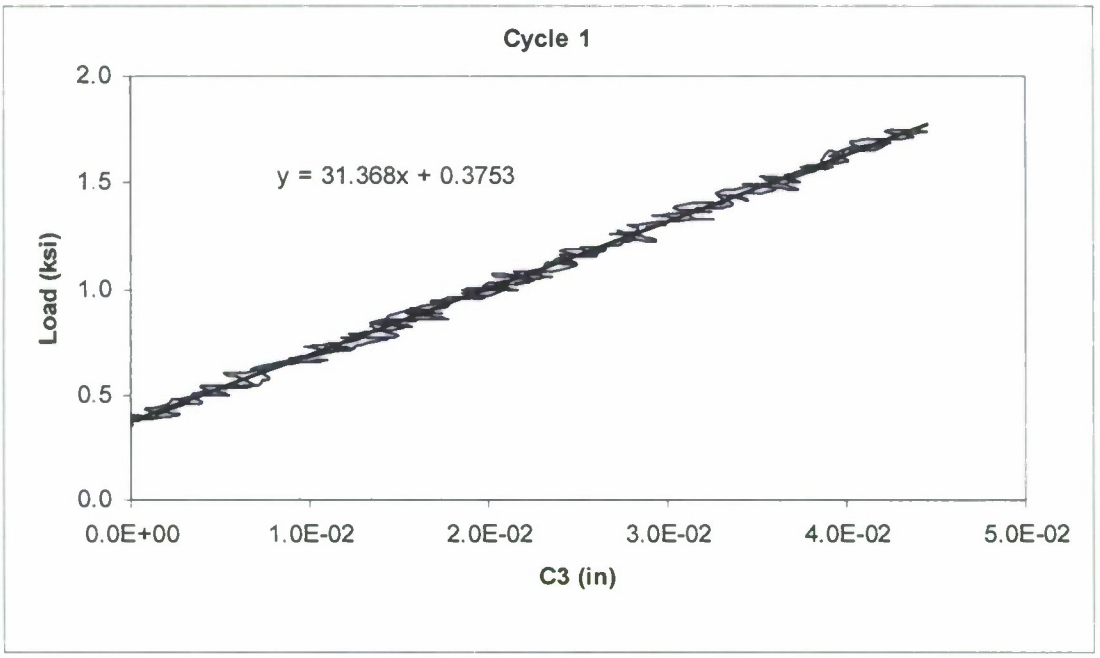

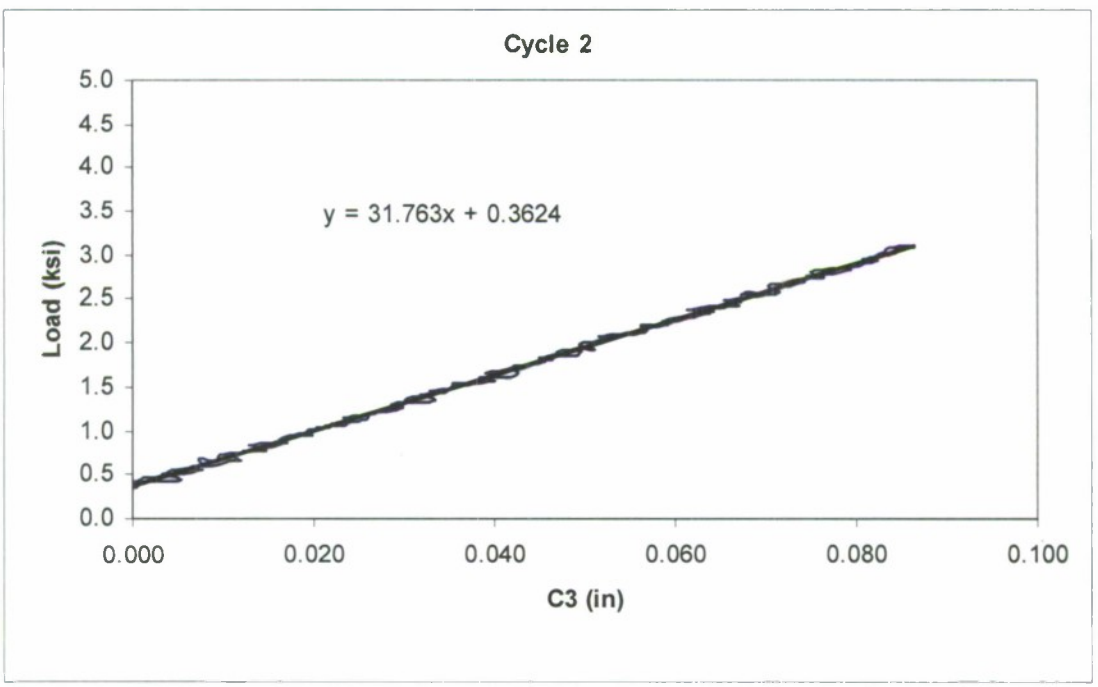

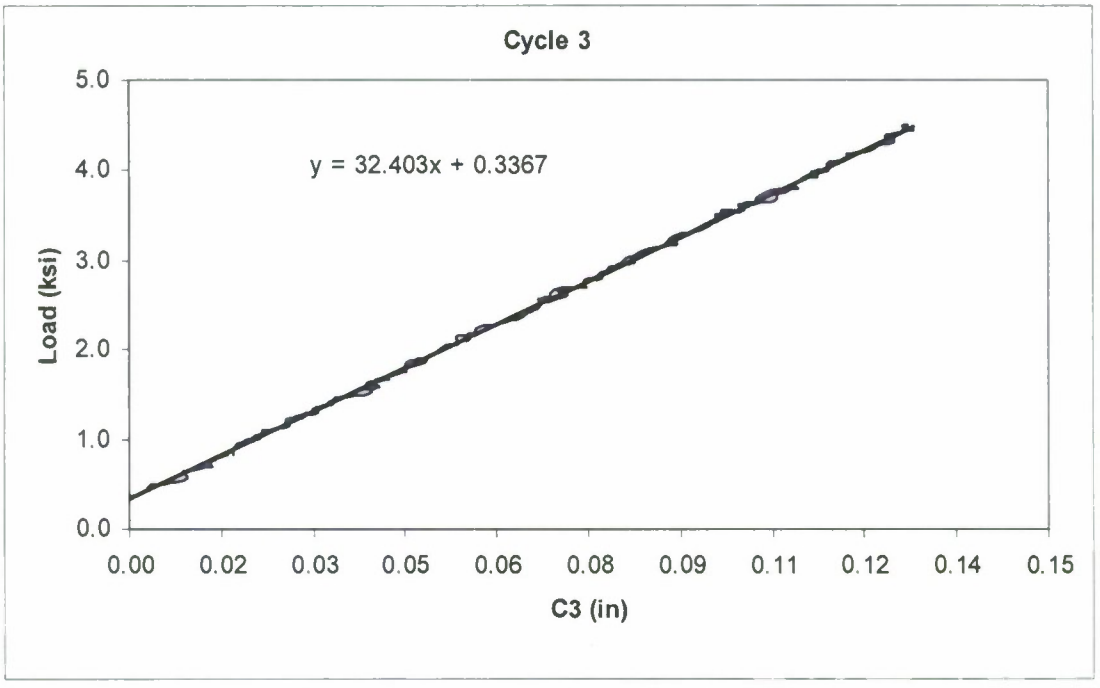
Cycle 3
y = 32.403x + 0.3367
Load (ksi)
5.0
4.0
3.0
2.0
1.0
0.0
0.00
0.02
0.03
0.05
0.06
0.08
0.09
0.11
0.12
0.14
0.15
C3 (in)

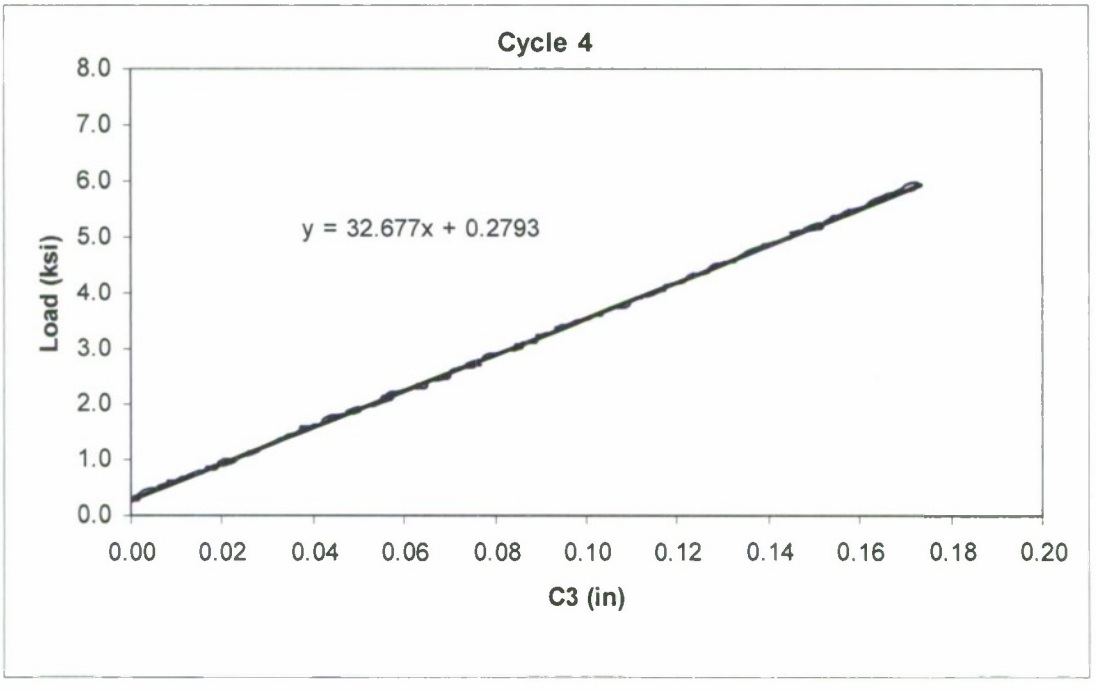
Cycle 4
y = 32.677x + 0.2793
Load (ksi)
8.0
7.0
6.0
5.0
4.0
3.0
2.0
1.0
0.0
0.00
0.02
0.04
0.06
0.08
0.10
0.12
0.14
0.16
0.18
0.20
C3 (in)

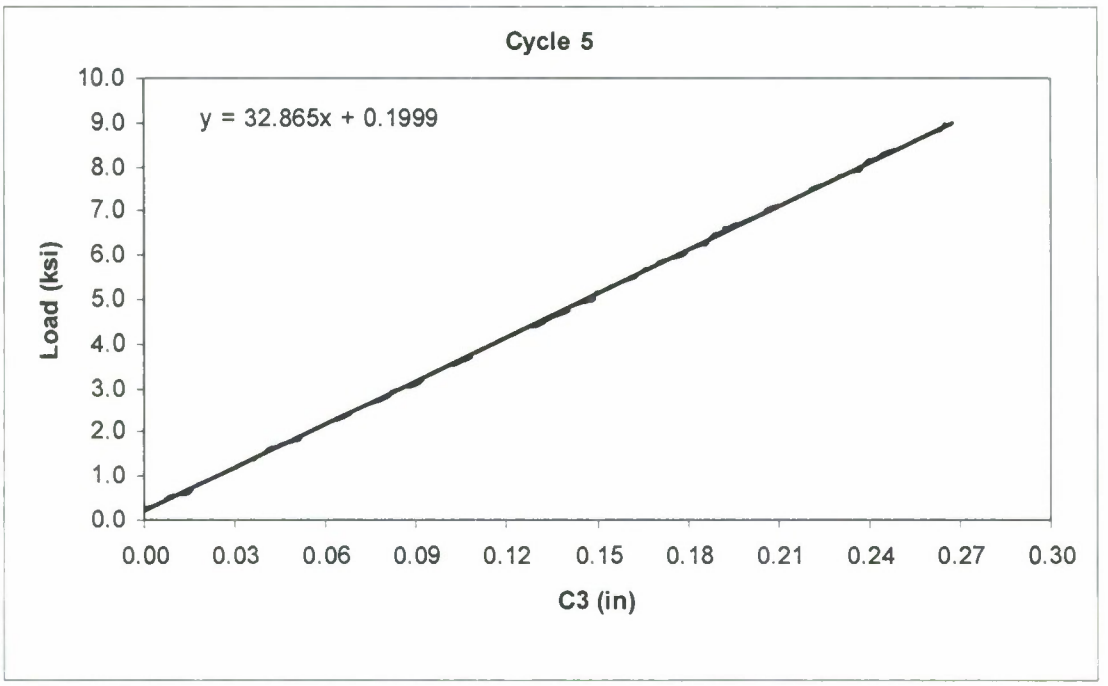
Cycle 5
y = 32.865x + 0.1999
Load (ksi)
10.0
9.0
8.0
7.0
6.0
5.0
4.0
3.0
2.0
1.0
0.0
0.00
0.03
0.06
0.09
0.12
0.15
0.18
0.21
0.24
0.27
0.30
C3 (in)

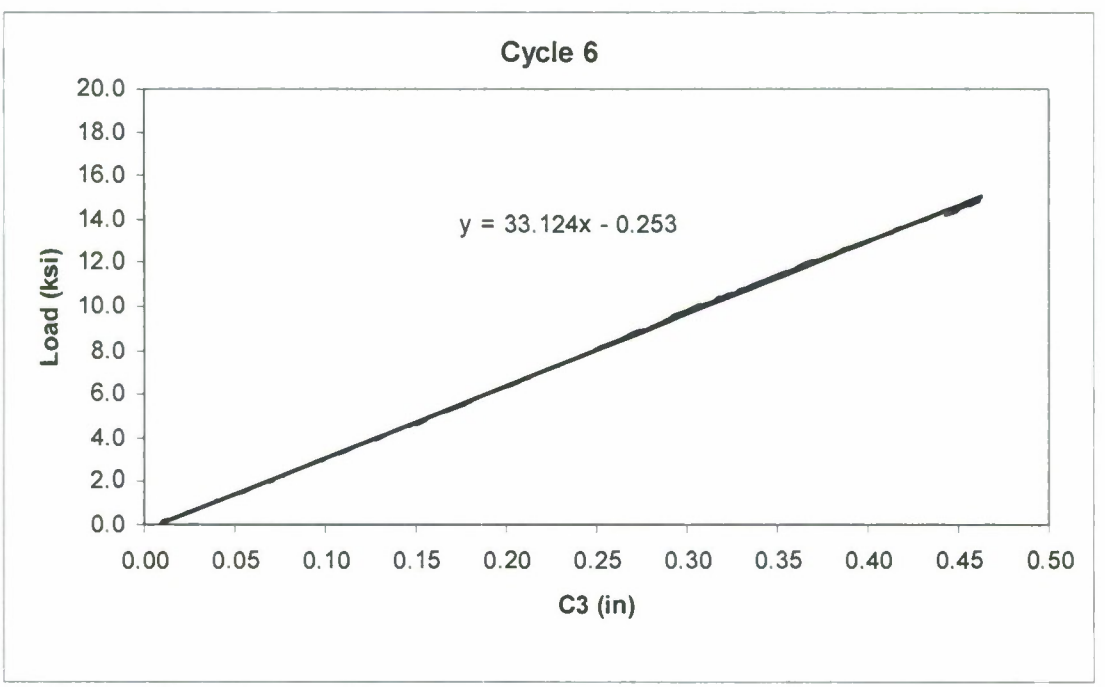
Cycle 6
y = 33.124x - 0.253
Load (ksi)
20.0
18.0
16.0
14.0
12.0
10.0
8.0
6.0
4.0
2.0
0.0
0.00
0.05
0.10
0.15
0.20
0.25
0.30
0.35
0.40
0.45
0.50
C3 (in)

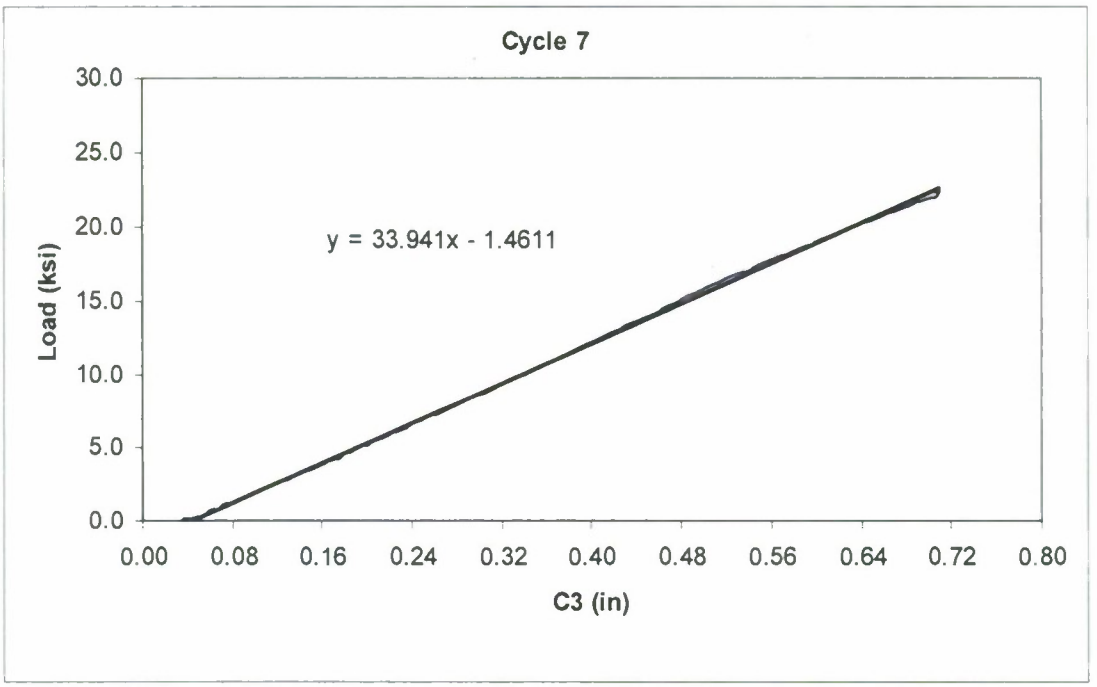
Cycle 7
30.0
25.0
20.0
15.0
10.0
5.0
0.0
Load (ksi)
y = 33.941x - 1.4611
0.00
0.08
0.16
0.24
0.32
0.40
0.48
0.56
0.64
0.72
0.80
C3 (in)

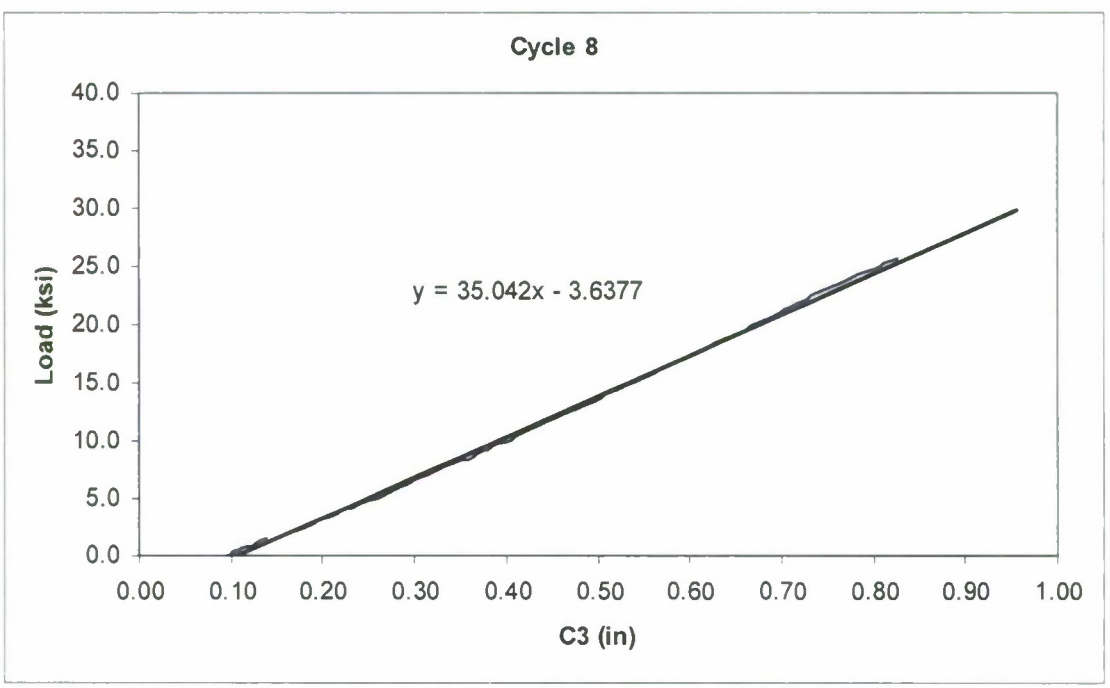
Cycle 8
40.0
35.0
30.0
25.0
20.0
15.0
10.0
5.0
0.0
Load (ksi)
y = 35.042x - 3.6377
0.00
0.10
0.20
0.30
0.40
0.50
0.60
0.70
0.80
0.90
1.00
C3 (in)

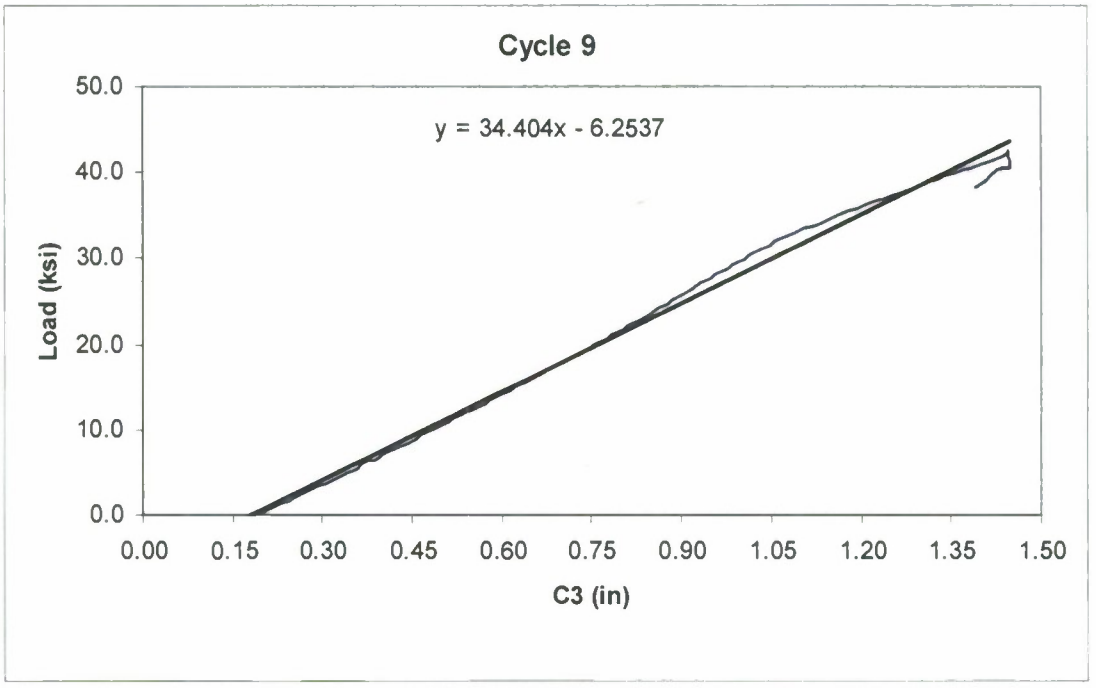
Cycle 9
y = 34.404x - 6.2537
Load (ksi)
50.0
40.0
30.0
20.0
10.0
0.0
0.00
0.15
0.30
0.45
0.60
0.75
0.90
1.05
1.20
1.35
1.50
C3 (in)

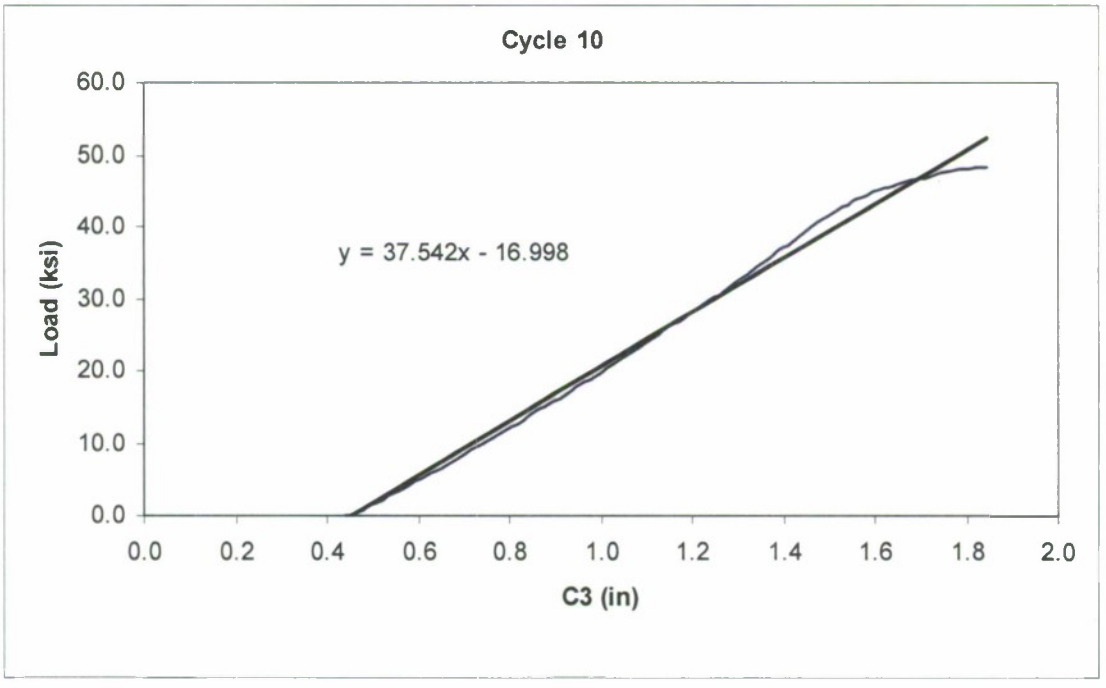
Cycle 10
y = 37.542x - 16.998
Load (ksi)
60.0
50.0
40.0
30.0
20.0
10.0
0.0
0.0
0.2
0.4
0.6
0.8
1.0
1.2
1.4
1.6
1.8
2.0
C3 (in)

APPENDIX D

Displaced Shape of Thick Panel

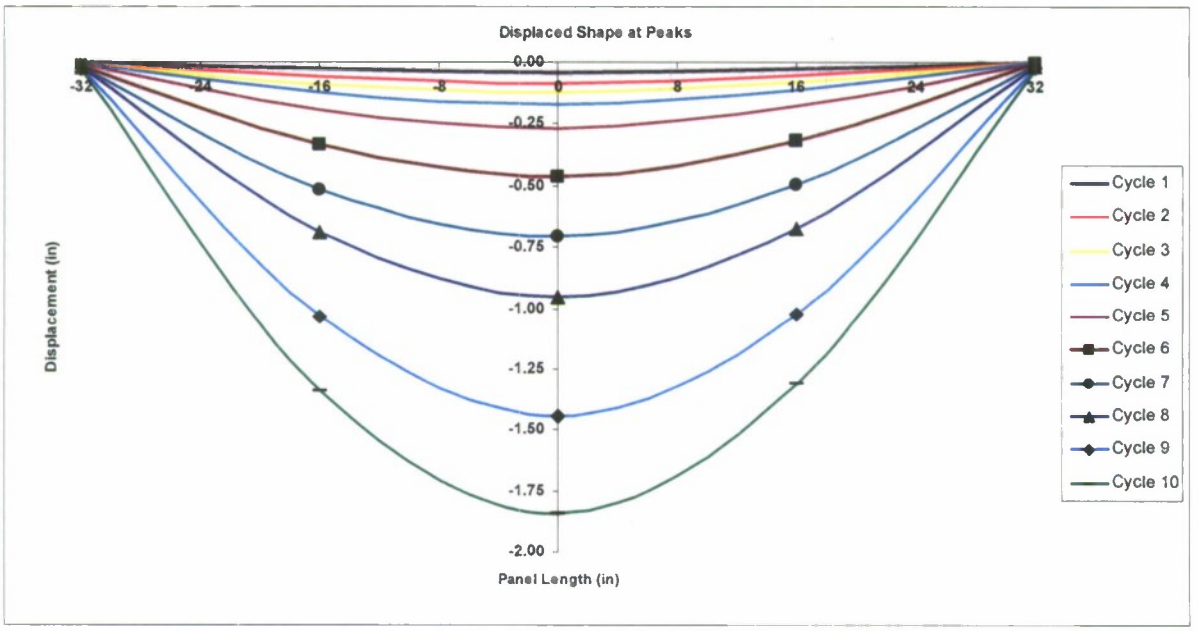

APPENDIX E

Thick Panel Strains at Strain Gage Locations

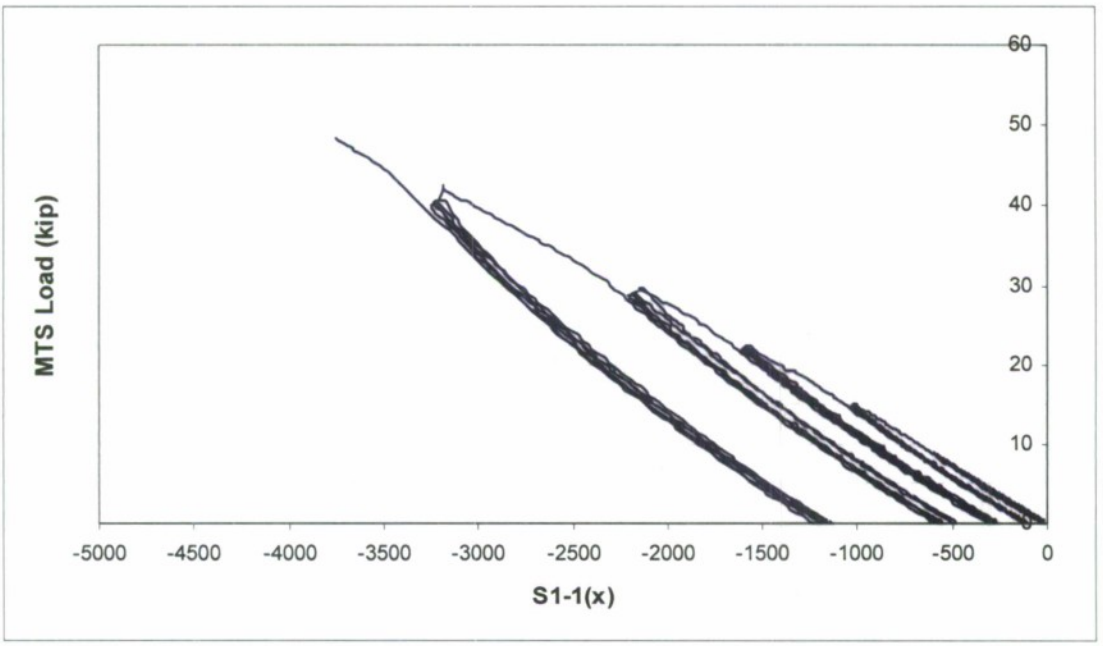

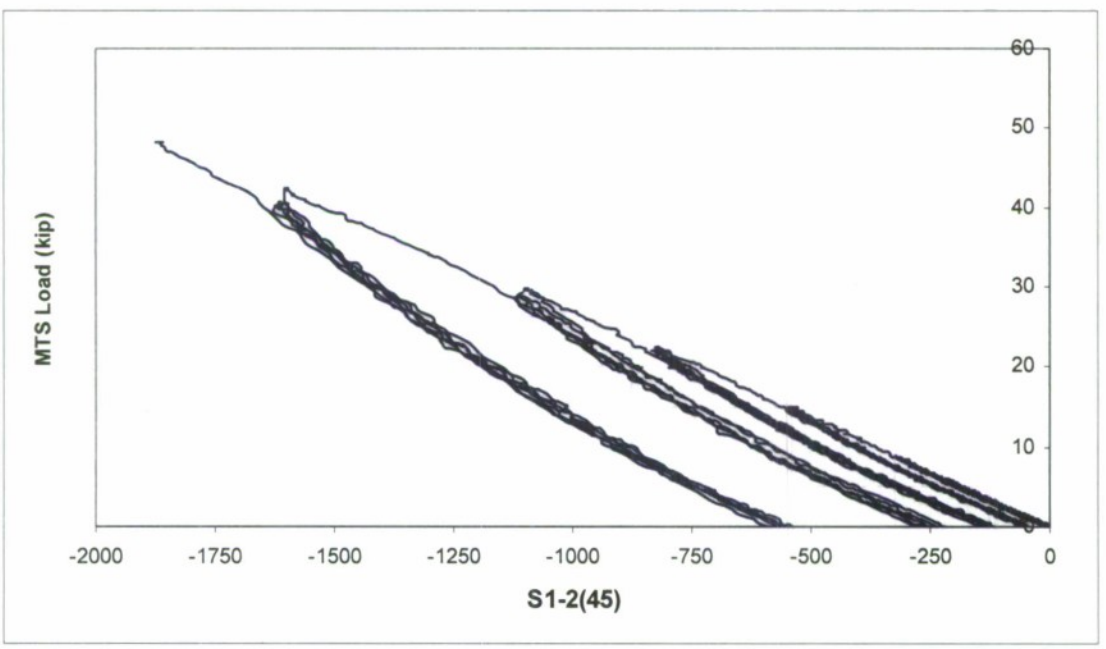

Appendix E Continued

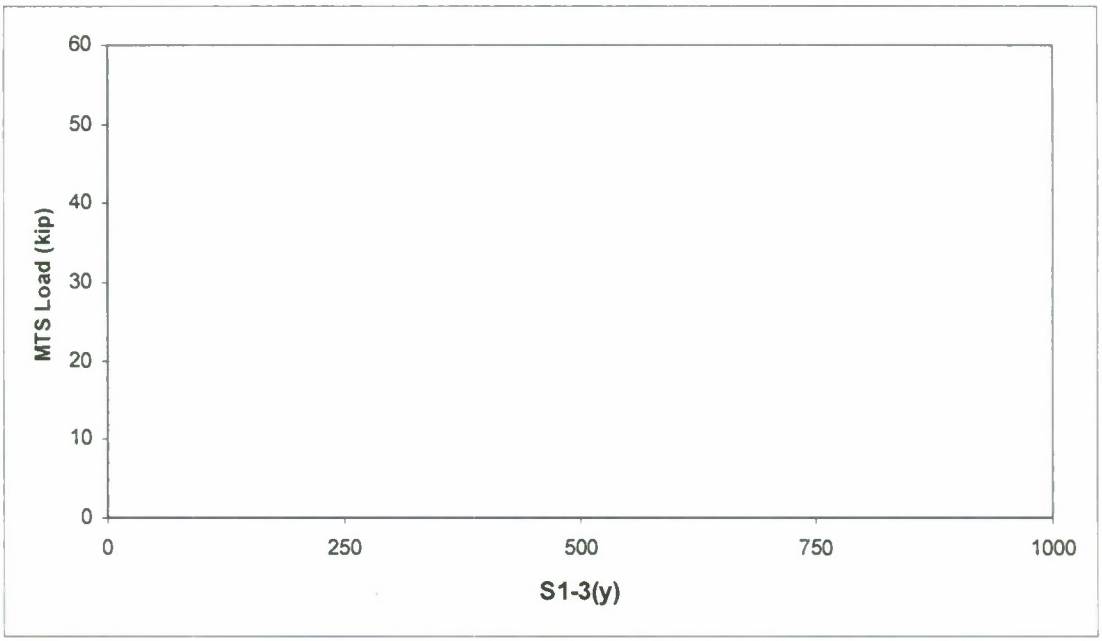

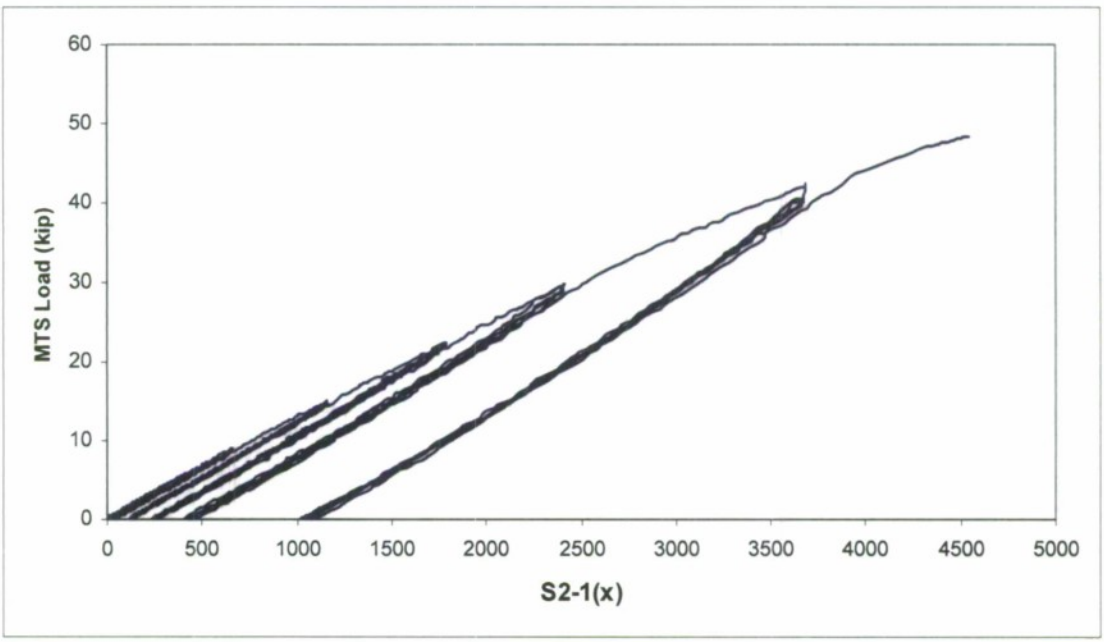

Appendix E Continued

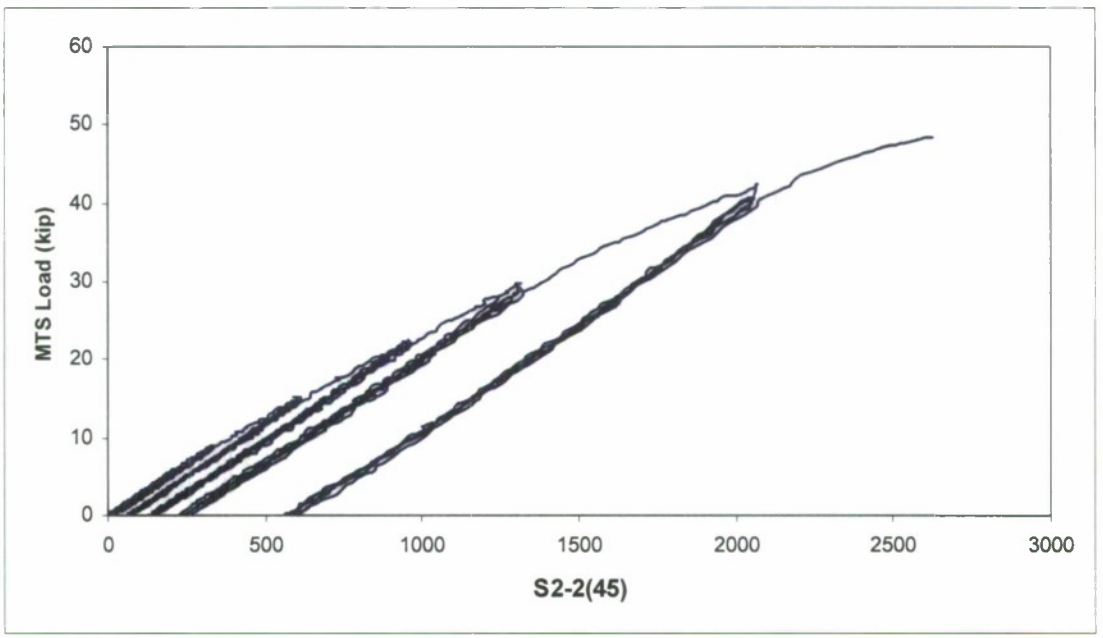

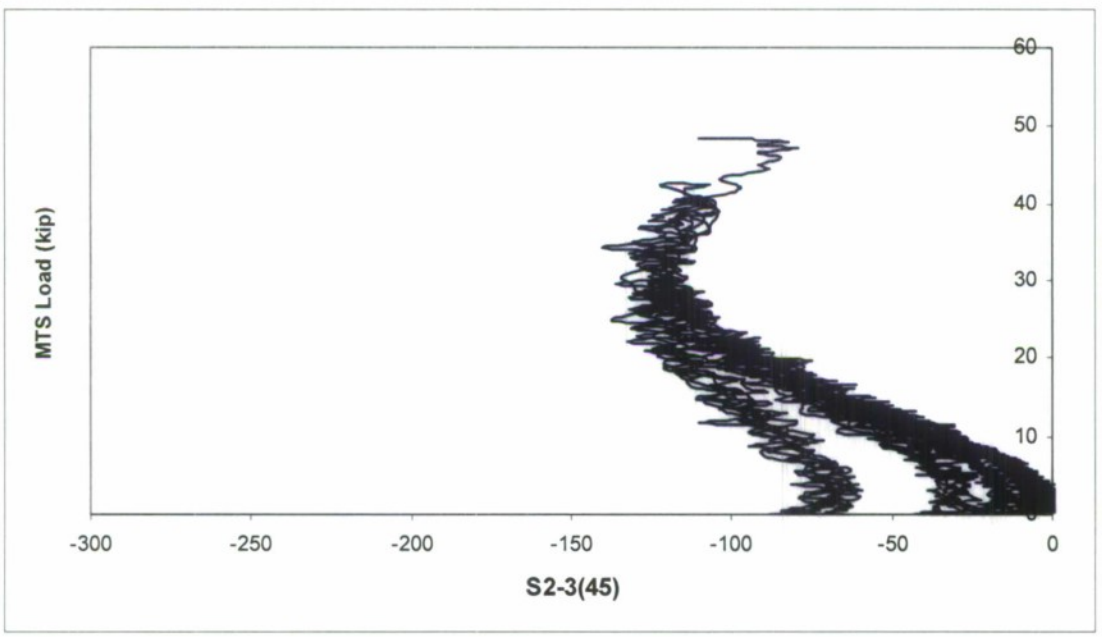

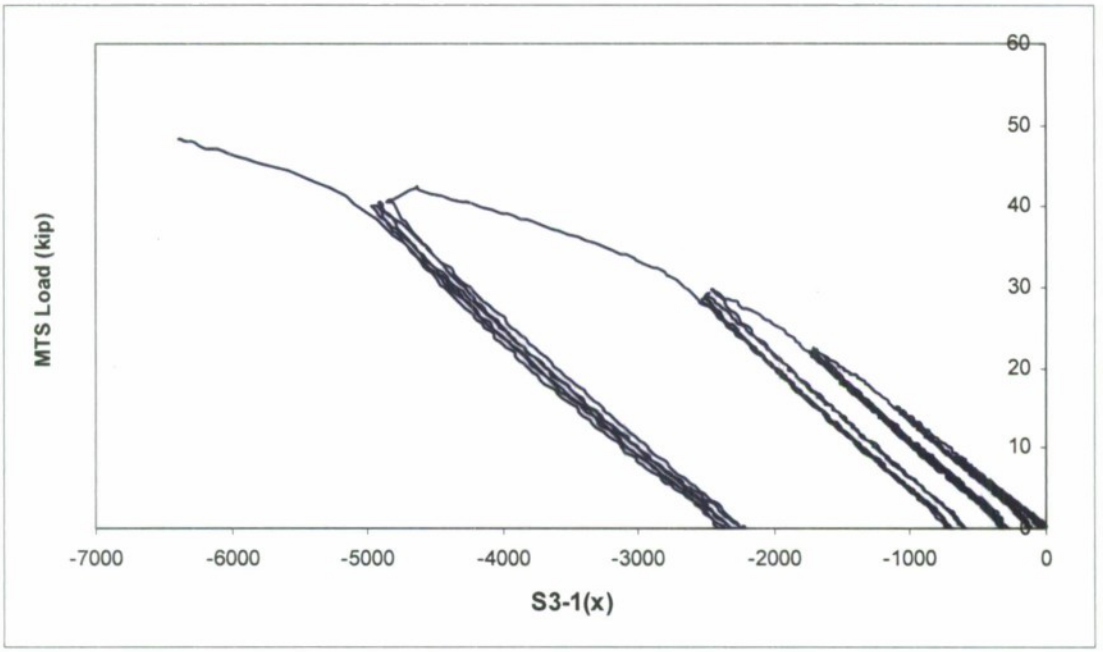
MTS Load (kip)
60
50
40
30
20
10
0
-7000
-6000
-5000
-4000
-3000
-2000
-1000
0
S3-1(x)

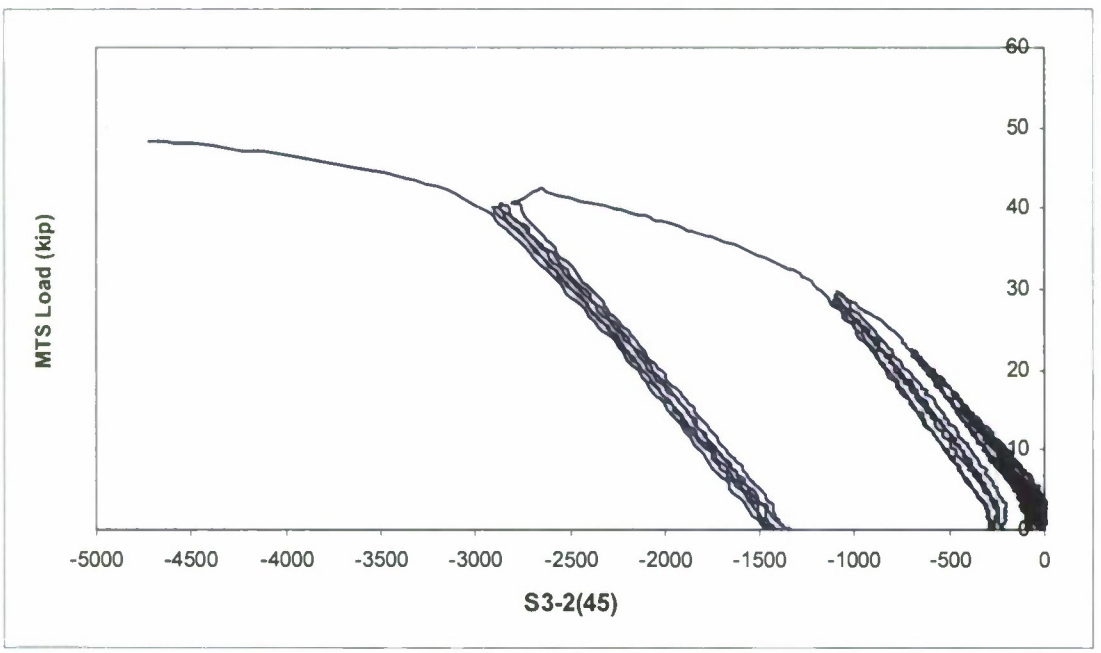
MTS Load (kip)
60
50
40
30
20
10
0
-5000
-4500
-4000
-3500
-3000
-2500
-2000
-1500
-1000
-500
0
S3-2(45)

Appendix E Continued

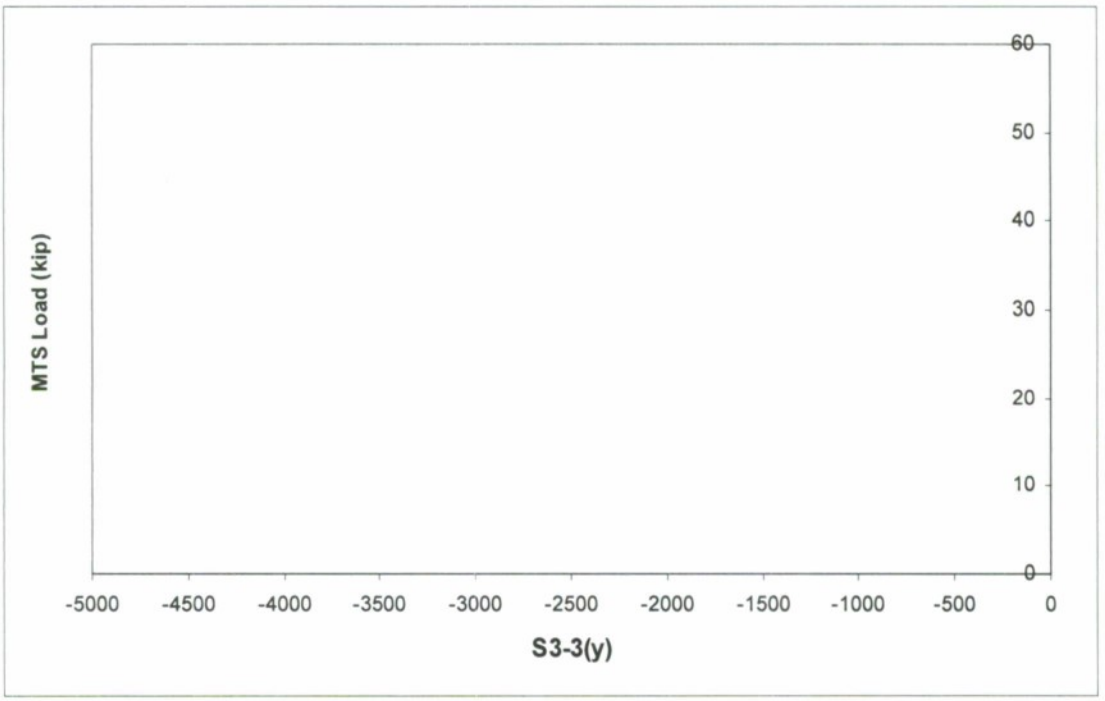

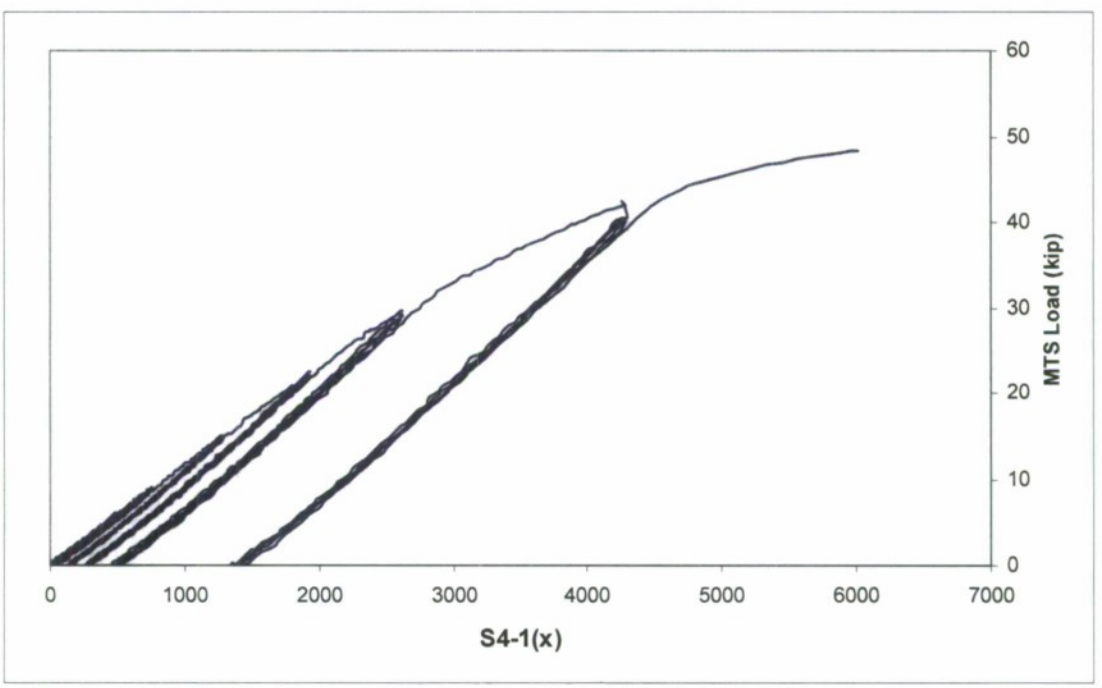

Appendix E Continued

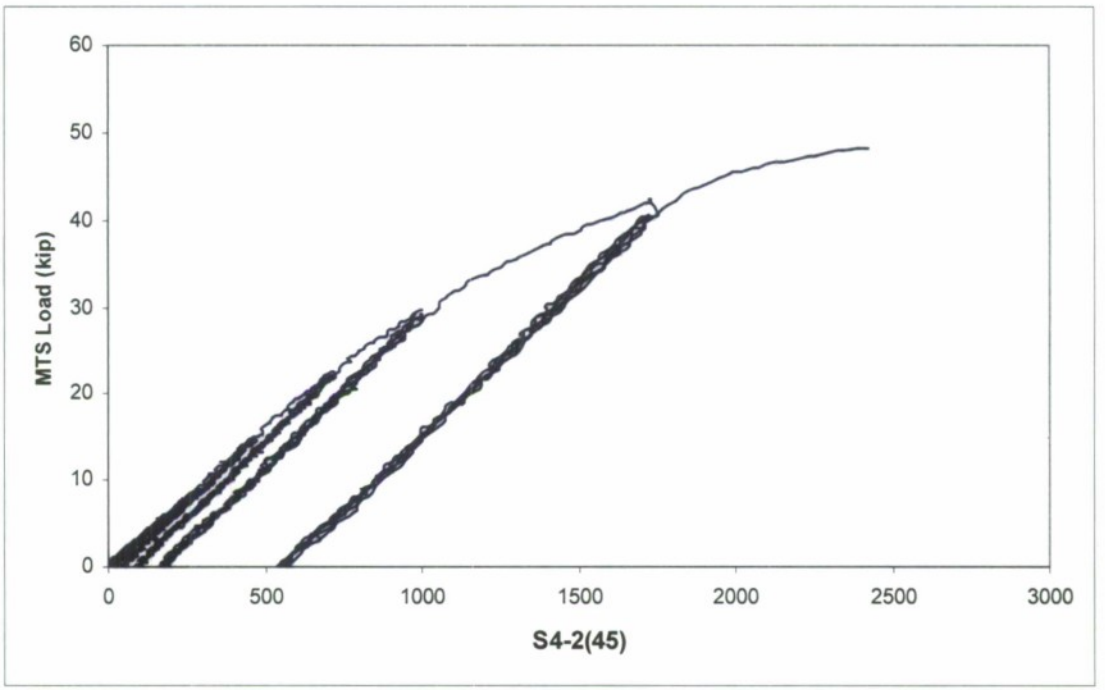

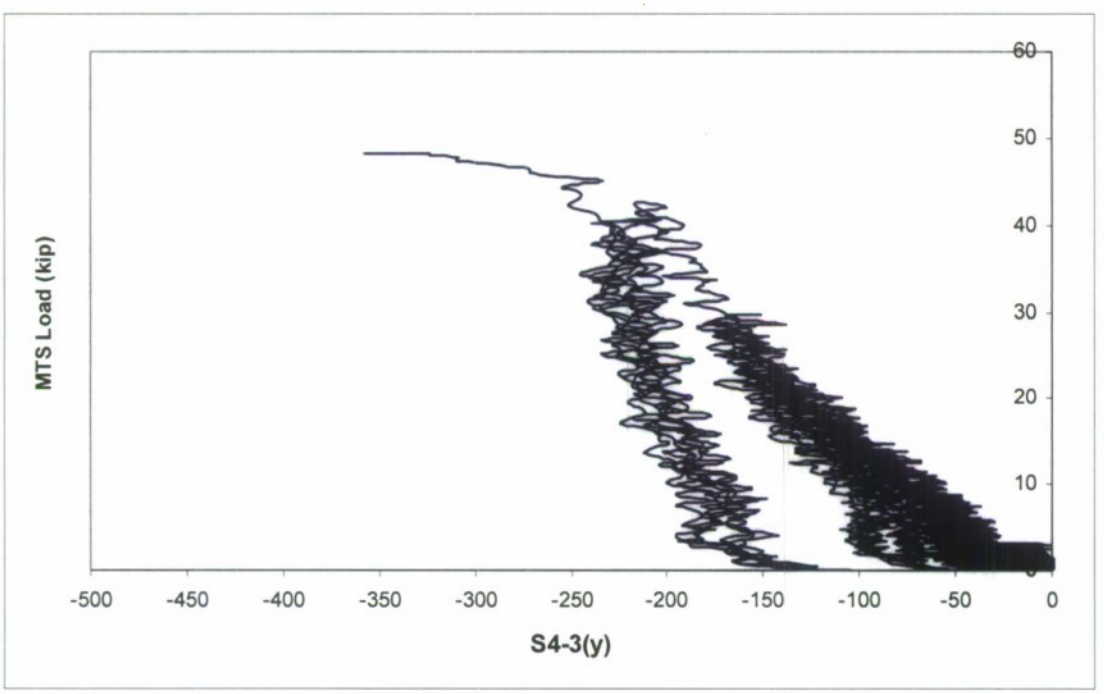

Appendix E Continued

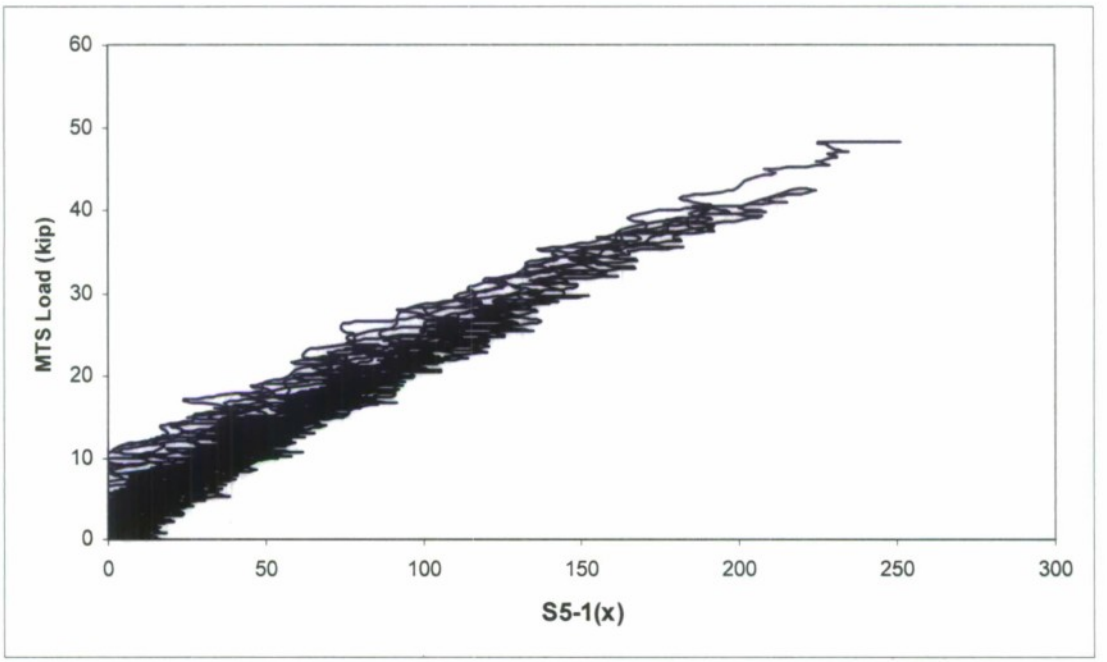

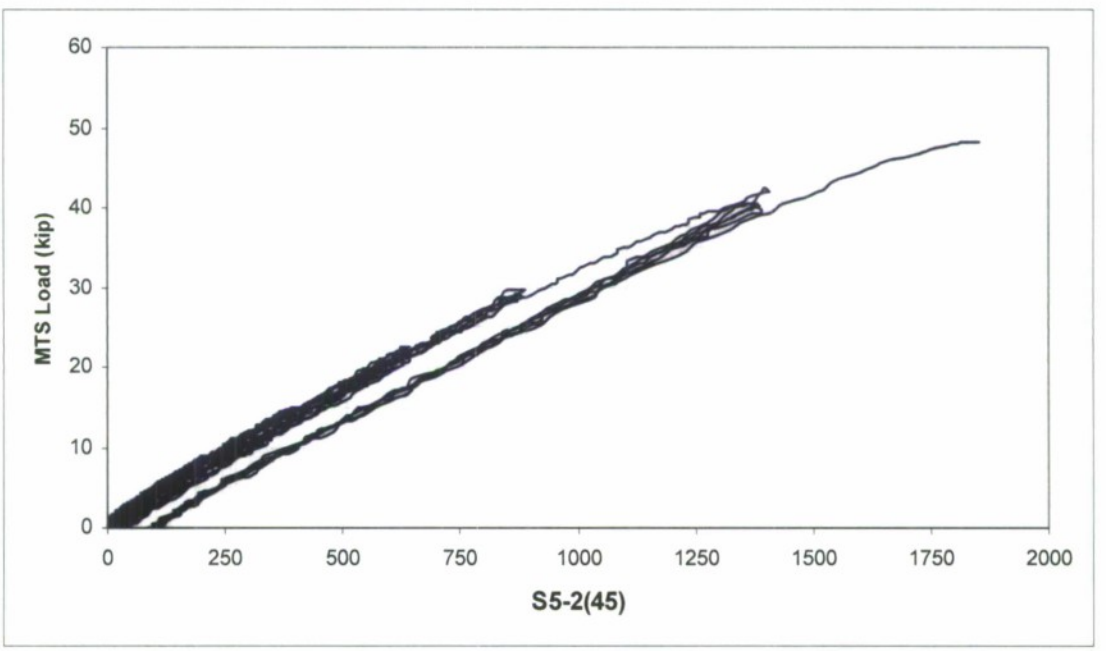

Appendix E Continued

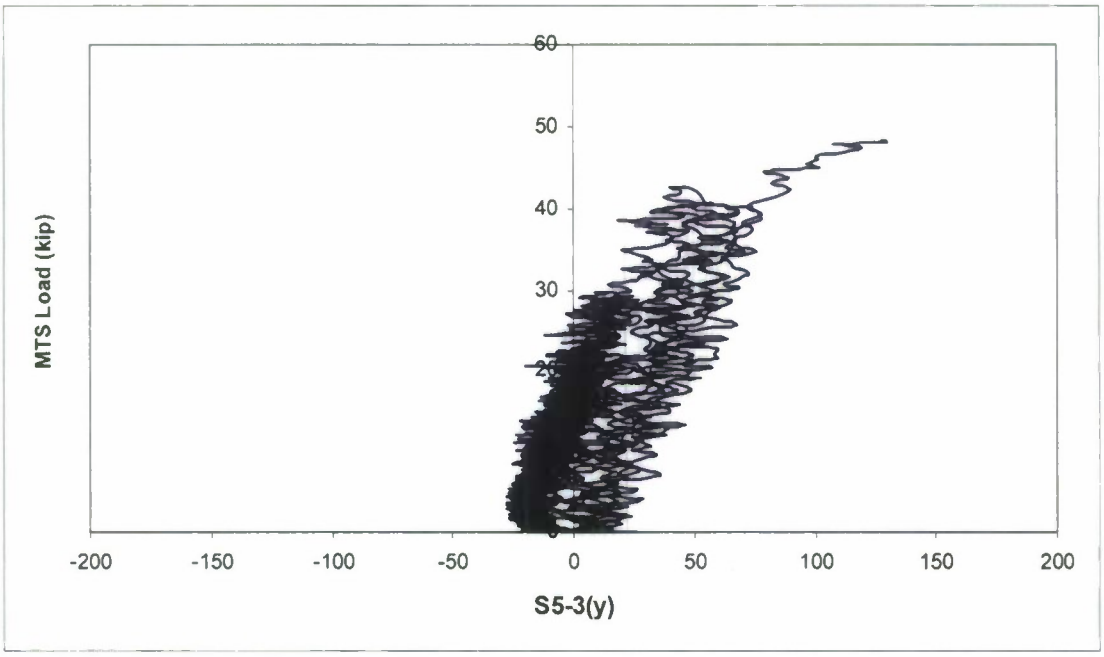

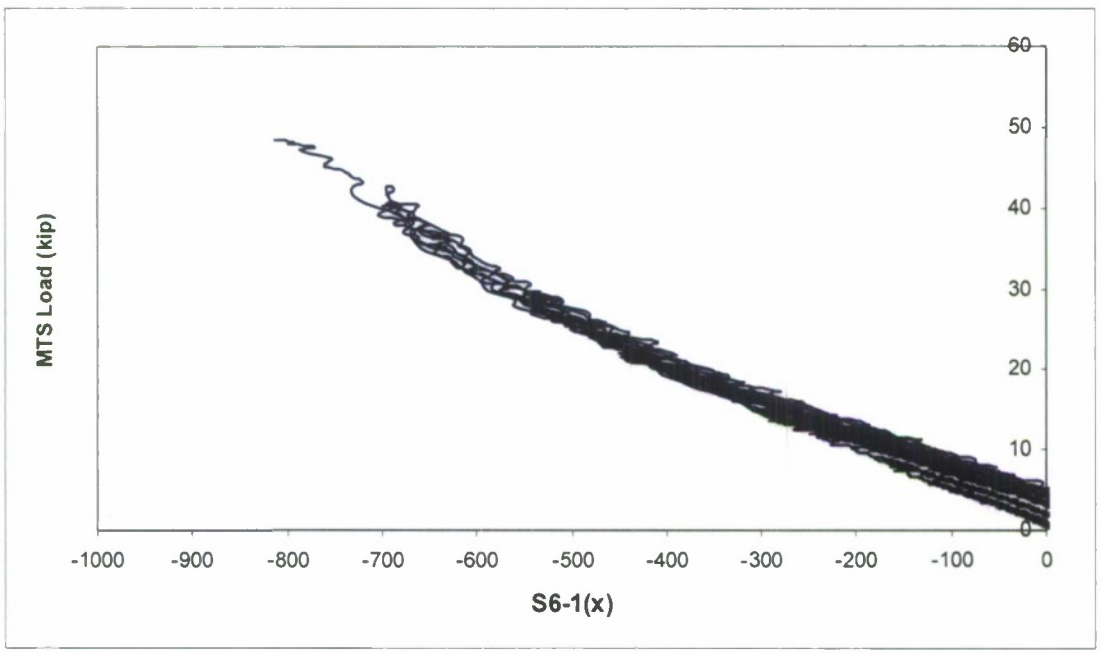

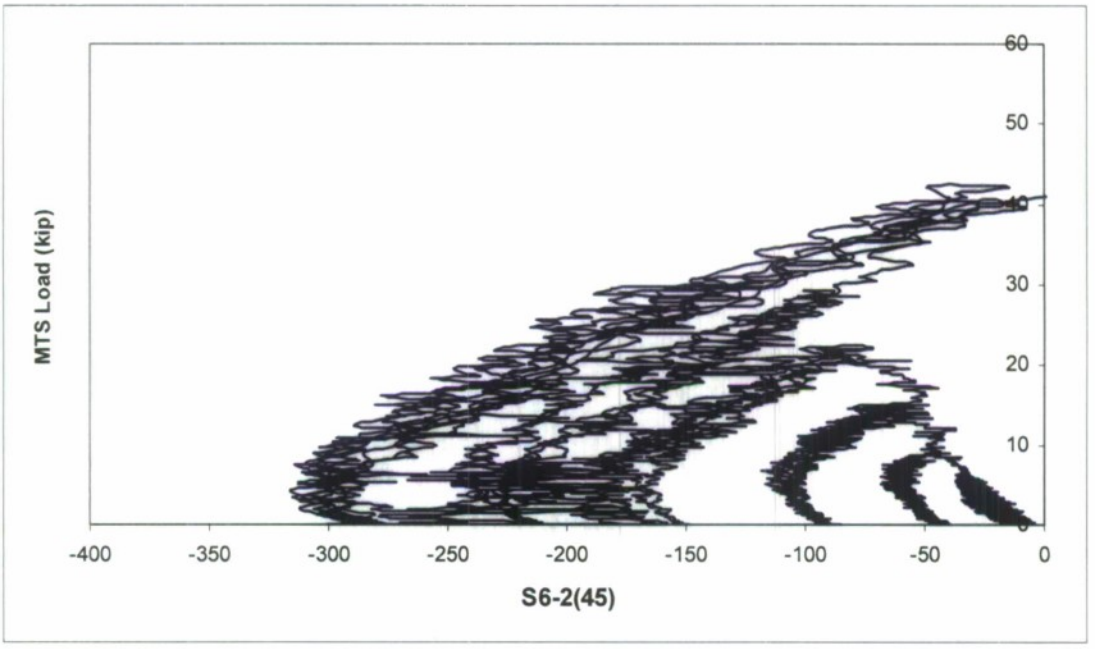
MTS Load (kip)
60
50
40
30
20
10
0
-400
-350
-300
-250
-200
-150
-100
-50
0
S6-2(45)

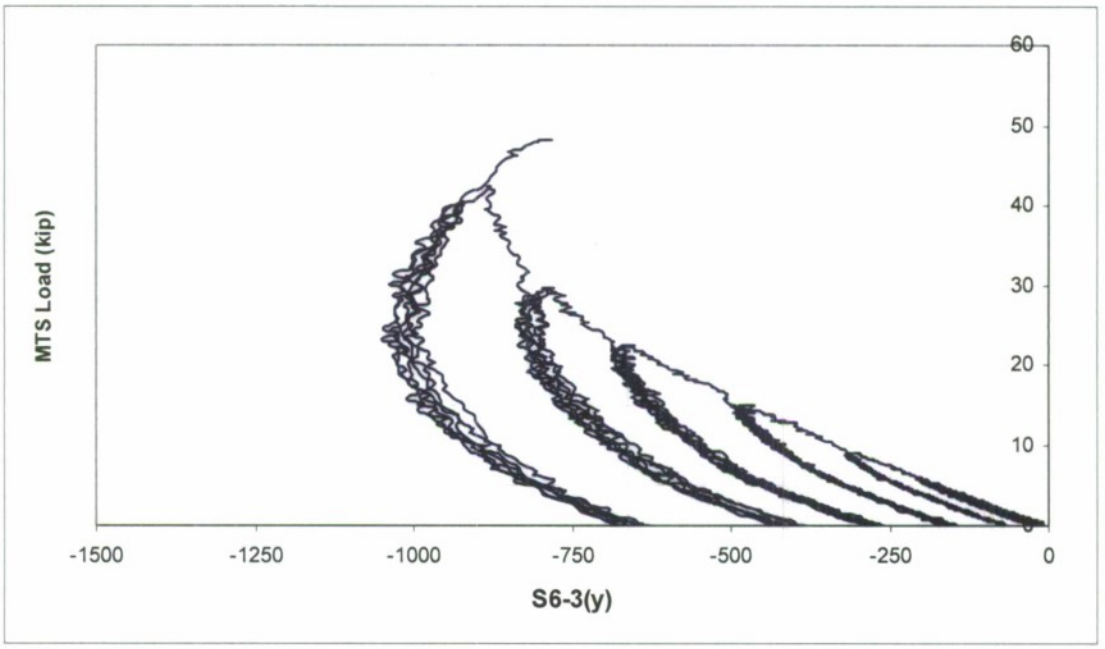
MTS Load (kip)
60
50
40
30
20
10
0
-1500
-1250
-1000
-750
-500
-250
0
S6-3(y)

APPENDIX F

Stress Strain Graps for Thick Panel

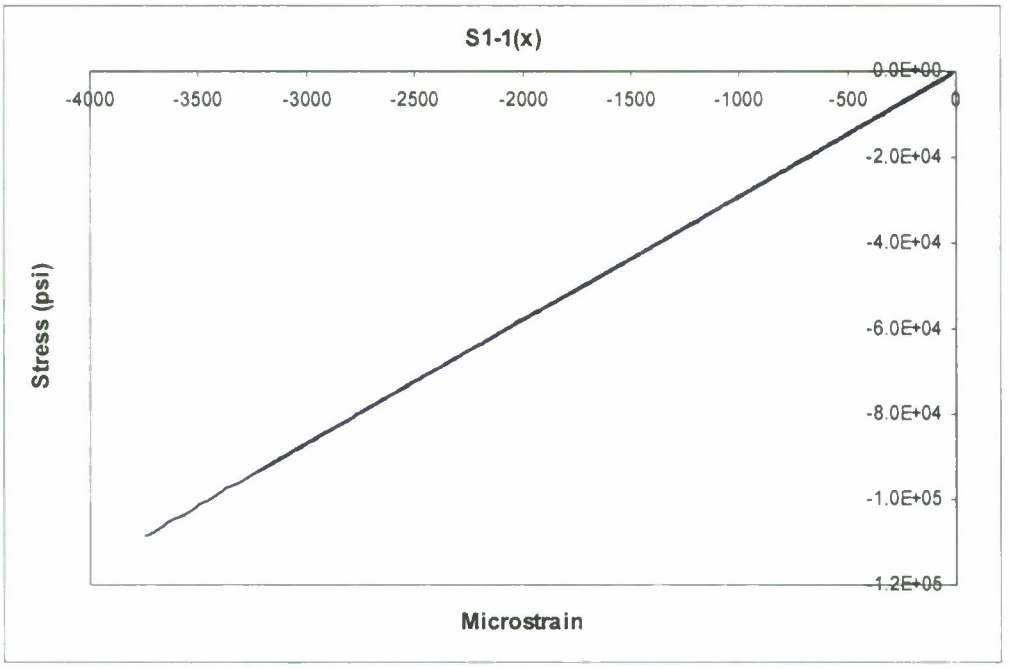

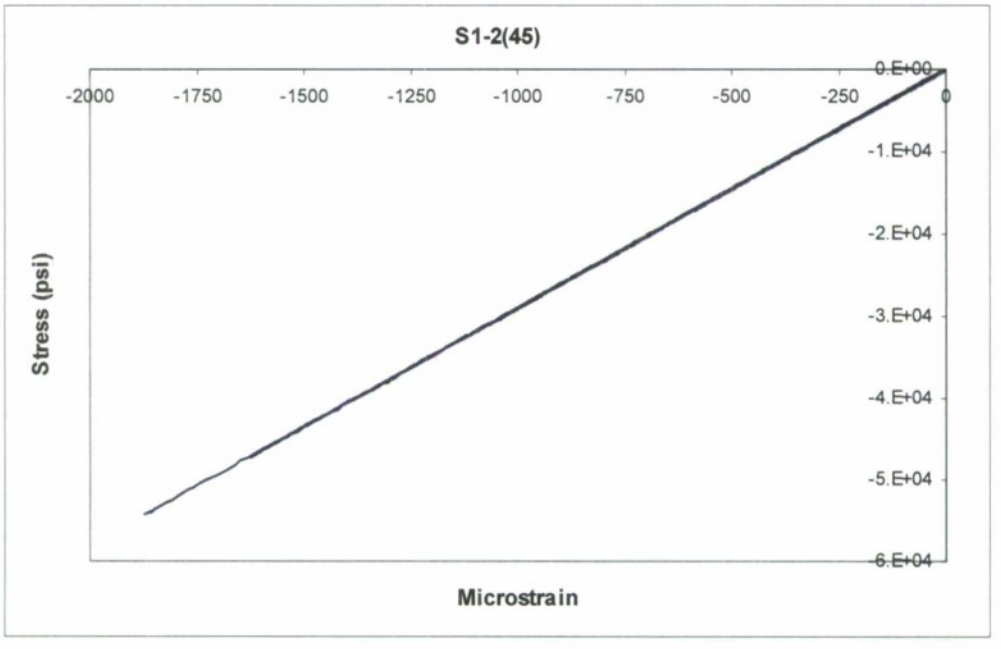

Appendix F Continued

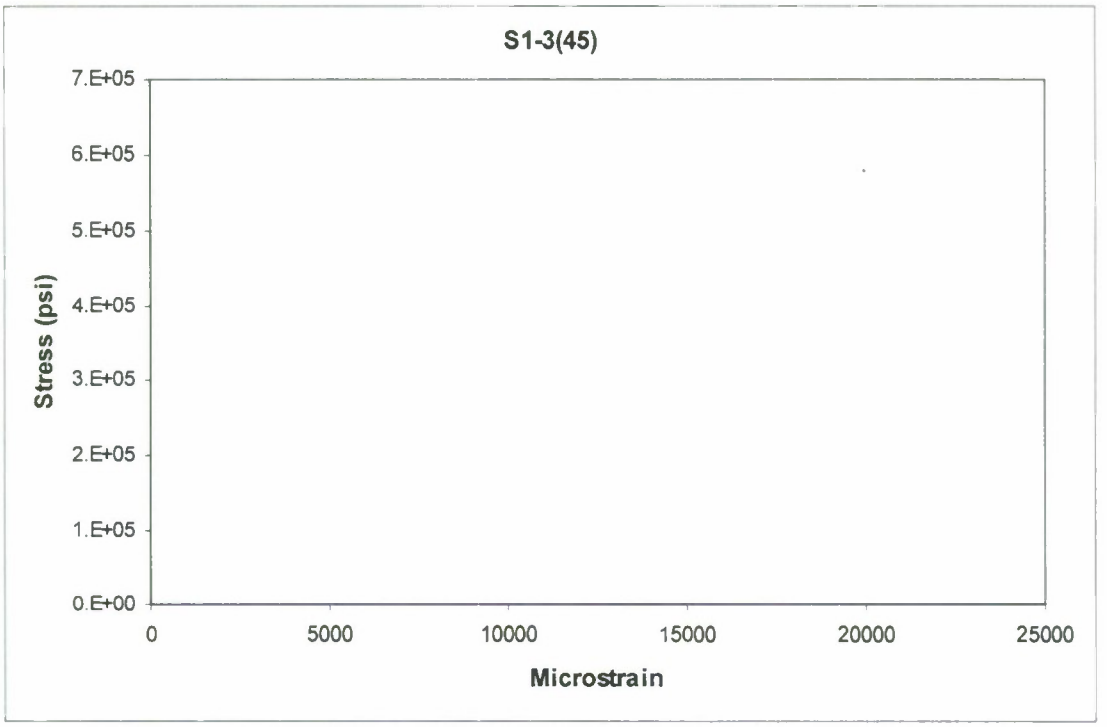

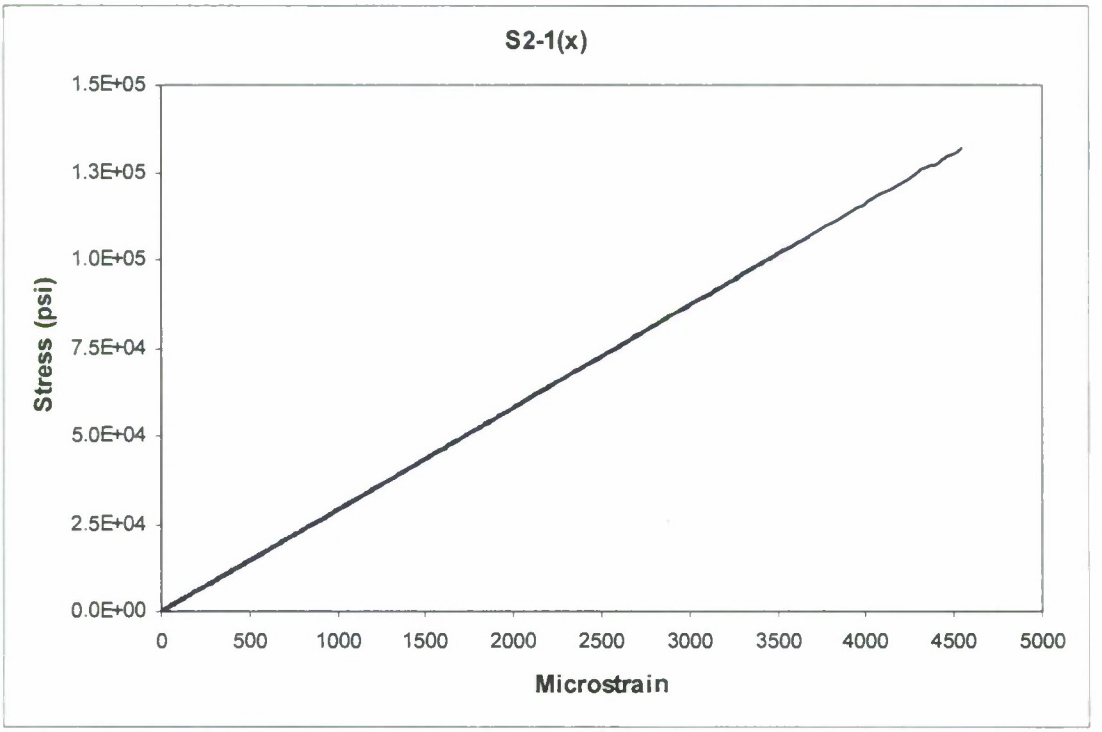

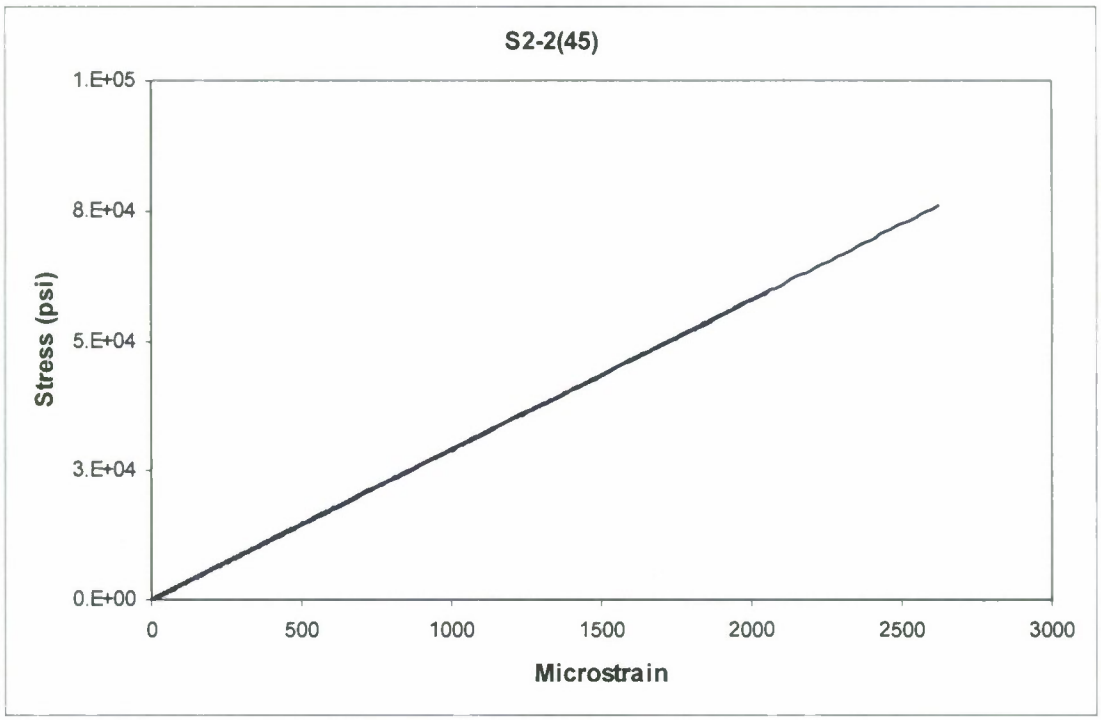
S2-2(45)
1.E+05
8.E+04
5.E+04
3.E+04
0.E+00
Stress (psi)
0
500
1000
1500
2000
2500
3000
Microstrain

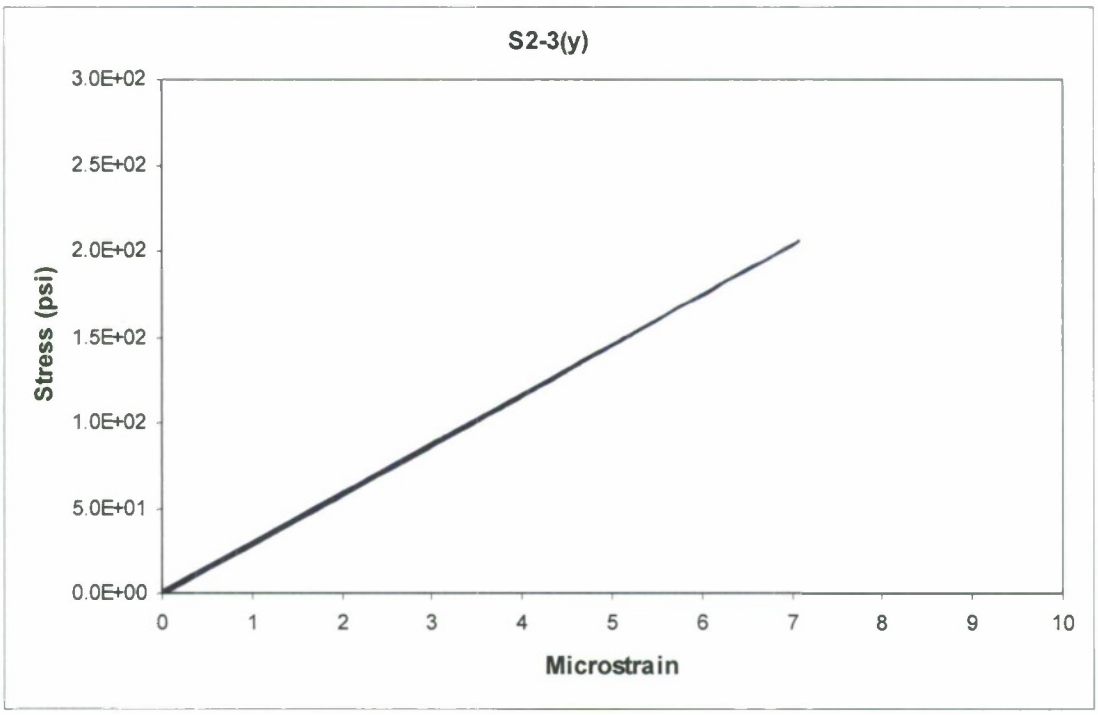
S2-3(y)
3.0E+02
2.5E+02
2.0E+02
1.5E+02
1.0E+02
5.0E+01
0.0E+00
Stress (psi)
0
1
2
3
4
5
6
7
8
9
10
Microstrain

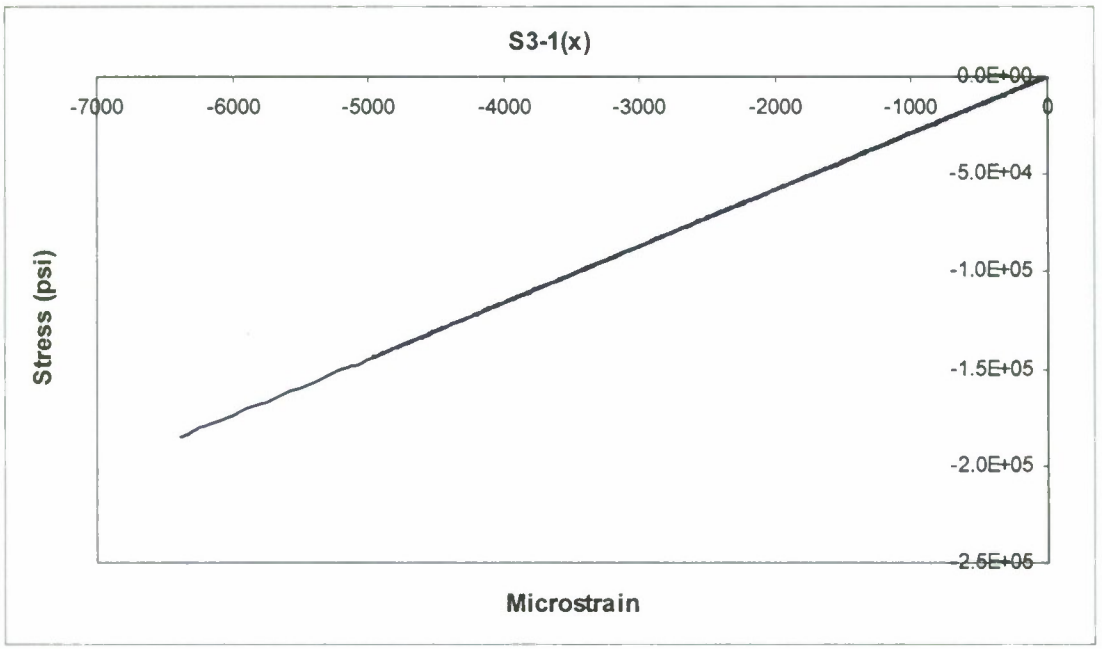
S3-1(x)
0.0E+00
-7000
-6000
-5000
-4000
-3000
-2000
-1000
0
-5.0E+04
-1.0E+05
-1.5E+05
-2.0E+05
-2.5E+05
Stress (psi)
Microstrain

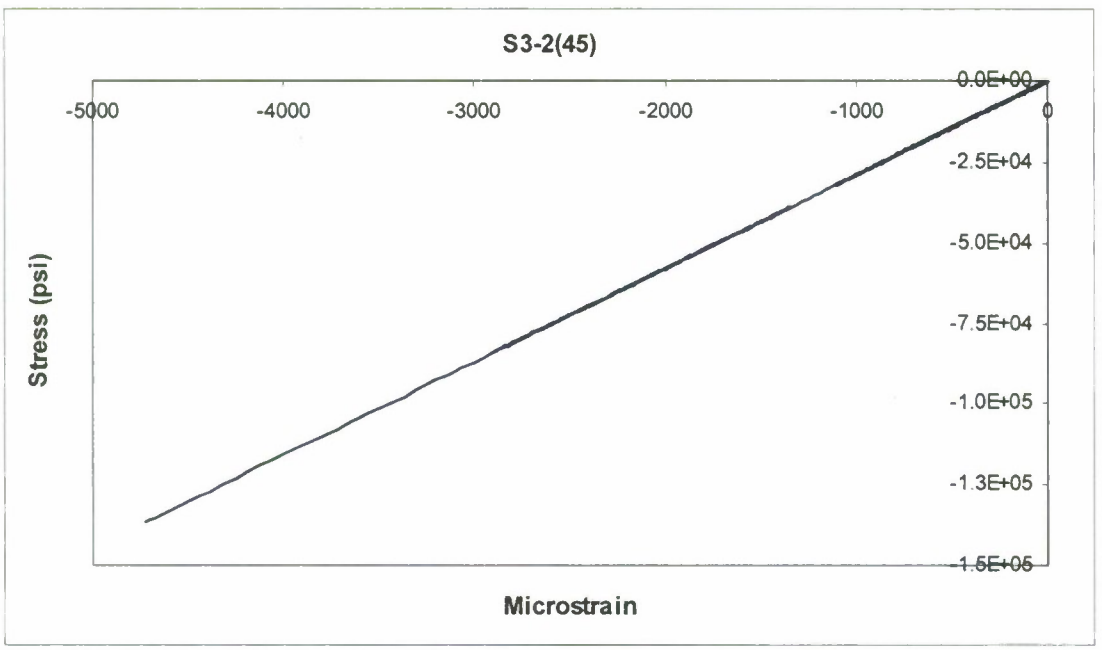
S3-2(45)
0.0E+00
-5000
-4000
-3000
-2000
-1000
0
-2.5E+04
-5.0E+04
-7.5E+04
-1.0E+05
-1.3E+05
-1.5E+05
Stress (psi)
Microstrain

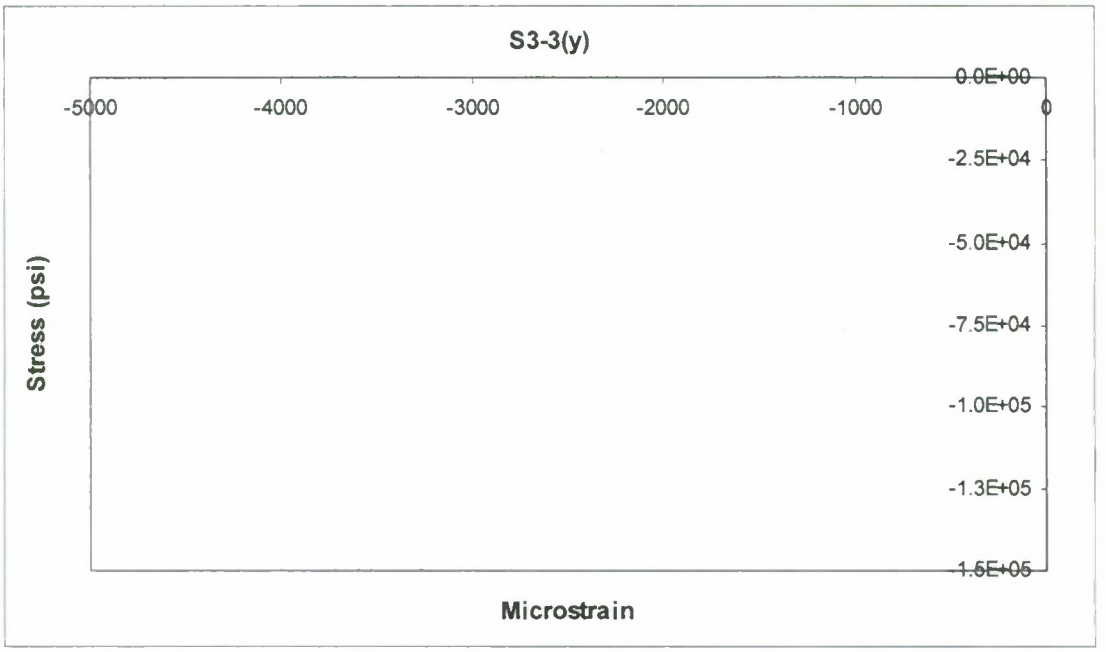
S3-3(y)
0.0E+00
-5000
-4000
-3000
-2000
-1000
0
-2.5E+04
-5.0E+04
-7.5E+04
-1.0E+05
-1.3E+05
-1.6E+05
Stress (psi)
Microstrain

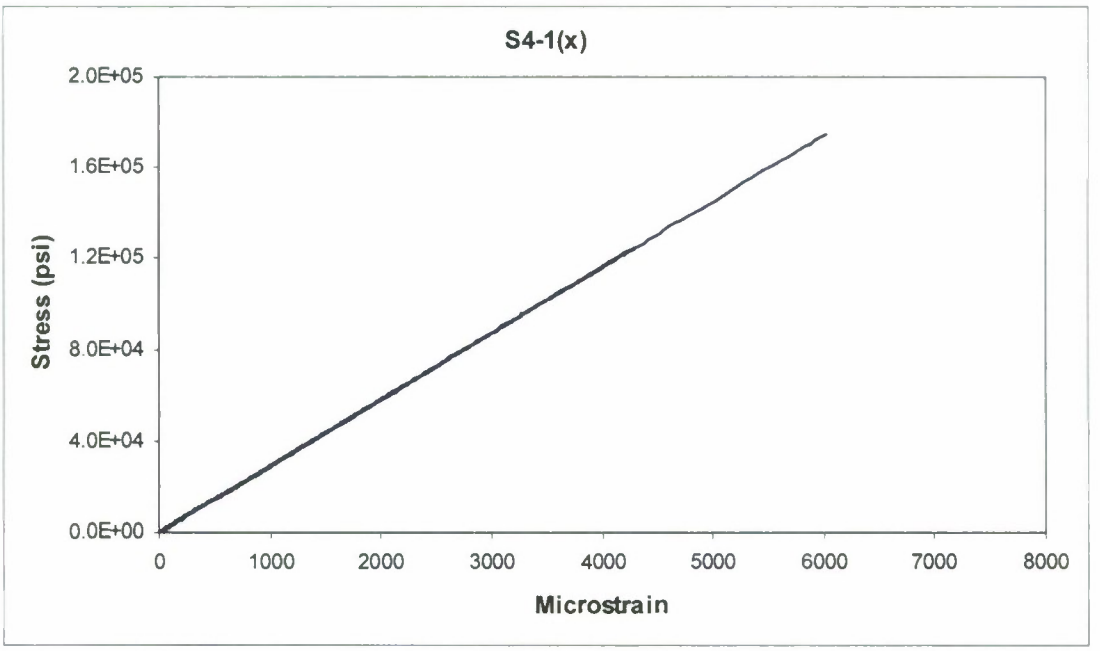
S4-1(x)
2.0E+05
1.6E+05
1.2E+05
8.0E+04
4.0E+04
0.0E+00
Stress (psi)
0
1000
2000
3000
4000
5000
6000
7000
8000
Microstrain

Appendix F Continued

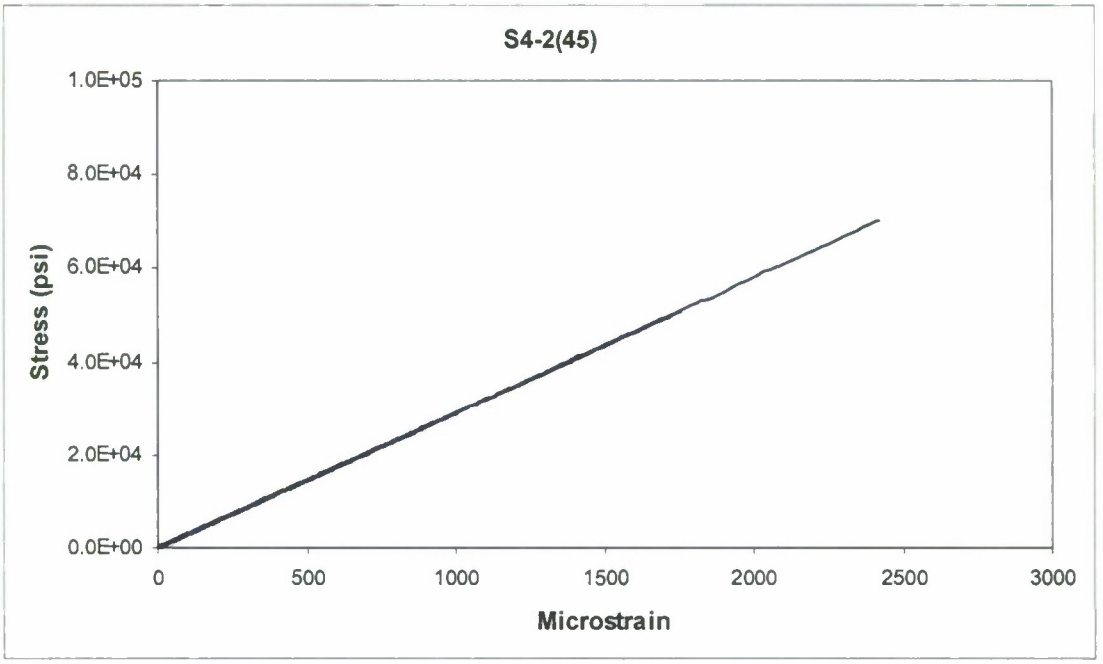

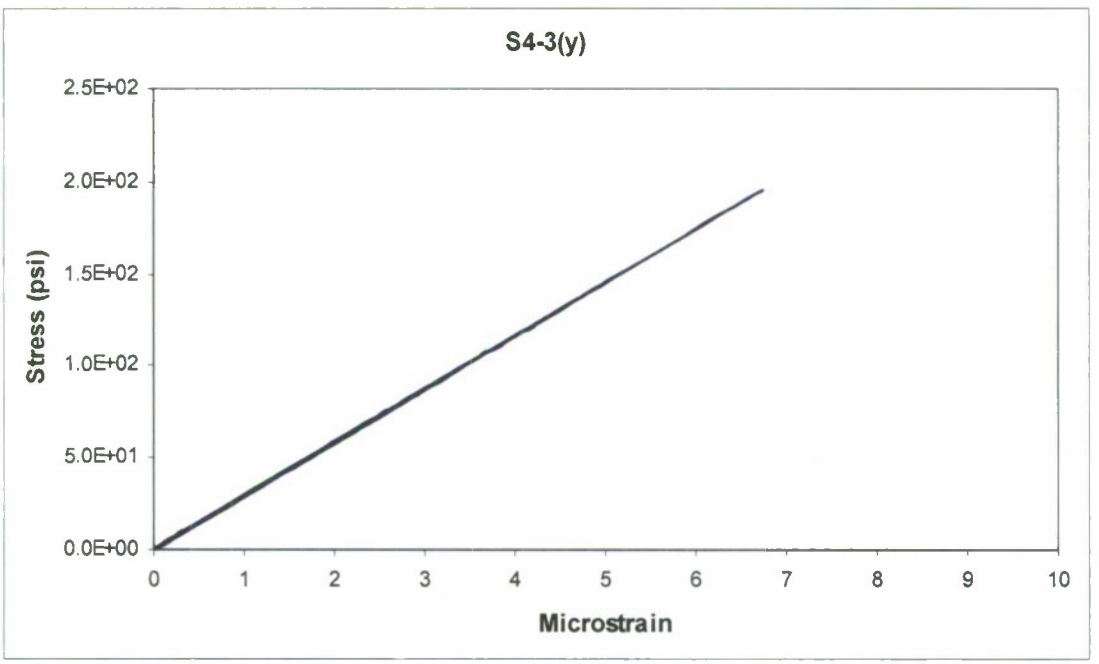

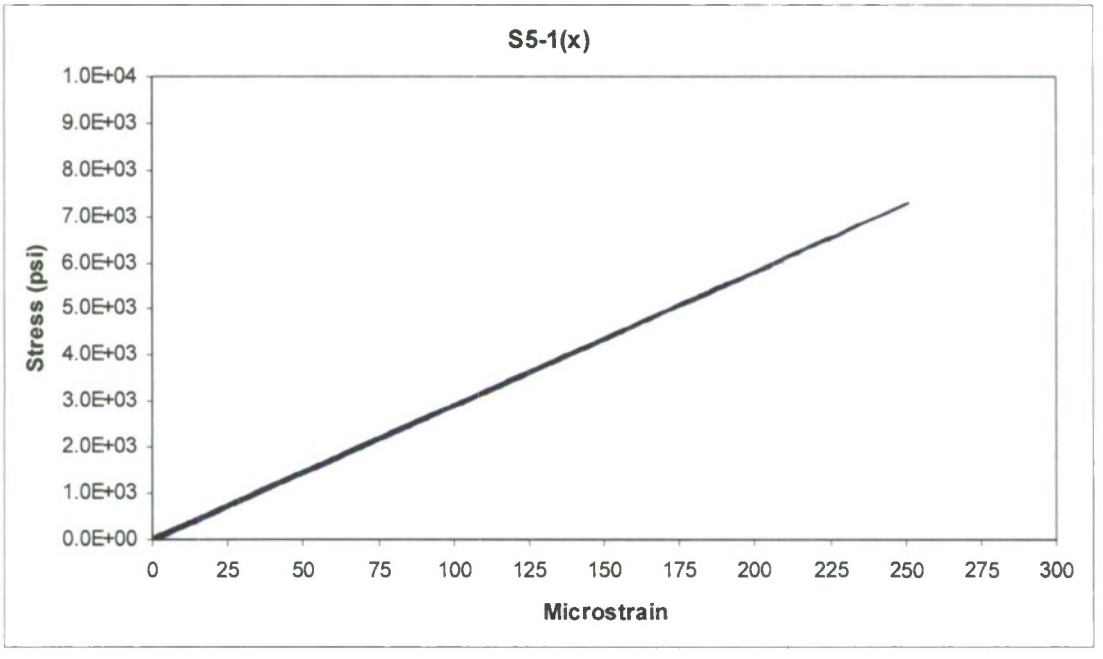
S5-1(x)
Stress (psi)
1.0E+04
9.0E+03
8.0E+03
7.0E+03
6.0E+03
5.0E+03
4.0E+03
3.0E+03
2.0E+03
1.0E+03
0.0E+00
0
25
50
75
100
125
150
175
200
225
250
275
300
Microstrain

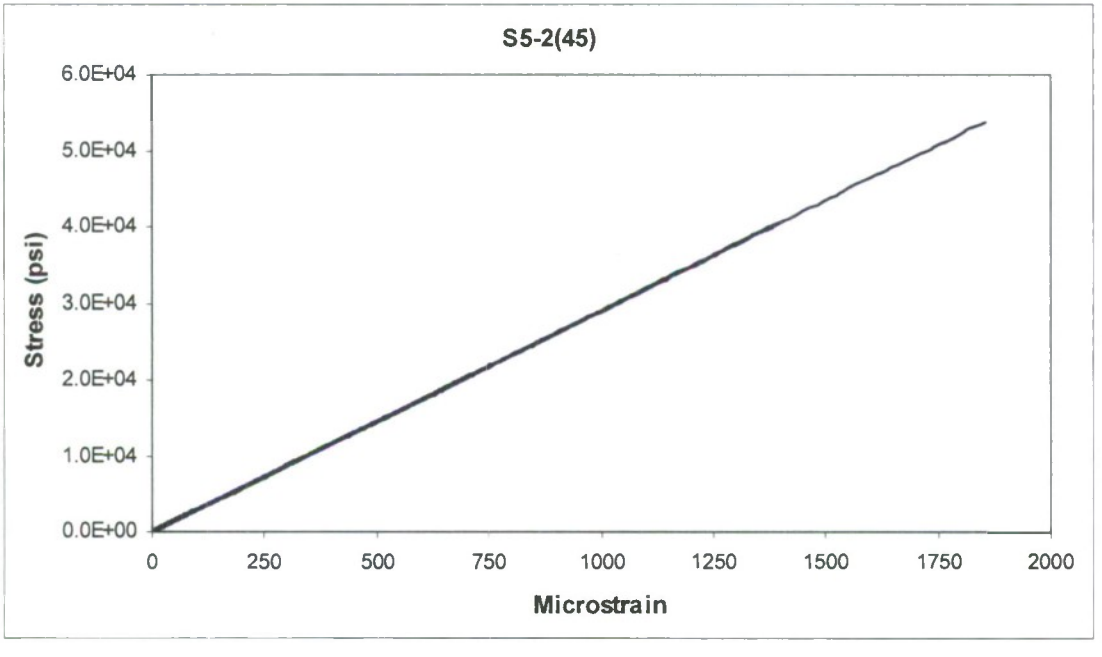
S5-2(45)
Stress (psi)
6.0E+04
5.0E+04
4.0E+04
3.0E+04
2.0E+04
1.0E+04
0.0E+00
0
250
500
750
1000
1250
1500
1750
2000
Microstrain

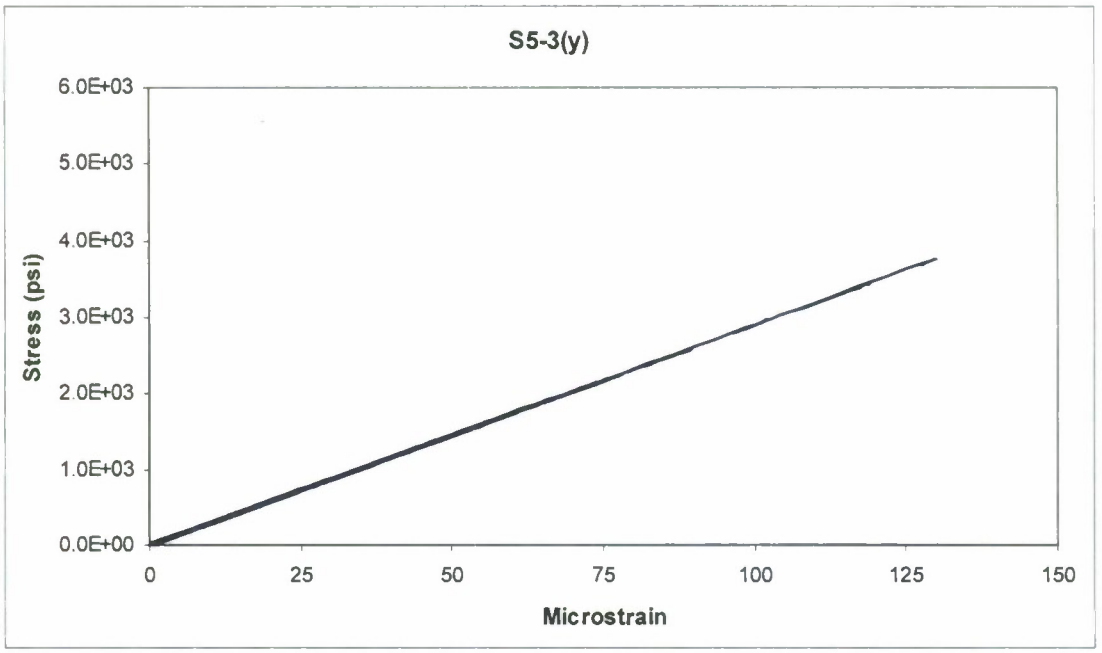
S5-3(y)
6.0E+03
5.0E+03
4.0E+03
3.0E+03
2.0E+03
1.0E+03
0.0E+00
Stress (psi)
0
25
50
75
100
125
150
Microstrain

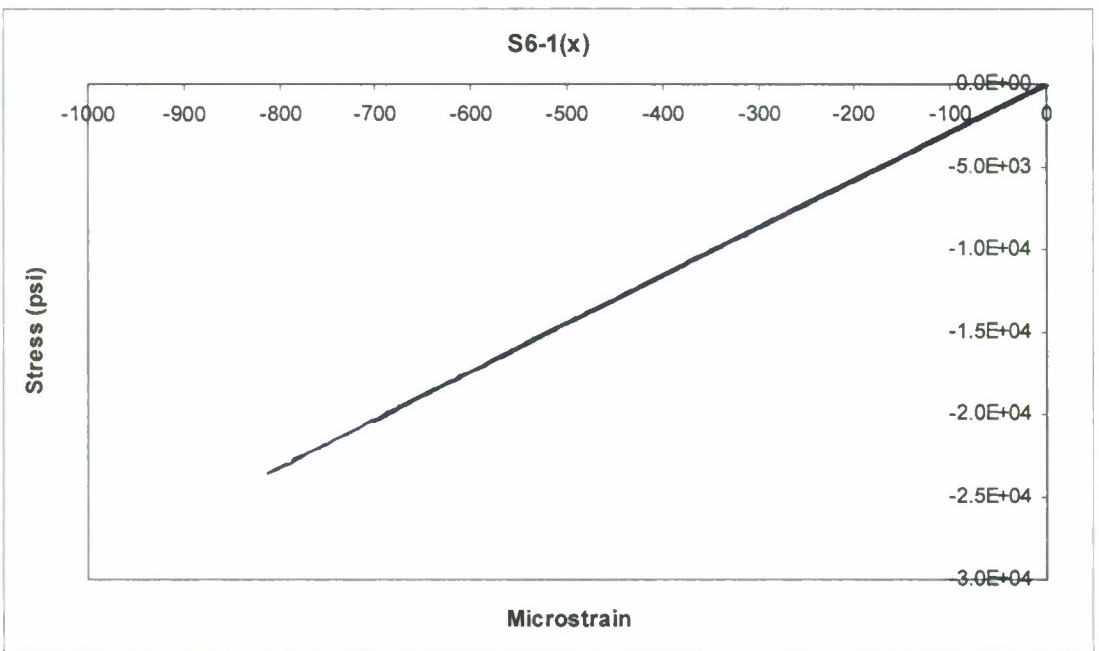
S6-1(x)
-1000
-900
-800
-700
-600
-500
-400
-300
-200
-100
0
0.0E+00
-5.0E+03
-1.0E+04
-1.5E+04
-2.0E+04
-2.5E+04
-3.0E+04
Stress (psi)
Microstrain

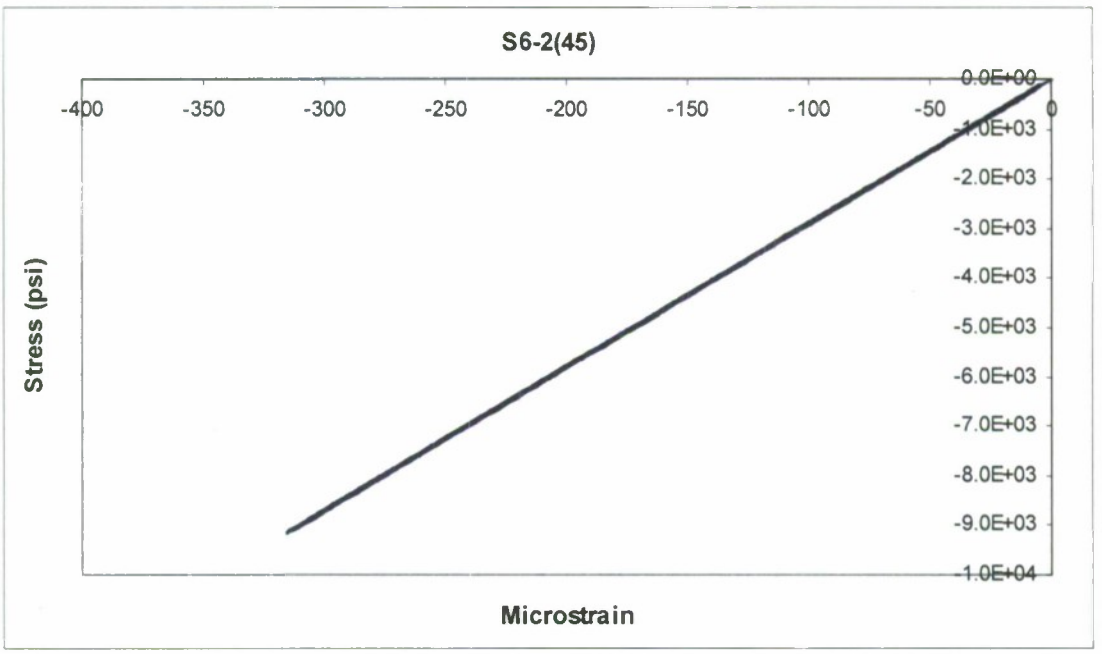
S6-2(45)
0.0E+00
-400
-350
-300
-250
-200
-150
-100
-50
0
-1.0E+03
-2.0E+03
-3.0E+03
-4.0E+03
-5.0E+03
-6.0E+03
-7.0E+03
-8.0E+03
-9.0E+03
-1.0E+04
Stress (psi)
Microstrain

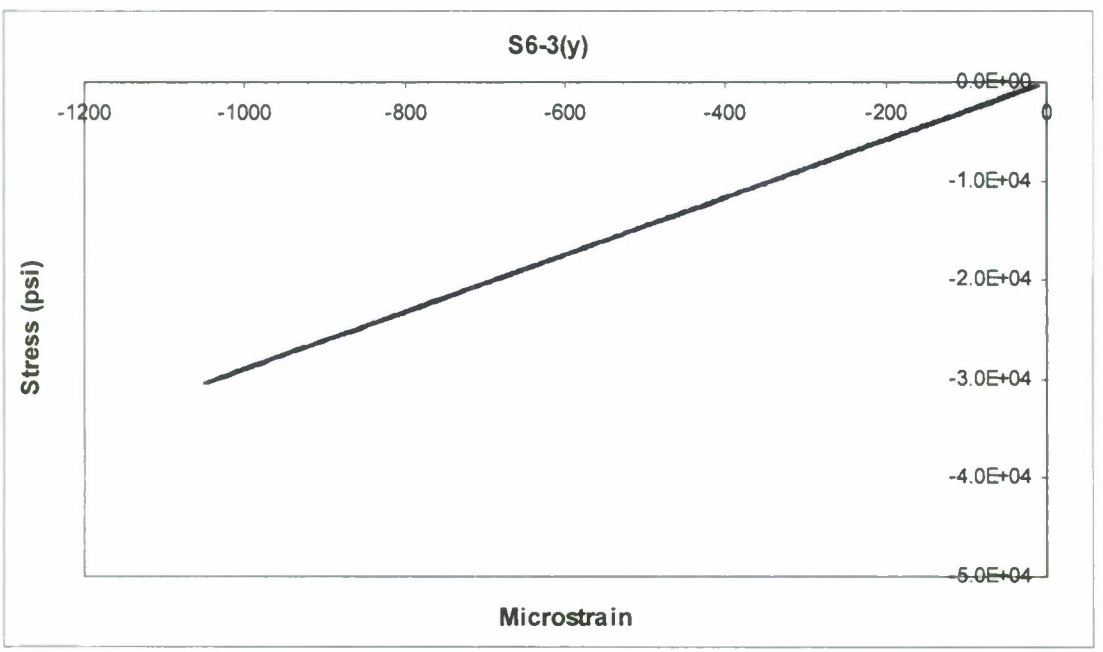
S6-3(y)
0.0E+00
-1200
-1000
-800
-600
-400
-200
0
-1.0E+04
-2.0E+04
-3.0E+04
-4.0E+04
-5.0E+04
Stress (psi)
Microstrain

APPENDIX G

Instrumentation Calibration Factors for Thin Panel

LDVT	Cal Factor
A-1	2.07E-01
B-1	4.76E-02
B-2	2.07E-01
B-3	1.05E-01
C-1	-1.03E-01
C-2	1.05E-01
C-3	1.05E-01
D-1	9.94E-02
D-2	1.04E-01
D-3	5.18E-02
E-1	-1.99E+03

Strain Gage	Cal Factor	Strain Gage	Cal Factor
S1-1	-2.00E+03	S4-1	-2.00E+03
S1-2	-2.01E+03	S4-2	-2.03E+03
S1-3	-2.01E+03	S4-3	-2.00E+03
S2-1	-2.01E+03	S5-1	-2.00E+03
S2-2	-2.00E+03	S5-2	-2.01E+03
S2-3	-2.01E+03	S5-3	-2.00E+03
S3-1	-2.01E+03	S6-1	-2.01E+03
S3-2	-2.02E+03	S6-2	-1.99E+03
S3-3	-1.99E+03	S6-3	0.00E+00

Modulus of Elasticity	2.90E+07 psi

APPENDIX H

Thin Panel Displacements at LVDT Locations

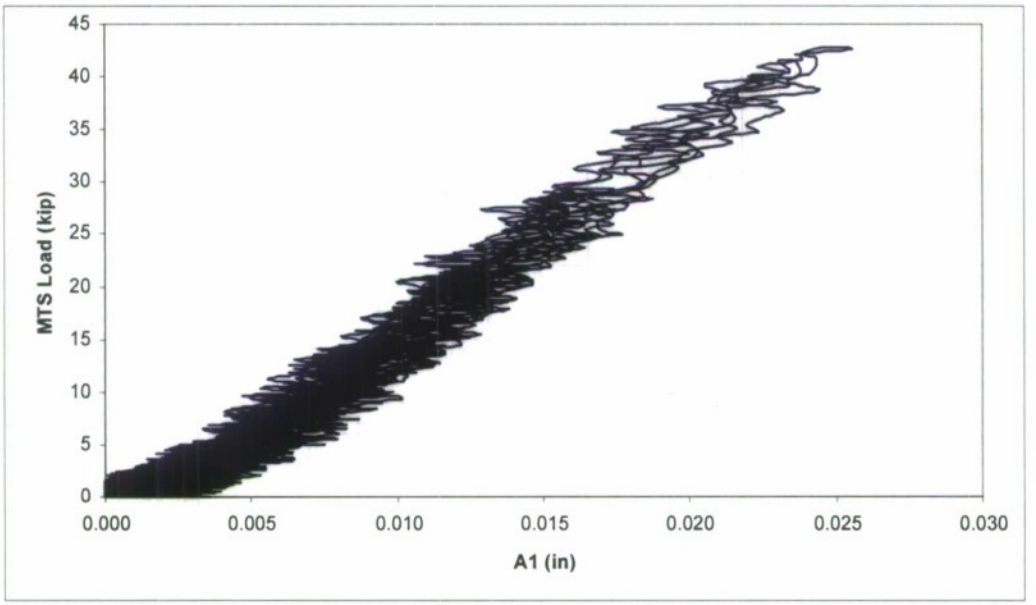

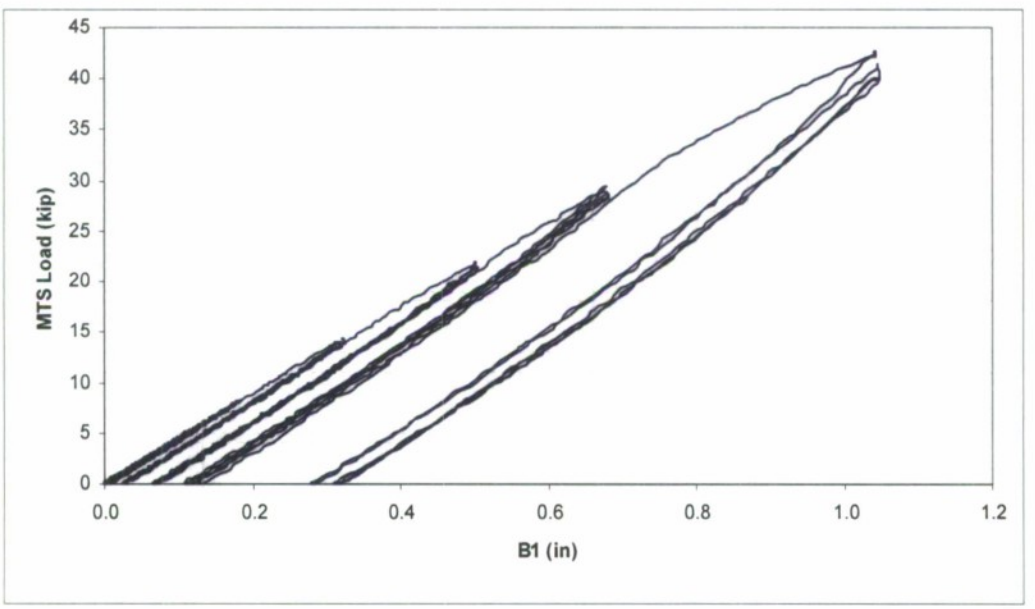

Appendix H Continued

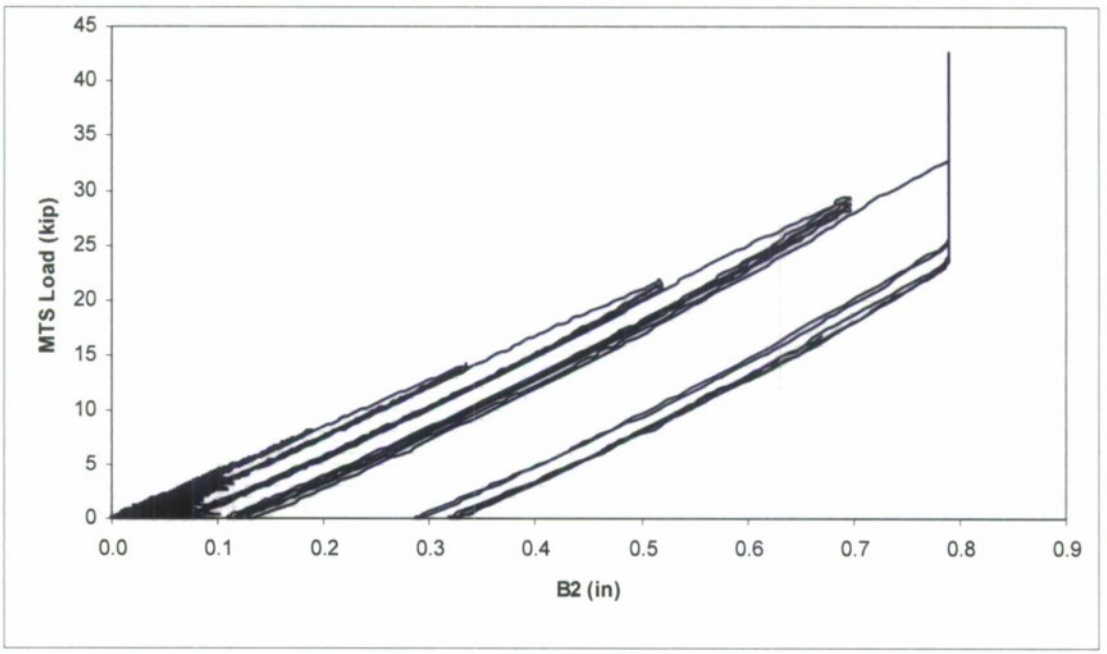

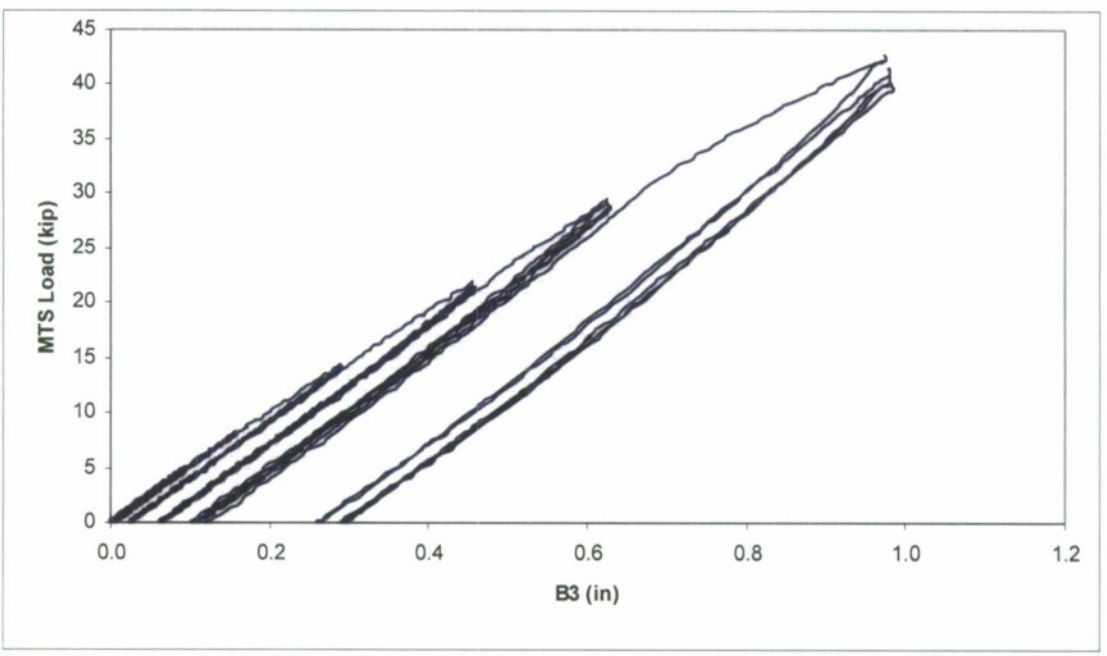

Appendix H Continued

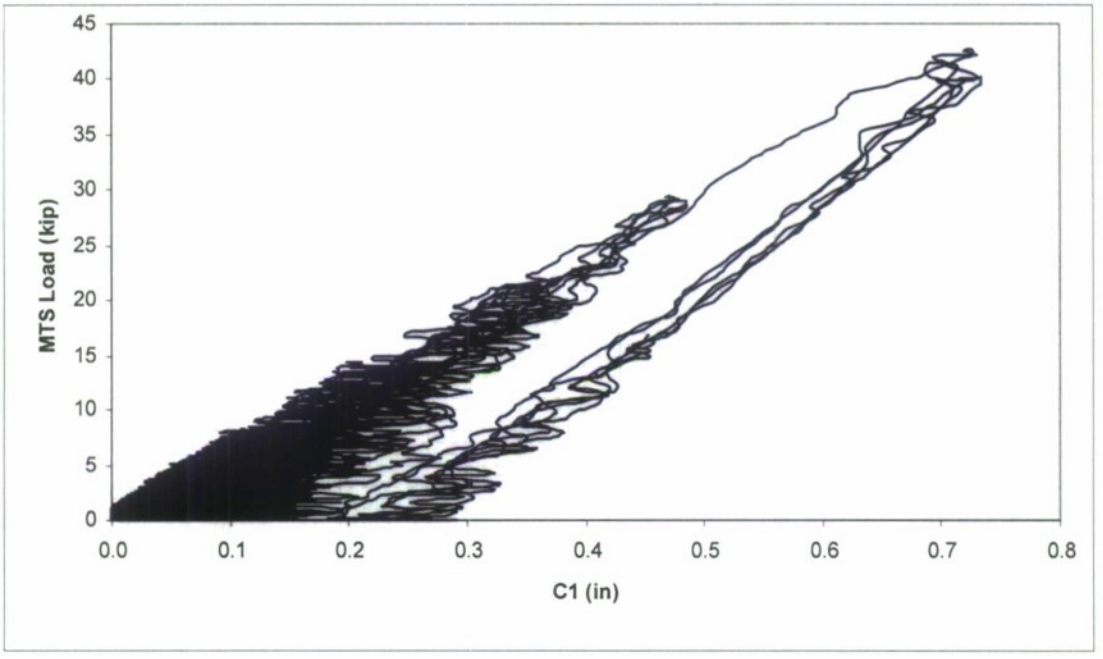

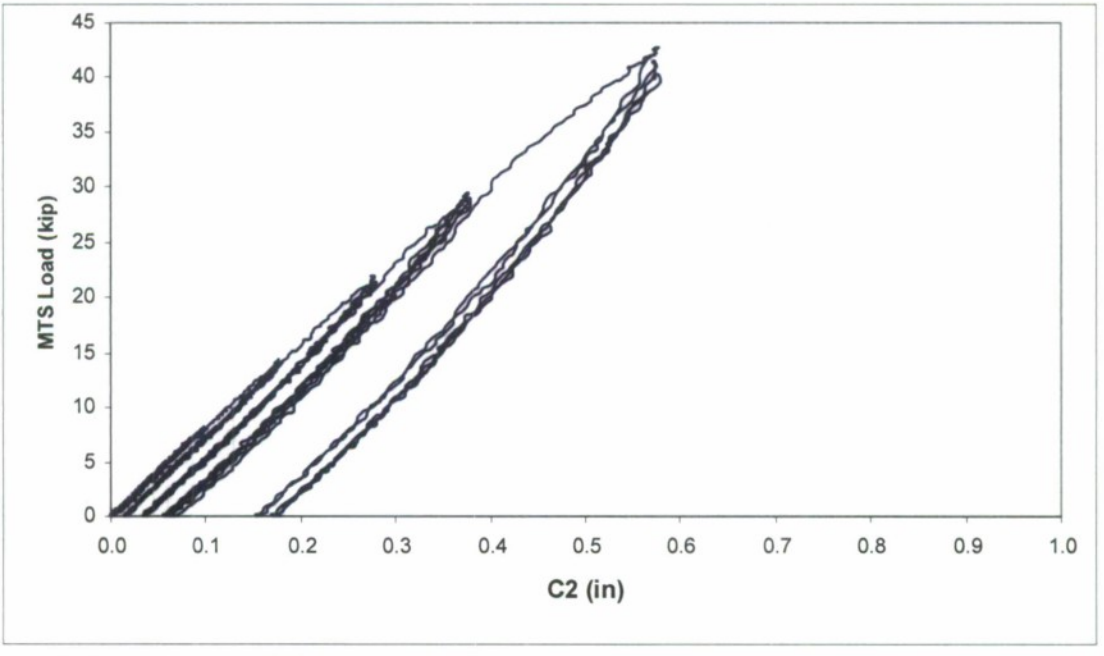

Appendix H Continued

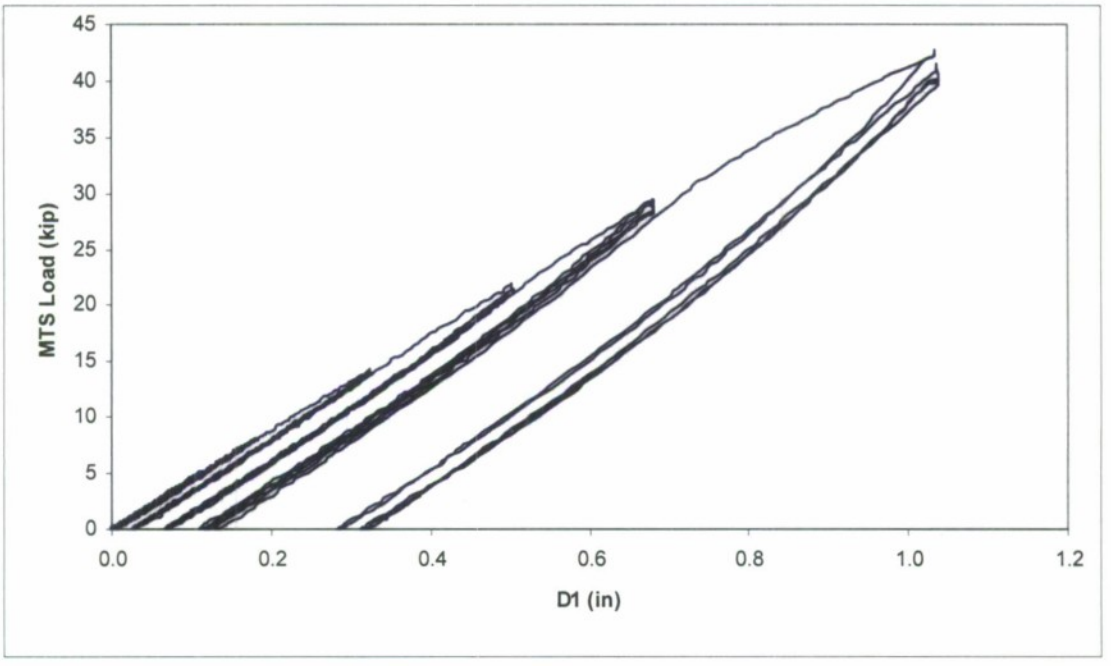

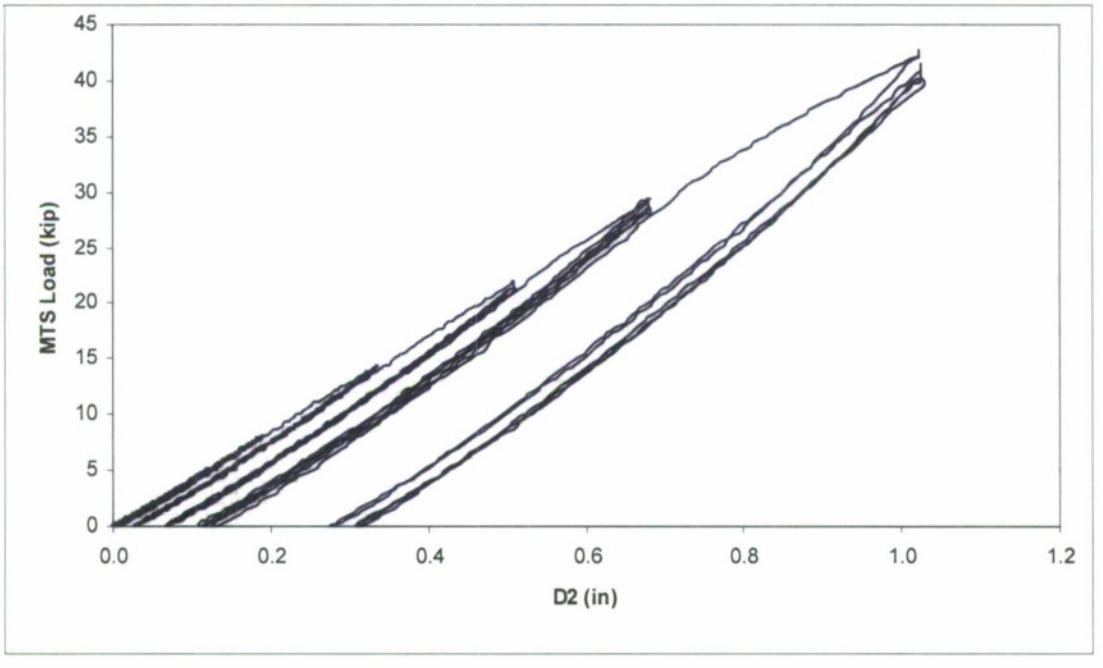

Appendix H Continued

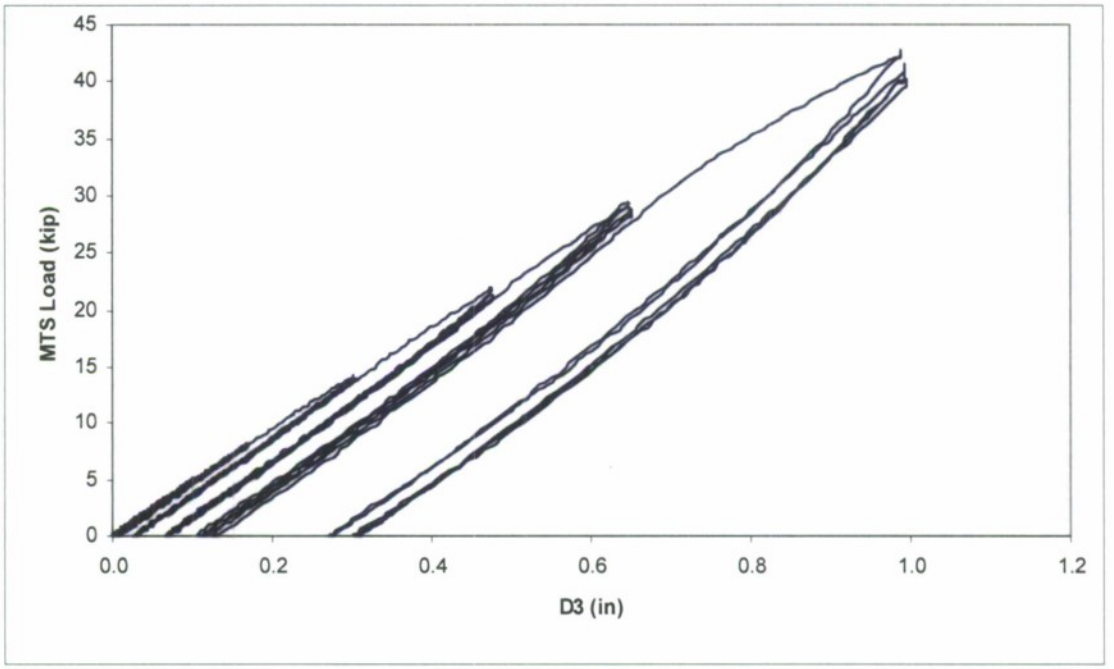

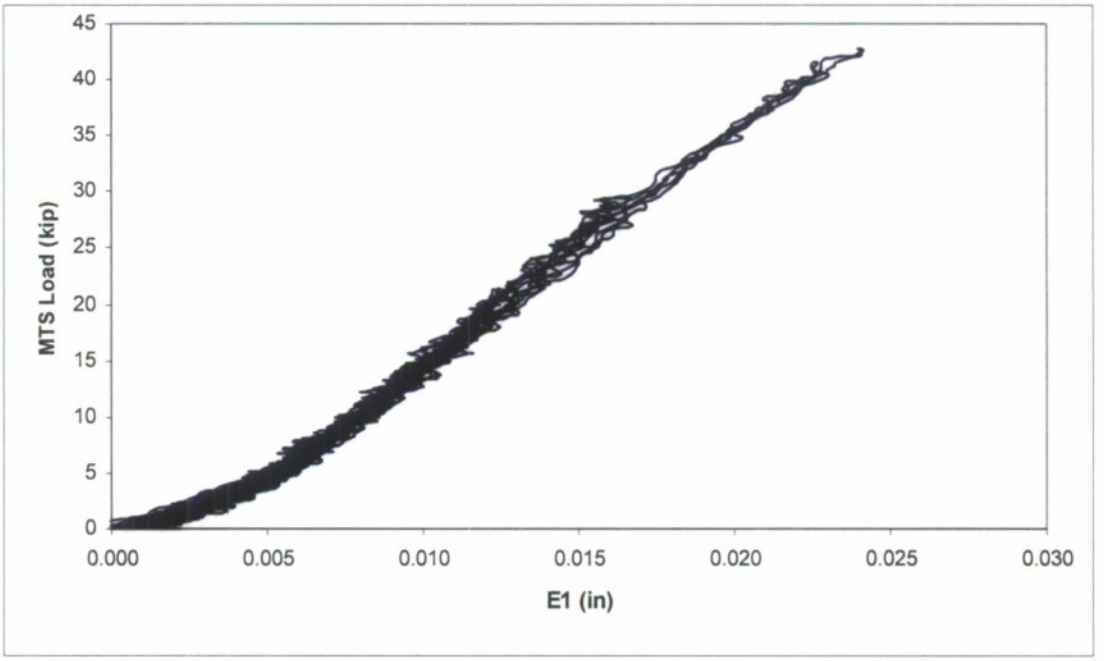

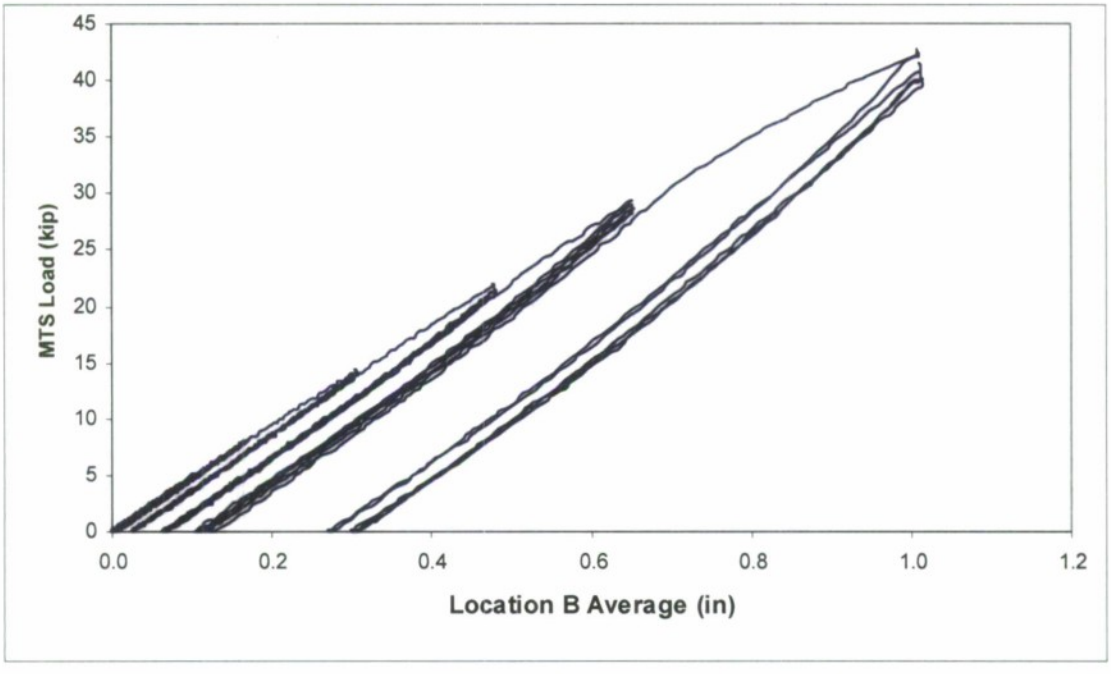
MTS Load (kip)
45
40
35
30
25
20
15
10
5
0
0.0
0.2
0.4
0.6
0.8
1.0
1.2
Location B Average (in)

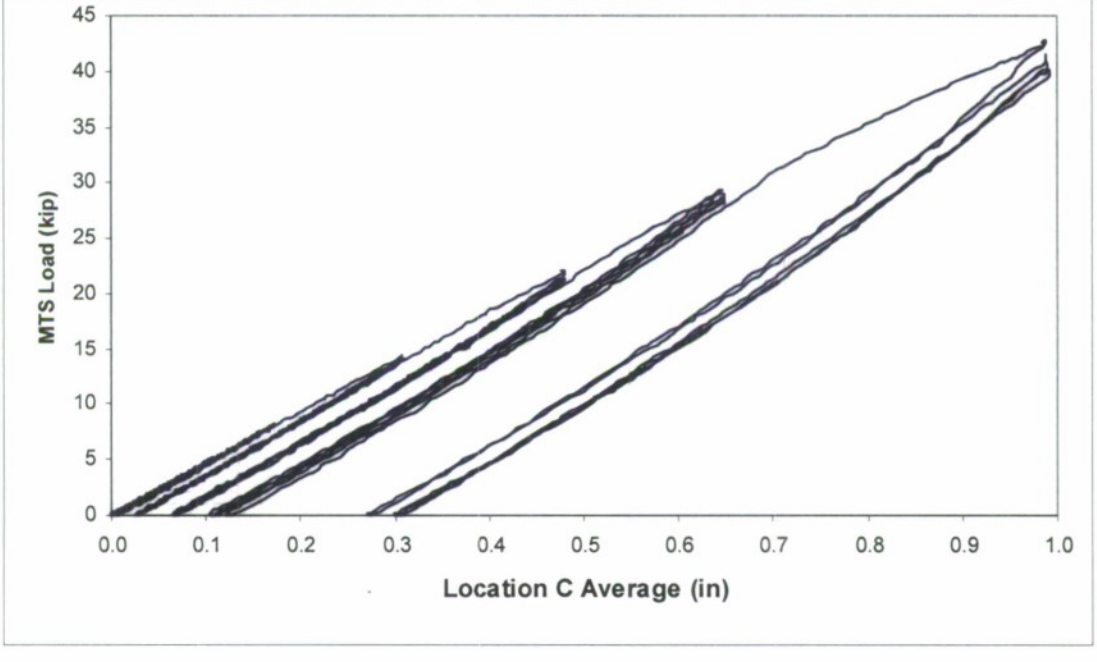
MTS Load (kip)
45
40
35
30
25
20
15
10
5
0
0.0
0.1
0.2
0.3
0.4
0.5
0.6
0.7
0.8
0.9
1.0
Location C Average (in)

Appendix H Continued

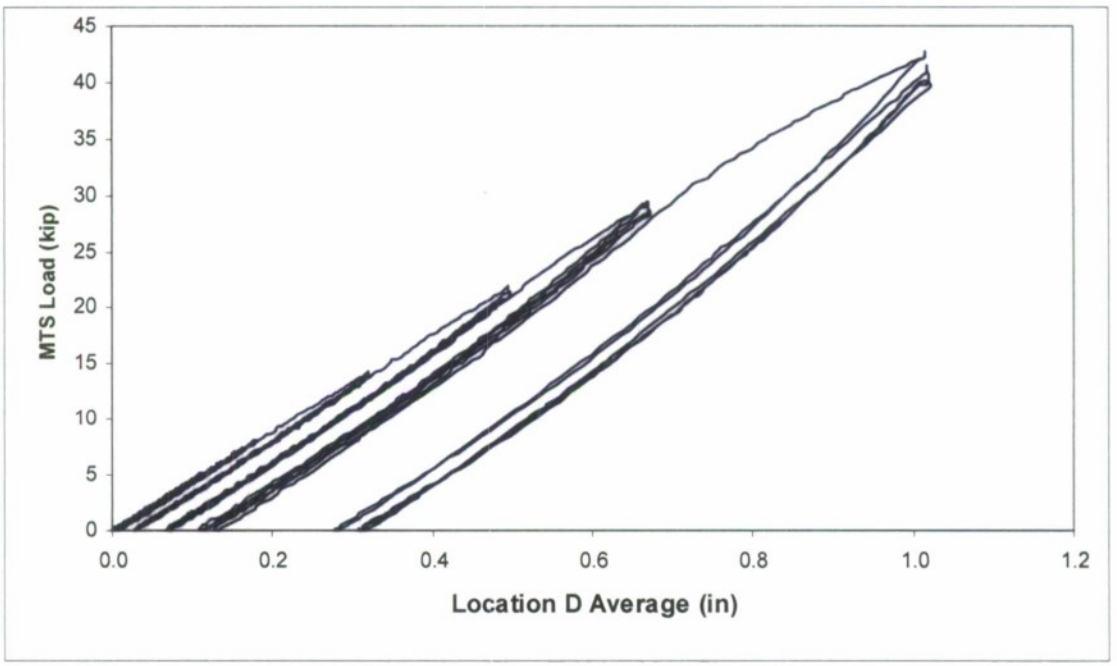

APPENDIX I

Thin Panel Displacements and Stiffness at the Center

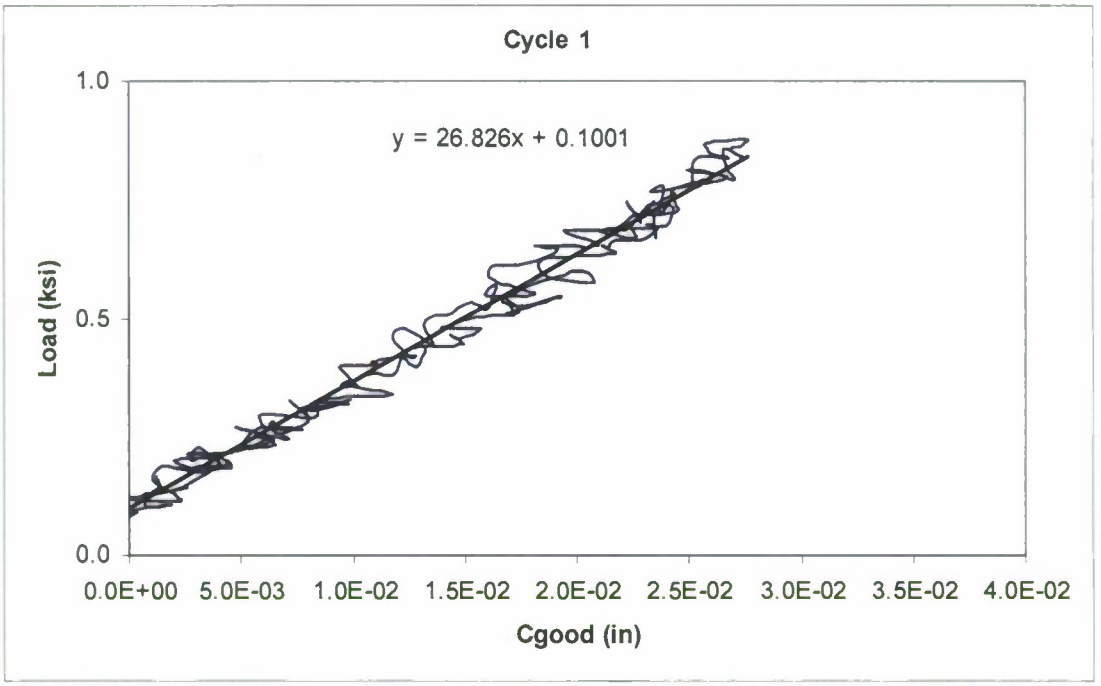

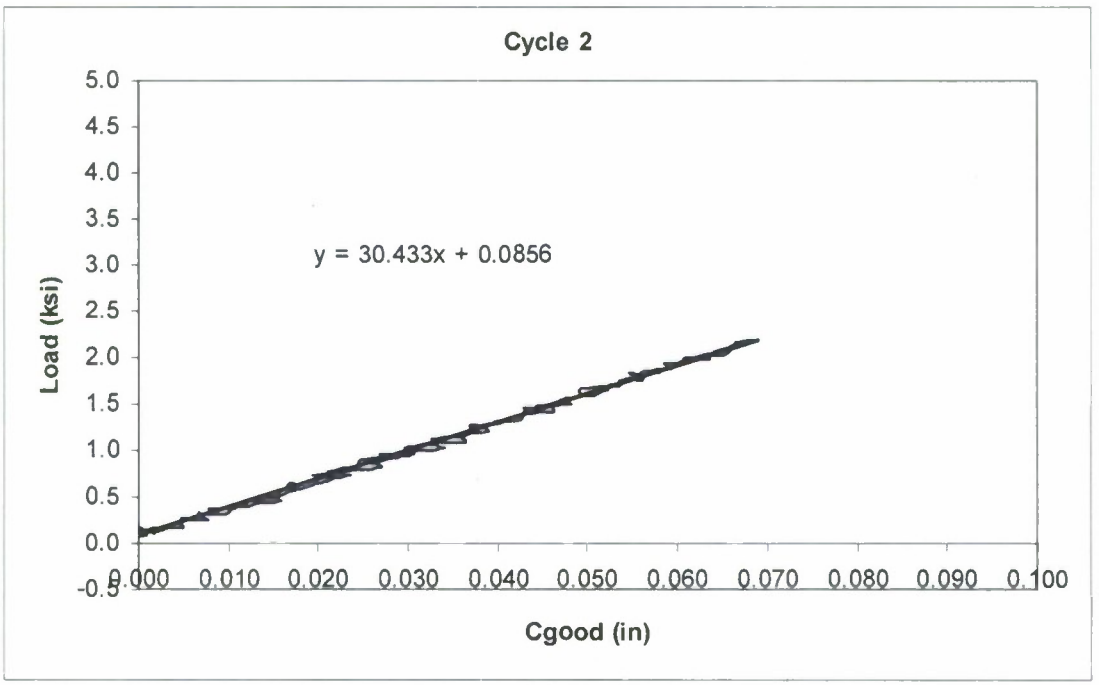

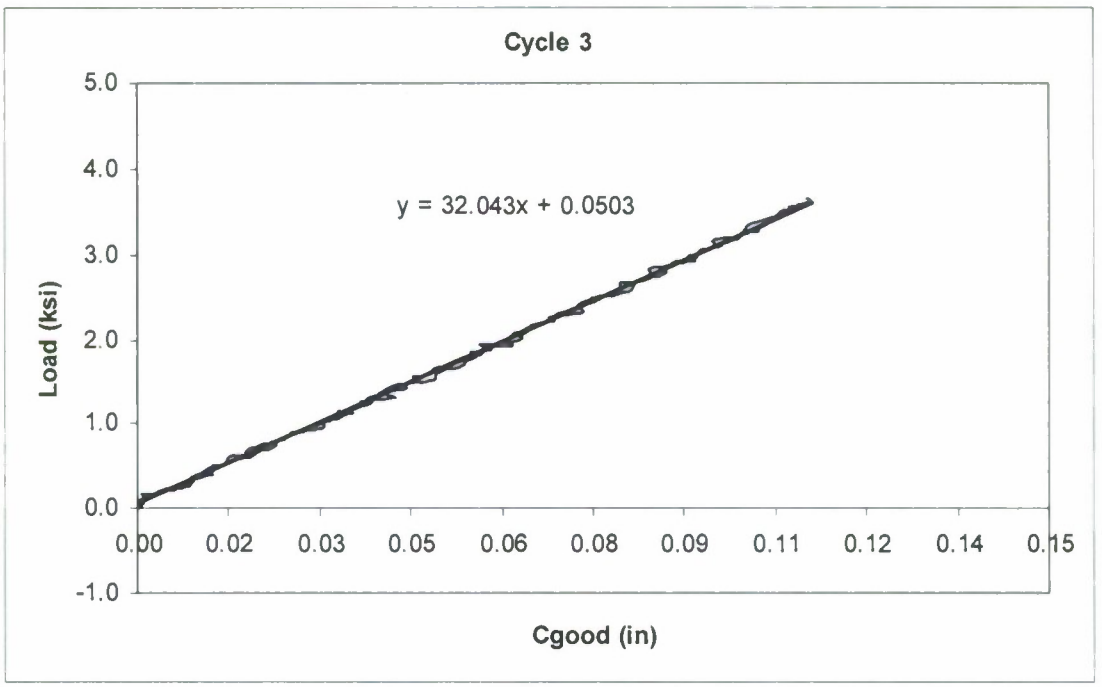
Cycle 3
y = 32.043x + 0.0503
Load (ksi)
5.0
4.0
3.0
2.0
1.0
0.0
-1.0
0.00
0.02
0.03
0.05
0.06
0.08
0.09
0.11
0.12
0.14
0.15
Cgood (in)

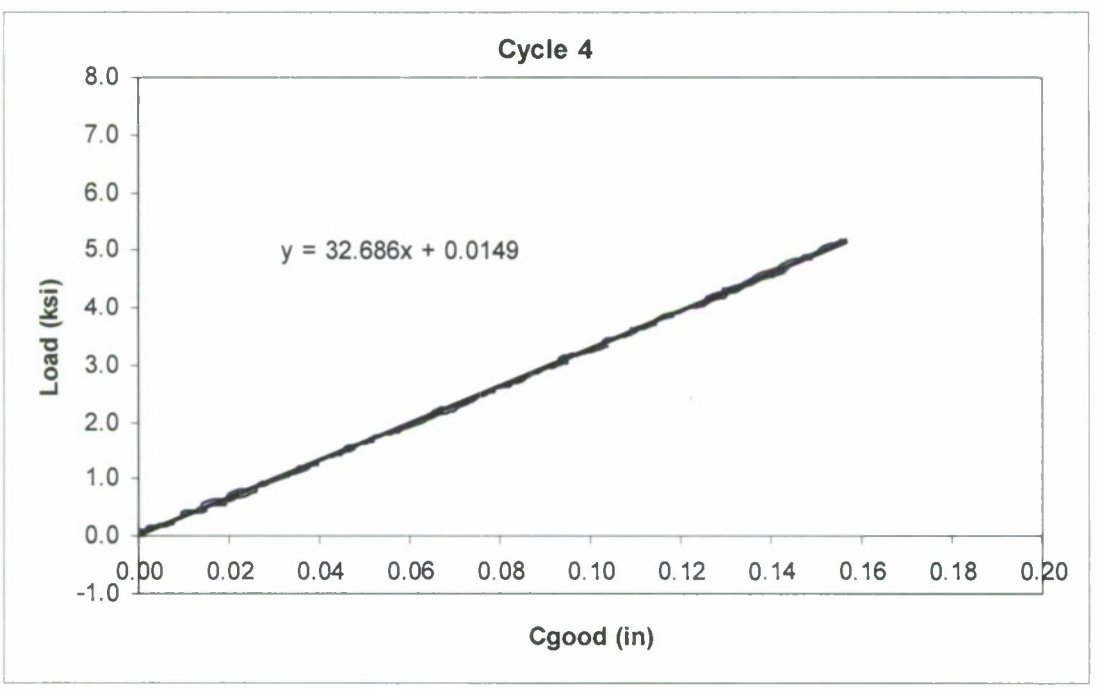
Cycle 4
y = 32.686x + 0.0149
Load (ksi)
8.0
7.0
6.0
5.0
4.0
3.0
2.0
1.0
0.0
-1.0
0.00
0.02
0.04
0.06
0.08
0.10
0.12
0.14
0.16
0.18
0.20
Cgood (in)

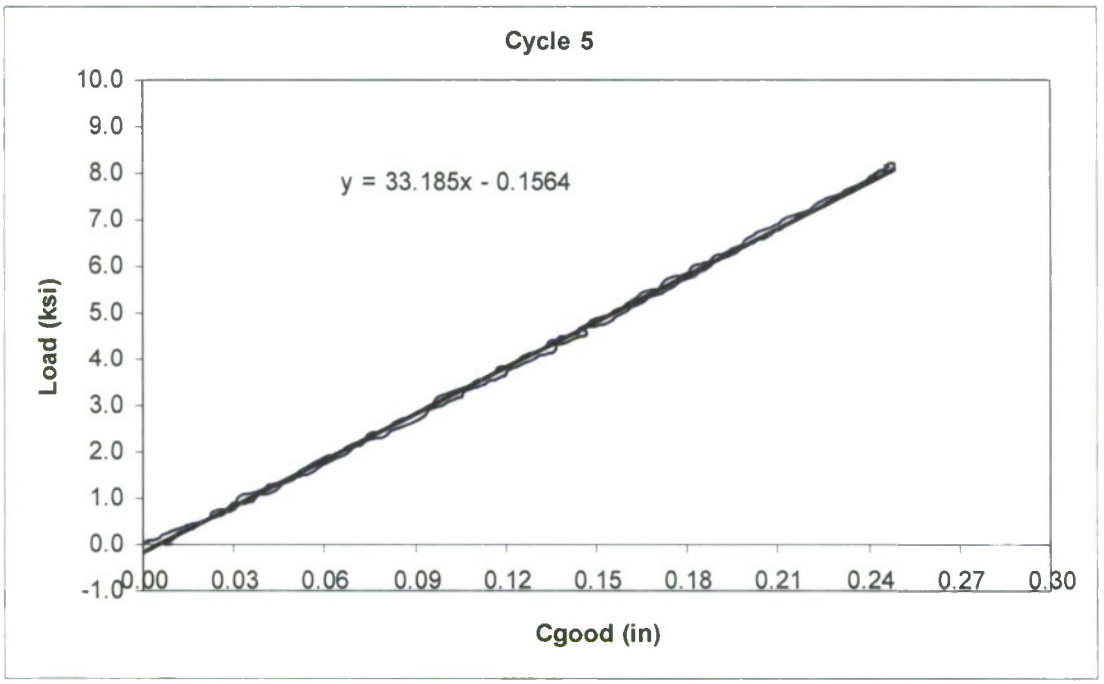
Cycle 5
y = 33.185x - 0.1564
Load (ksi)
10.0
9.0
8.0
7.0
6.0
5.0
4.0
3.0
2.0
1.0
0.0
-1.0
0.00
0.03
0.06
0.09
0.12
0.15
0.18
0.21
0.24
0.27
0.30
Cgood (in)

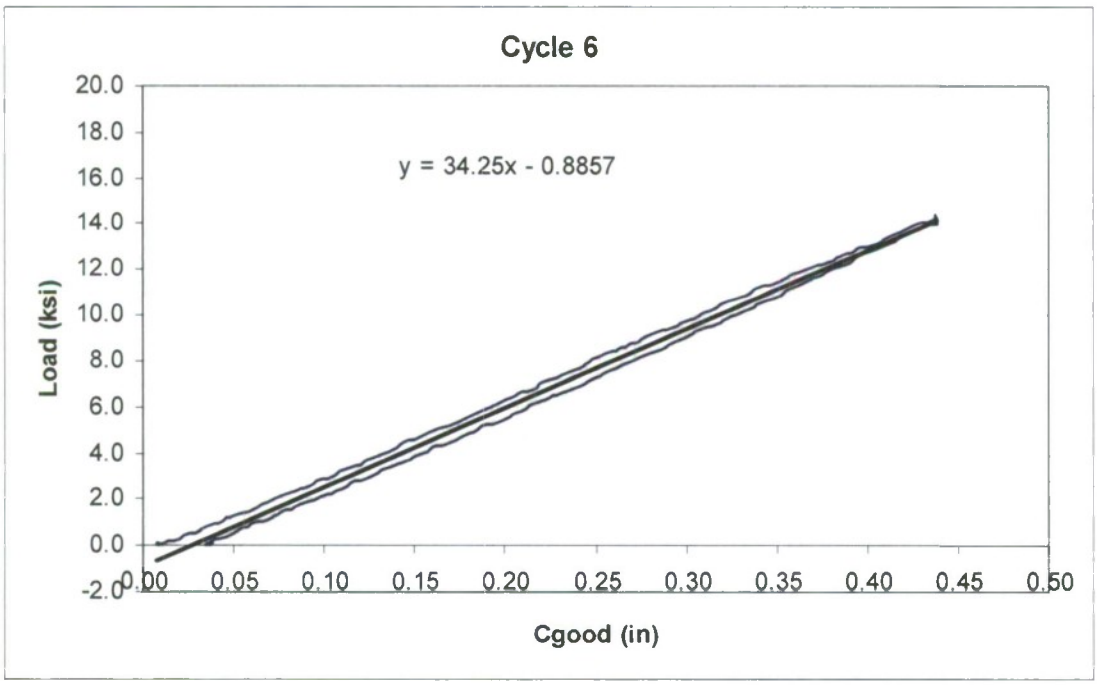
Cycle 6
y = 34.25x - 0.8857
Load (ksi)
20.0
18.0
16.0
14.0
12.0
10.0
8.0
6.0
4.0
2.0
0.0
-2.0
0.00
0.05
0.10
0.15
0.20
0.25
0.30
0.35
0.40
0.45
0.50
Cgood (in)

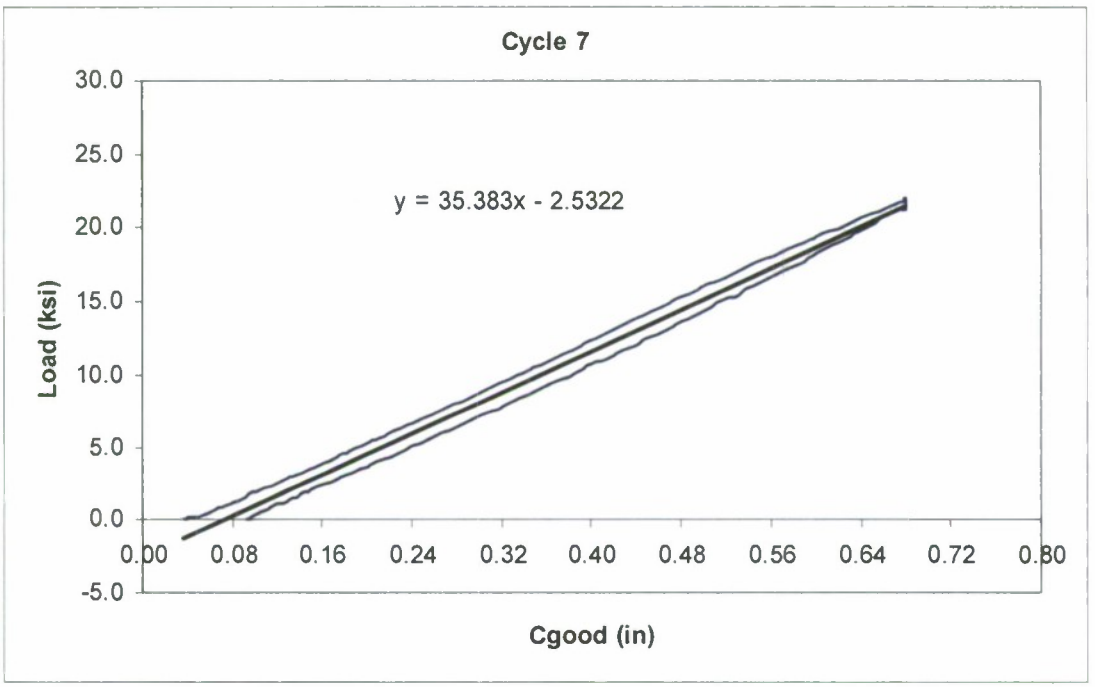
Cycle 7
y = 35.383x - 2.5322
Load (ksi)
30.0
25.0
20.0
15.0
10.0
5.0
0.0
-5.0
0.00
0.08
0.16
0.24
0.32
0.40
0.48
0.56
0.64
0.72
0.80
Cgood (in)

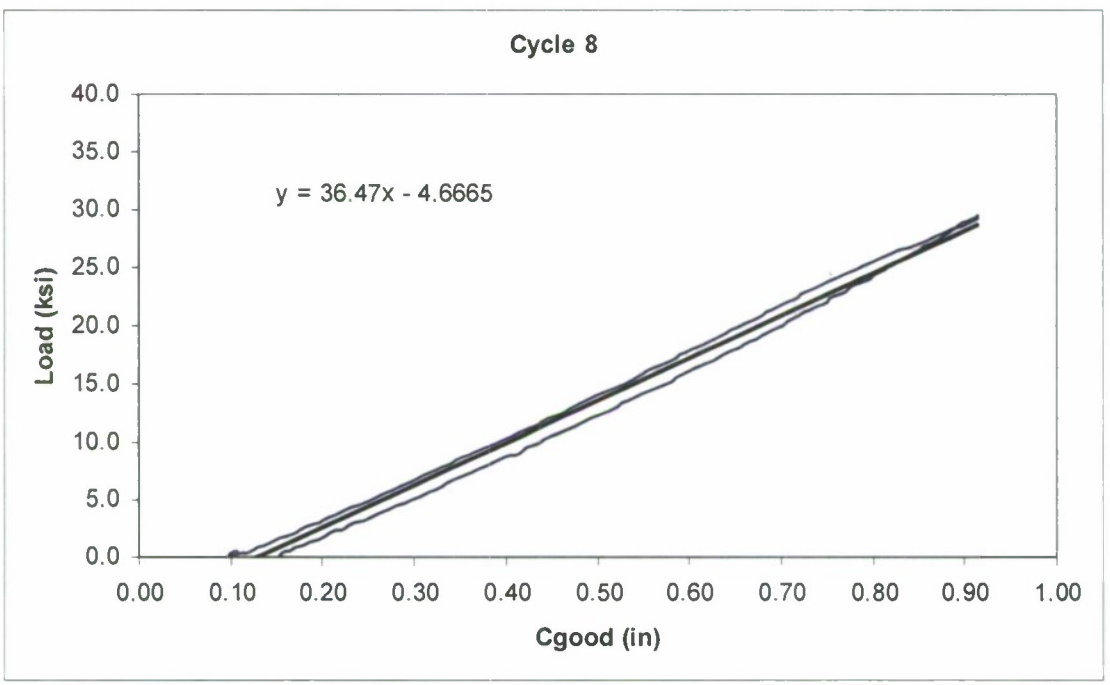
Cycle 8
y = 36.47x - 4.6665
Load (ksi)
40.0
35.0
30.0
25.0
20.0
15.0
10.0
5.0
0.0
0.00
0.10
0.20
0.30
0.40
0.50
0.60
0.70
0.80
0.90
1.00
Cgood (in)

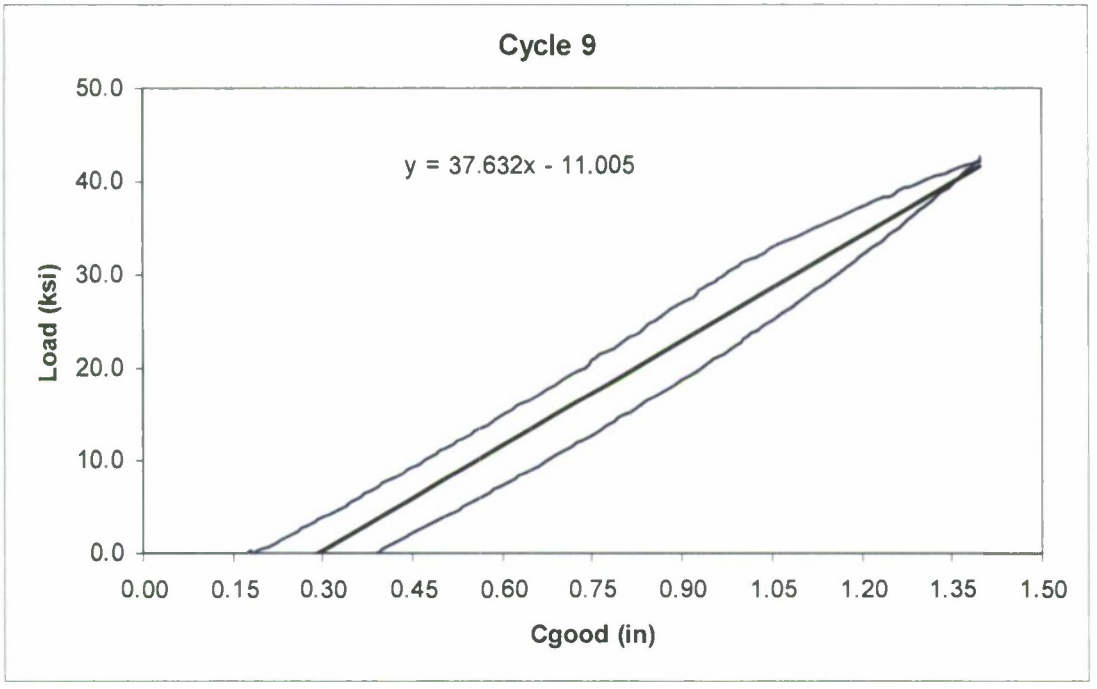
Cycle 9
y = 37.632x - 11.005
Load (ksi)
50.0
40.0
30.0
20.0
10.0
0.0
0.00
0.15
0.30
0.45
0.60
0.75
0.90
1.05
1.20
1.35
1.50
Cgood (in)

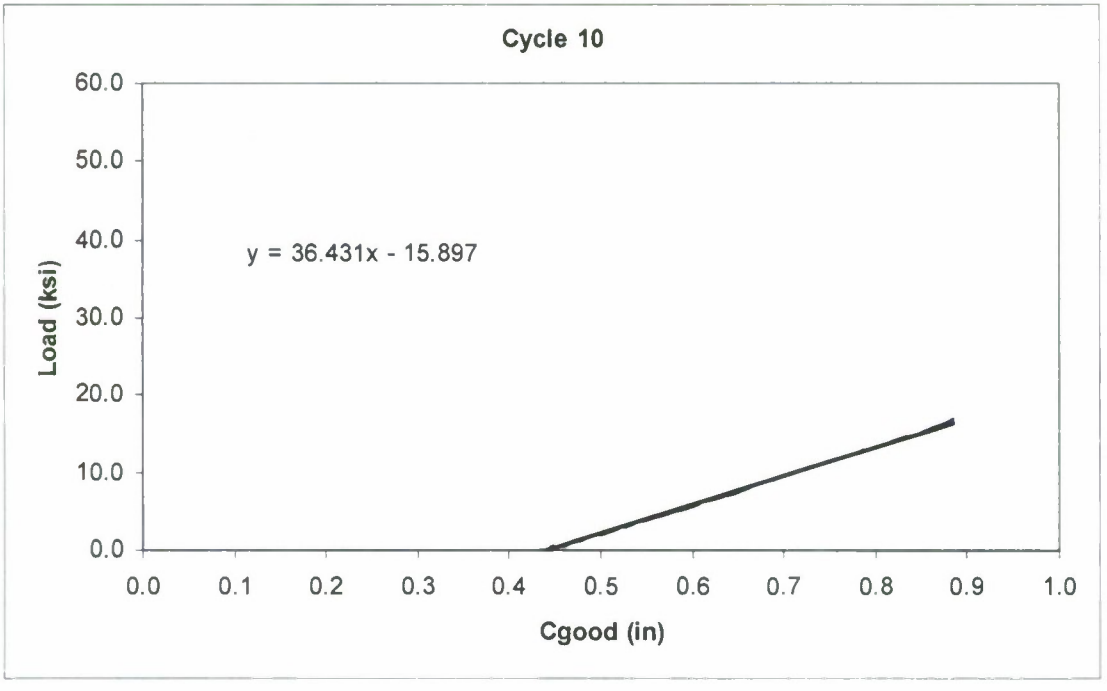
Cycle 10
y = 36.431x - 15.897
Load (ksi)
60.0
50.0
40.0
30.0
20.0
10.0
0.0
0.0
0.1
0.2
0.3
0.4
0.5
0.6
0.7
0.8
0.9
1.0
Cgood (in)

APPENDIX J

Displaced Shaped of Thin Panel

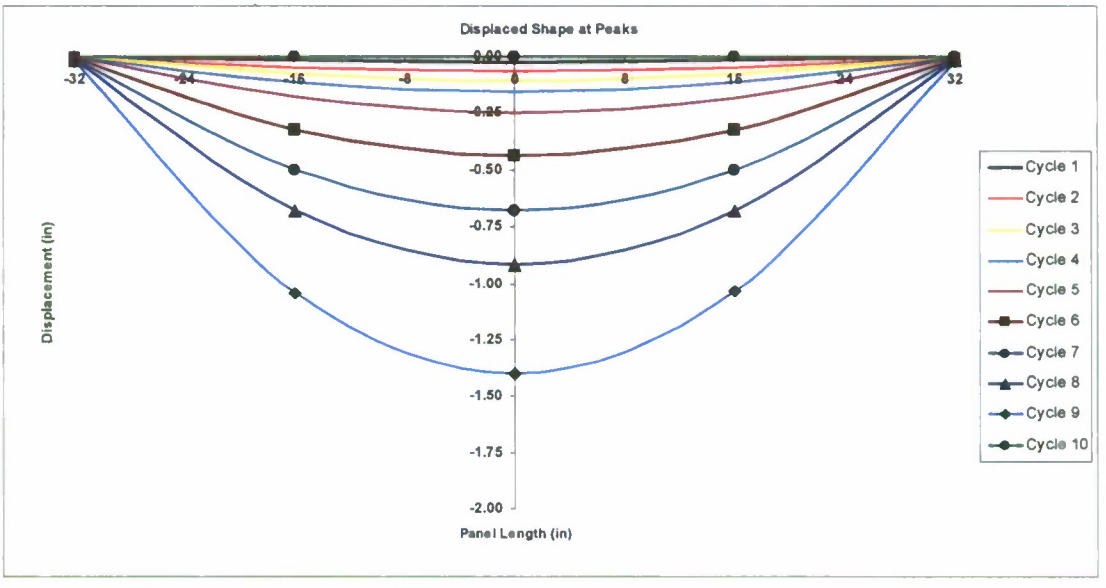

APPENDIX K

Thin Panel Strains at Strain Gage Locations

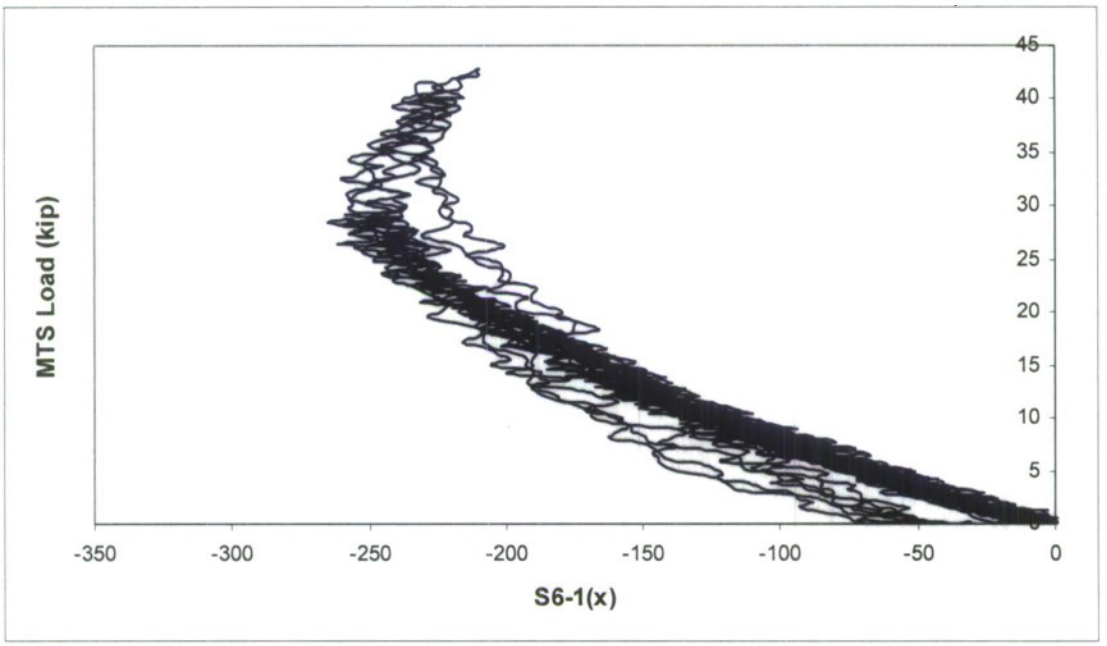

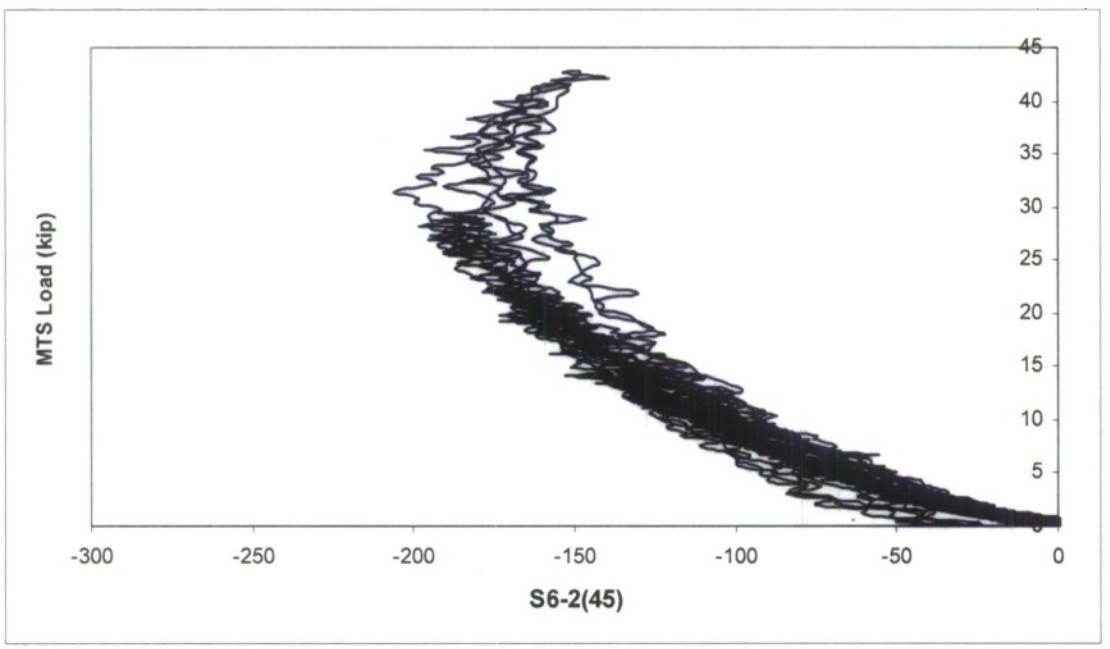

Appendix K Continued

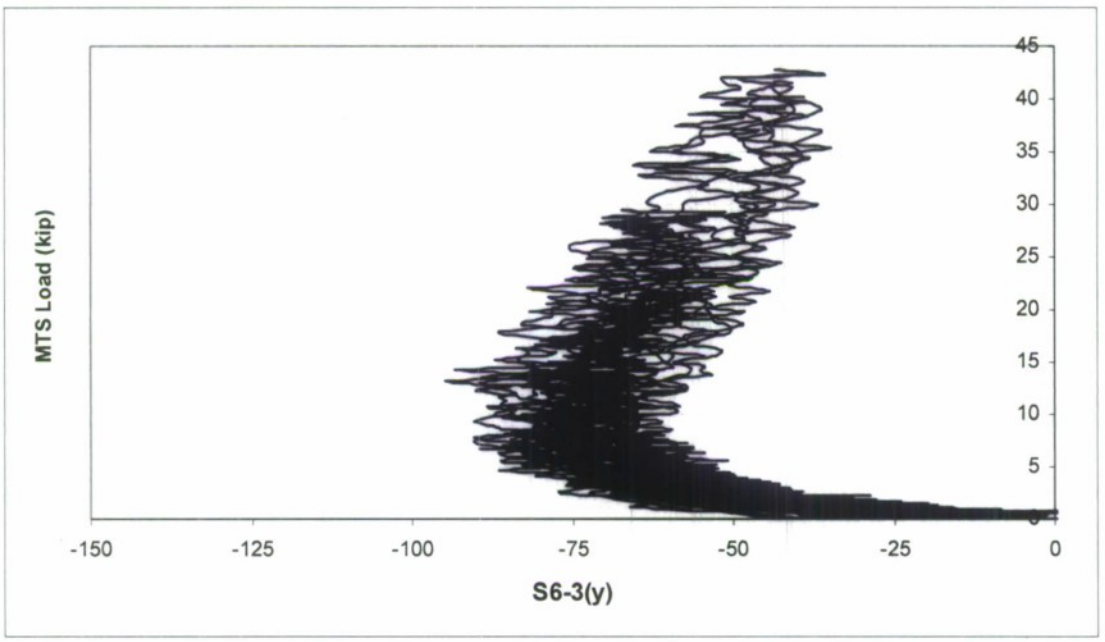

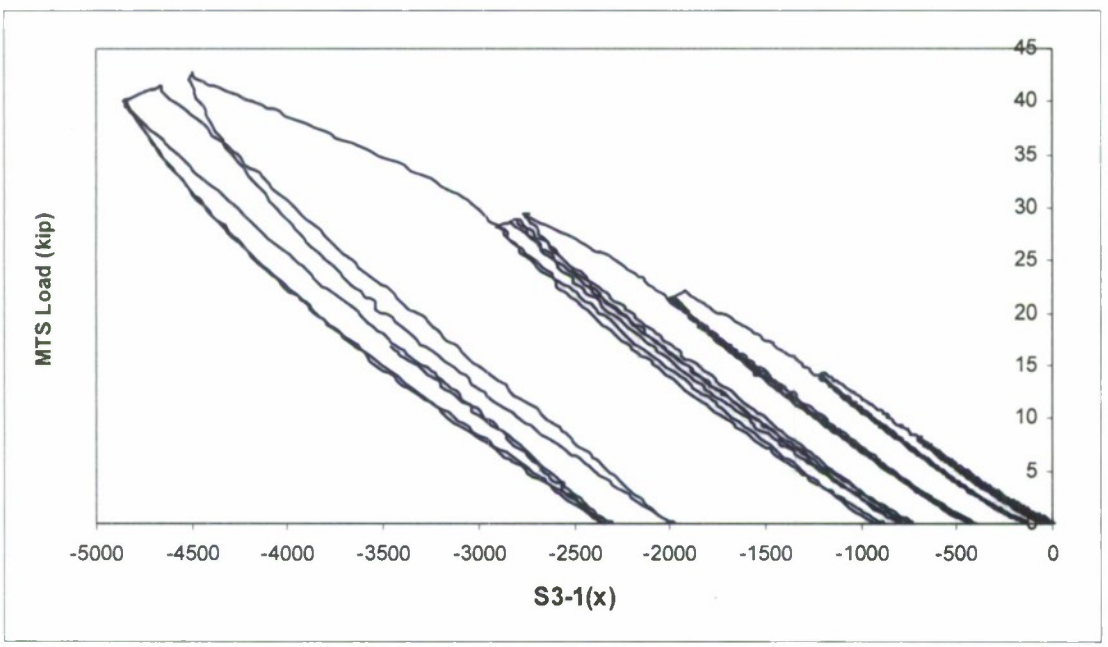

Appendix K Continued

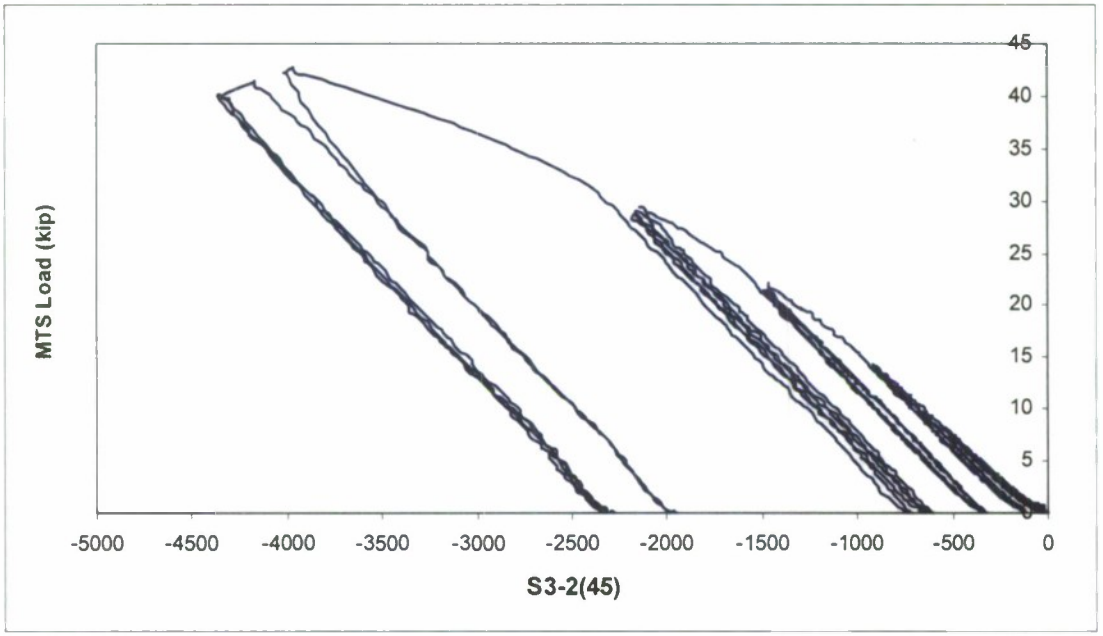

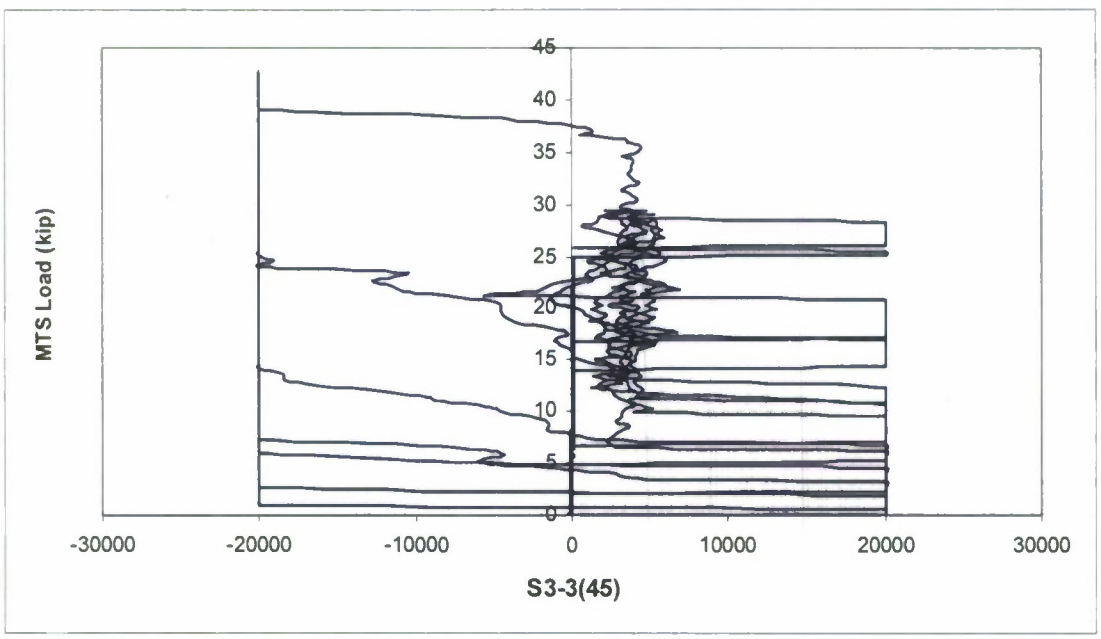

Appendix K Continued

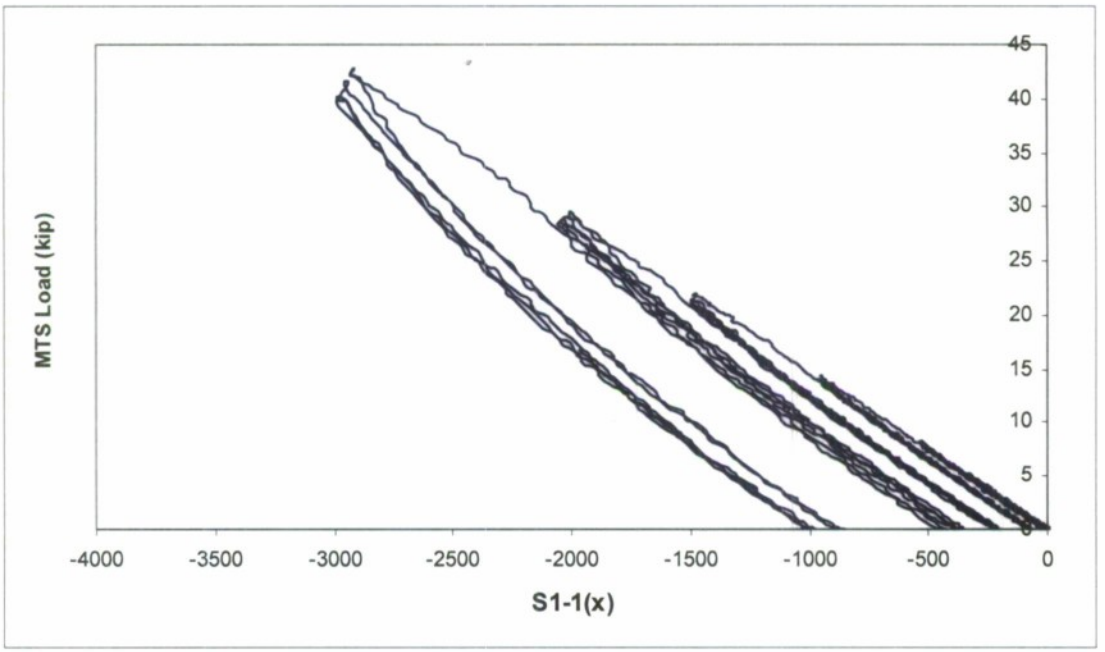

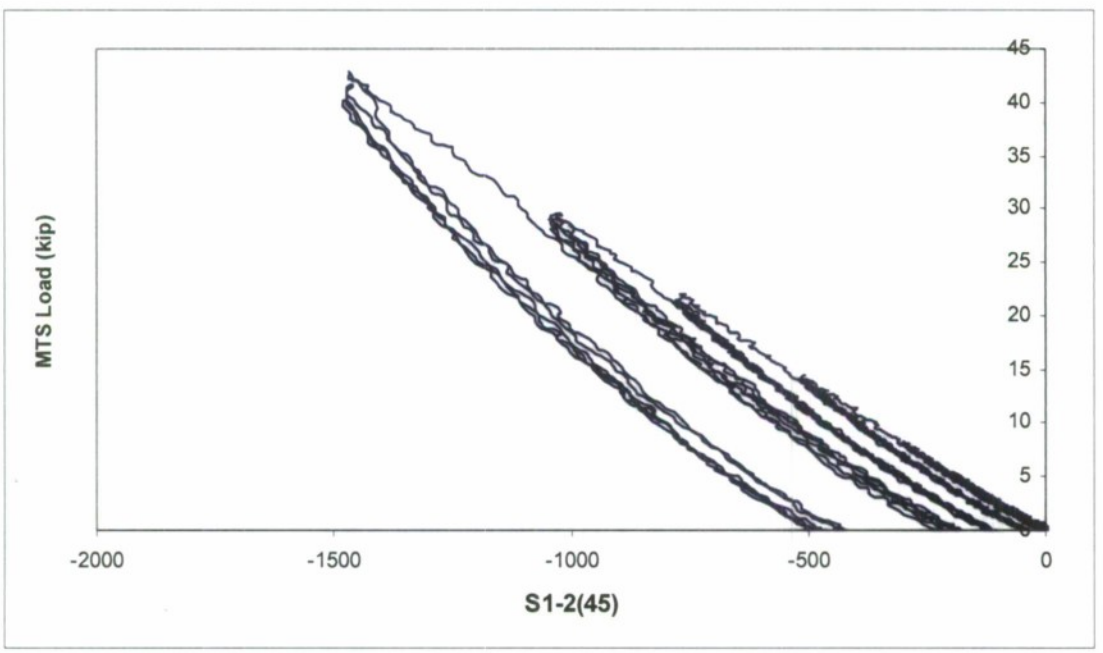

Appendix K Continued

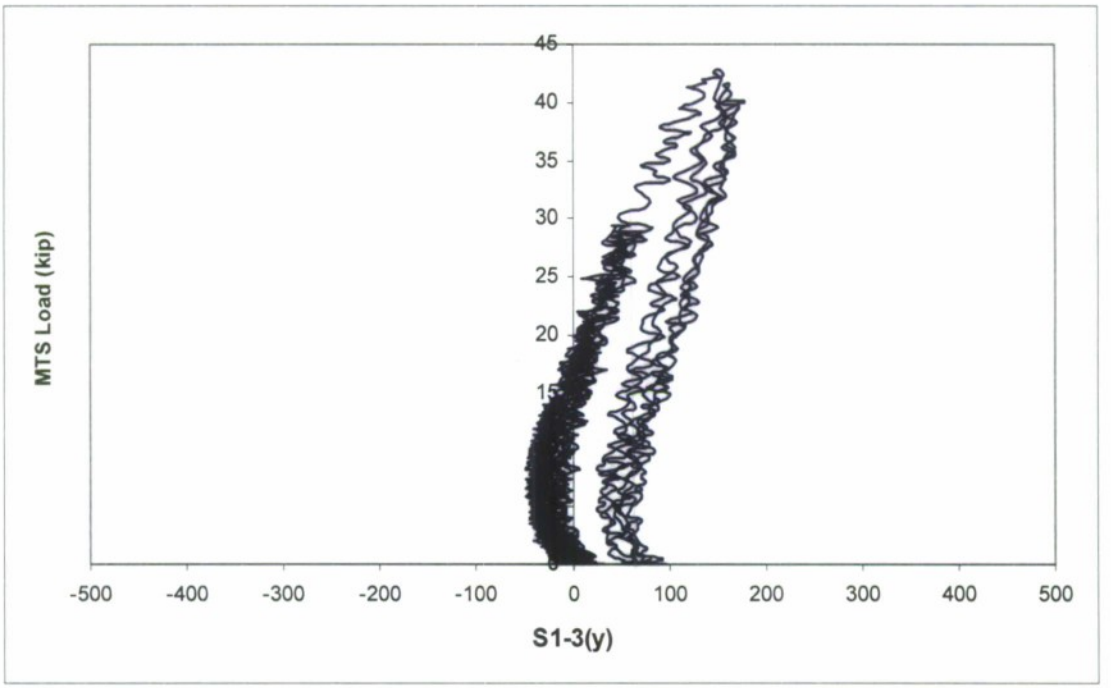

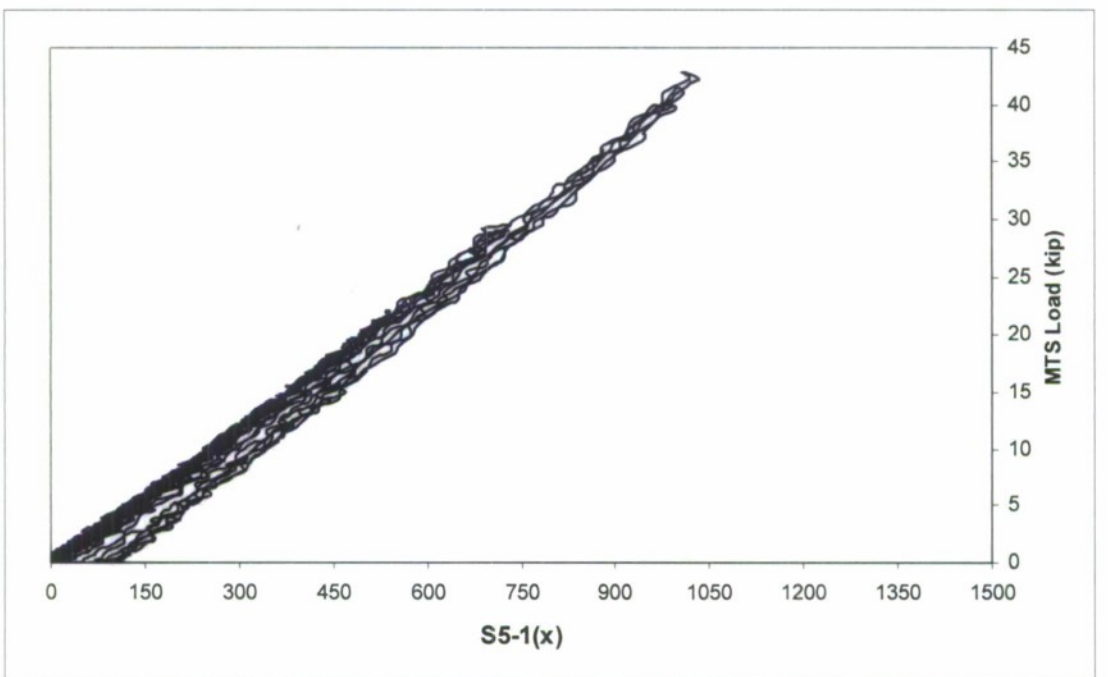

Appendix K Continued

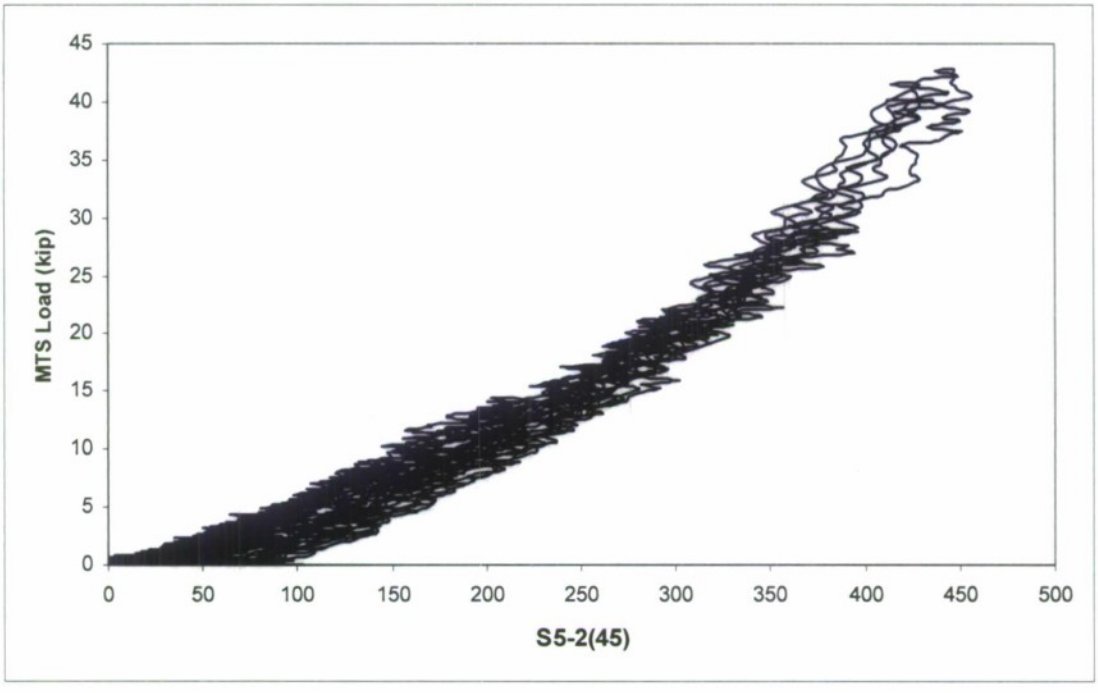

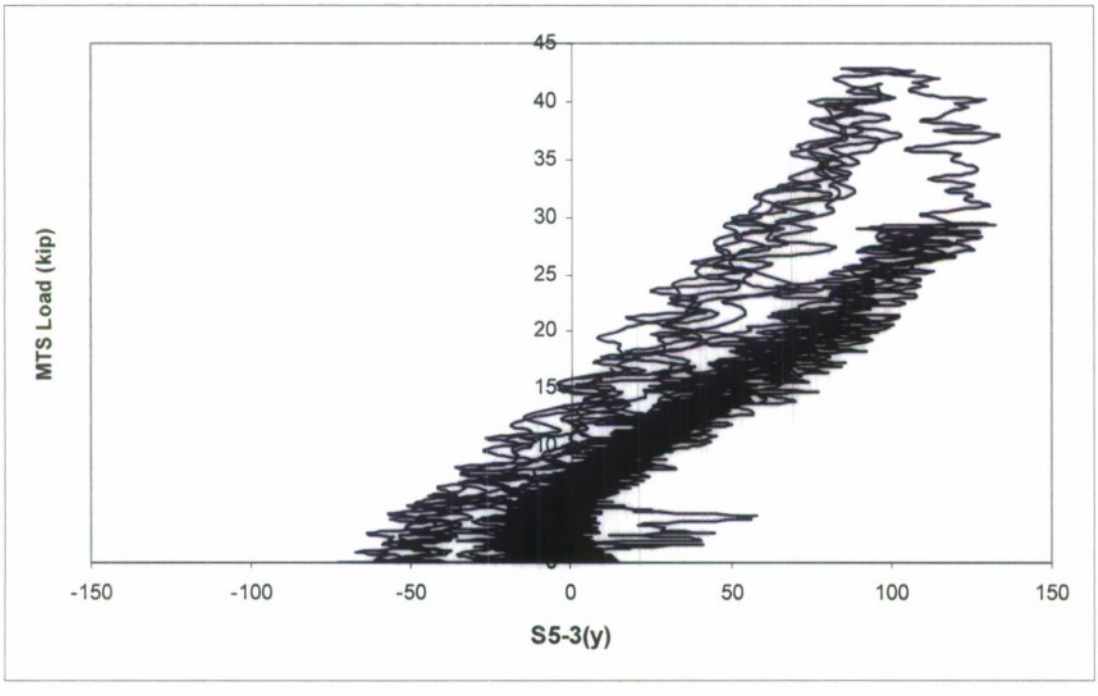

Appendix K Continued

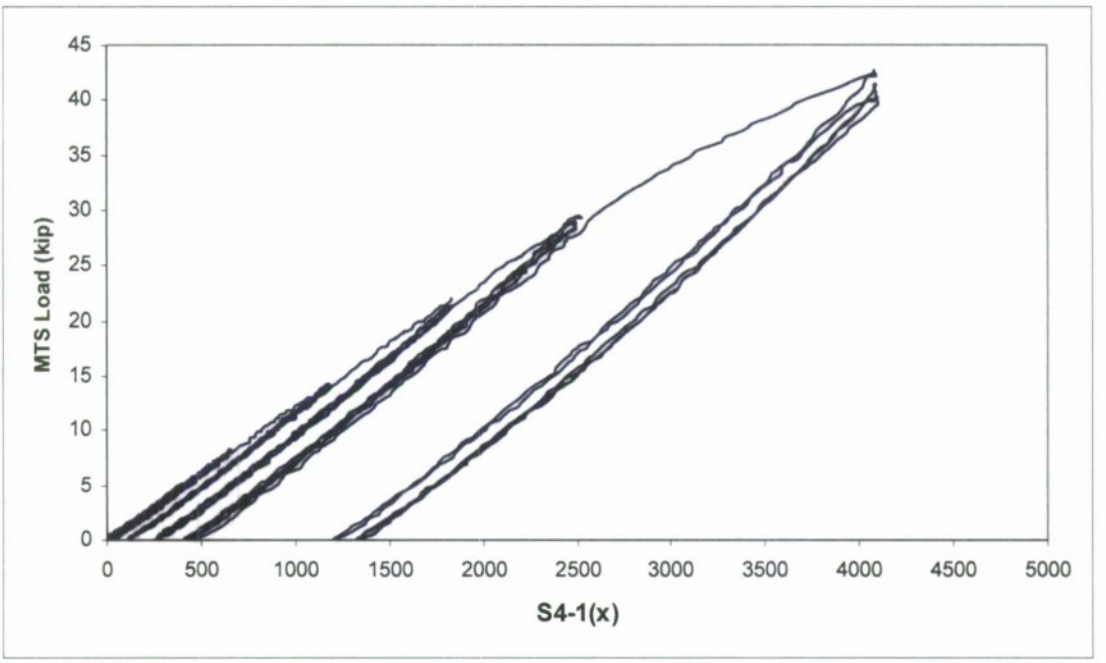

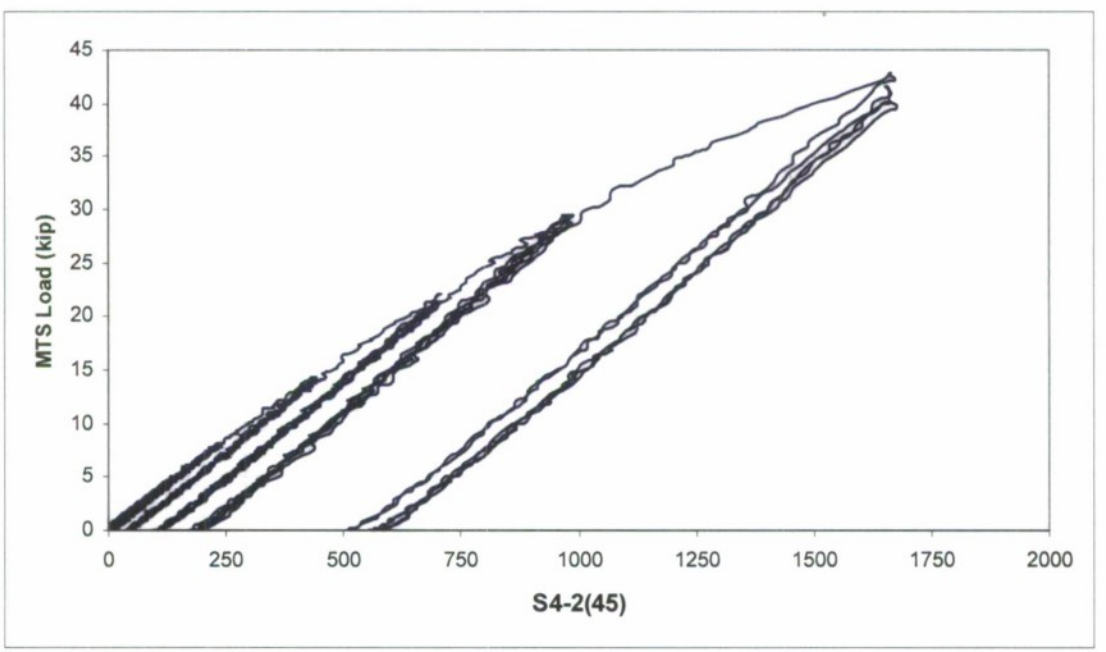

Appendix K Continued

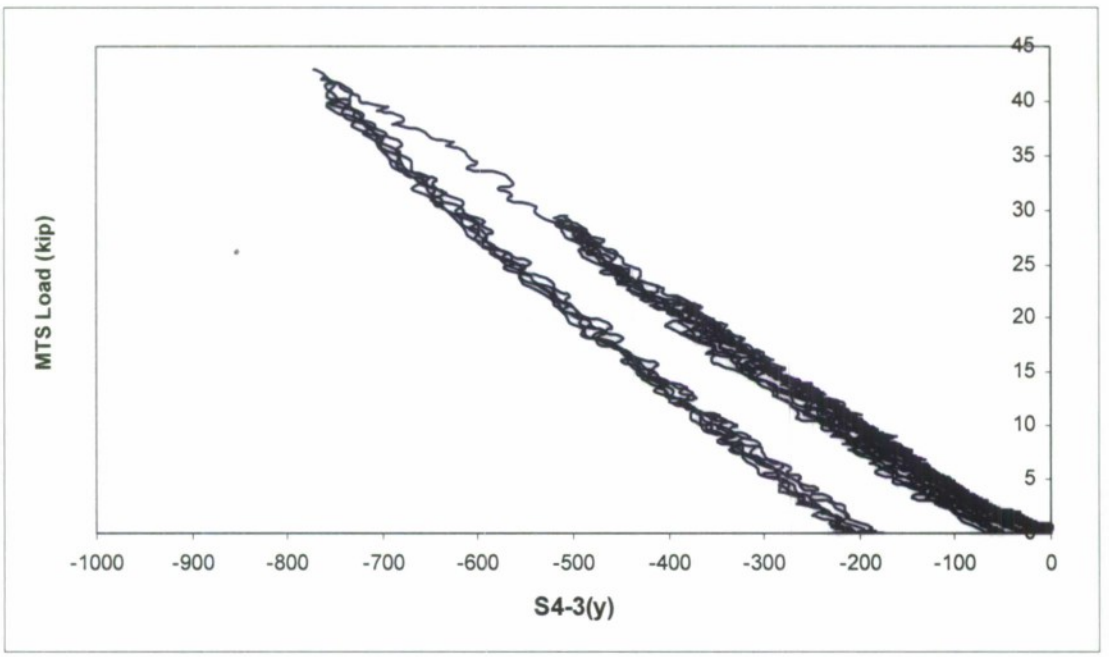

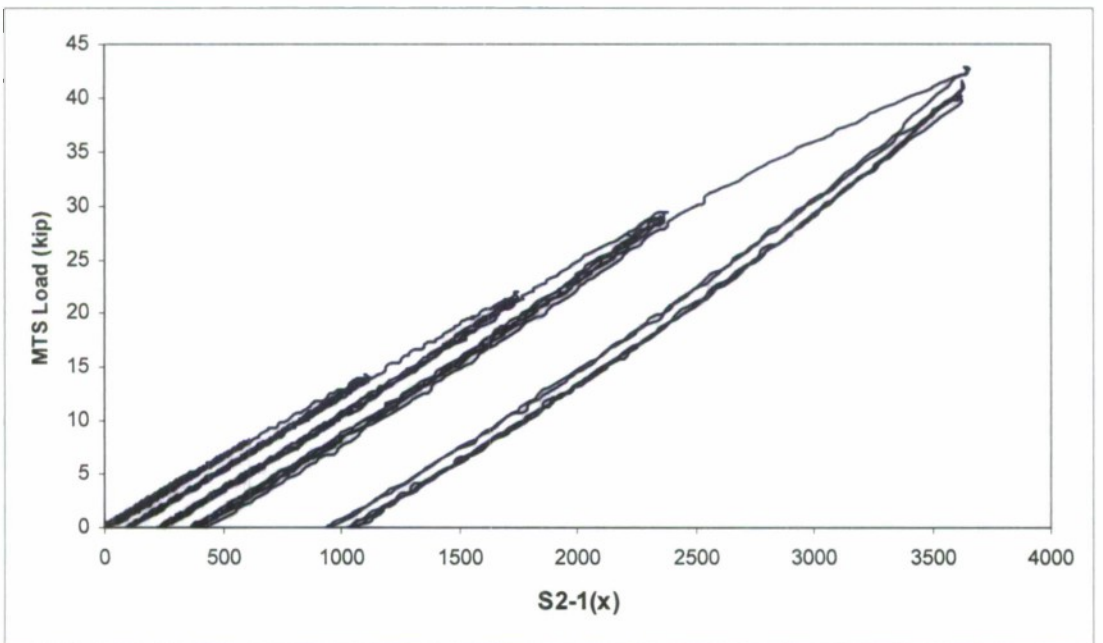

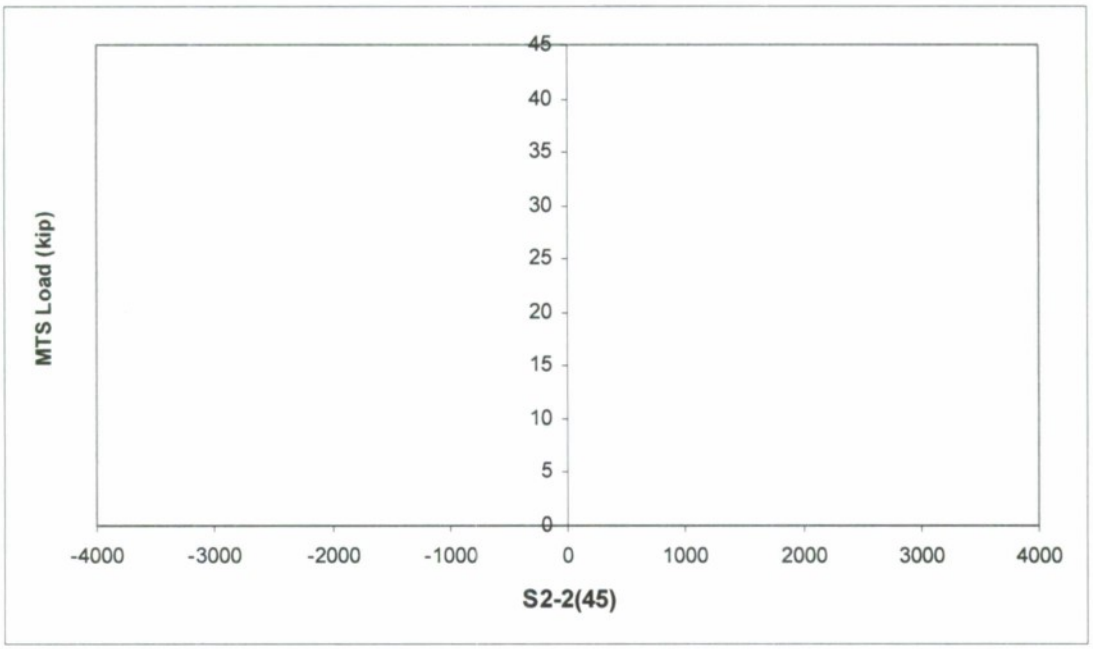
MTS Load (kip)
45
40
35
30
25
20
15
10
5
0
-4000
-3000
-2000
-1000
0
1000
2000
3000
4000
S2-2(45)

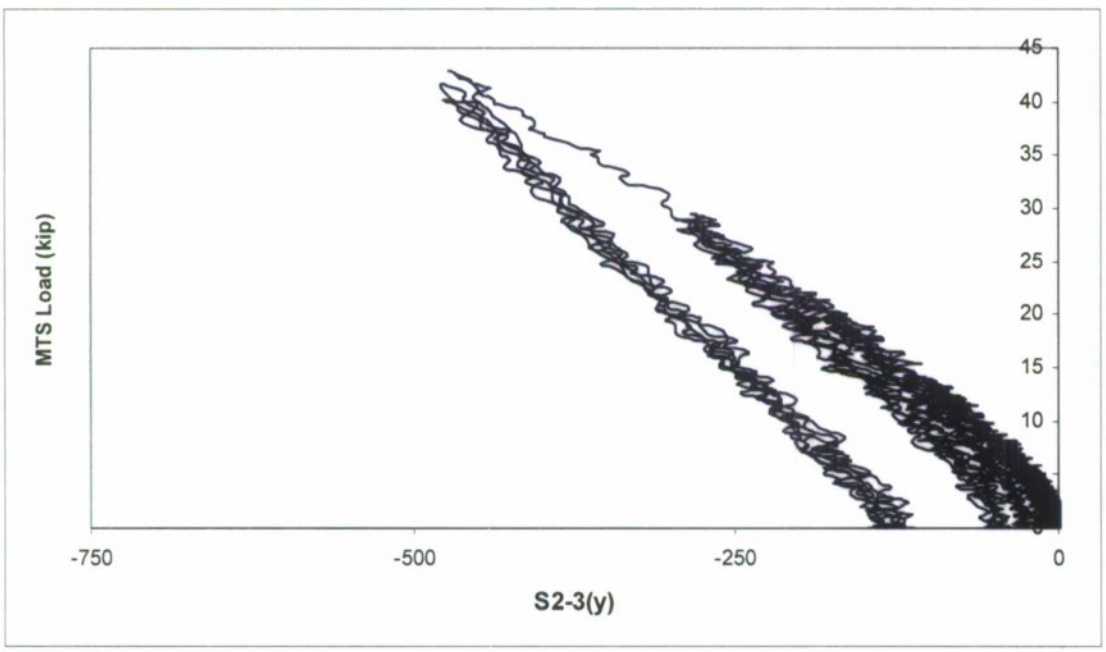
MTS Load (kip)
45
40
35
30
25
20
15
10
-750
-500
-250
0
S2-3(y)

Appendix K Continued

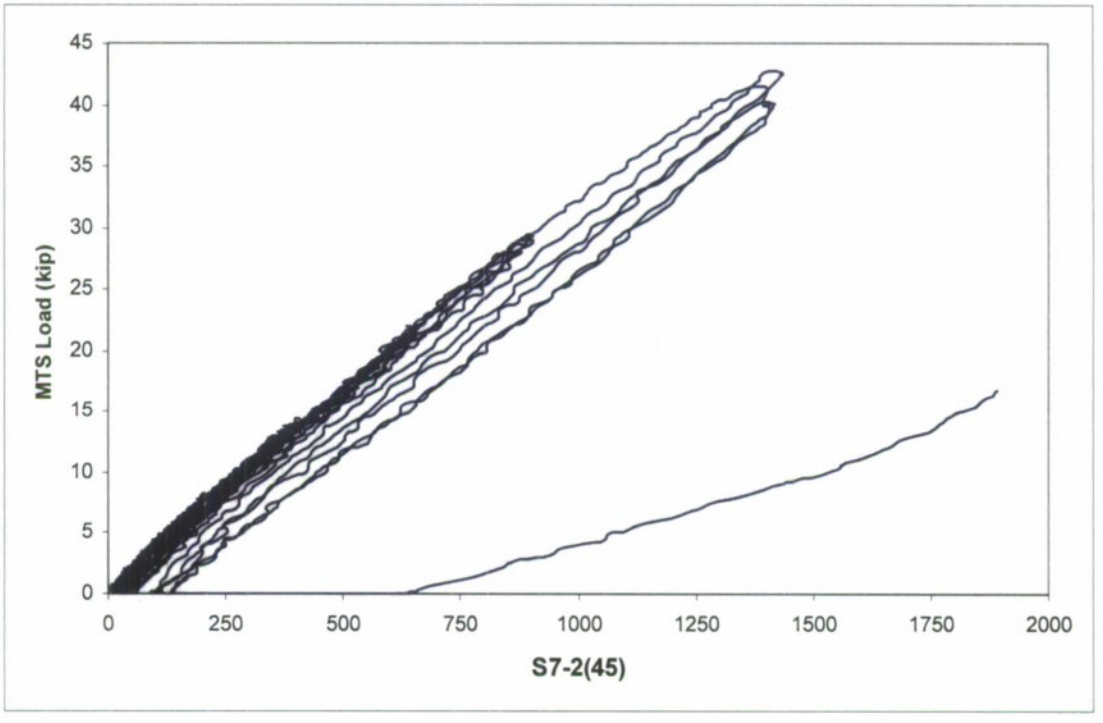

APPENDIX L – Stake Weld Lap-Shear Test Results

Longitudinal

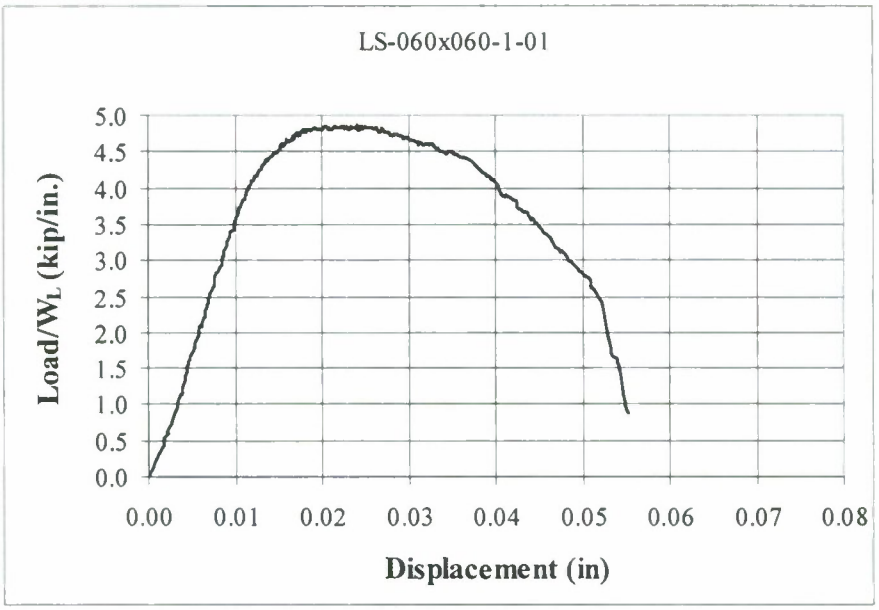

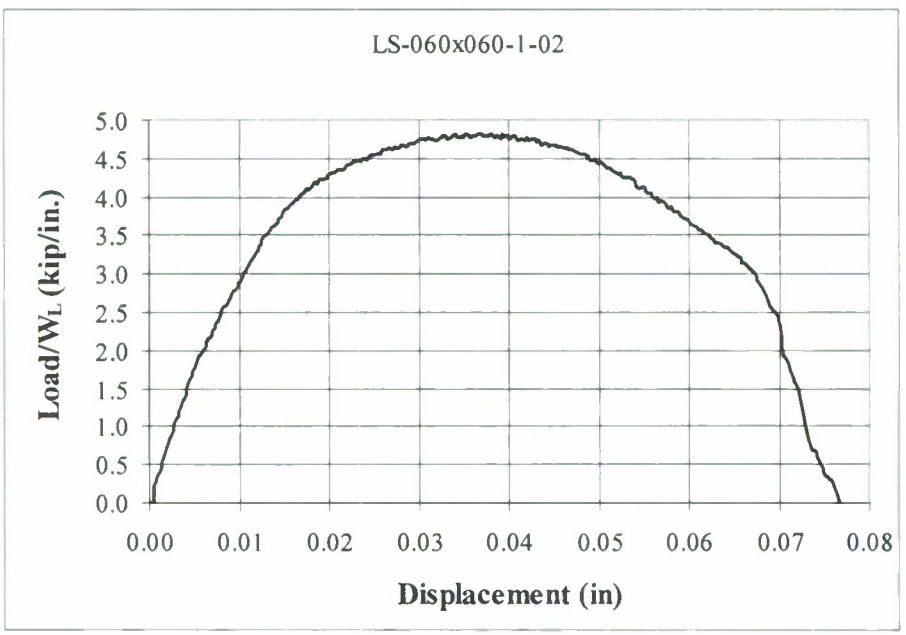

Appendix L Continued

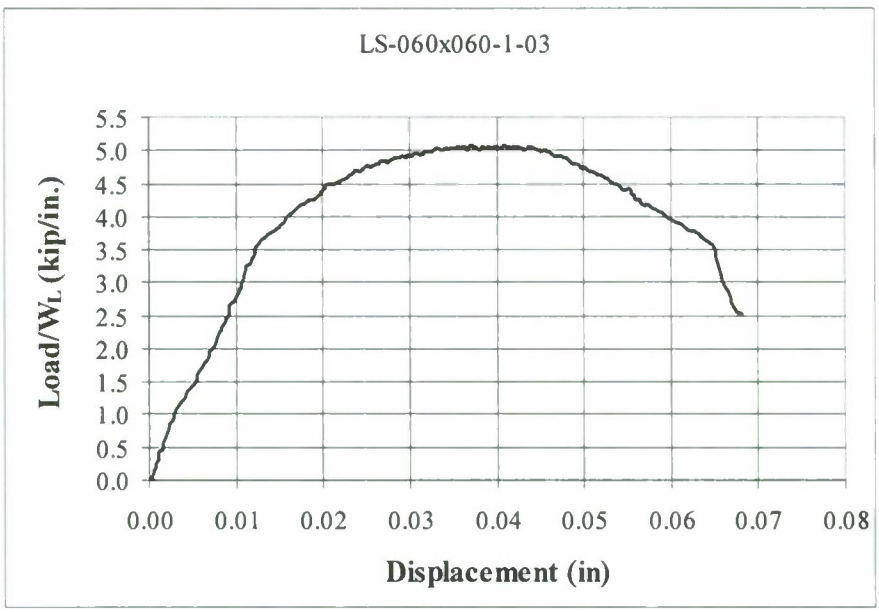

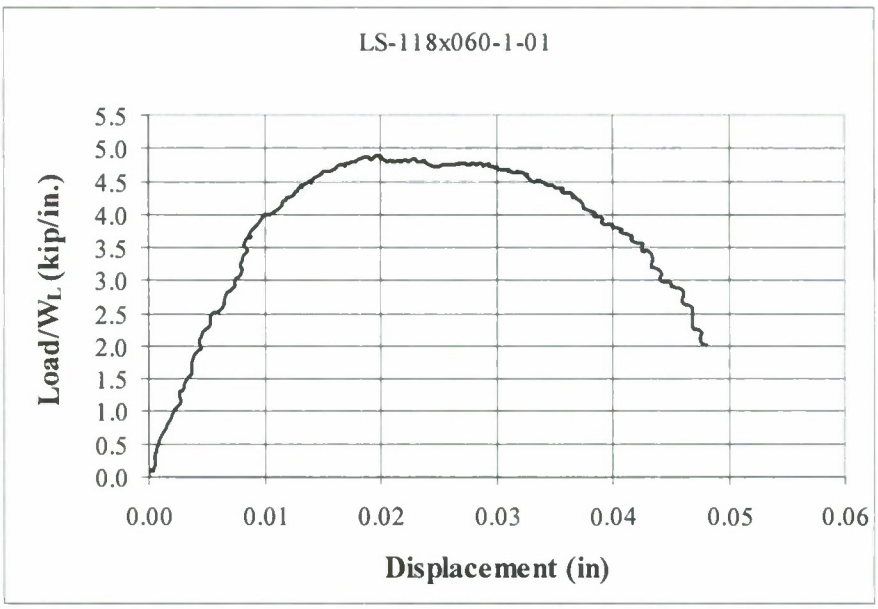

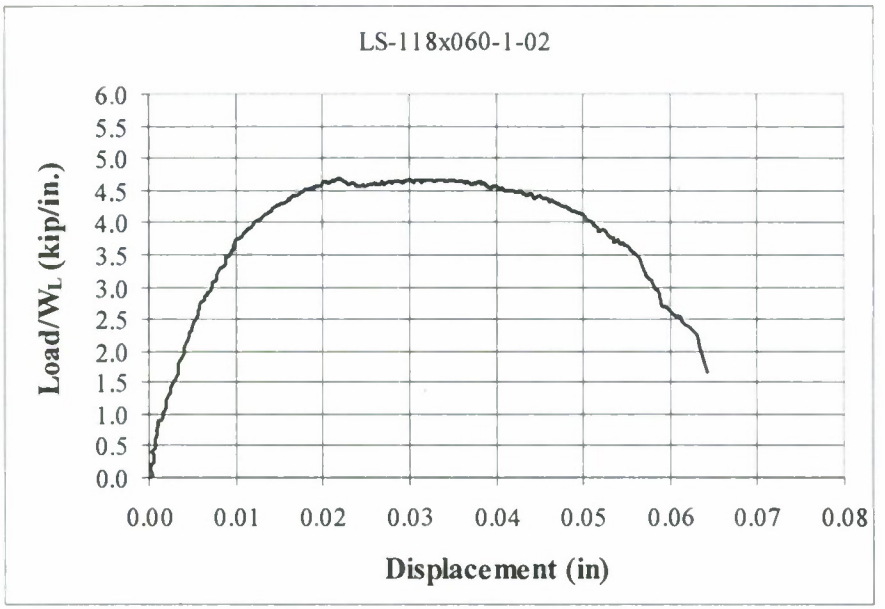
LS-118x060-1-02
Load/W_L (kip/in.)
6.0
5.5
5.0
4.5
4.0
3.5
3.0
2.5
2.0
1.5
1.0
0.5
0.0
0.00
0.01
0.02
0.03
0.04
0.05
0.06
0.07
0.08
Displacement (in)

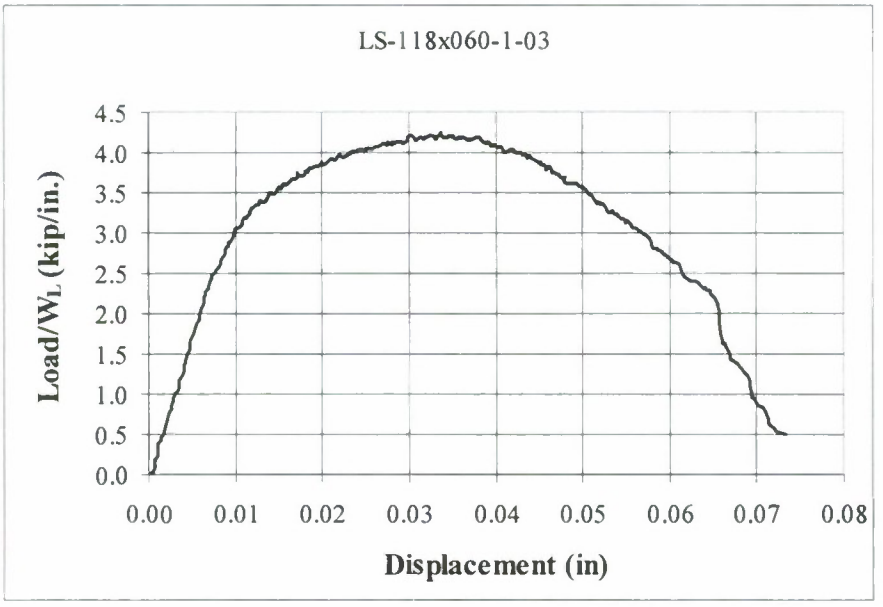
LS-118x060-1-03
Load/W_L (kip/in.)
4.5
4.0
3.5
3.0
2.5
2.0
1.5
1.0
0.5
0.0
0.00
0.01
0.02
0.03
0.04
0.05
0.06
0.07
0.08
Displacement (in)

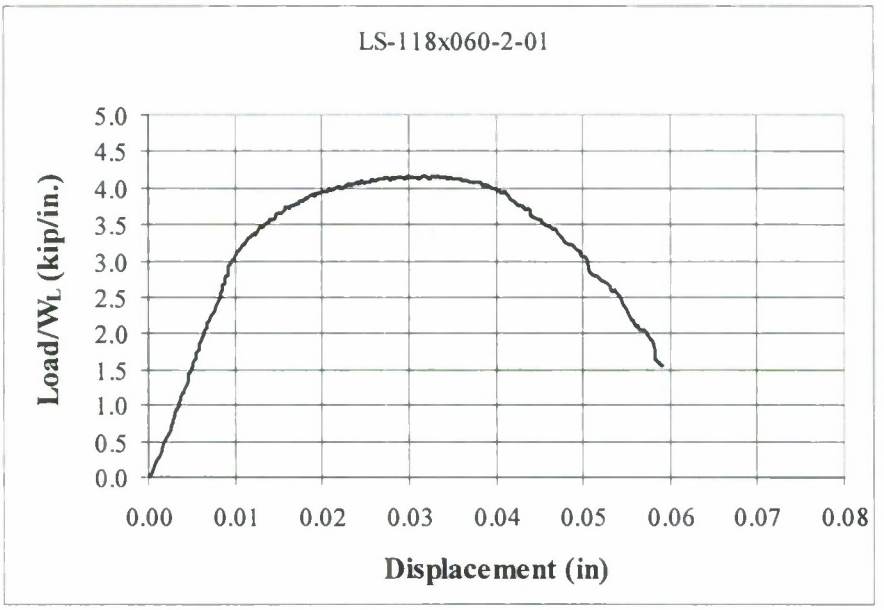
LS-118x060-2-01
Load/WL (kip/in.)
5.0
4.5
4.0
3.5
3.0
2.5
2.0
1.5
1.0
0.5
0.0
0.00
0.01
0.02
0.03
0.04
0.05
0.06
0.07
0.08
Displacement (in)

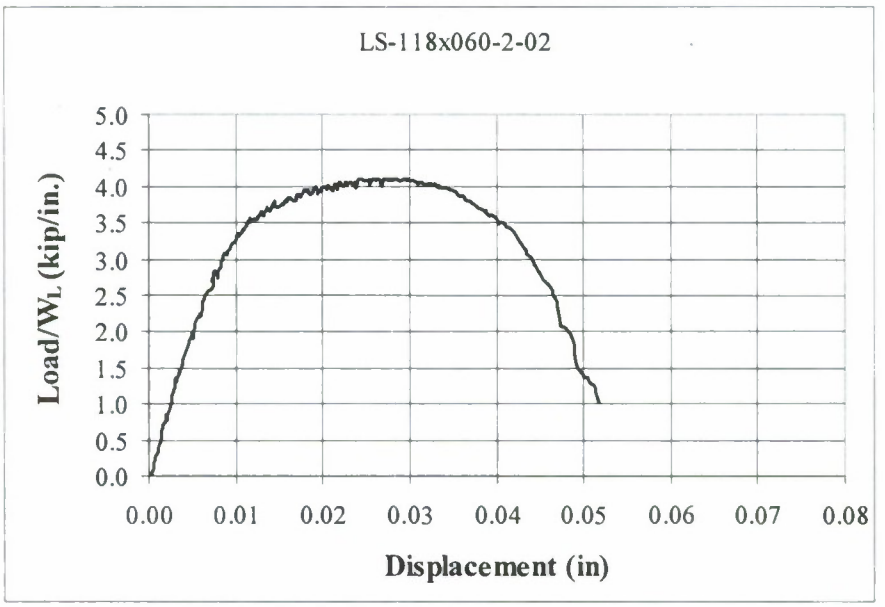
LS-118x060-2-02
Load/WL (kip/in.)
5.0
4.5
4.0
3.5
3.0
2.5
2.0
1.5
1.0
0.5
0.0
0.00
0.01
0.02
0.03
0.04
0.05
0.06
0.07
0.08
Displacement (in)

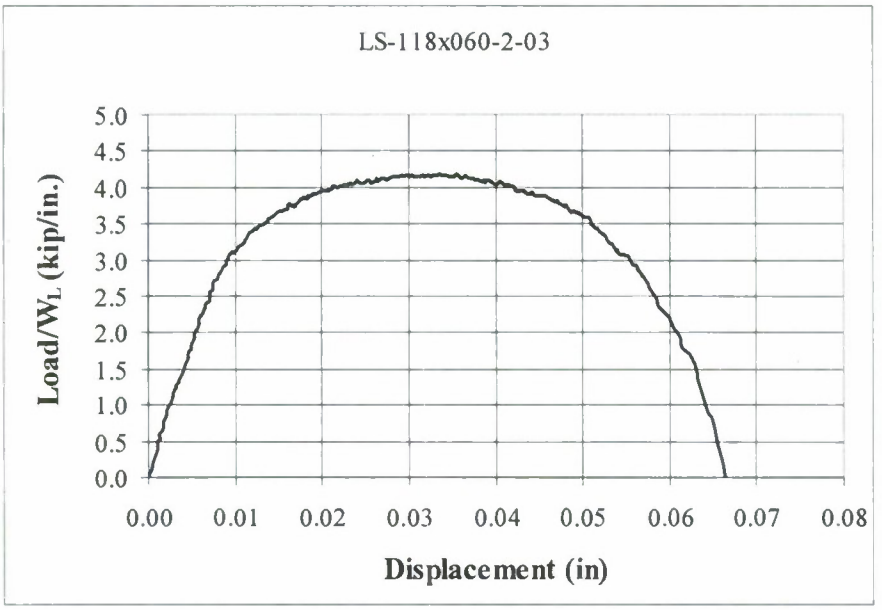
LS-118x060-2-03
Load/W_L (kip/in.)
5.0
4.5
4.0
3.5
3.0
2.5
2.0
1.5
1.0
0.5
0.0
0.00
0.01
0.02
0.03
0.04
0.05
0.06
0.07
0.08
Displacement (in)

Transverse

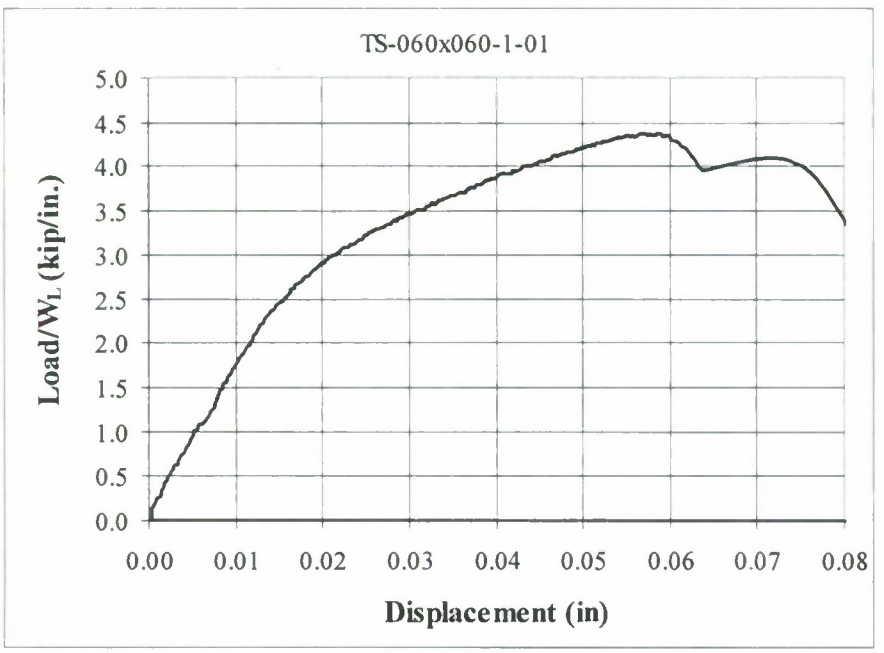
TS-060x060-1-01
Load/W_L (kip/in.)
5.0
4.5
4.0
3.5
3.0
2.5
2.0
1.5
1.0
0.5
0.0
0.00
0.01
0.02
0.03
0.04
0.05
0.06
0.07
0.08
Displacement (in)

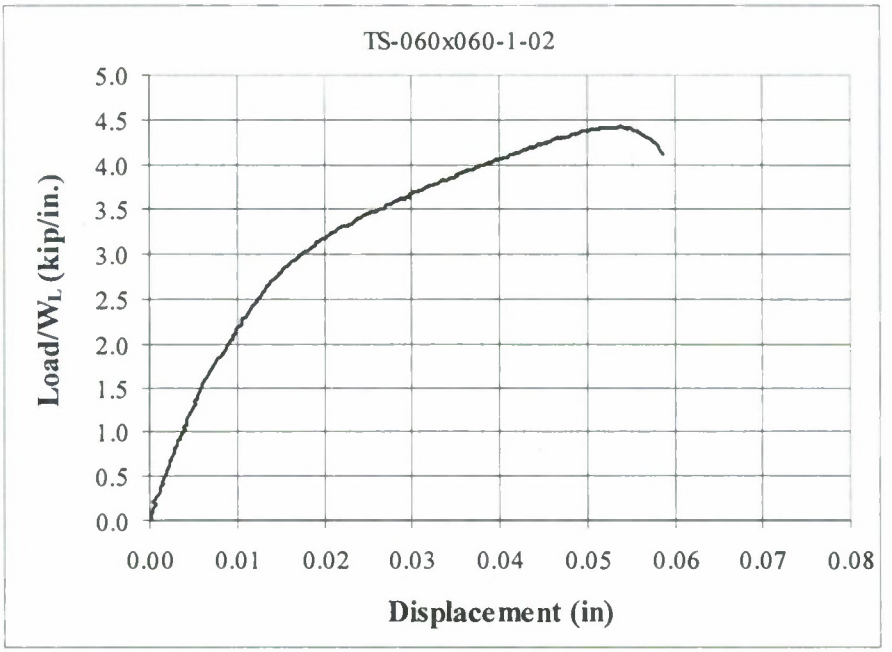
TS-060x060-1-02
Load/W_L (kip/in.)
5.0
4.5
4.0
3.5
3.0
2.5
2.0
1.5
1.0
0.5
0.0
0.00
0.01
0.02
0.03
0.04
0.05
0.06
0.07
0.08
Displacement (in)

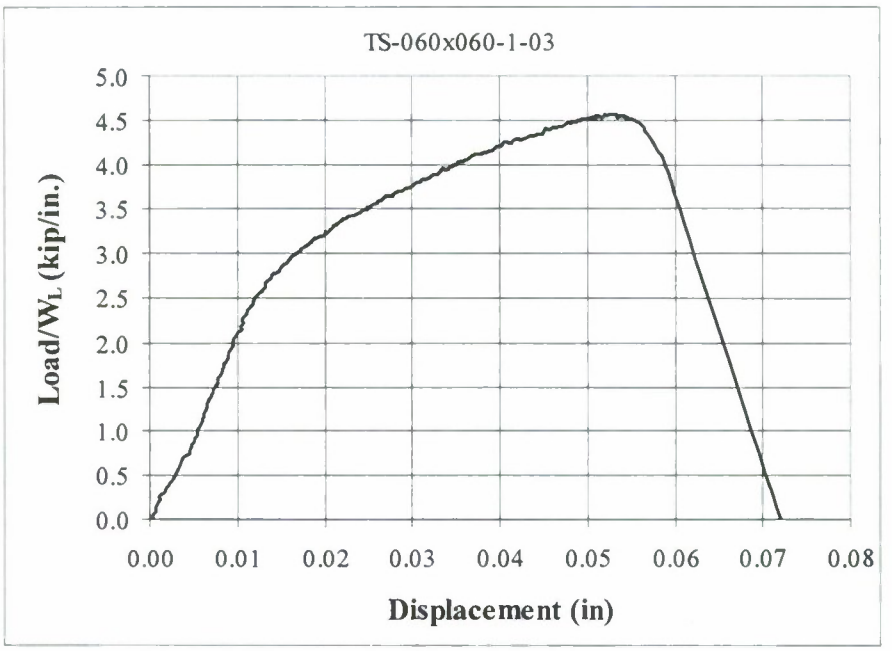
TS-060x060-1-03
Load/W_L (kip/in.)
5.0
4.5
4.0
3.5
3.0
2.5
2.0
1.5
1.0
0.5
0.0
0.00
0.01
0.02
0.03
0.04
0.05
0.06
0.07
0.08
Displacement (in)

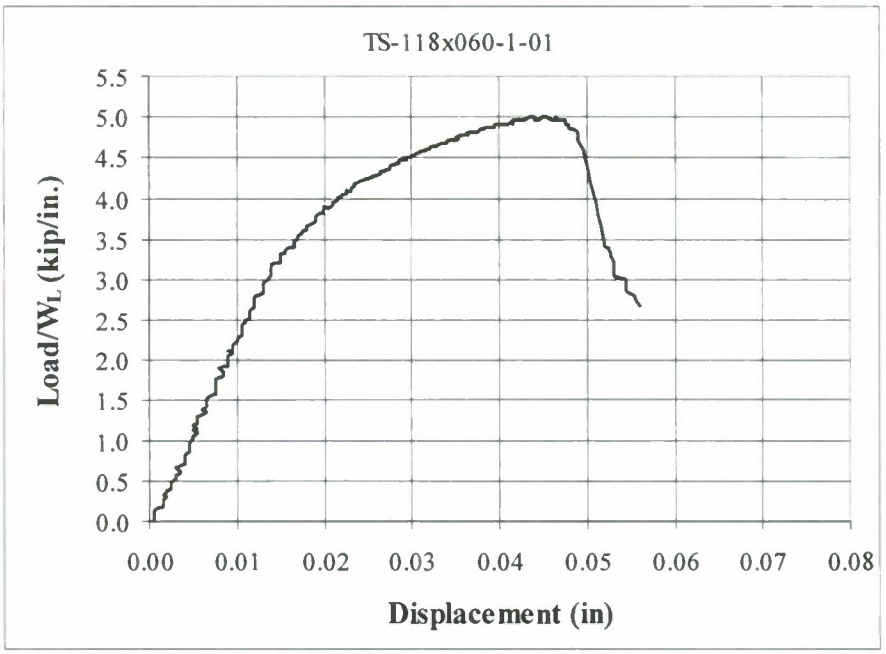
TS-118x060-1-01
Load/W_L (kip/in.)
5.5
5.0
4.5
4.0
3.5
3.0
2.5
2.0
1.5
1.0
0.5
0.0
0.00
0.01
0.02
0.03
0.04
0.05
0.06
0.07
0.08
Displacement (in)

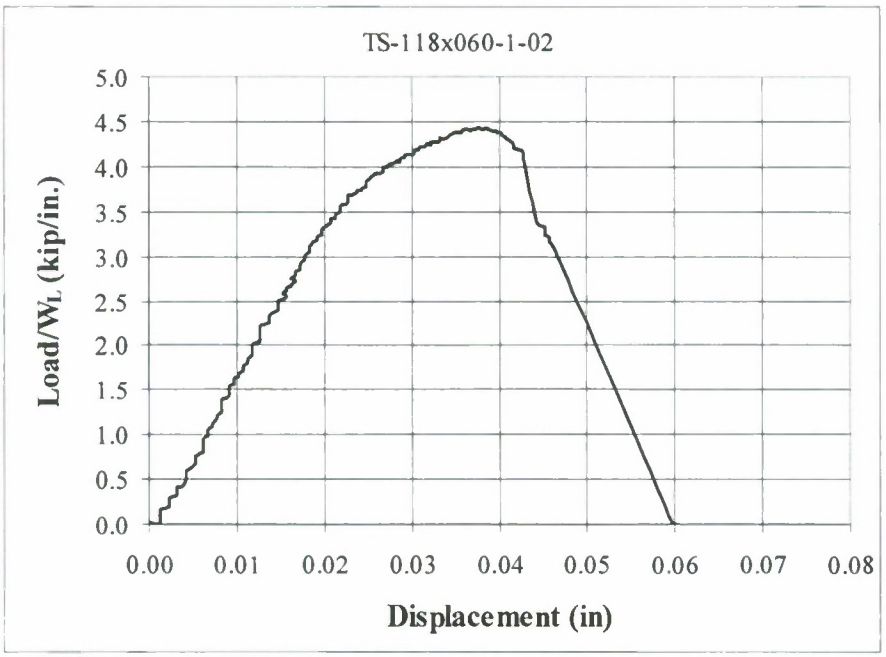
TS-118x060-1-02
Load/W_L (kip/in.)
5.0
4.5
4.0
3.5
3.0
2.5
2.0
1.5
1.0
0.5
0.0
0.00
0.01
0.02
0.03
0.04
0.05
0.06
0.07
0.08
Displacement (in)

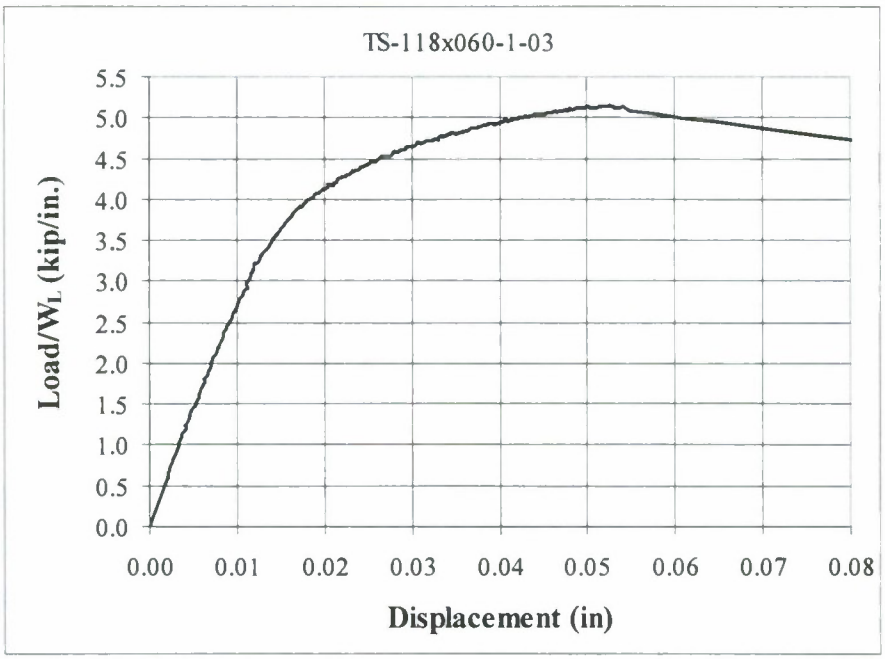
TS-118x060-1-03
Load/W_L (kip/in.)
5.5
5.0
4.5
4.0
3.5
3.0
2.5
2.0
1.5
1.0
0.5
0.0
0.00
0.01
0.02
0.03
0.04
0.05
0.06
0.07
0.08
Displacement (in)

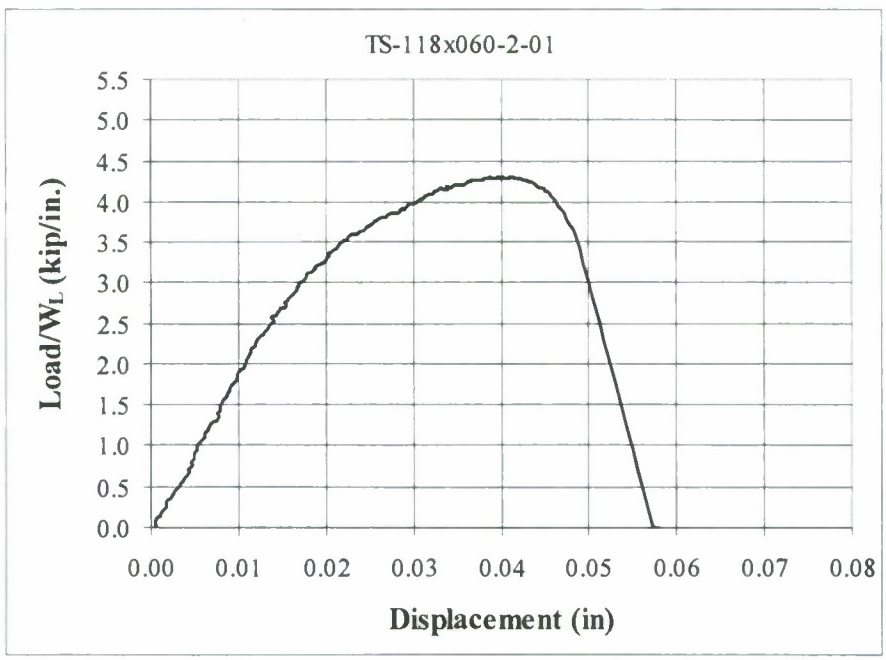
TS-118x060-2-01
Load/W_L (kip/in.)
5.5
5.0
4.5
4.0
3.5
3.0
2.5
2.0
1.5
1.0
0.5
0.0
0.00
0.01
0.02
0.03
0.04
0.05
0.06
0.07
0.08
Displacement (in)

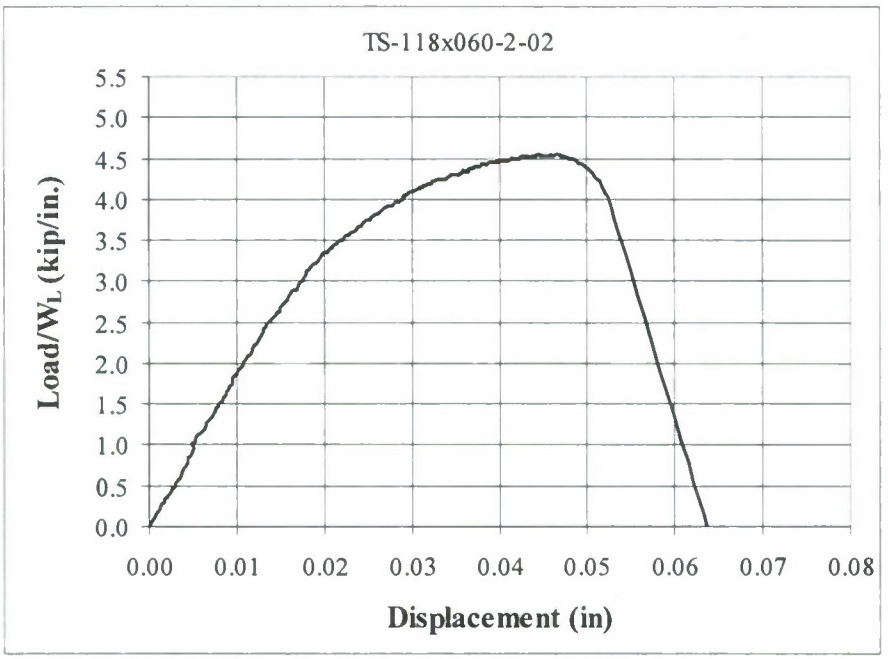
TS-118x060-2-02
Load/W_L (kip/in.)
5.5
5.0
4.5
4.0
3.5
3.0
2.5
2.0
1.5
1.0
0.5
0.0
0.00
0.01
0.02
0.03
0.04
0.05
0.06
0.07
0.08
Displacement (in)

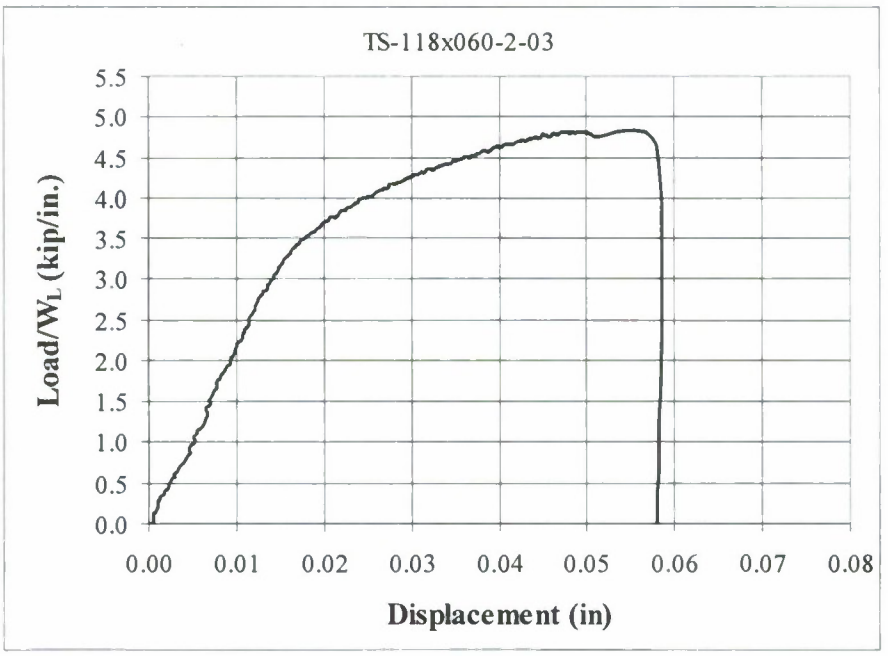
TS-118x060-2-03
Load/W_L (kip/in.)
5.5
5.0
4.5
4.0
3.5
3.0
2.5
2.0
1.5
1.0
0.5
0.0
0.00
0.01
0.02
0.03
0.04
0.05
0.06
0.07
0.08
Displacement (in)

REPORT DOCUMENTATION PAGE

Form Approved
OMB No. 0704-0188

1. REPORT DATE *(DD-MM-YYYY)*	2. REPORT TYPE	3. DATES COVERED *(From - To)*
31-July-2009	Project Report	1-Jun-2005 to 30-June-2009

4. TITLE AND SUBTITLE

ANALYSIS AND TESTING OF A TAPERED END CONNECTION FOR LASER WELDED STEEL SANDWICH PANELS

5a. CONTRACT NUMBER

5b. GRANT NUMBER
N00014-05-1-0735

5c. PROGRAM ELEMENT NUMBER

6. AUTHOR(S)

Yourlmaz, Serdar
Thompson, Lawrence
Caccese, Vincent
Vel. Senthil S.

5d. PROJECT NUMBER

5e. TASK NUMBER

5f. WORK UNIT NUMBER

7. PERFORMING ORGANIZATION NAME(S) AND ADDRESS(ES)

University of Maine
Office of Research and Sponsored Programs
5717 Corbett Hall
Orono, ME 04469-5717

8. PERFORMING ORGANIZATION REPORT NUMBER
C-2004-015-RPT-04

9. SPONSORING/MONITORING AGENCY NAME(S) AND ADDRESS(ES)

Office of Naval Research
Ballston Center Tower One
800 North Quincy St.
Arlington, VA 22217-5660

10. SPONSOR/MONITOR'S ACRONYM(S)
ONR

11. SPONSORING/MONITORING AGENCY REPORT NUMBER

12. DISTRIBUTION AVAILABILITY STATEMENT

Approved for Public Release, Distribution is Unlimited

13. SUPPLEMENTARY NOTES

14. ABSTRACT

This report summarize the analysis and cyclic testing of a laser welded steel sandwich panel end connection. Also included are monotonic tests of stake welded lap shear coupons with welds oriented both longitudinally and transverse. Steel sandwich panels offer substantial resistance to static and dynamic loads due to their high stiffness and substantial energy absorbing capacity. Panels of this kind are interest of potential use in ships and are especially efficient in resisting extreme events such as impact or shock loading. This research is conducted to investigate the mechanical behavior of a tapered steel sandwich panel end connection using finite element analysis techniques and experimental test methods. A verification study, performed comparing finite element analysis and an analytical model to an experimental study documented in the literature, demonstrates good agreement between the approaches. Finite element analyses are employed to study the response of a laser welded steel sandwich panel tapered end connection designed specifically for use in an aircraft hangar door. Performance of this connection is verified with experimental test procedures to demonstrate that the connection has adequate strength and the failure location is outside the connection region. Photogrammetry techniques are used to visualize the mechanical response. Static tests of the stake weld in a lap-shear configuration provide quantification of the weld resistance per unit length.

15. SUBJECT TERMS

Hybrid Structures; Laser Welding; Sandwich Construction; Stake Weld; Welded Connections.

16. SECURITY CLASSIFICATION OF:			17. LIMITATION OF ABSTRACT	18. NUMBER OF PAGES	19a. NAME OF RESPONSIBLE PERSON
a. REPORT	b. ABSTRACT	c. THIS PAGE			Vincent Caccese
U	U	U	UU	174	19b. TELEPONE NUMBER *(Include area code)* (207) 581-2131

Standard Form 298 (Rev. 8-98)
Prescribed by ANSI-Std Z39-18